UNIVERSITAT POLITÈCNICA DE CATALUNYA
BARCELONATECH

PhD Program in Signal Theory and Communications

Synergy between ground-based remote-sensing instruments for retrieving microphysical-optical-radiative properties of atmospheric aerosols

Doctoral thesis by:

Daniel Camilo Fortunato dos Santos Oliveira

Thesis advisor:

Michaël Sicard

Thesis tutor:

Alejandro Antonio Rodríguez-Gómez

Department of Signal Theory and Communications

Barcelona, July 2025

ACKNOWLEDGEMENTS

Thanks to everyone who helped me directly and indirectly with my PhD research.

I also thank the Spanish Ministry of Science and Innovation and Universities (PID2019-103886RB-I00) *and European Commission: H2020-Research and Innovation Framework Programme (ATMO ACCESS, grant no. 10100800 and GRASP ACE, grant no. 778349), as well as Horizon Europe Framework Programme (REALISTIC, grant no. 101086690) for their support.*

ABSTRACT

The improvements in retrieving microphysical, optical, and radiative properties of aerosols can contribute to more detailed local observations and research, support local or global climate modeling and air quality forecasting, validate satellite products, and contribute to public policies. This PhD thesis aims at achieving such improvements through synergies between ground-based remote-sensing instruments. The objectives are to (1) evaluate the potential of an inversion algorithm, namely GRASP, for retrieving aerosol properties from the synergy between a polarized Sun-sky-lunar photometer and a state-of-the-art ACTRIS/EARLINET multi-wavelength lidar, and (2) estimate long-term aerosol radiative effects by combining net radiative fluxes from pyranometers and Aerosol Optical Depth (AOD) from photometers, and assessing GRASP's ability to retrieve such effects on a case-by-case basis. To achieve Obj. 1, sensitive tests (noise-free and random noise retrievals) were performed with GRASP for several combinations of ground-based observations, including polarization information as GRASP inputs, for three aerosol scenarios in Barcelona, Spain. The sensitive tests showed that the addition of the Degree of Linear Polarization (DoLP) improved the noise-free and random-noise GRASP inversions, particularly under higher AOD. The gains were most notable for the coarse mode of the optical properties, and for the coarse mode of the Real Refractive Index. To achieve Obj. 2, a direct method was applied to estimate spectral Aerosol Forcing Efficiency (AFE) and Aerosol Radiative Forcing (ARF) for a 14-year database in Barcelona, Spain. The AFE-ARF estimations confirmed a dominant cooling forcing over Barcelona, with the strongest cooling effect caused by mineral dust, followed by urban/industrial-biomass burning and mixed aerosols. Furthermore, the GRASP inversions with DoLP were more accurate for the ARF, agreeing with the direct method in the high-AOD cases.

Keywords: Ground-based synergies; GRASP; DoLP; radiative fluxes; AOD; Aerosol Forcing Efficiency; Aerosol Radiative Forcing.

RESUMO

As melhorias na obtenção das propriedades microfísicas, ópticas e radiativas dos aerossóis podem contribuir para observações e pesquisas locais mais detalhadas, apoiar a modelagem climática em escala local ou global e a previsão da qualidade do ar, validar produtos de satélite e subsidiar políticas públicas. Esta tese de doutorado tem como objetivo alcançar tais melhorias por meio de sinergias entre instrumentos de sensoriamento remoto baseados em solo. Os objetivos são: (1) avaliar o potencial de um algoritmo de inversão, GRASP, para obter propriedades de aerossóis a partir da sinergia entre um fotômetro polarizado e um lidar multicomprimento de onda de última geração da rede ACTRIS/EARLINET; e (2) estimar os efeitos radiativos de aerossóis em longo prazo combinando fluxos radiativos líquidos obtidos por piranômetros e a Profundidade Óptica de Aerossóis (AOD) dos fotômetros, além de avaliar a capacidade de GRASP em calcular tais efeitos caso-a-caso. Para alcançar o Obj. 1, foram realizados testes de sensibilidade (inversões livres de ruído e com ruído aleatório) em GRASP, utilizando várias combinações de observações de solo, incluindo informações de polarização como entradas do algoritmo, de três cenários de aerossóis em Barcelona, Espanha. Os testes mostraram que a adição do Grau de Polarização Linear (DoLP) melhorou as inversões de GRASP, tanto para os casos livres de ruído quanto para os com ruído aleatório, especialmente sob condições de AOD elevado. Os ganhos foram mais notáveis para o modo grosso das propriedades ópticas e para o modo grosso do Índice de Refração Real. Para atingir o Obj. 2, foi aplicado um método direto para estimar a Eficiência do Forçamento dos Aerossóis (AFE) espectral e o Forçamento Radiativo dos Aerossóis (ARF) para 14 anos de dados em Barcelona, Espanha. As estimativas de AFE e ARF confirmaram um forçamento de resfriamento dominante, com o efeito de resfriamento mais intenso causado pela poeira mineral, seguido pelos aerossóis urbano/industriais-biomassa e pelos aerossóis mistos. Além disso, as inversões com DoLP realizadas por GRASP foram mais precisas para ARF, concordando com o método direto nos casos com AOD elevado.

Palavras-chave: Sinergias baseadas em solo; GRASP; DoLP; fluxos radiativos; AOD; Eficiência do Forçamento de Aerossóis; Forçamento Radiativo de Aerossóis.

RESUMEN

Las mejoras en la recuperación de propiedades microfísicas, ópticas y radiativas de los aerosoles pueden contribuir a observaciones e investigaciones locales más detalladas, apoyar la modelización climática local o global y la previsión de la calidad del aire, validar productos satelitales y contribuir a las políticas públicas. Esta tesis doctoral tiene como objetivo lograr tales mejoras mediante sinergias entre instrumentos de teledetección terrestres. Los objetivos son: (1) evaluar el potencial de un algoritmo de inversión, concretamente GRASP, para recuperar propiedades de los aerosoles a partir de la sinergia entre un fotómetro solar-celeste-lunar polarizado y un lidar multicanal de última generación de ACTRIS/EARLINET, y (2) estimar los efectos radiativos a largo plazo de los aerosoles combinando flujos radiativos netos de piranómetros y la Profundidad Óptica de Aerosoles (AOD) de fotómetros, evaluando la capacidad de GRASP para recuperar dichos efectos caso por caso. Para alcanzar el Obj. 1, se realizaron pruebas de sensibilidad (recuperaciones sin ruido y con ruido aleatorio) con GRASP para varias combinaciones de observaciones terrestres, incluyendo la información de polarización como entrada en GRASP, en tres escenarios de aerosoles en Barcelona, España. Las pruebas mostraron que la adición del Grado de Polarización Lineal (DoLP) mejoró las inversiones de GRASP tanto sin ruido como con ruido aleatorio, particularmente bajo altos valores de AOD. Las mayores mejoras se observaron en el modo grueso de las propiedades ópticas y en el índice de refracción real del modo grueso. Para alcanzar el Obj. 2, se aplicó un método directo para estimar la Eficiencia del Forzamiento de Aerosoles (AFE) y el Forzamiento Radiativo por Aerosoles (ARF) espectrales en una base de datos de 14 años en Barcelona. Las estimaciones de AFE-ARF confirmaron un forzamiento de enfriamiento dominante sobre Barcelona, siendo el polvo mineral el responsable del efecto de enfriamiento más fuerte, seguido por los aerosoles urbanos/industriales y de quema de biomasa, y los aerosoles mixtos. Además, las inversiones de GRASP con DoLP fueron más precisas para el ARF, coincidiendo con el método directo en los casos con AOD alto.

Palabras clave: Sinergias desde tierra; GRASP; DoLP; flujos radiativos; AOD; Eficiencia del Forzamiento de Aerosoles; Forzamiento Radiativo de Aerosoles.

RESUM

Les millores en la recuperació de les propietats microfísiques, òptiques i radiatives dels aerosols poden: contribuir a observacions i investigacions locals més detallades, donar suport a la modelització climàtica local o global i a la previsió de la qualitat de l'aire, validar productes de satèl·lit i contribuir a les polítiques públiques. Aquesta tesi doctoral té com a objectiu assolir aquestes millores mitjançant sinergies entre instruments de teledetecció terrestres. Els objectius són: (1) avaluar el potencial d'un algoritme d'inversió, concretament GRASP, per recuperar propietats dels aerosols a partir de la sinergia entre un fotòmetre solar-celeste-lunar polaritzat i un lidar multiespectral d'última generació ACTRIS/EARLINET, i (2) estimar els efectes radiatius a llarg termini dels aerosols combinant els fluxos radiatius nets mesurats amb piranòmetres i la profunditat òptica d'aerosols (AOD) obtinguda amb fotòmetres, i avaluar la capacitat de GRASP per recuperar aquests efectes cas per cas. Per assolir l'Objectiu 1, es van dur a terme proves de sensibilitat (sense soroll i amb soroll aleatori) amb GRASP per a diverses combinacions d'observacions terrestres, incloent-hi la informació de polarització com a entrada al GRASP, per a tres escenaris d'aerosols a Barcelona. Les proves van mostrar que l'addició del Grau de Polarització Lineal (DoLP) millorava les inversions de GRASP tant sense soroll com amb soroll aleatori, especialment en condicions d'AOD elevat. Els guanys més destacats es van observar en el mode gros de les propietats òptiques i en l'índex de refracció real del mode gros. Per assolir l'Objectiu 2, es va aplicar un mètode directe per estimar l'Eficiència del Forçament dels Aerosols (AFE) i el Forçament Radiatiu dels Aerosols (ARF) espectral en una base de dades de 14 anys a Barcelona. Les estimacions d'AFE-ARF van confirmar un forçament de refredament dominant sobre Barcelona, sent el pols mineral el responsable del refredament més intens, seguit pels aerosols urbans/industrials i de combustió de biomassa, i pels aerosols mixtos. A més, les inversions de GRASP amb DoLP van resultar més precises per a l'ARF, coincidint amb el mètode directe en els casos amb AOD elevat.

Paraules clau: Sinergies des de terra; GRASP; DoLP; fluxos radiatius; AOD; Eficiència del Forçament dels Aerosols; Forçament Radiatiu dels Aerosols.

RÉSUMÉ

Les améliorations de la restitution des propriétés microphysiques, optiques et radiatives des aérosols peuvent contribuer à des observations et recherches locales plus détaillées, à un meilleur soutien à la modélisation climatique locale, régionale ou globale ainsi qu'à la prévision de la qualité de l'air, à valider les produits satellitaires et à contribuer aux politiques publiques. Cette thèse de doctorat vise à atteindre de telles améliorations grâce à des synergies entre instruments de télédétection au sol. Les objectifs sont : (1) évaluer le potentiel d'un algorithme d'inversion, à savoir GRASP, pour restituer les propriétés des aérosols à partir de la synergie entre un photomètre solaire-céleste-lunaire polarisé et un lidar multi-longueurs labélisé ACTRIS ; et (2) estimer les effets radiatifs des aérosols à long terme en combinant les flux radiatifs nets mesurés par pyranomètres avec l'épaisseur optique des aérosols (AOD) mesurée par photomètres, et en évaluant la capacité de GRASP à restituer ces effets au cas par cas. Pour atteindre l'Objectif 1, des tests de sensibilité (sans bruit et avec bruit aléatoire) ont été réalisés avec GRASP pour plusieurs combinaisons d'observations au sol, en incluant l'information de polarisation parmi les entrées de GRASP, pour trois scénarios d'aérosols à Barcelone, Espagne. Les tests de sensibilité ont montré que l'ajout du Degré de Polarisation Linéaire (DoLP) a amélioré les inversions GRASP, tant sans bruit qu'avec bruit aléatoire, en particulier pour des AOD élevées. Les gains les plus notables ont été observés pour le mode grossier des propriétés optiques et pour l'indice de réfraction réel du mode grossier. Pour atteindre l'Objectif 2, une méthode directe a été appliquée pour estimer l'Efficacité du Forçage des Aérosols (AFE) et le Forçage Radiatif des Aérosols (ARF) spectral à partir d'une base de données de 14 ans à Barcelone. Les estimations AFE-ARF ont confirmé un forçage de refroidissement dominant à Barcelone, le plus fort étant dû aux poussières minérales, suivi des aérosols urbains/industriels issus de la combustion de biomasse, puis des aérosols mixtes. En outre, les inversions GRASP avec DoLP se sont révélées plus précises pour l'ARF, en accord avec la méthode directe dans les cas de forte AOD.

Mots-clés : Synergies au sol ; GRASP ; DoLP ; flux radiatifs ; AOD ; Efficacité du Forçage des Aérosols ; Forçage Radiatif des Aérosols.

LIST OF FIGURES

LIST OF TABLES

LIST OF ABBREVIATIONS AND ACRONYMS

AA	Azimuth Angle
AAOD	Spectral Absorption AOD
ACTRIS	Aerosol, Clouds and Trace Gases Research Infrastructure
AD-NET	Asian Dust and Aerosol Lidar Observation Network
AE	Ångström Exponent
AEP	Ångström Exponent Profile
aer	"aerosol" suffix
AERONET	AErosol RObotic NETwork
AF	Asymmetry Factor
AFE	Aerosol Forcing Efficiency
AOD	Aerosol Optical Depth
APD	Avalanche Photodiode
ARF	Aerosol Radiative Forcing
AT	Aerosol types
ATLID	ATmospheric LIDar
ATMF	Atmospheric forcing
AVC	Aerosol Column-integrated Volume Concentration
AVP	Vertical distribution of the aerosol concentration or Aerosol Vertical Profile
B	Direct radiation
BC	Black Carbon
BMX	Beam expander
BOA	Bottom of the Atmosphere
BPDF	Bidirectional Polarization Distribution Function
BRDF	Bidirectional Reflectance Distribution Function
BSRN	Baseline Surface Radiation Network
CALIOP	Cloud-Aerosol Lidar with Orthogonal Polarization
CALIPSO	Cloud-Aerosol Lidar and Infrared Pathfinder Satellite Observations
CCN	Cloud Condensation Nuclei
CH_2O	Formaldehyde
CH_4	Methane
CI95	95% Confidence Interval
CIS-LiNet	Commonwealth of Independent States Lidar Network
CO_2	Carbon dioxide
COBALD	Compact Optical Backscatter AerosoL Detector
Comb.	Combination(s)
corr	Correlation coefficient
D	Diffuse radiation or daytime combination
DA	Day Angle
DBFA	Downward Broadband Flux with Aerosol
$DBFA_0$	Downward Broadband Flux without Aerosol
DD	Desert Dust
DIAL	Differential-Absorption Lidar

Diff	Difference
DoLP	Degree of Linear Polarization
EARLINET	European Aerosol Research Lidar NETwork
EarthCARE	Earth Cloud Aerosol and Radiation Explorer
ESD	Relative Earth-Sun Distance
ESRL	Earth System Research Laboratories
F	Radiative flux
FMF	Fine Mode Fraction
FOV	Field of view
G	Global (or total) radiation
GARRLiC	Generalized Aerosol Retrieval from Radiometer and Lidar Combined data
GASSP	Global Aerosol Synthesis and Science Project
GAW	Global Atmosphere Watch
GRASP	Generalized Retrieval of Atmosphere and Surface Properties
GT	Ground Temperature
H_2O	Water vapor
HCl	Hydrochloric acid
IAGOS	In-service Aircraft for a Global Observing System
IG	Initial guess
IMP	Institute of Mathematics of Potsdam University
INC	Integrated number concentration
interp	Interpolated
IR	Infrared
IRI	Spectral Imaginary Refractive Index
KFS	Klett-Fernald-Sasano
L1.5	Level 1.5
L2	Level 2
Lag	Lagrange
LALINET	Latin American Lidar Network
Laser	Light Amplification by Stimulated Emission of Radiation
LH	Latent heat fluxes
LidAlm	Lidar and Almucantar
Lidar	light detection and ranging
LIRIC	LIdar-Radiometer Inversion Code
LOA	*Laboratoire d'Optique Atmosphérique*
LR	Lidar Ratio or linear regression
LRP	Lidar Ratio Profile
LSM	Least Squares Method
LW	Long-wave radiation
MA	Mixed Aerosols
Manufac.	Manufacturer
max	“maximum” suffix
min	“minimum” suffix
MISR	Multi-angle Imaging SpectroRadiometer
MK	Mann-Kendall test
MODIS	MODerate resolution Imaging Spectroradiometer

mol	“molecule” suffix
MPLNET	Micro-pulse Lidar Network
N	Complex refractive index or simple size
N_2	Nitrogen
N_2O	Nitrous oxide
NADH	Nicotinamide Adenine Dinucleotide Phosphate with hydride donors
NAF	Net Aerosol Forcing
NASA	National Aeronautics and Space Administration
nat	“natural or unpolarized light” suffix
Nd:YAG	Neodymium-doped Yttrium Aluminum Garnet
NDACC	Network for the Detection of Atmospheric Composition Change
NF	Noise-free
NFIR	Net Far Infrared Radiation
NH_4	Ammonium
NMB	Normalized Mean Bias
NO	Nitric oxide
NO_2	Nitrogen dioxide
NOAA	National Oceanic and Atmospheric Administration
NR	Net (total) Radiation
NSD	Number size distribution
NSR	Net Solar Radiation
O_2	Oxygen
O_3	Ozone
PAR	Photosynthetically Active Region
PARASOL	Polarization and Anisotropy of Reflectances for Atmospheric Sciences coupled with Observations from a Lidar
PE	Percentage Error
PFR	Precision Filter Radiometer
PHOTONS	*PHOtométrie pour le Traitement Opérationnel de Normalisation Satellitaire*
P-MPL	Polarized-Micro-Pulse Lidar
PMT	Photomultiplier Tube
pol	“polarized light” suffix
POLDER	POLarization and Directionality of the Earth’s Reflectances
POLIPHON	Polarization Lidar Photometer Networking
PRR	Pure-Rotational Raman
QF	Quadratic fitting
Ra	Raman
RCS	Range Corrected Signal
RCS_n	Normalized lidar profile
Ref(s).	Reference(s)
Resid.	Residuals
RH	Relative Humidity
RMSE	Root Mean Square Error
RN	Random noises
RRI	Spectral Real Refractive Index
RT	Radiative Transfer

RTC	Radiative Transfer Code
Sc.	Aerosol scenario
SCC	Single Calculus Chain
SD	Size Distribution
SData	Sensor Data
SF	Sphere Fraction
SH	Sensible heat fluxes
SKYNET	Sky Radiometer Network
SO_2	Sulfur dioxide
SolRad-Net	Solar Radiation Network
SORD/SOS	Successive ORDers of scattering
SP	Size Parameter
sr	steradian
SSA	Single Scattering Albedo
SSAP	Single Scattering Albedo Profile
SSP	Shared Socio-economic Pathway scenarios
ST	Sky Temperature
std	Standard deviations
SURFRAD	SURFace RADiation Budget
SW	Short-wave radiation
SZA	Solar Zenith Angle
TOA	Top of the Atmosphere
UBFA	Upward Broadband Flux with Aerosol
$UBFA_0$	Upward Broadband Flux without Aerosol
UI-BB	Urban/Industrial-Biomass Burning aerosols
UPC	Universitat Politècnica de Catalunya
UV	Ultraviolet
V2	Version 2
V3	Version 3
VC	Volume Concentration Profile
VRR	Vibro-Rotational Raman
VSD	Volume Size Distribution
WDCA	World Data Centre for Aerosols
WRMC	World Radiation Monitoring Center
YAML	YAML Ain't Markup Language
Yr	Year
ZA	Zenith Angles

LIST OF SYMBOLS

0*	Vector of zeros
A	Albedo
a*	Vector of *a priori* estimates
a^p	Inputs of the Forward Model at the p-th iteration
A_T	Effective telescope area
b	Wien's constant
c	Speed of light in the vacuum
C	System constant
Cc0-3	Calibration coefficients
dσ/dΩ	Backscatter cross-section
E_L	Emitted energy per laser pulse
f	Frequency shift
$f(a^p)$	Simulated observations at the p-th iteration
$f(RH)$	Hygroscopic growth factor
f*	Set of measurements
F_{1-3}	Filter 1 to 3
F_B	Fractional bias
f_s	Frequency of λ_s
$g_i(\lambda_z)$	Optical data in a specific range
h	Planck's constant
I	Emitted/transmitted radiation
$I_{(R, max)}$	Integral of the RCS
I_0	Incident radiation
ik	Imaginary part of the complex refractive index
I_n	Spectral normalized radiances
I_{net}	Net irradiance on the surface and without aerosol (subscript 0)
I_{total}	Total radiance (polarized + unpolarized)
$I_{\lambda,0}$	Incident monochromatic beam
J	Function that governs the electromagnetic-radiation transfer
k	Raman shift for a specific molecule
K_i	Kernel efficiency
L	Lidar signal or RCS
M	Matrix of coefficients of the derivatives
m	Optical airmass
n	Real part of the complex refractive index
N_{Ra}	Molecule number density of the reference gas
nw	Number of modes
Ø	Diameter
O	Overlap function
$Ø_{eff}$	Effective particle diameter
$Ø_g$	Geometric median diameter
P	Optical return power
P	Polarization

$P(\Theta)$	Phase function
Pg	Pyrgeometers
Pm	Polynomials
Py	Pyranometers
Q	Magnitude of linear polarization
Q_{abs}	Absorption efficiencies
Q_{sca}	Scattering efficiencies
r	Particle radius
R	Vertical height
r^2	Coefficient of determination
r_{eff}	Effective radius
R_{stp}	Altitude step
r_v	Volume mean radius
s	Shape of the particles
S	Stokes' parameters
Sg	Electromagnetic signal
T	Transmittance
T_b	Absolute temperature of the blackbody
Tg	Interaction target
T_L	Lidar transmission
T_{max}^2	Two-way total transmittance of the lidar maximum range
Ts	Temperature of the sensors
T_y	Transmission of absorbing gases
U	Direction of linear polarization
v	Frequency of the wavelength
V	Magnitude of circular polarization
V_0	Extraterrestrial voltage
V_λ	Digital voltage observed at λ
w	Each aerosol mode
x	experimental voltage
y	Normalized total extinction coefficient
α	Raman channels or extinction coefficient
α_{ct}	Constant extinction
β	Elastic channels or backscatter coefficient
$\beta_\perp$	Linearly polarized backscatter in the perpendicular direction (cross-polar)
$\beta_\parallel$	Linearly polarized backscatter in the parallel direction (co-polar)
β_{ct}	Constant backscatter
γ	Hygroscopic fit parameter
Δ	Errors in the system of equations or a parameter variation
δ(R)	Linear depolarization ratio
Δ(Δa)	Vector of the uncertainties characterizing the deviations of the differences from the zeros
Δa*	Vector of the uncertainties in *a priori* estimates
δAE	AE difference
Δf	Vector of measurement errors
δ^p	Particle depolarization ratio

δ^{v}	Volume depolarization ratio
ϵ^{exp}	Data error
η	Fractional contribution to the total AOD
Θ	Scattering angle
λ	(Reference) Wavelength
λ^{-ex}	Scattered wavelength dependency
λ_{Ra}	Raman Wavelength
λ_{s}	Scattered wavelength
ξ	Dependency of the lidar wavelength
σ_{abs}	Aerosol absorption
σ_{ext}	Aerosol extinction
σ_{g}	Geometric standard deviation
σ_{sca}	Aerosol scattering
τ	Atmospheric optical thickness
υ	Volume concentration of particles per radius interval dr
υ_{D}	Relative speed along the line of sight of the lidar Doppler
Φ	Azimuthal angle
$\mathbb{C}$	Klett's constant

TABLE OF CONTENTS

1 INTRODUCTION

*I dedicate this chapter to Prof. Judith Johanna Hoelzemann for **introducing** me to the world of aerosols.*

Reuse!

1.1 RELEVANCE AND MOTIVATION OF THE THESIS

Aerosols, also known as atmospheric particles, play a fundamental role in climate because of their abilities to scatter and absorb solar and terrestrial radiation, and to act as nuclei upon which cloud droplets and ice particles form and aggregate into cloud structures known to dominate the Earth's albedo [1]. According to Ref. [2], aerosol emissions also lead to a net global warming[1] by 2100 of likely 0.4 to 0.9 °C relative to 2019 in high and very high greenhouse-gas-emissions scenarios (SSP3-7.0 and SSP5-8.5)[2]. Furthermore, these particles have an impact on human health [4–6], visibility [4,7,8], and provide nutrients to the ocean [9–13] and forests [14,15], as dust particles [16–18], the long-distance transport of which contributes significantly to the global aerosol burden [19].

Regarding aerosol effects on climate, the direct effect is the radiation attenuation. Nowadays, this effect is named as aerosol-radiation interaction [20]. In general, scattering affects the climate by reflecting part of the available radiation back to space, and absorption can cool the surface and warm the atmosphere [21]. The indirect effect or aerosol-cloud interactions [20] modifies the cloud microphysics and its lifetime [22,23], altering cloud properties [24] like albedo, thickness, and cloud coverage in response to changes in droplet concentrations [25] due to the aerosols are Cloud Condensation Nuclei (CCN), which influence the number, size, and atmospheric lifetime of cloud droplets [26]. Both effects contribute to the radiative budget and the meteorological events, especially monsoon circulation [27]. Instantaneous change in the radiative budget [20], known as radiative forcing, impacts the climate [28]. Additionally, Ref. [20] distinguished forcing from rapid adjustments, which modify the radiative budget indirectly through fast atmospheric and surface changes. Figure 1.1 outlines how aerosols induce meteorological

[1] Concerning to local climate change, Ref. [3] showed that the Mediterranean region observed increase in hydrological and agricultural and ecological droughts, with medium confidence, projected increase in aridity and fire weather conditions at global warming of 2°C and above, with high confidence.

[2] SSP means Shared Socio-economic Pathway scenarios. They were developed by the Intergovernmental Panel on Climate Change to study the future climate projections with different levels: five scenarios (1 to 5) plus radiative forcing (1.9, 2.6, 4.5, 7.0, and 8.5 Wm^{-2}) associated with temperature increases ~1.5, ~1.8-2, ~2.7-3, ~3.6-4.5, and ~4-5 ºC, respectively.

parameters (temperature, wind, and humidity, for example), hence, atmospheric circulation and precipitation.

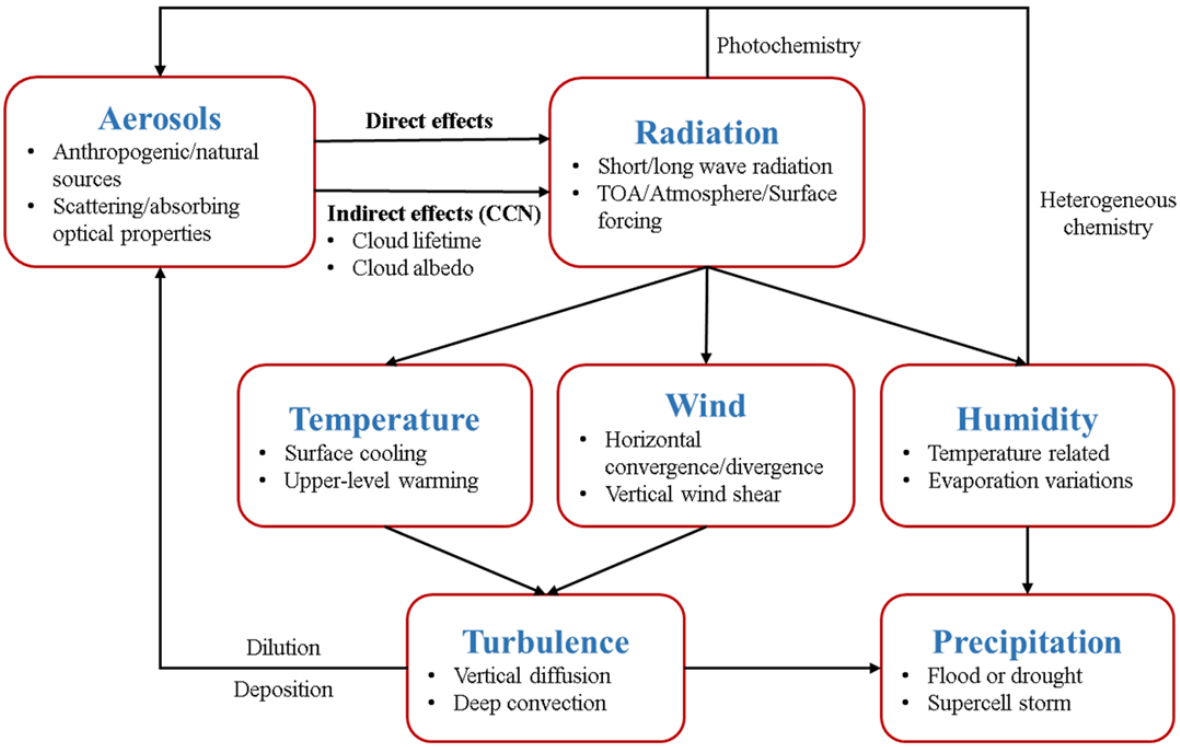

Figure 1.1. Scheme of the aerosol direct and indirect radiative forcings and their potential impact on the meteorological parameters. This figure is available in Ref. [27].

The mentioned forcing depends on the aerosol load and type, and quantifies the contribution of aerosols to the climate. It is often expressed by the Aerosol Radiative Forcing (ARF) and the Aerosol Forcing Efficiency (AFE). The ARF is the difference between the shortwave net irradiances with and without aerosols, i.e., the change in the radiation flux produced by the particles [29], and the AFE is the change in the net radiation per unit of Aerosol Optical Depth (AOD) [30,31] at a specific wavelength. Furthermore, the AOD is an important optical property that impacts the radiation budget. It characterizes the aerosol load in the atmospheric column, and it enhances or reduces solar radiation at the surface, brightening and dimming effects, respectively [32].

Atmospheric aerosol is itself a non-linear system, and the impact on climate depends on the microphysical and chemical properties of the particles [33]. The

microphysical and chemical properties of aerosols define their optical and radiative properties, which directly modify the Earth-atmosphere radiative forcing sign, based on the scattering and absorption of the incoming solar and outgoing thermal radiation [34]. The optical properties (absorption and scattering) sum up and form the extinction [35], which depends on the pathway through the atmosphere and its components. These optical properties are also dependent on the aerosol type [36]: e.g., while the absorption increases with increasing wavelength for mineral dust and urban pollution, the scattering decreases (with increasing wavelength) for mineral dust and increases for urban pollution [37].

Furthermore, the radiative properties usually refer to the term of single scattering albedo, which is defined as the fraction of extinction due to scattering [38], the phase function describes how radiation is scattered by a particle [4], and the Asymmetry Factor indicates the direction of scattering. These aerosol properties and the complex refractive index (which governs both scattering and absorption [39] in a medium, atmosphere) contribute to the aerosol forcing.

In the last decades, advances in aerosol monitoring have increased because the aerosol impact on Earth's radiation has large sources of uncertainties [40–42]. These uncertainties rely on the variability of aerosol optical properties and the spatial-temporal distribution [43], leading to aerosol observations by using ground-based remote-sensing instruments, such as lidar systems, photometers, and others, to invert the measured signal into aerosol properties or to measure the attenuated global radiation that reaches the ground (in the case of pyranometers). In light of this, the Universitat Politèctica de Catalunya (UPC) in Barcelona, Spain, has been performing aerosol observations for more than two decades in the Aerosol, Clouds and Trace Gases Research Infrastructure (ACTRIS) framework, needing to establish a long-term time series of ARF in Barcelona.

It is worth noting that some algorithms have been developed to enhance the inversions of aerosol properties, e.g., the AErosol RObotic NETwork (AERONET) inversions from sun-photometer data [44–49], among others. Moreover, those ground-based instruments have been widely used to improve the retrieval of the

optical-microphysical properties of aerosols through synergies between them, especially since the 2000s. For example, Ref. [50] pioneered estimating aerosol forcing with pyranometers and radiometers. Another synergy is the well-known inversion that combines lidars and photometers, owing to the first instrument delivering a vertical structure of the atmosphere, including the aerosol distribution, and the second delivering integrated aerosol properties in the atmospheric column, both at multiple wavelengths. Specifically, lidar observations improve sensitivity to the columnar properties of aerosol, while radiometric observations provide sufficient constraints on aerosol amount and type that are generally missing in lidar signals [51].

Ref. [52] proposed one of the first combinations between lidar and photometer to retrieve the optical properties of the altitude-inhomogeneous aerosol layer. Then, Refs. [53–55] presented a code combining lidar, photometer, and particle counter data with a regularization software tool for aerosol microphysical property retrieval. Refs. [56–58] developed lidar-radiometer synergetic algorithms named LIdar-Radiometer Inversion Code (LIRIC) for processing data from European AErosol Research LIdar NETwork (EARLINET). Ref. [59] developed the Lidar and Almucantar (LidAlm), combining elastic backscatter lidar and AERONET inversions; likewise, Refs. [60,61] developed a code called Polarization Lidar Photometer Networking (POLIPHON) to retrieve the vertical profile of the fine and coarse modes of particle mass concentrations for ash and non-ash particles. Ref. [62] presented another synergic technique, which derived the concentration of aerosol components from AERONET inversions and Micro-pulse Lidar Network (MPLNET) measurements.

A promising algorithm was developed recently by Ref. [51], Generalized Aerosol Retrieval from Radiometer and Lidar Combined (GARRLiC) data, to invert coincident lidar and radiometer observations and to derive a united set of aerosol parameters [51,63]. It is now integrated in the Generalized Retrieval of Atmosphere and Surface Properties (GRASP) algorithm, and it was adapted from the method developed by Ref. [64].

Following up on the aerosol retrievals, the observations with polarimetric capabilities can improve the retrieval accuracy of aerosol properties [65–69], because the light scattered by the particles is not only affected in intensity but also in the direction of the electric field associated [70], defined by the polarization. Therefore, the polarization information may be of help to improve the accuracy of aerosol property inversion.

1.2 OBJECTIVES OF THE THESIS

The first goal of this PhD is to evaluate the potential of the GRASP code to retrieve aerosol properties from the synergy between a polarized Sun-sky-lunar photometer and the UPC/EARLINET three-wavelength elastic lidar (the state-of-the-art lidar + photometer). This goal will allow assessing some unique combinations of the state of the art that have not been inverted yet.

The second goal aims to estimate long-term aerosol radiative effects by combining net radiative fluxes from pyranometers and AOD from photometers (ground-based observations) in the direct method [71], focusing on the global solar radiation at the Bottom of the Atmosphere (BOA). Furthermore, this goal also aims to assess GRASP's ability to retrieve such effects on a case-by-case basis.

It is important to note that this PhD is ambitious in answering the following questions: Are the inversions from the synergy algorithm (GRASP) sensitive to the Degree of Linear Polarization (DoLP)? What is the contribution of this synergy to the retrieval of optical and microphysical properties of aerosols? Will this synergy be able to retrieve the aerosol radiative forcing adequately? What is the contribution of aerosols to the radiative forcing over Barcelona, Spain?

1.3 ESTRUCTURE OF THE THESIS

This manuscript is organized into seven chapters and five appendices, with complementary information about the development and discussion of the research, as follows:

- Chapter I introduces the relevance of aerosols in the Earth's radiative balance and describes the objectives of this thesis;
- Chapter II presents the main background information about the radiation-aerosol interaction and the ground-based instruments used in this research;
- Chapter III presents the main aerosol inversion algorithms, focusing on the GRASP/GARLLiC code;
- Chapter IV describes the methodology employed to retrieve optical-microphysical-radiative aerosol properties from ground-based synergies;
- Chapter V discusses the results of the GRASP code for retrievals from the synergy of the state-of-the-art lidar + photometer;
- Chapter VI discusses the results of the estimation of the long-term aerosol radiative effects and GRASP retrievals on a case-by-case basis;
- Chapter VII concludes and presents the perspectives of the overall study;
- Appendix A contains an example of the UPC SData file;
- Appendix B presents the hybrid profiles as an initial-guess attempt to create synthetic data from GRASP algorithm;
- Appendix C contains the long-term spectral AFE-ARF, continuing the results of Chapter VI;
- Appendix D contains other AFE-ARF definitions;
- Appendix E contains the publications developed during the research period.

2 RADIATION, ATMOSPHERIC AEROSOLS, AND THEIR GROUND-BASED OBSERVATIONS

*I dedicate this chapter to my family, my country of birth (Brazil), God, and my friends. They are my **background**!*

Reduce!

This chapter provides a background about aerosol, radiation, their interactions, and how they are observed by ground-based instruments such as lidar systems, photometers, and pyranometers. An introduction to the atmosphere's composition, basic concepts, and characteristics of solar-terrestrial radiation are essential for understanding their role in the climate. The aerosols and their interaction with solar radiation, which contribute to the Earth's radiative budget, are approached in this chapter, focusing on their optical-microphysical-radiative properties. The cloud-radiation and aerosol-cloud interactions are not the focus of this manuscript.

2.1 ATMOSPHERE

The Earth's atmosphere is divided into concentric layers: troposphere, stratosphere, mesosphere, thermosphere, and exosphere, where some of the main features of the atmosphere are temperature variations in each layer and the density-pressure decrease of the atmosphere's components with height [36]. These components are quantified by considering a clean-dry air condition, containing 78.08% nitrogen, 20.95% oxygen, 0.93% argon [26], and 0.04% other components. In addition, the Earth's atmosphere contains important constituents that influence the surface temperature: (i) carbon dioxide, (ii) ozone, (iii) methane, (iv) water vapor, and (v) particulate matter or atmospheric aerosols such as dust and soot, which are highly variable in time and space [36]. Water drops, ice crystals, and clouds are part of this composition. Thus, the composition of the atmosphere is a key determinant of Earth's climate [26] because its interaction with solar radiation interferes with the radiative budget[3].

2.2 RADIATION

2.2.1 Definition and Characteristics

The Sun is the Earth's main energy source, emitting electromagnetic radiation through space with an initial solar flux density of ~6.4×10^7 Wm^{-2} at the photosphere

[3] Balance between incoming and outgoing radiation.

[26]. This radiation behaves as a wave or particle (wave-particle duality) as approached by Quantum theory, making it possible for radiation to reach the Earth. The wave behavior is most helpful for understanding the scattering by particles or surfaces [26], where the radiation waves have frequency, wavelength, and amplitude. The particle behavior is related to the absorption and emission of radiation by cause of photons, a bundle of energy (quanta) emitted by an excited molecule, atom, or electron as it returns from a high-energy level to a lower energy level [72].

The radiation emission ranges from short wavelengths (γ-ray) to long ones (Radio) as detailed in Figure 2.1, which also shows the visible spectrum (light), varying between 400 and 700 nm, and its lower and upper limits: the ultraviolet (UV) from 100 to 400 nm and the near-infrared (near-IR) from 700 to 100 μm[4].

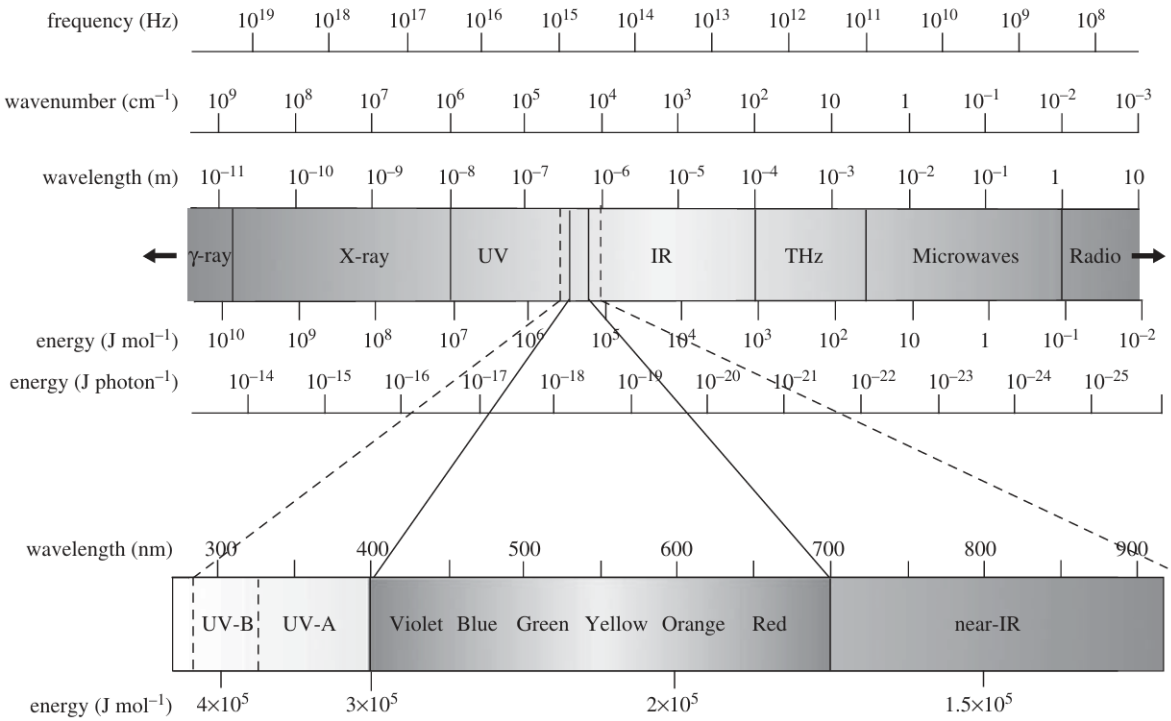

Figure 2.1. Distribution of the wavelengths, frequency, and energy in the radiation spectrum. This figure was adapted from Ref. [73] in Ref. [74].

[4] Note that 1 μm = 10^3 nm, 1 nm = 10^{-9} m, and 1 μm = 10^{-6} m.

Short wavelengths have high frequency and high photon energy content, conforming to the relation between Planck's constant and the frequency of the wavelengths. Equation 2.1 computes the energy of a photon (E, in J or Nm):

$$E = \frac{hc}{\lambda} = hv \quad (2.1)$$

where λ (m) is a certain wavelength, h is Planck's constant (~6.63×10^{-34} Js), c is the speed of light in a vacuum (~3×10^{8} ms^{-1}), and v is the frequency of the wavelength (c/λ).

The UV spectrum (λ < 400 nm) has a high frequency and hence high energy, interfering with the ozone production in the stratosphere. The ozone layer filters a large part of the UV radiation, avoiding harm to human health [75,76] and Earth's ecosystems [77–79]. In the visible spectrum, solar radiation has a peak radiation emission of around 500 nm, considered the central wavelength in the Photosynthetically Active Region (PAR) [80]. PAR is the radiation spectrum (400-700 nm) for photosynthesis, where about 40% of the solar energy is concentrated [4]. Furthermore, the Earth's atmosphere presents some atmospheric windows, covering the IR range from 8 to 13 μm and the visible range[5], where the interaction between gases and radiation is low without clouds and aerosol [38].

In these atmospheric windows, the transmittance caused by gases is high, i.e., a high radiation fraction that passes through the atmosphere without attenuation [26]. The IR window is crucial for the Earth's cooling by the emission of terrestrial radiation. Therefore, only the UV, visible, IR, and microwave parts are relevant for most atmospheric processes [38].

Regarding other definitions, the irradiance or flux or radiant flux density (Wm^{-2}), the radiance ($Wm^{-2}sr^{-1}$), and the albedo are relevant to this manuscript. Irradiance is the rate of the incoming radiation per unit area, radiance is the radiant flux as a function of the solid angle[6] crossing a surface perpendicular to the axis of the

[5] In this manuscript, region, range, and spectrum are synonyms.

[6] A solid angle is the ratio of the area of a spherical surface intercepted at the core to the square of the radius, and its unit is expressed in terms of the steradian [81], sr.

radiation beam [4], and albedo is the reflectance of the incident sun radiation [36] by Earth's surface and clouds, for example.

2.2.2 Atmosphere and Radiation

After incoming solar radiation passes the vacuum of space and reaches the TOA, it crosses the atmosphere, interacting with gases, particles, and clouds. Then, it reaches the Earth's surface, which emits terrestrial radiation. The interaction of incoming solar radiation with the atmosphere and the surface is in charge of the distribution of solar heating among atmospheric layers and the surface [26], protecting against harmful radiation, sustaining life, and influencing weather and natural cycles.

The (incoming) solar radiation and terrestrial radiation are also known as short-wave radiation (SW) and long-wave radiation (LW), respectively. The SW[7] is called extraterrestrial solar radiation when it reaches the TOA, 97% of which is confined to the spectral range of 290 to 3000 nm [82]. Once at the TOA, the SW has a ±3.4% variation in intensity due to the variation of the Earth-Sun distance throughout the year [83]. The LW has wavelengths longer than 3000 nm and is emitted by the Earth's surface, clouds, and components of the atmosphere. Approximately half of the LW goes to space because of the atmospheric window in the IR region (Figure 2.2 and Subsection 2.2.1), contributing to balance the energy budget [84].

The atmosphere interacts with the SW by absorbing and scattering it, while it can also emit SW radiation. These processes modify the SW intensity that passes through the atmosphere, removing photons from the incident radiation. These interactions compose the radiation attenuation, which depends on the pathway through the atmosphere and its components.

Absorption. Absorption occurs at the molecular level and is explained by quantum physics as the transition of electrons of the molecule to higher quantized energy levels [38]. In this process, an electron absorbs a photon, moving to an

[7] From now on, the incoming or downward solar radiation will be called SW.

excited state. Then, the electron starts (re)emitting a photon, converting the SW into thermal energy, for example.

Emission. In contrast to absorption, the emission occurs when electrons are de-excited to valence shells of lower energies [38] or owing to the body's temperature (thermal radiation). The emission also contributes to the radiative balance. In terms of the body's emissions, the blackbody is the surface that emits and absorbs perfectly the radiation [72], as drawn by Kirchhoff's law[8], being the reference to compare the radiation performance from a real surface [36]. The amount of emitted radiation is quantified by Planck's law, which only depends on the temperature of the emitting body and the wavelengths [38]. Furthermore, Stefan-Boltzmann's and Wien's laws also run radiation studies. The first one rules the total energy emitted by a blackbody, while the second rules the wavelength of a maximum emission for a blackbody at a given temperature [72], as indicated by Equation 2.2:

$$\lambda_{max} = \frac{b}{T_b} \tag{2.2}$$

where T_b is the absolute temperature of the blackbody (in Kelvin, K) and b is Wien's constant, 2897 μmK. For instance, if the Sun emits radiation at a temperature of 5777 K, λ_{max} is 0.5 μm (peak mentioned in Subsection 2.2.1).

Scattering. Scattering refers to a change in the direction of propagation of an electromagnetic wave [38]. The incident photons are scattered in all directions and produce diffuse radiation (D) mostly at short wavelengths, while the unabsorbed-unscattered photons in a collimated beam are the direct radiation (B) [83]. When D plus B hits a horizontal surface, the radiation is called global (or total) radiation (G).

As the atmosphere is composed mostly of molecules (Subsection 2.1), the absorption and emission of the SW by gases such as nitrous oxide (N_2O), oxygen (O_2), carbon dioxide (CO_2), ozone (O_3), methane (CH_4), and water vapor (H_2O) occur by a selective process, i.e., these gases interact with only certain discrete energy level photons and discrete wavelengths [72]. When absorption occurs over some

[8] This manuscript does not deeply approach Kirchhoff's, Planck's, and Stefan-Boltzmann's laws.

wavelengths very close to each other, it is called band absorption [36]. For instance, the ozone absorbs SW, ~100%, in the UV region (λ < 290 nm) with a weak band absorption in the visible region and a strong band absorption of the LW around 9.6 μm as shown in Figure 2.2, whereas, the N_2O, O_2, CO_2, CH_4, and H_2O absorb better the LW in the IR region due to the energy level being related to vibrational or rotational states of the molecules. This makes the atmosphere opaque to LW in the IR spectrum.

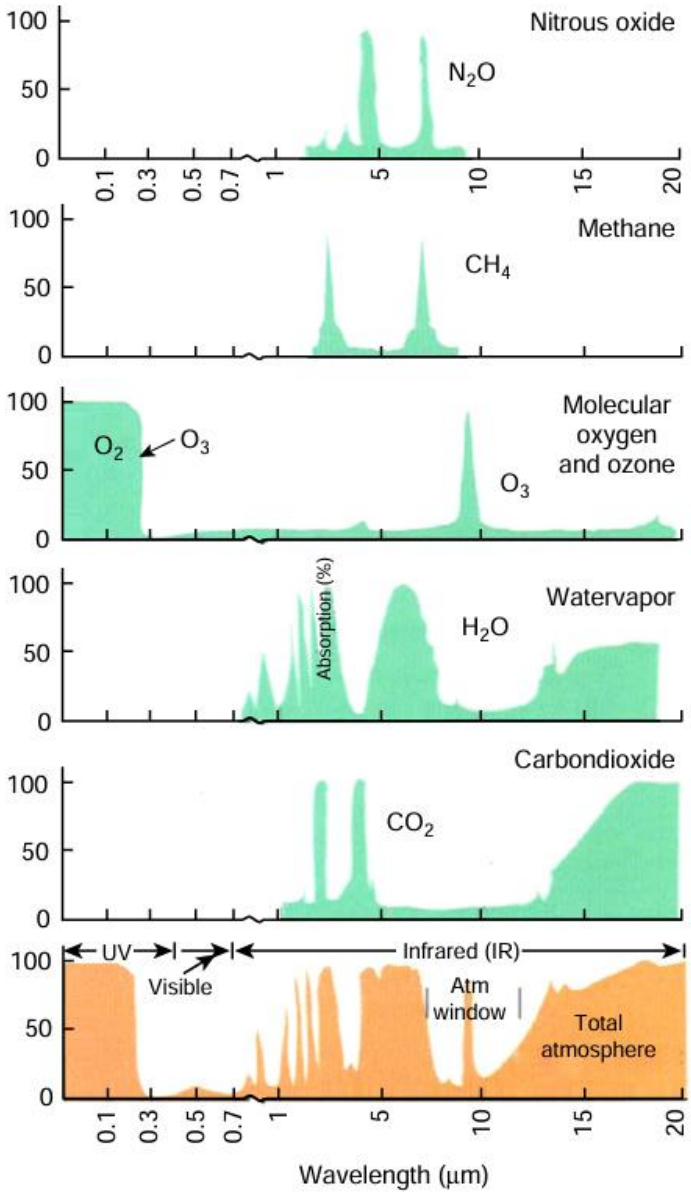

Figure 2.2. Selective absorption of radiation by gases in the electromagnetic radiation spectrum. This figure was adapted from Ref. [85] in Ref. [72].

The invisible region has weak gas absorption because this spectrum is too energetic to be absorbed by most of the gases in the atmosphere and not energetic enough to photo-dissociate them, making the atmosphere almost transparent to it [26], but expressive scattering and absorption by particles dominate the SW attenuation in this spectrum. It is important to mention that this chapter, like the entire manuscript, will focus on the radiation attenuation by aerosols.

2.3 RADIATION-AEROSOL INTERACTION

Radiation-aerosol interaction is the attenuation of the SW and LW, which depends on the properties of the aerosols and their chemical composition. For instance, components such as salts, acids, and many organic compounds do not absorb solar radiation; conversely, Black Carbon (BC), some minerals in soil, and desert dust absorb radiation [25].

Subsection 2.2.2 explains that SW absorption by gases is a selective process. However, the attenuation (scattering or absorption or both combined) of the SW by particles is a continuous function of the wavelength [36]; hence, particle sizes in the visible range scatter radiation efficiently, while absorption by air molecules is weak [25]. In terms of the radiation scattering, the radiation interacts with the aerosol by mechanisms based on the conservation or shifts of energy, like Elastic, Quasielastic, and Inelastic scatterings[9] and by regimes based on the particle sizes like Mie's theory, Rayleigh's theory, and Geometric scattering (Subsection 2.3.3.1).

2.3.1 Atmospheric Aerosols

Refs. [86,87] proposed the first aerosol definition as a colloidal solution of dust and water (droplets) in the air, and called it aerosol, once the solutions of colloids in water are called hydrosols and in alcohol, *alkosols*. Some decades later, a modern

[9] Ref. [4] explained the elastic scattering that occurs when the wavelength or frequency of the scattered monochromatic beam (λ_s) is the same as that of the incident beam (λ); the quasielastic scattering takes place when λ_s or frequency shifts owing to Doppler effects and diffusion broadening; and Inelastic scattering occurs when λ_s or frequency is different from λ. The Mie, Rayleigh, and geometric scatterings do not change the energy of λ, so they are elastic scatterings, nevertheless, Raman and fluorescence are inelastic mechanisms (more details in Subsection 2.4.1). Thus, the Elastic mechanism is major for studies of radiation-aerosol interaction

definition of aerosols was presented by Ref. [88], in which aerosols are dispersed solid or liquid matter in a gaseous medium (air). Ref. [36] also defined aerosol, adding the air's influence on the particle: “An aerosol is a small solid or liquid particle that remains suspended in the air and follows the motion of the air within certain broad limits”. Therefore, the term “atmospheric aerosol” denotes a suspension of microscopic and submicroscopic particles in air [89]. Additionally, Ref. [2] extended the aerosol definition to “a suspension of airborne solid or liquid particles, with typical particle size in the range of a few nanometres to several tens of micrometres and atmospheric lifetimes of up to several days in the troposphere and up to years in the stratosphere”. These particles in the air have a spatial-temporal concentration variability and are very diverse in shape, size (varying from 10^{-3} to 10^{2} μm in radius), and chemical composition.

The sizes of the particles, in radius, are classified as Aitken particles, 10^{-3} to 10^{-1} μm, large particles, 0.1 to 1 μm, and giant ones from 1 to 100 μm. The aerosols can also be classified in two modes (fine and coarse) or more modes according to their diameters (nucleation, < 10^{-2} μm; Aitken, ~10^{-2}-10^{-1} μm; accumulation, ~10^{-1} to 1 μm; and coarse, > 1 μm). Figure 2.3 shows the size distribution, atmospheric processes, and the modes of the aerosols. Some studies range the fine mode from 0.1 and 0.25 μm[10] and sometimes from 0.1 to 1 μm, with the coarse mode being the larger particles [90].

The aerosols are emitted directly into the atmosphere by natural sources such as sandstorms, sea spray, volcanoes, natural wildfires, and biogenic emissions [89] or anthropogenic activities like construction and cement production, agriculture, and combustion of biomass and fossil fuels [91]. These particles are called primary [2]. Further, secondary particles are formed in the atmosphere by gas-to-particle conversions [2,92], and their sources are the same as the previous one [89]. Some microphysical processes[11] are responsible for their formation, like (i) nucleation,

[10] In air pollution studies, the Particulate Matter 2.5 μm (PM2.5) refers to diameters < 2.5 μm, which is considered fine mode [4,90].

[11] Water uptake or hygroscopicity is also a microphysical process for formatting secondary aerosols, but it is approached in Subsection 2.3.3.1.

when gases can nucleate to form molecular clusters [92]; (ii) coagulation, collision and sticking of particles owing to Brownian diffusion [92], or as a result of their motion produced by hydrodynamic, electrical, gravitational, or other forces [4]; and (iii) condensation, when vapor condenses on a particle population or when a material evaporates from the aerosol to the gas phase [4], as drawn in Figure 2.3. These processes change the shape and size of the aerosols and can separate the aerosols into fine or coarse modes. As detailed by Ref. [4], the accumulation and Aitken modes are the result of primary emissions from combustion sources and secondary aerosols (secondary sulfate, nitrate, ammonium, and organics) from the condensation process and the coagulation of smaller particles. However, the coarse mode generally results from mechanical processes such as wind or erosion (soil dust, sea salt, fly ash, pollens, and others).

There are processes responsible for aerosol formation in the atmosphere, as well as for their removal. Aerosol removal occurs by wet and dry deposition. Wet deposition is the natural process by which material is scavenged by atmospheric hydrometeors such as cloud and fog drops, rain, and snow and is consequently delivered to the Earth's surface [4]. Rainout and washout are important processes of wet deposition. In the first process, droplets are formed by CCN, and in the second process, the aerosols are removed by falling rain [92]. Dry deposition is the transport of gaseous and particulate species from the atmosphere onto surfaces without precipitation [4]. It depends on particle size, surface type (water and vegetation, e.g.), and meteorological factors (wind speed and stability, e.g.), and it occurs by turbulent mixing, Brownian diffusion, impaction, and sedimentation [92].

Regarding the chemical composition, the aerosols can be composed of sulfate, ammonium, organic and elemental carbon, sodium, chloride, and trace metals, which are found predominantly in fine mode, whereas, silicon, calcium, magnesium, aluminum, iron, and biogenic organic particles (pollen and spores, e.g.) are usually in the coarse mode [36]. Furthermore, nitrate can be found in both modes. Elemental carbon, also called BC or graphitic carbon, is emitted directly into the atmosphere, predominantly from combustion processes, while the organic carbon is emitted directly by sources or can result from the atmospheric

condensation of low-volatility organic gases [4]. The particles can be classified according to their origins, such as urban aerosols, marine aerosols, biomass burning, mineral dust, and bioaerosols. Other classifications are not approached here.

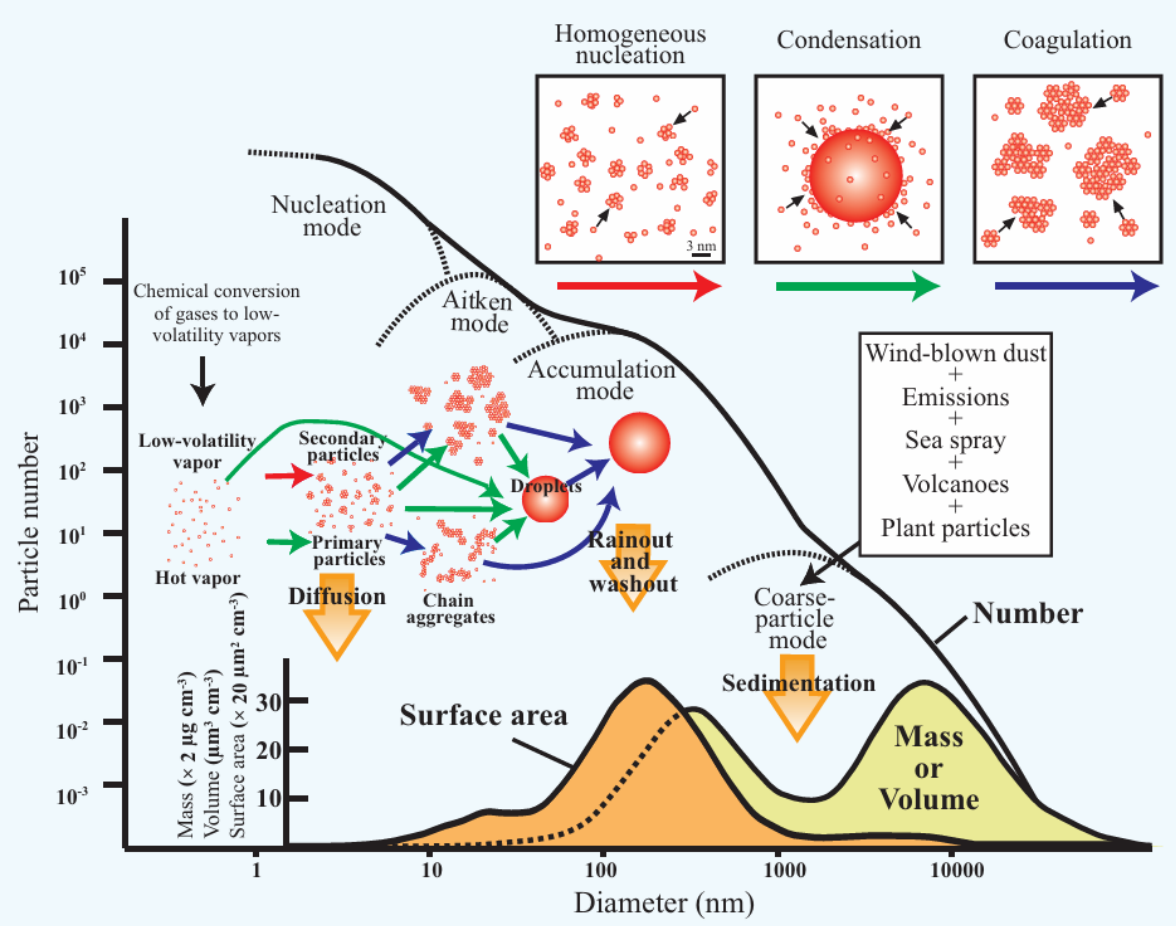

Figure 2.3. Illustration of the aerosol formation and removal for modes and their size distribution (number, mass, volume, and surface area) in an idealized atmospheric sample. This figure was adapted from Ref. [93].

Urban aerosols. They are a mixture of primary particles, such as industries, transportation, power generation, natural sources, and waste incineration [94], and secondary particles. Their dominant modes are Aitken and accumulation because of the fresh combustion with a coarse mode presence due to the resuspension of dust particles from traffic [4].

Marine aerosols. They are primary particles formed at the air-sea interface from the interaction of wind stress with the ocean surface, typically resulting from

whitecap generation [4], and they are an important source of CCN whose production rate depends on temperature and wind speed [33]. This aerosol type has a dominant coarse mode, while the small particles have a defined separation of the Aitken and accumulation modes caused by cloud processing [38] with submicrometric particles down to radii of 20 nm [95]. Marine aerosols can also be secondary particles formed via nucleation of stable clusters (0.5 to 1 nm in size) that can grow to larger sizes via condensation processes, and heterogeneous reactions and aqueous phase oxidation of dissolved gases in existing aerosol particles [95].

Biomass burning. It is emitted by burning vegetation and is the major source of BC, soot (a mixture of organic and elemental carbons), and ozone precursors in the tropics [4]. Biomass burning is also emitted by wildfires [33]. This aerosol warms the atmosphere because soot absorbs strongly [96]. In general, the aerosols from wildfires contribute to either warming or cooling the climate, depending on which season, region, or ecosystems they are emitted [33]. Furthermore, deposition of these absorbing particles on snow and ice reduces the albedo and may accelerate warming of Arctic regions [97]. The smoke from biomass burning has particles in the accumulation mode that grow in size [38].

Mineral dust. It is a coarse-mode particle emitted by arid and semiarid regions and human activities. According to Refs. [19,98], the dust emission varies, approximately, from 1000 to 3000 $Tgyr^{-1}$. The mineral dust is naturally transported over long distances owing to the particles smaller than 10 μm, in diameter, particles as large as 100 μm are found in the source regions, and its main compounds are quartz, clays, calcite, gypsum, and iron oxides [4], interfering with their optical properties. These particles can scatter and absorb both SW and LW because of their size and composition, e.g., in the visible range, the scattering dominates with an overall cooling effect, but in the IR region, the absorption dominates and they act like a greenhouse gas [4]. At the TOA, mineral dust has a negative radiative forcing by increasing SW albedo over the ocean, but it reduces the planetary albedo over bright surfaces [33]. Additionally, these particles provide nutrients to phytoplankton after atmosphere-to-ocean deposition [33,99] and to plants after atmosphere-to-soil deposition [18,100].

Bioaerosols. This kind of aerosol is solid airborne particles derived from diverse sources within the biosphere, including bacteria (~0.25-10 µm), viruses (< 0.3 µm), pollen grains (10-100 µm), fungal spores (1-30 µm), algae, plant debris, cell fragments, insect excrements etc., differing in size and abundance [33,101]. However, they are dominated by fungi and pollen grains, which are the most important producers of outdoor airborne allergens [102]. Furthermore, the bioaerosols can act as CCN [103] and ice nuclei [104,105].

2.3.2 Aerosol Effects on Earth's Climate

Aerosols affect Earth's climate by scattering and absorbing radiation in the atmosphere, interacting with clouds, and altering the albedo of snow and ice [25]. These particle effects are known as direct and indirect. The radiation attenuation in cloud-free or cloudy conditions causes the direct effect. The scattering affects the climate by reflecting part of the available radiation back to space (cooling the surface), and the absorption can cool the surface and heat the atmosphere [21]. Thus, aerosols directly influence the SW and LW transmission [26]. The aerosol direct radiative effect is also called aerosol-radiation interaction [2,20]. A summary diagram of the effects of aerosols on climate is shown in Figure 1.1.

Transmission occurs when the radiation passes a medium (atmosphere) without being completely absorbed or reflected. This process can be quantified by the transmittance (T), which is the ratio of radiation emerging from a medium (transmitted radiation, I) to incident radiation (I_0) [36]. The transmittance can be computed by the equation below:

$$T = \frac{I}{I_0} \tag{2.3}$$

When T is zero, there is no transmission, i.e., all incident radiation is absorbed or reflected, and T = 1 (100%), there is no absorption or reflection of the radiation, i.e., the atmosphere is transparent at a certain wavelength. Figure 2.4 shows the transmission of the SW and LW in the electromagnetic spectrum. The transmission changes in the spectrum according to the absorption and scattering of the aerosols

and gases (radiation attenuation). Low transmission means high absorption (black solid line). Furthermore, the reduction in transmission due to the scattering, scattering loss (dashed line), is larger at short wavelengths (UV and visible) and smaller at long wavelengths. So, the atmosphere transmission depends on aerosol attenuation and contributes to the Earth's radiative balance.

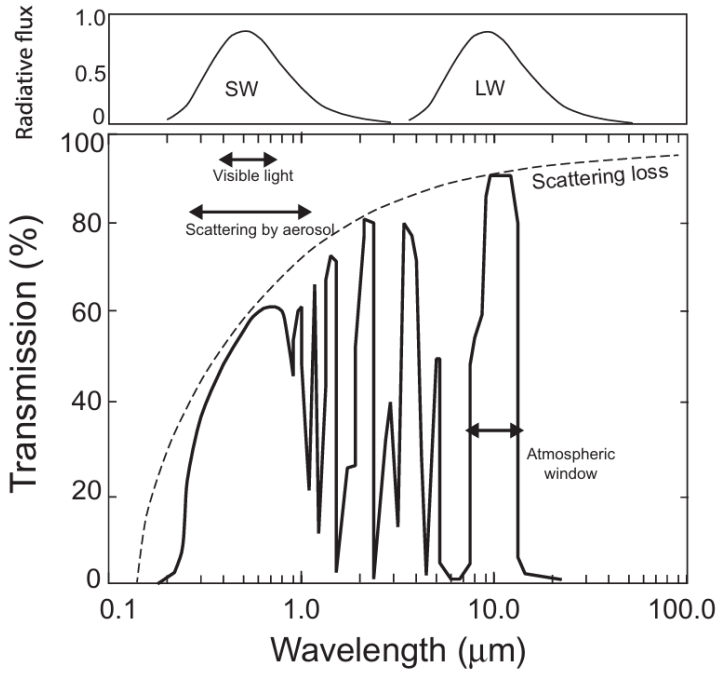

Figure 2.4. Atmospheric transmission of SW and LW in the electromagnetic spectrum. The solid black line is the transmission, and the dashed line is the loss in the transmission caused by scattering. The top panel is the approximate radiative fluxes of a blackbody with peaks at ~0.5 μm (visible range) and ~10 μm (IR range). This figure was adapted from Ref. [25].

The aerosol direct radiative effect changes the thermodynamic profile of the atmosphere, interfering with the evaporation of the Earth's surface [21]. For instance, the aerosol cooling effect reduces evaporation, then it reduces cloud formation. In the past, this secondary effect was called an indirect effect [24,106]. The indirect effect occurs when the aerosol alters cloud properties [24] like albedo, thickness, and coverage in response to changes in droplet concentrations [25] because the aerosols are CCN, which influence the number, size, and atmospheric lifetime of cloud droplets [26]. Today, this effect is under the denomination of aerosol-cloud interactions [2,20]. The CCNs are particles that can become activated to grow into

fog or cloud droplets in the presence of a water-vapor supersaturation [4]. Additionally, the aerosol can be an ice-nucleating particle by heterogeneous freezing, i.e., a particle that can cause ice nucleation in a water droplet or from deposition of water vapor [92], and they may affect the reflectivity of the surface, as absorbing aerosol deposited on snow-covered surfaces [89].

Therefore, the aerosols act by cooling or heating the atmosphere and Earth's surface because of the radiation attenuation. For example, particles of diameters less than 1 μm are highly effective at scattering SW, sending a portion of that scattered radiation back to space [4], which has a cooling effect. In contrast, BC is a stronger absorber of SW and LW in the atmosphere [107], which results in the heating effect.

Regarding the aerosol forcing, the magnitude of the ARF at a particular time and location depends on the amount of radiation scattered back to space, which depends on the size, abundance, and optical properties of the particles and the SZA [4]. These effects also depend on the height; for example, the AFE produced by desert dust in the visible range may differ by a factor of 2 at the surface and by a factor of 3 at the TOA [29].

Radiative forcing is the change in the net downward (incoming minus outgoing) radiative flux at the TOA in the solar and terrestrial spectra caused by changes in an external forcing agent (aerosols, greenhouse gases, solar flux, etc.) over a defined period [25]. When the radiative forcings are produced by the presence of aerosols in the atmosphere, they are called ARF and AFE. The first refers to radiative forcing per unit AOD [108], while the second refers to the change in the radiation flux produced by the aerosols [29]. Both are responsible for the aerosol radiative effects, radiative perturbations from any change in the Earth system due to the aerosol-radiation interactions [25].

A positive value of the radiative forcing causes heating in the climate system, whereas a negative value causes cooling. According to Ref. [25], a purely scattering aerosol enhances the reflected solar radiation and causes a negative radiative forcing at the TOA; meanwhile, a purely absorbing aerosol reduces LW and causes

a positive radiative forcing and, like scattering particles, also reduces radiation at the surface. A negative forcing generally takes place by particles (Ø < 1 μm) that are highly effective at scattering SW, sending scattered radiation back to space [4], and a positive forcing is generated by greenhouse gases, reducing the LW emission to space.

The ARF can be estimated at the TOA and BOA, respectively, as the following equations:

$$ARF_{TOA} = \left(F_{TOA}^{\downarrow aer} - F_{TOA}^{\uparrow aer}\right) - \left(F_{TOA}^{\downarrow} - F_{TOA}^{\uparrow}\right) \quad (2.4)$$

$$ARF_{TOA} = \left(F_{TOA}^{\downarrow aer} - F_{TOA}^{\uparrow aer}\right) - \left(F_{TOA}^{\downarrow} - F_{TOA}^{\uparrow}\right) \quad (2.5)$$

where F is the radiative flux in Wm^{-2}, ↑ stands for upward flux, ↓ stands for downward flux, and aer stands for the presence of aerosol in the atmosphere. Therefore, the contribution of the aerosols in the whole atmospheric column is quantified by the atmospheric forcing [109], ATMF:

$$ATMF = ARF_{TOA} - ARF_{BOA} \quad (2.6)$$

The AFE at a certain λ is defined as the change in the ARF per unit of AOD [31] or the change in the ATMF per unit of AOD:

$$AFE(SZA, \lambda) = \frac{dATMF}{dAOD} \quad (2.7)$$

However, they can be estimated by other methods, e.g., the direct method [71], see Subsection 4.3.2. Figure 2.5 illustrates the radiative balance at the TOA and BOA. The maximum, minimum, and mean fluxes (Wm^{-2}) are from a 16-model ensemble. The TOA budget shows a small imbalance, probably associated with forced climate change [84]. The same occurs at the BOA (Fig. 2.5b), in which the latent heat flux is caused by evaporation and the sensible heat is caused by convection, making the budget more complex. The high standard deviations from the observations also reinforce the complexity of the processes involved in the surface budget.

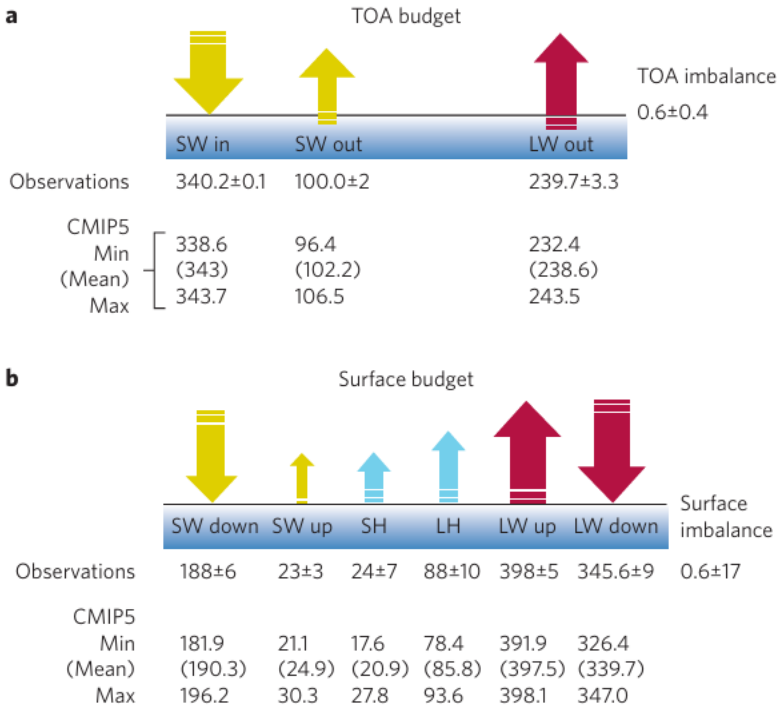

Figure 2.5. Radiative budgets at the TOA (**a**) and BOA (**b**). In and out refer to the incoming and outgoing fluxes at the TOA; down and up refer to downward and upward fluxes at the BOA; SH and LH refer to sensible and latent heat fluxes, respectively. The climate model fluxes are from simulations archived under the World Climate Research Programme's Coupled Model Intercomparison Project phase 5 (CMIP5) twentieth-century experiments. This figure was adapted from Ref. [84].

The forcing varies with the Solar Zenith Angle (SZA)[12] and the wavelengths [110]. The larger the SZA, the thicker the atmosphere layer is, and there is more radiation attenuation from aerosols [111]. Figure 2.6 is an example of the angular dependency of the ARF for biomass-burning aerosol layer in the presence or absence of clouds. Furthermore, the spectral dependence of the optical properties is propagated to the aerosol radiative properties [112].

This figure shows that the ARF in the presence of clouds has a heating effect with almost constant values till 50º and then decays to values close to zero at 90º. The ARF, in the absence of clouds, has a maximum (>10 Wm^{-2}, in absolute values) at around 65-70º and then decays to values close to zero at 90º as well. The forcings

[12] SZA is the angle between the Sun and the zenith and whose referential is the Earth's surface, varying from 0º (Sun is overhead) to 90º (horizon).

reach zero at the highest SZAs owing to the higher radiation attenuation by the aerosols. At small SZA, the dependence of aerosol forcing (upscattered flux) depends mainly on the phase function (Subsection 2.3.3.2) and the particle size, governed by Rayleigh and Mie scatterings in which the phase function is nearly symmetric [112]. Thus, for small particles, the forcing weakens as SZA increases from zenith to horizon as governed by increased Rayleigh scattering, and, for larger particles, phase function scatters in the forward direction, i.e., low upscatter fraction[13], at small SZA and then it increases to the maximum at intermediate SZA (forcing raises), finally, the aerosol scattered flux decreases at the highest SZA because the slant path is no longer optically thin [112]. The aerosol forcing also reaches lower values at the highest SZA at the BOA [113,114].

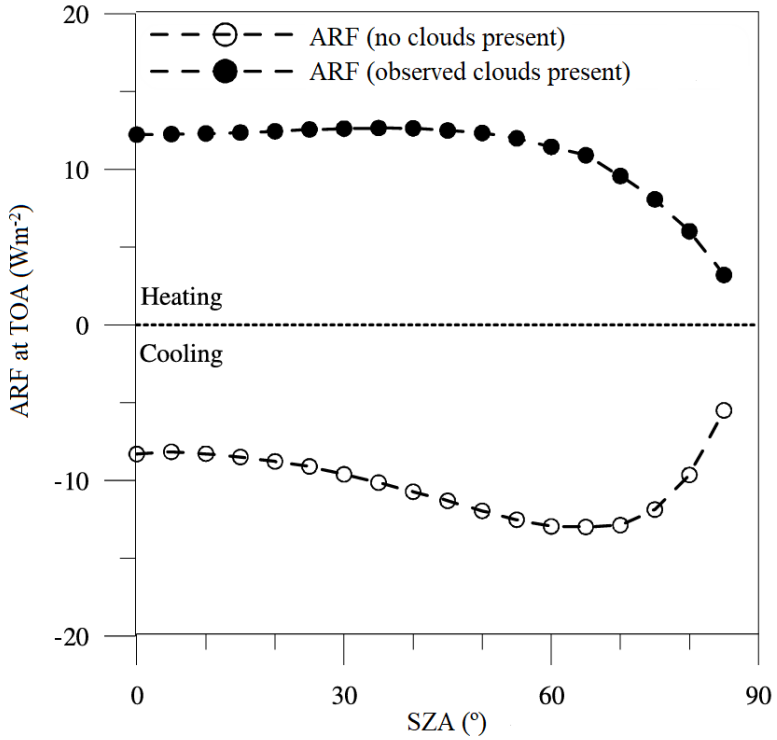

Figure 2.6. Angular dependence of the ARF at the TOA for a biomass-burning layer with and without clouds in the atmosphere. This figure was adapted from Ref. [110].

[13] According to Ref. [4], the fraction of light that is scattered by a particle into the upward hemisphere relative to the local horizon is the fraction of the integral over the angular distribution of scattered radiation that is in the upward hemisphere. So, it depends on particle size and SZA.

2.3.3 Aerosol Optical-Microphysical-Radiative Properties

The aerosol properties are classified into microphysical and optical-radiative properties in this manuscript.

2.3.3.1 Microphysical properties of the atmospheric aerosols

The microphysical properties are the physical and chemical characteristics, which are essential to the assessment of optical and radiative properties [96,115] and to understanding the radiation-aerosol interaction. Even though chemical components of the aerosols (BC, organic carbon, ammonium sulfate-like, among others) are not the focus of this manuscript, they can be quantitatively estimated from microphysical properties as performed by Ref. [115].

As mentioned previously, the Elastic scattering happens in three scattering regimes (Mie, Rayleigh, and Geometric). These regimes consider the aerosol as a spherical particle and depend on (i) incident wavelength (λ); (ii) the complex refractive index (N); and (iii) the size parameter (SP) [4].

N governs both particle scattering and absorption [39] and depends on the chemical composition of the particle, including water for soluble particles [38]. This property is represented by real and imaginary parts as in Equation 2.8:

$$N = n + ik \tag{2.8}$$

where the real part n (non-absorbing part) is the ratio between the velocity of the radiation in a vacuum and the velocity in the particle, and the imaginary part ik (absorbing part) measures the degree of attenuation during the propagation through the particle [38]. Both components are functions of the wavelength [4].

SP infers the effect of particle size on scattering [81] and can be calculated as a function of the particle radius (r) or its diameter (Ø):

$$SP = \frac{2\pi r}{\lambda} = \frac{\pi Ø}{\lambda} \tag{2.9}$$

The values of SP define the scattering regimes. If SP ≈ 1 or, as a function of N, 0.6/N < SP < 5, the scattering is ruled by Mie's theory; if SP << 1 or SP < 0.6/N,

the scattering is ruled by Rayleigh's theory; and if SP >> 1, the scattering is governed by the Geometric regime. The particles responsible for scattering range in size from gas molecules (~10-4 μm) to aerosols (~1 μm), water droplets (~10 μm), ice crystals (~100 μm), and large raindrops and hail particles (~1 cm) [81].

Mie's theory. Mie's theory calculates the scattering and absorption of a monochromatic beam[14] by spherical particles as a function of wavelength [116]. It was developed by Gustav Mie [117], who applied Maxwell-Heaviside's equations to homogeneous spheres in which the particle size is about the same size as the incident wavelength. In this theory, more energy is scattered in a forward direction than in a backward direction [36]. Mie's theory is well applied to the estimation of the optical-radiative properties of aerosols and remote sensing research.

Rayleigh's theory. Lord Rayleigh formulated this theory in the nineteenth century. Rayleigh scattering occurs when the particle is much smaller than the incident wavelength, and it is usually referred to as the scattering caused by molecules in the atmosphere. The scattered monochromatic beam is proportional to λ^{-4}, i.e., the spectral transmittance of air molecules rapidly increases with wavelength, and it decreases with increasing optical air mass [36], characteristic of non-absorbing particles [4]. In the Rayleigh mode, the scattering process is identical in forward and backward directions [36], as illustrated in Figure 2.7, in which an incident 0.5-μm beam is scattered by different particle sizes, producing patterns of scattering directions. Rayleigh's theory explains the blue sky and sky polarization [81].

Geometric scattering. This regime is related to the scattering by large particles compared with the incident wavelength and is governed by the geometric optics of reflection, refraction, and diffraction [4], i.e., the scattered light depends on particle shape and orientation relative to the incident wavelength. This scattering is responsible for rainbows, halo phenomena, and the brightness of clouds [116]. Table 2.1 summarizes the dominant scattering regimes by spectral regions.

[14] A monochromatic beam is a beam of electromagnetic radiation that consists of a single wavelength (or frequency).

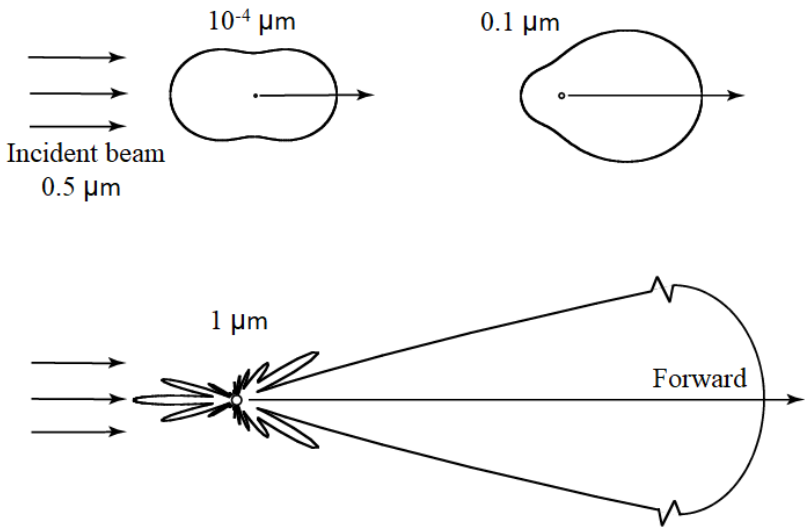

Figure 2.7. Scattering directions produced by an incident beam (0.5 μm) on three different particle sizes (10-4, 0.1, and 1 μm). This figure was adapted from Ref. [81].

Table 2.1. Spectral boundaries and elastic scattering regimes of the aerosols used in the atmospheric sciences. This table was adapted from [38].

Spectral regions	Spectral boundaries (μm)	Atmospheric components
UV	0.01-04	O_2, O_3, and particles
Visible	0.4-0.7	Particles
IF	0.7-8 8-15	N_2O, O_3, CO_2, CH_4, H_2O, and particles

The particle size distribution represents how the number, surface area, mass, or volume concentrations of particles are distributed according to size [90]. Generally, it is distributed in bins; for example, the AERONET distributes the particles in 22 logarithmically equidistant discrete points in sizes from 0.05 to 15 μm [67]. The distribution by different sizes of bins causes some biases. Because of this, it is necessary to normalize the distribution by dividing the concentration by the corresponding size range to avoid such biases from the range bins [4]. However, this approach compresses small sizes in the bins, while particle concentrations at large sizes have very low normalized concentrations [90]. As a solution, the size distributions are shown per logarithmic interval of radius or diameter. So, a lognormal size distribution function, i.e., a Gaussian normal distribution against log(Ø) is the

best way to represent the number or volume size distributions of the aerosol concentrations as in the following equations [118], respectively:

$$\frac{dNSD}{d\log Ø} = \sum_{w=1}^{nw} \frac{INC_w}{\sqrt{2\pi}\log\sigma_{g,w}} e^{\left[-\frac{(\log Ø - \log Ø_{g,w})^2}{2(\log\sigma_{g,w})^2}\right]} \quad (2.10)$$

$$\frac{dVSD}{d\log Ø} = \sum_{w=1}^{nw} \frac{INC_w \frac{\pi}{6} Ø^3}{\sqrt{2\pi}\log\sigma_{g,w}} e^{\left[-\frac{(\log Ø - \log Ø_{g,w})^2}{2(\log\sigma_{g,w})^2}\right]} \quad (2.11)$$

where NSD is the number size distribution, w is each mode, nw is the number of modes, INC is the integrated number concentration for each mode w, σ_g is the geometric standard deviation, $Ø_g$ is the geometric median diameter, and VSD is the Volume Size Distribution. The units of number and volume size distributions are usually cm^{-3} and $\mu m^3 cm^{-3}$, respectively. Furthermore, aerosols are usually represented by fine and coarse modes in the size distribution (bimodal), i.e, nw = 2. A synthetic representation of the particle number size distributions, the effective particle diameter, $Ø_{eff}$, is defined:

$$Ø_{eff} = \frac{\int \frac{Ø^3}{8} \frac{dNSD}{d\log Ø} dØ}{\int \frac{Ø^2}{4} \frac{dNSD}{d\log Ø} dØ} \quad (2.12)$$

Another aerosol microphysical property that significantly changes the particle size is hygroscopicity. Aerosols increase in size due to the water uptake, which depends on high Relative Humidity (RH) conditions and the chemical composition of the aerosols. For example, a particle diameter of up to a factor of 2 between 0% and 90% of RH can cause an increase in surface area by a factor of 4 [92]. The hygroscopic growth [119] makes part of the aerosol-cloud interaction [120] by forming clouds. It also affects the aerosol size distribution, hence their optical and other microphysical properties. The aerosols can be very hygroscopic (marine aerosols) or hydrophobic (fresh mineral dust and fresh soot), but the oxidation of the organic material from combustion in the atmosphere converts much of the mass into hygroscopic material on the timescale of hours [121]. The hygroscopicity can be

estimated by the hygroscopic growth factor (f(RH)) and Hänel parameterization [122,123]:

$$f(RH) = \left(\frac{1 - RH/100}{1 - RH_{ref}/100}\right)^{-\gamma} \quad (2.13)$$

where γ is the hygroscopic fit parameter, which depends on the hygroscopic nature of the aerosol [122], with RH_{ref} increasing up to RH. The RH typically ranges from 40% (RH_{ref}) to 85% (dry and wet references, respectively), with 40% the bottom limit of the RH [123–128]. Values of f(RH) > 1 mean particle growth by water uptake, f(RH) ≈ 1 means no hygroscopicity as fresh soot, and f(RH) > 2, extremely hygroscopic particles as salts. Additionally, active remote sensing systems, like lidars (Subsection 2.4.1), have revealed adequate techniques for the identification and analysis of the aerosol hygroscopic growth because they provide high vertical and temporal resolutions, they preserve the ambient conditions (no humidification or dehydration is applied on the sample), and they can measure under RHs close to saturation [129]. For instance, Ref. [129] used the aerosol backscatter ($\beta_{aer}(\lambda)$), Subsection 2.4.1, to estimate γ, therefore, Equation 2.13 is written as a function of $\beta_{aer}(\lambda)$:

$$\frac{\beta_{aer}(\lambda, RH)),}{\beta_{aer}(\lambda, RH_{ref})),} = \left(\frac{1 - RH/100}{1 - RH_{ref}/100}\right)^{-\gamma(\lambda)} \quad (2.14)$$

Lastly, Sphere Fraction (SF) is the proportion of aerosol particles that have a spherical shape, relating to the total particles in the atmosphere. When this optical property is close to 0%, as in the case of desert dust, the particles are considered non-spherical; otherwise, if it is close to 100%, the particles are considered as spheres.

2.3.3.2 Optical-radiative properties of the atmospheric aerosols

This subsection is about the optical and radiative properties of the aerosols, gathered in a unique subsection because these parameters are linked, i.e., the radiative properties depend directly on the optical properties, which implies the amount of attenuated radiation. For instance, the two main quantities describing how

aerosols influence the radiative balance are the AOD and the Single Scattering Albedo (SSA) [108]. The asymmetry factor also makes a significant contribution to the radiative balance.

According to Ref. [130], modeling the effects of aerosols on atmospheric radiation requires key aerosol optical properties, such as aerosol optical thickness, phase function, and single scattering albedo; thereby, variations in these properties influence radiative forcing sensitivity, shaping the impact of atmospheric aerosols on climate change. The chemical composition, concentration, size, shape, and internal structure of the liquid and solid particles suspended in the air determine the optical properties [131]. On the one hand, optical-radiative properties, such as the AOD, Ångström Exponent (AE), Asymmetry Factor (AF), polarization, among others, are discussed in the manuscript. On the other hand, aerosol scattering, absorption, and extinction coefficients, which are functions of the SP, N, and λ [4], are not discussed deeply here. These properties determine how the aerosols interact with the SW and LW and also exhibit a dependence on the wavelengths and the microphysical properties.

Equation 2.3 shows the transmittance in which the radiation attenuation can be deduced by the direct relation between the incident beam (I_0) and the emitted beam (I). However, Beer-Bouguer-Lambert's law states that the decrease in the incident monochromatic beam ($I_{\lambda,0}$) traversing a homogeneous extinction medium follows a simple exponential function [81] whose argument is the product of the total atmospheric optical thickness (τ) and its optical airmass (*m*):

$$I_\lambda = I_{\lambda,0} e^{-\tau m} \tag{2.15}$$

m increases when the SZA increases; hence, the optical thickness increases. When *m* is calculated as the relative path length concerning the zenith, the path length is:

$$m = \frac{1}{\cos SZA} = \sec SZA \tag{2.16}$$

However, this equation holds for SZA less than ~75° [4], causing cosine errors for the larger angles. The optical airmass equals 1 for a vertical path through

the atmosphere and is roughly proportional to 1/cos(SZA) [82]. A review about optical airmass formulation is found in Ref. [132]. So, Equation 2.15 can be rewritten as follows:

$$I_\lambda = I_{\lambda,0} e^{-\tau/\cos SZA} \tag{2.17}$$

The τ/cos(SZA) is called slant path optical depth, which increases when the SZA increases [112]. Finally, the atmospheric optical depth is computed by rearranging Equation 2.18:

$$\tau = \cos SZA \ln\left(I_{\lambda,0}/I\right) \tag{2.18}$$

The total atmospheric optical depth considers the attenuation by all atmospheric components (scattering by gas molecules, extinction by aerosol particles, absorption of trace gases, and others); thus, the AOD needs to be subtracted from τ:

$$AOD = \tau - \tau_{mol} \tag{2.19}$$

where τ_{mol} refers to the attenuation caused by molecules and other atmospheric components that do not include the aerosols. The AOD can also be estimated by the integral of the spectral extinction (scattering plus absorption) related to the aerosol, $\alpha_{aer}(\lambda)$, in the atmospheric column:

$$AOD(\lambda) = \int_0^{TOA} \alpha_{aer}(\lambda, R)\, dz \tag{2.20}$$

where R denotes the vertical height from 0 at the surface to the TOA. The aerosol transmittance (Equation 2.3) related to the AOD is:

$$T = e^{-AOD} \tag{2.21}$$

The AOD is a dimensionless measure of the amount of aerosol through the depth of the atmosphere [38], i.e., the normal aerosol optical thickness. Its ranges are difficult to identify, e.g., for an AOD(440 nm) varies from 0.1 to 1.8 (urban-industrial and mixed aerosols), from 0.1 to 3 (biomass burning), from 0.1 to 1.5 (desert dust), and from 0.01 to 0.2 (oceanic aerosols) [130], thereby, the AOD is usually associated to the AE to classify the aerosols by their thresholds better.

Regarding the aerosol scattering, absorption, and extinction coefficients of an ensemble of particles, their relationship is quite simple [116]:

$$\sigma_{ext} = \sigma_{sca} + \sigma_{abs} \tag{2.22}$$

The absorption and scattering coefficients can be calculated by integrating over the whole size distribution their absorption and scattering cross sections (Q_{abs} πr^2 and $Q_{sca}\pi r^2$, respectively)[15]. The extinction coefficient is an appropriate measure of how efficiently a particle attenuates light.

The AE represents the wavelength dependence of the AOD conforming to the Ångström formulae [133]:

$$AOD(\lambda) \approx \lambda^{-AE} \tag{2.23}$$

where AE is also known as the Ångström parameter. To obtain the AE value, Equation 2.23 is rewritten as follows:

$$AE = \frac{-\ln AOD}{\ln \lambda} \tag{2.24}$$

As the AOD depends on λ, the AE is usually calculated between two pairs of wavelengths (λ_1, λ_2):

$$AE = -\frac{\ln(AOD\,(\lambda_1)/AOD(\lambda_2))}{\ln(\lambda_1/\lambda_2)} \tag{2.25}$$

The AE is an indicator of the aerosol size: the larger the AE, the smaller the mean particle radius [38], thereby, Rayleigh scattering is associated with the largest AE > 2.5, and the Mie scattering is associated with smaller ones, varying between 0 and 2.5 and, occasionally, they have negative values in the coarse mode. According to the climatology of Ref. [130], AE(440-870 nm) associated with AOD(440 nm) varies from 1 to 2.3 for urban-industrial and mixed aerosol, from 1 to 2.3 for biomass burning, from 0.1 to 0.9 for desert dust, and from 0 to 1.55 for oceanic aerosols.

[15] Q_{abs} and Q_{sca} are the absorption and scattering efficiencies, respectively, and πr^2 is the particle section. In this case, the absorption and scattering cross sections are calculated according to Mie's theory (Subsection 2.3.3.1), i.e., the particles are considered spheres.

The SSA is the fraction of extinction due to scattering and is not directly related to the amount of aerosol [38], but this ratio depends on the refractive index, mainly its imaginary part [130], such as material, shape, particle size, some optical properties of aerosol particles [36], and wavelengths. So, by definition:

$$SSA = \frac{\sigma_{sca}}{\sigma_{ext}} = \frac{\sigma_{sca}}{\sigma_{sca} + \sigma_{abs}} \tag{2.26}$$

When SSA = 1, there is a total scattering, whereas SSA = 0, there is a total absorption caused by aerosol attenuation. Ref. [130] calculated SSA(670 nm), which ranges from 0.88 to 0.97 for urban-industrial and mixed aerosols, from 0.84 to 0.94 for biomass burning, from 0.95 to 0.98 for desert dust, and SSA > 0.97 for oceanic aerosols. It demonstrates that most observed particle mixtures have SSA larger than 0.7 in the visible spectrum [38]. Refs. [24,130] showed that SSA determines the sign (cooling/heating) of the aerosol radiative forcing, while the asymmetry of the phase function with the optical thickness drives the magnitude of the forcing.

The phase function or the scattering phase function, denoted here as P(Θ), is the angular distribution of light intensity scattered by a particle at a given wavelength [4]. The scattering angle is Θ and the value of P(Θ) dΩ/4π gives a conditional probability of light scattering in the solid angle dΩ = sin(Θ) dΘdΦ [131], 4π being the probability of scattering in any direction. Therefore:

$$\frac{1}{4\pi}\int_0^{2\pi} d\Phi \int_0^{\pi} P(\Theta)\sin\Theta\, d\Theta = 1 \tag{2.27}$$

Like the other aerosol optical properties, P(Θ) considers the particle as a sphere, i.e., it is assumed to be rotationally symmetric [38], making it independent of the azimuthal angle (Φ). So, the angular distribution of scattered light is represented by just one parameter [131], such as the AF:

$$AF = \frac{1}{2}\int_0^{\pi} P(\Theta)\cos\Theta\sin\Theta\, d\Theta \tag{2.28}$$

Ref. [4] defined the AF as the intensity-weighted average of the cosine of the scattering angle. When AF = 1 for total scattering at Θ = 0°, AF = -1 for total scattering at Θ = 180°, and AF = 0 for the same scattering in all directions (isotropically). Its

positive value indicates the forward direction of scattering, and the opposite indicates the backward direction of scattering. Ref. [130] found AF(440 nm) values ranging from 0.68 to 0.74 for urban-industrial and mixed aerosols, from 0.64 to 0.69 for biomass burning, from 0.68 to 0.73 for desert dust, and 0.75 for oceanic aerosols, which agree with typical values for atmospheric aerosols, 0.5 < AF < 0.9 [38].

Additionally, Heyney-Greenstein's empirical approach obtains the P(Θ) as a function of AF:

$$P(\Theta) = \frac{1 - AF^2}{(1 + AF^2 - 2AF\cos\Theta)^{3/2}} \tag{2.29}$$

This phase function is useful for the mathematical modeling of radiative transfer in aerosol media with non-spherical particles [131].

The last optical property is called Polarization. It occurs, for example, when the unpolarized light emitted by the Sun [81,116] is polarized by reflection, transmission, and scattering [131] of the aerosols in the atmosphere. Polarization[16] is a property that specifies the direction and magnitude of the waves' electric field. Its effects play an important role in aerosol optics [135] and are sensitive to the size and refractive index of particles [131]. Considering a scattered light in the atmosphere is composed of unpolarized and polarized components, this radiation is represented in terms of Stokes' parameters [136]:

$$\begin{bmatrix} I_{total} \\ Q \\ U \\ V \end{bmatrix} = \begin{bmatrix} I_{nat} \\ 0 \\ 0 \\ 0 \end{bmatrix} + \begin{bmatrix} I_{pol} \\ Q \\ U \\ V \end{bmatrix} \tag{2.30}$$

where I_{total} is the total radiance, Q and U are the magnitude and direction of linear polarization [137,138], V is the magnitude of circular polarization, and subscripts nat/pol mean natural or unpolarized and polarized light, respectively. The condition for the light to be natural is Q = U = V = 0 [81], while for a polarized light $I_{pol} = I_{total} - I_{nat}\sqrt{Q^2 + U^2 + V^2}$, and for a partially polarized light, the relation among these parameters is an inequality, ${I_{total}}^2 \geq Q^2 + U^2 + V^2$ [139].

[16] The content of this property was adapted from [134].

The degree of polarization of a scattering light is the ratio of the intensity of the polarization component to the total intensity [70] and it can be extracted from Stokes' parameters presented as follows:

$$degree\ of\ polarization = \frac{\sqrt{Q^2 + U^2 + V^2}}{I_{total}} \tag{2.31}$$

When its value is 0, the light is non-polarized, and when it is 1, the light is completely polarized. Macroscopic particles such as dust grains and ice crystals have a smaller polarization ability at a scattering angle of 90º; otherwise, they also polarize light, producing quite large values of the degree of polarization in some selected directions [131]. The DoLP is calculated when Stokes' circular parameter is neglected due to the small values within the range of 10^{-2} to 10^{-5} [140]:

$$DoLP = \frac{\sqrt{Q^2 + U^2}}{I} \tag{2.32}$$

as well as the degree of circular polarization is V/I_{total}.

2.4 GROUND-BASED INSTRUMENTATIONS

Optical-microphysical-radiative characteristics of the aerosols can be deduced from the analysis of solar light scattered or attenuated by the atmosphere using instruments placed on the ground, a ship, an aircraft, or a satellite [131]. For this purpose, remote sensing and *in situ* measurements are employed as observational techniques. While the remote sensing technique involves measured radiation at some distance away, characterized by a specific wavelength that is sensitive to some physical aspect of the medium [81], the *in situ* techniques perform their observations within the medium.

Based on the instrumentation used to measure the aerosols and radiation, remote sensing can be classified as active or passive. The first employs a radiation source generated by artificial means, such as the lasers used in lidar or the microwaves used in radar, and the second utilizes the natural radiation sources of the Sun or the Earth-atmosphere system [81], such as radiometers. Passive remote sensing allows the global inference of atmospheric and surface temperatures,

composition profiles, surface properties, and radiative budget components from orbiting meteorological satellites [81]. Active remote sensing can measure the vertical distribution of the atmospheric components, locate aerosol layers and clouds, and infer some atmospheric parameters, such as wind and temperature [141]. Therefore, the radiation-aerosol interaction leaves a scattered signature obtained by a passive or active sensor that can be used for aerosol identification.

Furthermore, remote sensing can be classified as space-based and ground-based observations. Most space-based sensors are passive and measure irradiances at multiple wavelengths, some at multiple viewing angles [141]. There are a few active remote sensing satellites, e.g., the Cloud-Aerosol Lidar and Infrared Pathfinder Satellite Observations (CALIPSO) spacecraft with the Cloud-Aerosol Lidar with Orthogonal Polarization (CALIOP) [142,143] onboard, or ATmospheric LIDar (ATLID) onboard EarthCARE (Earth Cloud Aerosol and Radiation Explorer) currently in orbit [144–146]. Ground-based observations, the focus of this manuscript, are vital for satellite aerosol-retrieval validation [141], satellite calibration, and model validation. They are composed of active and passive sensors, and the synergy between them improves the aerosol property retrievals. The ground-based instruments have high precision and continuous measurements, but have restricted spatial coverage.

Ground-based remote sensing has been established as a means of monitoring aerosols, climate, and air quality, among other variables. It can be carried out on research cruises, onboard aircraft, and ground sites which requires aerosol databases, leading to the development of some networks, research centers, projects, and programmes such as the Global Atmosphere Watch (GAW) World Data Centre for Aerosols (WDCA) <last access: May 28th, 2025>, National Oceanic and Atmospheric Administration (NOAA) Earth System Research Laboratories (ESRL) Federated Aerosol Network [147], ACTRIS <last access: May 28th, 2025>, In-service Aircraft for a Global Observing System (IAGOS) [148], Global Aerosol Synthesis and Science Project (GASSP) [149], and others.

This chapter also presents the main remote sensing instruments employed to perform this research. The CommSensLab Optical Remote Sensing group at the UPC operates some ground-based remote sensing instruments as part of the ACTRIS/EARLINET [150]. These instruments include:

- A multi-wavelength high-power lidar system;
- A Polarized Sun-Sky-Lunar Photometer (CE318-TP9) manufactured by Cimel Electronique;
- Three radiometers (a Skye Instruments SKE-510 PAR, a Kipp and Zonen CM 21 pyranometer, and a Kipp and Zonen CNR 4 Net Radiometer); and
- A National Aeronautics and Space Administration (NASA) Polarized-Micro-Pulse Lidar (P-MPL) system.

They are located on the rooftop of the CommSensLab-UPC building <last access: May 28th, 2025>, in Barcelona, Spain.

2.4.1 Lidar Systems

The light detection and ranging (lidar) [151] is an active remote sensing instrument that provides detailed profiles of the atmosphere with high spatial (when on board a satellite) and temporal resolution of the measurements. Lidars have been used to investigate turbulent processes and the diurnal cycle of the planetary boundary layer, meteorological phenomena (frontal passages, hurricanes, and others), and polar stratospheric clouds; to monitor emission rates, concentration levels of trace gases and volcanic plumes; to distinguish water droplets from ice crystals in clouds; to study the climatic effects of aerosols; to detect local and intercontinental transport of air pollution, desert dust, and forest-fire smoke [152]; and other applications. Ref. [141] emphasized that the ground-based lidar data also contributes to constraining and validating aerosol transport models and validating satellite data. The first steps of the modern lidar took place in 1960 with the laser invention [153], favoring the creation of the Q-switched laser [154] and the current lidar systems.

A lidar operates on principles similar to those of radar (radio detection and ranging) or sonar (sound navigation and ranging), in which a transmitter and receiver compose the system. There is a large variety of lidar systems, but this document will focus on the general operation. Figure 2.8 illustrates the transmitter and receiver of a lidar system. A laser[17] emits a monochromatic beam (short light pulses in nanoseconds)[18] to reach a target (aerosol layers, clouds, etc.) up to 100 km, then the beam-target interaction scatters back a portion of the beam (backscattered light with scattering angle is about 180º) toward the receiver. It consists of a telescope to collect the scattered photons, an optical analyzer to select specific wavelengths or polarization states out of the collected light [152], a detector to convert the optical signal into an electrical signal (analog), and a data acquisition computer to digitize the electrical signal as a function of time or the light-source range as well as controlling the other basic functions of the system [156].

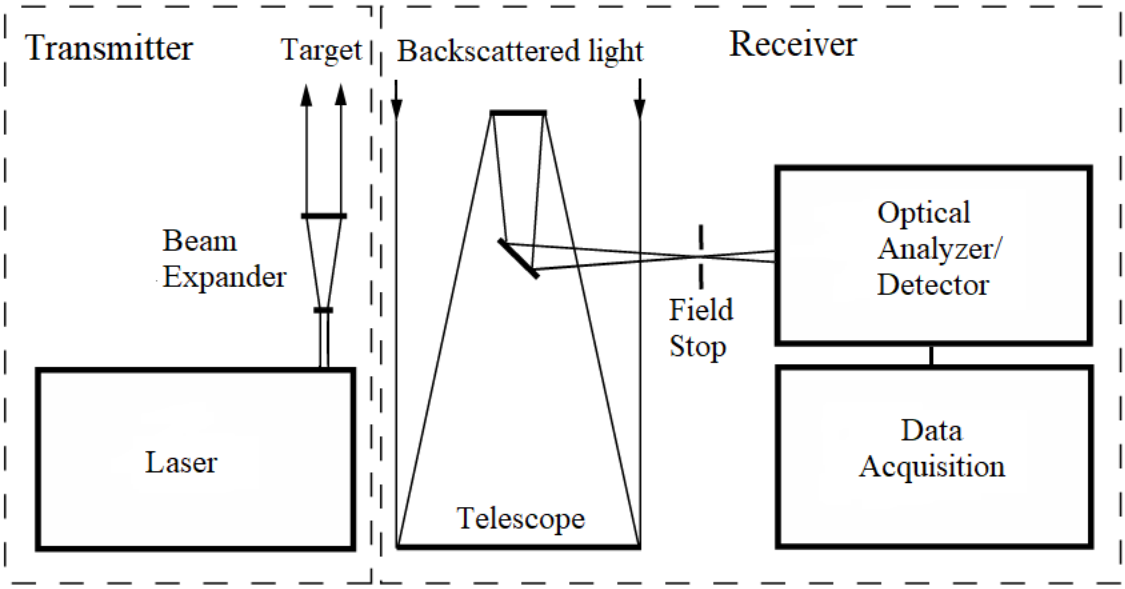

Figure 2.8. Lidar system composed of by transmitter and receiver. This figure was adapted from Ref. [152].

[17] A Light Amplification by Stimulated Emission of Radiation (laser) is a device that amplifies light and produces a highly directional, high-intensity beam that most often has a very pure frequency or wavelength [155].

[18] A beam expander (BMX) is used within the transmitter unit to reduce the divergence of the light beam before it is sent out into the atmosphere [152], i.e., it is used to collimate the laser beam.

The configuration of a lidar system also depends on the location of the constituents; for instance, a monostatic setup collocates the transmitter and receiver in which the height information is actively deduced from a measurement of the round-trip time between pulse emission and signal detection [152], range bin:

$$\Delta R = \frac{c\Delta t}{2} \tag{2.33}$$

where c is the speed of light and Δt is the time interval between the emission and reception of the lidar pulses. This setup was possible due to the development of Q-switching techniques, where monochromatic high-power short pulses are generated [81,116]. A bistatic setup separates the emitter and receiver [116].

A monostatic lidar system is divided into two configurations according to the axis of the laser and the telescope. A biaxial system requires the laser and telescope's axes to be parallel and different; in contrast, in a coaxial system, the laser and telescope's axes are the same. Lasers can be of several types and their wavelengths vary from UV to IR (250 nm to 11 μm), which are important regions for atmospheric applications [81]. The ruby, nitrogen, copper-vapor, CO_2, and excimer lasers were first used. However, the Neodymium-doped Yttrium Aluminum Garnet (Nd:YAG) lasers are the most common ones nowadays. The Nd:YAG lasers emit in the IR spectrum (1064 nm), in which frequency doubling, tripling, and quadrupling with nonlinear crystals is widely used to convert the primary Nd:YAG radiation to 532, 355, and 266 nm (second, third, and fourth harmonics, respectively) [152]. Overall, this type of laser is very well suited to lidar systems because of the low beam divergence, very narrow bandwidth, i.e., monochromaticity of the beam, and intense and short pulses [155].

Regarding the receiving system, it is necessary to have a field of view (FOV) as small as possible to decrease the background noise (background light)[19]. At the same time, the FOV needs to be large enough for a reduced laser divergence to be completely or partially within it. When the entire laser beam is within the receiver's

[19] It is light coming from other sources than the laser beam such as the Sun, street light, moon, stars, etc.

FOV, there is a complete overlap (better setup for efficient observations of a lidar system). Usually, a field stop (Figure 2.8) in the focal plane of the receiver optics is necessary to limit the background light [152]. According to the purpose of the investigation, a field stop can be a chopper[20], optical fiber bundle, lenses, interference filters[21], among others.

After the backscattered beam passes by the field stop, the optical components can select the signal according to specific wavelengths or send it to the signal detectors: Photomultiplier Tubes (PMTs), Avalanche Photodiodes (APDs), or both. These detectors convert light into analog electrical signals (current or voltage) [157]. The PMT amplifies the electrical signal, multiplying photons by secondary electron emission in the dynodes. The APD is a photodiode that works under high reverse voltage, which allows internal amplification of the signal through the avalanche effect. To improve the signal-to-noise ratio[22] and select the wavelength of interest, avoiding background light, it is useful to place an interference narrow-band filter before the PMTs. Then, the photons are recorded by the photon counting technique or an analog recording. The first one detects photons as separated pulses owing to a weak scattering process or when the investigated region is far away from the instrument [152], and the second one measures and records the average current produced by the photo pulses, which is more efficient for strong backscatter signals and short distances. Finally, the signal goes to the data acquisition software, where it is stored, and the analog signal is converted into a digital one.

The main monostatic lidar systems are Elastic, Depolarization, Raman, Differential-Absorption Lidar (DIAL), Doppler, and Fluorescence.

Elastic technique. This kind of lidar system captures the light that is elastically scattered (Mie-Rayleigh-Geometric scatterings) by the atmospheric target after

[20] The chopper opens the field stop only when light from the region of interest arrives and thus blocks the strong backscatter signal from the lower atmosphere to avoid an overload of the detectors [152].

[21] An interference filter is in charge of the transmission of the beam in a passband close to the wavelength of interest and avoids the light outside the desired passband.

[22] The signal-to-noise ratio indicates the contamination of the lidar signal by a background noise. The higher ratio means less contamination in the signal.

interacting with a laser beam. In this process, the wavelengths remain unchanged (Subsection 2.3.3.1) and the magnitude of the received signal at a given range depends on the backscatter cross-section of scatters along the path to that range [82]. Some characteristics of an elastic lidar made it widely used: high spatial resolution because the cross sections for elastic scattering are quite large, the amount of returning light is comparatively large, the time required to scan a volume of space is relatively short, and the laser light is practically monochromatic [156]. Considering a non-multiple-scattering condition, the simplified elastic lidar equation is:

$$P(\lambda, R) = \frac{C}{R^2}\beta(\lambda, R)O(R)e^{\left[-2\int_0^R \alpha(\lambda,R)dR\right]} \quad (2.34)$$

where:

- P(λ, R) is the optical return power, in W, as a function of the emitted wavelength (λ) and the range (R) in m^{-1}. The R is a function of time (Equation 2.33);
- C is the system constant, in Wm^3: C = ((EL c)/2) AT, where EL refers to the emitted energy per laser pulse and AT refers to the effective telescope area, in m^2;
- β(λ, R) is the backscatter coefficient, in $m^{-1}sr^{-1}$, and is calculated as the contribution of the molecule scattering (β_{mol}) and the aerosol scattering (β_{aer}):

  $$\beta(\lambda, R) = \beta_{mol}(\lambda, R) + \beta_{aer}(\lambda, R) \quad (2.35)$$

  The molecule scattering, mainly occurring from nitrogen and oxygen molecules (the most concentrated gases in the atmosphere), primarily depends on air density and thus decreases with height, i.e., backscattering decreases with distance if the observation is made from the ground [152]. However, aerosol scattering is a highly spatial-temporal variable in the atmosphere;
- O(R) is the overlap function, 0 ≤ O(R) ≥ 1. In the short distances (areas close to the lidar), where the laser beam and the telescope's FOV do not intersect,

no signal is obtained, so O(R) = 0, but, with the increase of R, where the laser beam is completely within the telescope's FOV, O(R) = 1 [156];

- The final part of Equation 2.34 is the transmission term $T_L(R)$, which is the fraction of light that gets lost on the way from the lidar to the scattering volume and back [152]. According to the Lambert-Beer-Bouguer law for a lidar system, Equation 2.21 is written as:

$$T_L(R) = e^{\left[-2\int_0^R \alpha(\lambda,R)dR\right]} \tag{2.36}$$

$T_L(R)$ has values between 0 and 1. The integral considers the path from the lidar to the distance R, and factor 2 stands for the two-way transmission path [152].

- α(λ, R) is the extinction coefficient, in m^{-1}, i.e., the sum of the losses from molecule (mol) and aerosol (aer):

$$\alpha(\lambda, R) = \alpha_{mol}(\lambda, R) + \alpha_{aer}(\lambda, R) \tag{2.37}$$

Depolarization technique. This technique involves the transmission of a linearly polarized laser pulse[23] and the detection requires the separation of the backscattered light parallel and orthogonal to the initial emitted polarization [152]. The transmitted beam can be orthogonally or parallelly polarized by aerosols, influencing the receiver's design to capture two parallel and cross-polarized components of the backscattered beam. Therefore, the ratio of the cross-polarized lidar return signal to the parallel-polarized backscatter signal [158] is the linear depolarization ratio (δ(R))[24]:

$$\delta(R) = \frac{\beta_{\perp}(R)}{\beta_{\parallel}(R)} \tag{2.38}$$

where $\beta_{\perp}(R)$ refers to the backscatter that is linearly polarized in the perpendicular direction (cross-polar) and $\beta_{\parallel}(R)$ refers to the backscatter that is linearly polarized in

[23] The lidar lasers naturally produce linear polarization because of the crystalline lasing medium [152].

[24] The Volume Depolarization Ratio and the Particle Depolarization Ratio are detailed in Subsection 3.2.3.

the parallel direction (co-polar) to the plane of the linearly polarized laser beam. Typical values of δ(R) below ~5% refer to spherical particles, and values between 10 and 40% refer to nonspherical particles [144]. Volcanic and desert dust particles cause depolarization ratios greater than 30% at 532 nm, whereas spherical particles and fine-mode particles lead to depolarization ratios less than 3% [61]. Backscattering from a nonspherical particle can be produced by internal reflections that rotate the initial vibration plane of the electric vector and produce depolarization [81]. Depolarization is applied to infer the water and ice content in clouds [81] or to identify the dry, the liquid and the ice phase of aerosols [158].

Raman technique. As explained in Subsection 2.3.1, the Raman signal (λ_{Ra}) is an inelastic scattering because the scattered light is wavelength-shifted concerning the emitted light (λ):

$$\lambda_{Ra} = \frac{\lambda}{1 - k\lambda} \tag{2.39}$$

k is the Raman shift for a specific molecule (in cm^{-1}), e.g., k = 2331 cm^{-1} for N_2. The Raman scattering results when the incident photon can excite vibrational modes (higher energy state, hence, increases in the vibrational amplitude) in the polarizable molecules; then, the deexcited molecules (with less energy by the amount of the vibrational transition energies) scatter photons [152]. Therefore, this scattered signal identifies scattered lights from specific molecules in high atmospheric concentrations (N_2 and O_2). The Raman lidar is usually used to retrieve water vapor, temperature, and aerosol extinction coefficient profiles.

DIAL technique. The DIAL technique detects atmospheric gases (O_3, NO_2, NO, N_2O, SO_2, CH_4, HCl, NH_4, water vapor, and other greenhouse gases) with high sensitivity by determining the differential molecular absorption coefficient [152] and it can detect gas concentrations as low as a few hundred parts per billion [156]. This technique is based on emitting two (or more) wavelengths in which one of them is strongly absorbed by the atmospheric constituent of interest and the light at the second wavelength is not absorbed at all or only minimally absorbed [156].

Doppler technique. This technique applies the Doppler principle for determining the motion of particulates and molecules [81], where the frequency shift along the lidar line of sight is proportional to the ratio of wind speed and the speed of light [152]. It is widely used to measure wind profiles, atmospheric turbulence, and others. The frequency shift (f) is:

$$f = f_s(1 + 2v_D/c) \tag{2.40}$$

where f_s is the frequency of λ_s, u_D is the relative speed along the line of sight of the lidar Doppler, and c is the speed of light.

Fluorescence technique. It is also called resonance scattering lidar. This lidar system captures the reemitted light by atoms, molecules, or aerosols after they have absorbed the laser beam and reemits it, i.e., a large variety of substances exhibit their unique autofluorescence spectrum more or less if lasers irradiate them, so the fluorescence spectrum is a good index for the identification [159]. For instance, 266 nm is used to excite fluorescence from tryptophan, while 355 nm is used from Nicotinamide Adenine Dinucleotide Phosphate with hydride donors (NADH)[25] [160]. The beam reemission can occur at longer wavelengths and due to the extremely high cross sections, there are strong lidar signals, distinguishing atom or ion number concentrations from distances between 80 and 110 km [152]. Thus, these changes in the fluorescence spectrum provide information about the target in the atmosphere, such as measurements of soot, pollen, fungal spores, and dust, among other particles. The next two lidar techniques are used in this research.

Therefore, the lidar techniques play a valuable role in monitoring and classifying aerosols and measuring aerosol concentration, gas, temperature, and water vapor profiles. In addition to those applications, the calibration and validation of satellites, weather forecasting, climate modeling, studies on climate change, and other drove the creation of lidar networks worldwide such as the Asian Dust and Aerosol Lidar Observation Network (AD-NET) [161,162], Commonwealth of Independent States Lidar Network (CIS-LiNet) [163]; EARLINET [150,164,165];

[25] The tryptophan and the NADH are molecules that emit fluorescence.

Latin American Lidar Network (LALINET) [166,167]; Micro-Pulse Lidar Network (MPLNET) [168]; Network for the Detection of Atmospheric Composition Change (NDACC) [169]; among others.

Regarding the UPC/EARLINET multi-wavelength high-power lidar system, the following overview/description is based on Ref. [134]. The first UPC lidar system had two elastic channels (532 nm and 1064 nm) and has been operated since 1996. Then, another elastic channel at 355 nm and a Nitrogen-Raman channel (607 nm) were added to the system [170]. One decade later, the main upgrade was designed and implemented by Ref. [171], including a wavelength separation unit that provided the lidar backscattered returns of the three elastic channels (355, 532, and 1064 nm) and three Vibro-Rotational Raman (VRR) channels (387 and 607 nm excited at 355 and 532 nm, respectively, for nitrogen, and 407 nm excited at 355 nm for water vapor) [171]. In a row, two cross-polarization channels at 532 and 355 nm were implemented, employing attached auxiliary telescopes without altering the original system [172,173], followed by the incorporation of a Pure-Rotational Raman (PRR) channel at 354 nm [174]. The advantage of using a PRR channel instead of VRR is more relevant during daytime conditions [174], permitting measurements with a much larger cross section and improving the inversion of optical data to particle microphysics [175].

The last upgrade of the UPC/EARLINET multi-wavelength high-power lidar system added a PRR channel at 530 nm [176], implementing the current configuration of the lidar system. In summary, it provides backscattering at three wavelengths (elastic channels at 1064, 532, and 355 nm), extinction at 532 and 355 nm (PRR channels at 530 and 354 nm), depolarization ratio at 532 and 355 nm, and water vapor mixing ratio (VRR channel at 407 nm). This system collects the backscattered light by an optical fiber bundle to lead the light towards the separation unit before the detectors (APD and PMT). These configurations make the UPC/EARLINET lidar system a unique instrument within the EARLINET community. Figure 2.9 shows the coaxial laser beam, the main telescope, and the two telephoto lenses for depolarization detection.

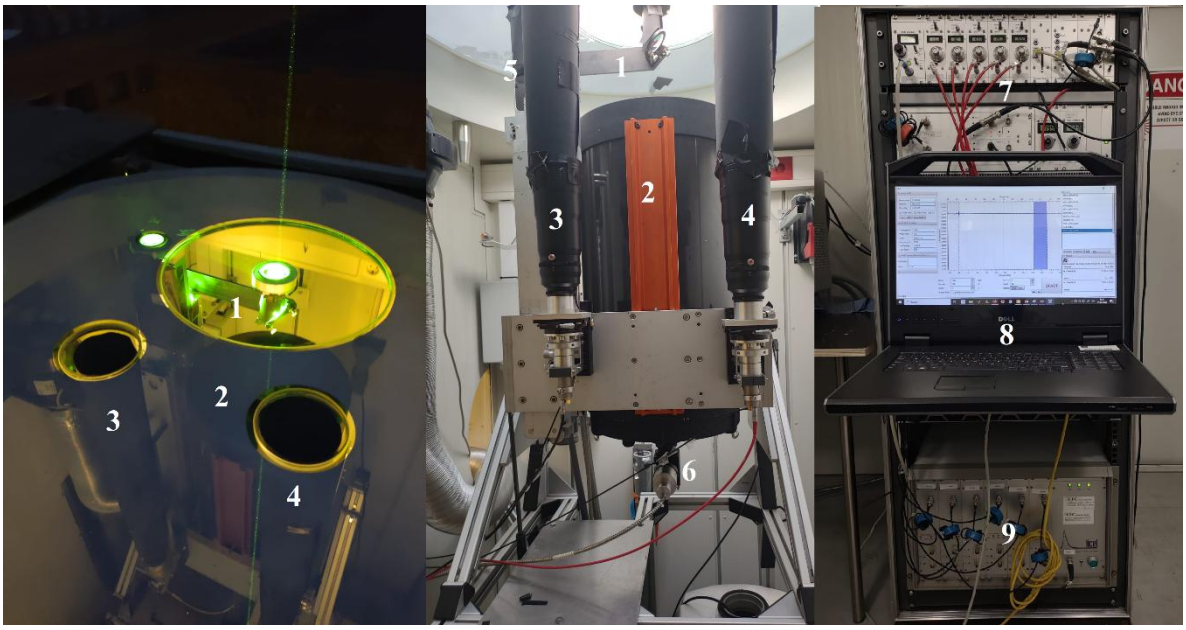

Figure 2.9. UPC/EARLINET multi-wavelength high-power lidar system: 1-Peliscope to set up a coaxial system, 2-Main telescope, 3-Telephoto lens for 355-nm depolarization, 4-Telephoto lens for 532-nm depolarization, 5-Harmonic generators (laser), 6-Optical fiber bundle, guiding the backscattered light to the wavelength separation unit and defining the FOV, 7-Channel supply, 8-Control computer and acquisition software, and 9-Transcient recorders. Picture credit: Author.

The technical details about the laser, telescopes, and acquisition units of the UPC/EARLINET lidar system are in Table 2.2. Additionally, the UPC Optical Remote Sensing group has maintained a NASA MPL since 2016, providing continuous observations owing to its full-time-unattended operation.

2.4.2 Sun-sky-lunar Photometer

The radiometers are passive remote sensing instruments for measuring solar-sky-unar radiation. The Sun photometer is a pointing radiometer mounted on a two-axis solar tracker that measures solar spectral irradiance in narrow spectral bands [82], i.e., it measures the spectral atmospheric transmittance [131], utilizing the direct beam of solar radiation at specific wavelengths in the UV and visible spectra [81]. Thus, Beer-Bouguer-Lambert's law (Equation 2.15) is written in terms of the Sun photometer observations according to Ref. [44]:

$$V_\lambda = V_{\lambda,0} ESD^2 e^{(\tau m)T_y} \tag{2.41}$$

V_λ stands for digital voltage observed at λ, V_0 is the extraterrestrial voltage, ESD is the relative Earth-Sun Distance, τ is the total optical depth, *m* is the optical air mass, and T_y is the transmission of absorbing gases. Photometers cannot be used to determine the vertical structure of aerosol, but they refer to the average aerosol properties along extended vertical columns [131] from the ground to the TOA.

Table 2.2. Technical specifications of the UPC/EARLINET multi-wavelength high-power lidar system. This table was adapted from [134].

Technical specifications		
Setup	Characteristics	UPC lidar system
Transmitter	Laser	Innolas Spitlight Compact 400
	Zenith angle	0º
	Emitted wavelengths	355, 532, and 1064 nm
	Energy per pulse	~90 mJ at the three wavelengths
	Divergence	28 mrad
	Repetition rate	20 Hz
	Pulse duration	3.6 ns
	System setup	Monostatic coaxial
	Spatial resolution	3.75 m
Receiver	Telescope model	Celestron CGE 1400
	Elastic wavelengths	355, 532, and 1064 nm
	PRR wavelengths	530 and 354 nm
	Depolarization receiver	TAIR-3S Telephoto lens for 355 and 532 nm
	VRR water vapor	407 nm
	Focal length of the telescope	3.91 m
	Telescope aperture (Ø)	0.35 m
	Detector	APD and PMT
	Voltage responsivity	1.9×10^6 (355 nm), 1.5×10^6 (532 nm), and 3.7×10^5 (1064 nm) in VW^{-1}
	Acquisition	Licel transient recorder TR40-80, mixed 250 MHz PC+ADC40Msps/12bit

AERONET started in 1993 due to the need for a standard source of aerosol optical depth measurements to evaluate and refine the MODerate resolution Imaging Spectroradiometer (MODIS) [177] and Multi-angle Imaging SpectroRadiometer (MISR) [178] retrieval products [141]. This network is a federation of ground-based remote sensing aerosol networks established by NASA and *Laboratoire d'Optique*

Atmosphérique - PHOtométrie pour le Traitement Opérationnel de Normalisation Satellitaire (LOA-PHOTONS) and it provides a long-term, continuous, and readily accessible public-domain database of aerosol optical, microphysical, and radiative properties for aerosol research and characterization, validation of satellite retrievals, and synergism with other databases (AERONET, last access: May 28th, 2025). The AERONET standardizes, calibrates, processes, and distributes its photometers, ensuring more reliable observations worldwide. It provides data accuracy at three levels of Version 3 [49]: (i) Level 1.0 does not have any processing (raw data), but it is preprocessed to convert the data into a unified format; (ii) Level 1.5 (L1.5) is processed by some algorithms such as the screening codes [49,179] and sky radiance inversion codes (Subsection 3.3); and (iii) Level 2 (L2) is the highest AERONET level due to the quality assured and a reprocessing to implement new parameters.

In addition to AERONET, there are other networks called GAW - Precision Filter Radiometer (GAW-PFR) <last access: May 28th, 2025> that uses PFRs to measure AOD at GAW baseline stations; Sky Radiometer Network (SKYNET) that researches the aerosol-cloud-solar radiation interaction by Sun-sky radiometer POM-01 and POM-02 [180,181]; and Pandonia Global Network that measures columnar amounts of trace gases (O_3, NO_2, CH_2O) in the atmosphere (UV spectrum) by the Pandora spectrometer [182].

The UPC had maintained a standard Sun-sky photometer (CE318) [183] from 2004 to July 2021, when it was replaced by a Sun-sky-lunar Cimel Electronique CE318-TP9 Multiband Photometer [184], as displayed in Figure 2.10. The new photometer provides measurements at eight wavelengths from 340 to 1640 nm. The 937-nm channel is used to determine the water vapor content. It also provides polarization data [185,68], direct-sun measurements, angular sky radiances [183], direct-lunar measurements, and columnar water vapor content [186–188]. The CE318-TP9 has an additional filter wheel containing 3 sets of 3 polarizers oriented with 120º separation, operating in UV, visible, and IF ranges. More technical specifications are displayed in Table 2.3.

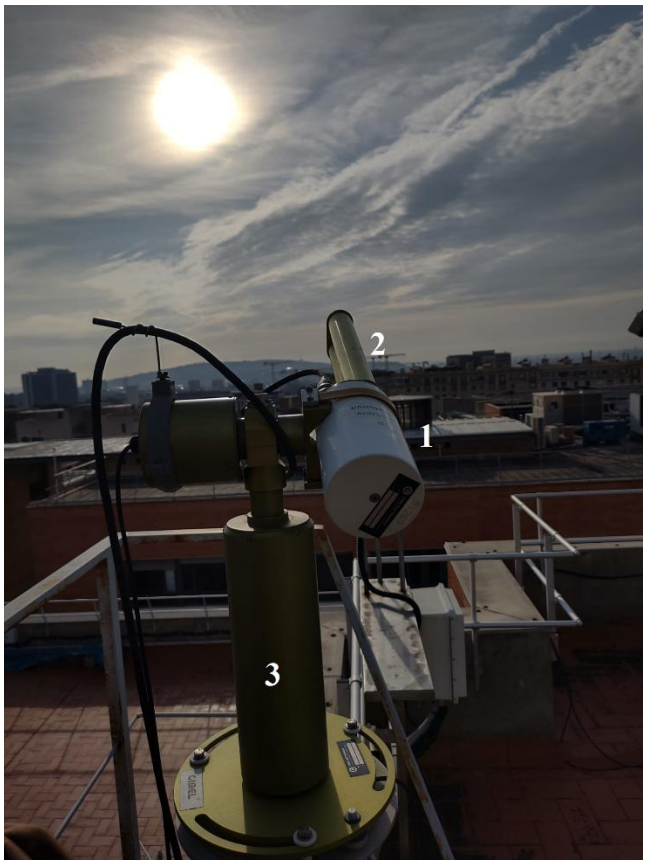

Figure 2.10. The Sun-sky-lunar Cimel CE318-TP9 Multiband Photometer performs a direct measurement at the UPC rooftop in Barcelona, Spain. 1-Sensor head with filter wheels, 2-Collimator to narrow and focus solar radiation, and 3-Robot that points the collimator in any direction in the sky (zenith and azimuth angles). Picture credit: Author.

Table 2.3. General technical specifications of the CE318-TP9. This table was adapted from Ref. [189].

Characteristics	Values
Irradiance precision	< 0.1%
Viewing angle	0.02 sr or 1.29˚
Minimal scattering angle from the sun	2º
Optical filter drift	< 1% per year
Solar tracking precision	0.01º
Interferential filter bandwidth	< 30 nm
Solar and moon scanning	4-quadrant sensor
Mechanical precision spot	0.003º

The sky radiances and the direct measurements are performed at eight wavelengths (340, 380, 440, 500, 675, 870, 1020, and 1640 nm), with azimuth angles varying from 0º to 180º for the left and right almucantars. Therefore, a scan for both left and right branches for an assumed homogeneous atmosphere can help

to reduce observational uncertainties as the value of optical mass remains constant during the measurements [190]. The frequency of the sky scans depends on the cloud-free conditions, the time of day, and the air masses. About 14 direct sun measurements per hour, more than 10 standard almucantar sequences, and around 8 polarized almucantar sequences per day are performed at the UPC. The almucantar, the almucantar polarized, the principal plan, and the principal plan polarized[26] scenarios are techniques for measuring sky radiances. The two almucantars keep a constant polar angle equal to the SZA with variable azimuthal angles, whereas the two principal planes keep a constant azimuthal angle with variable SZAs [189]. Figure 2.11 illustrates the sky measurement scenarios.

Regarding the polarization observations, the UPC photometer measures the DoLP at seven wavelengths (380, 440, 500, 675, 870, 1020, and 1640 nm) during daytime in the azimuthal range from 25º to 160º for left and right almucantar. Cimel Electronique company implemented the first polarizer in the 870 nm channel [185], extending to the other channels, from 340 to 1640 nm [68] to provide DoLP at a scan-azimuth-angle bunch.

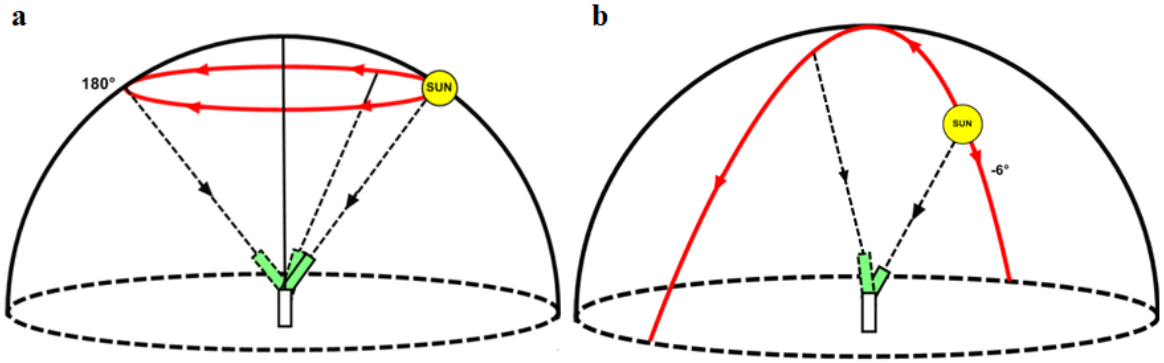

Figure 2.11. The almucantar scenario (**a**) and principal plan scenario (**b**) performed by all Sun photometers. This figure was adapted from Ref. [189].

The polarized photometers only have three linear polarized filters referring to I-Q-U parameters (Subsection 2.3.3.2). If I, Q, and U are computed as a function of

[26] The principal plane ranges from -6º to 150º and the principal plane polarized ranges from -85º to 175º.

the polarized radiances from the photometer's filters (F_1, F_2, and F_3, respectively), the Stokes' parameters (S) are directly obtained by Ref. [137]:

$$S = \begin{bmatrix} I \\ Q \\ U \end{bmatrix} = \begin{bmatrix} \frac{2}{3}(F_1 + F_2 + F_3) \\ \frac{2}{3}(2F_1 - F_2 - F_3) \\ \frac{2}{\sqrt{3}}(F_3 - F_2) \end{bmatrix} \tag{2.42}$$

where subscripts 1 to 3 refer to the orientations of the filters: 0º (1), 120º (2), and 240º (3) in which the observed radiances are in $Wcm^{-2}sr^{-1}nm^{-1}$. Conforming to the system in Equation 2.42, Equation 2.31 can be rewritten as a function of F_1, F_2, and F_3:

$$DoLP = \frac{\sqrt{\left[\frac{2}{3}(2F_1 - F_2 - F_3)\right]^2 + \left[\frac{2}{\sqrt{3}}(F_3 - F_2)\right]^2}}{\frac{2}{3}(F_1 + F_2 + F_3)} \tag{2.43}$$

Equation 2.43 can be simplified as shown by next formula:

$$DoLP = \frac{2\sqrt{F_1^2 + F_2^2 + F_3^2 - F_1F_2 - F_1F_3 - F_2F_3}}{F_1 + F_2 + F_3} \tag{2.44}$$

Figure 2.12 shows a real example of the DoLP from two dominant aerosol modes in Barcelona. The coarse aerosol is dominated by dust, and the fine aerosol is influenced by urban particles. The DoLP takes values close to 0 at small scattering angles and increases with high Φ. The coarse-particles DoLP has a peak at 120º (0.43), then it decreases, while the fine-particles DoLP has a maximum (0.51) at 160º. Thus, the DoLP increases at higher Φ, mainly for fine particles, because the scattered light is stronger for small particles (high AE) than coarse ones (maximum at 120º in this case). According to Ref. [191], aerosols with radii in the range 0.1 to 0.3 μm polarize scattered radiation for scattering angles within 30-150º. The measurements are not performed at angles less than 25º due to the photometer design and the solar saturation. So far, the AERONET inversions do not use DoLP.

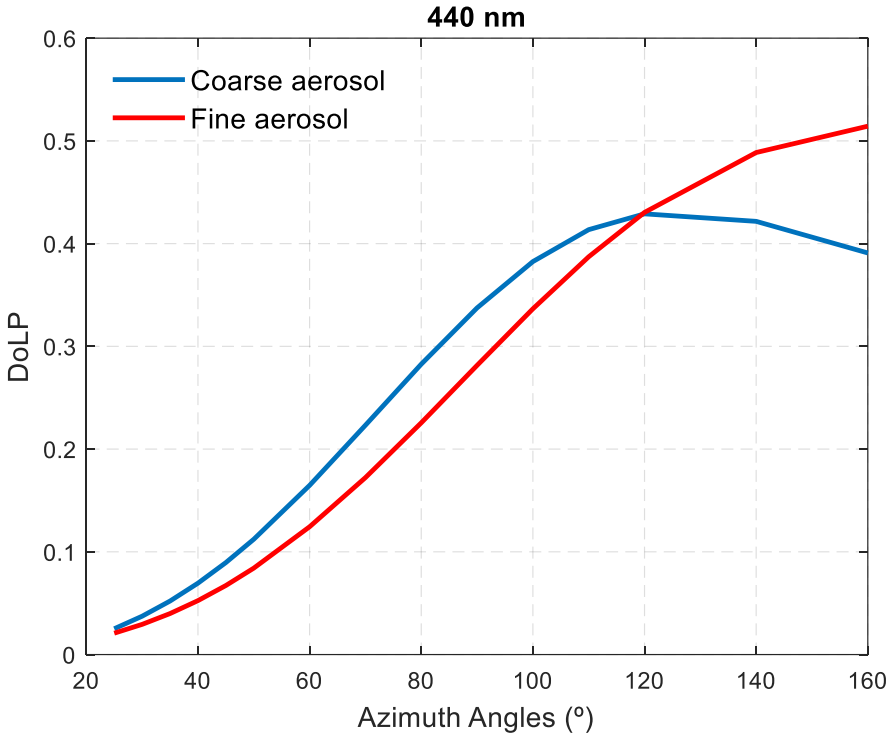

Figure 2.12. DoLP for two types of aerosols (coarse and fine modes) at 440 nm in Barcelona, Spain.

2.4.3 Pyranometers

The pyranometers measure G, Wm^{-2}, in broadband spectral ranges [82], i.e., this instrument integrates G at all wavelengths within a spectral range. Generally, it has a short temporal resolution (≤ 2 min). Pyrgeometers only measure the LW. The sensors within the instruments (thermoelectric or photodiode) convert solar energy (thermal) into a proportional electrical signal, then this signal is registered by a datalogger, where there is a conversion to irradiances according to calibration coefficients provided by the manufacturer. The World Radiometric Reference is the measurement reference standard of irradiance for solar radiometry to ensure worldwide homogeneity of solar radiation measurements with an estimated precision of 0.1%, accuracy of 0.3%, and stability of better than 0.01% per year [83].

As mentioned, the UPC also obtains radiation observations by a CNR 4 Net Radiometer (installed in February-March 2021), known as the UPC CNR 4; a CM 21 pyranometer (since 2009); and a SKE-510 PAR Quantum Sensor (same period as CM 21). Figure 2.13 depicts the radiometers at the UPC.

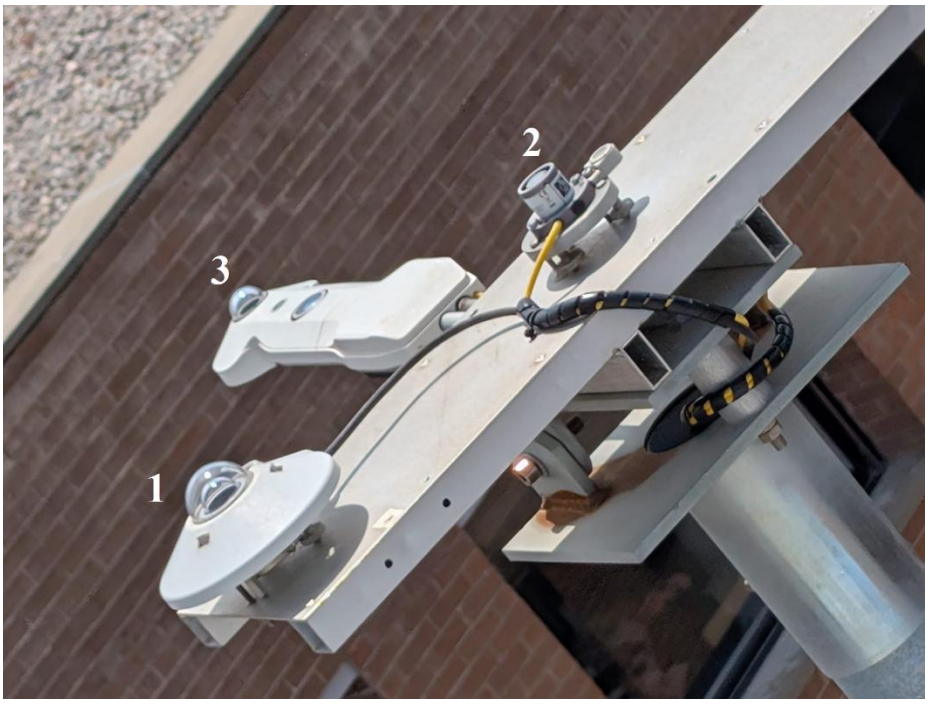

Figure 2.13. UPC radiometers. 1-CM 21, 2-PAR Quantum, and 3-CNR 4. Picture credit: Author.

The UPC CNR 4 includes four sensors that measure the energy balance between SW and LW far-infrared radiation *versus* surface-reflected SW and LW [192]. Table 2.4 shows the main differences between pyranometers and pyrgeometers at UPC.

Table 2.4. Pyranometers applied in the current research. This table was adapted from Refs. [82,193]. Manufac. stands for manufacturer.

Instrument	Model	Parameters to be measured	Viewing angle (sr)	Manufac.
Pyranometer	CM 21	Global (solar) radiation in broadband spectral ranges	2π	Kipp and Zonen
*Pyranometer	CNR 4	Upward short-wave radiation (facing-downward sensor) Downward short-wave radiation (facing-upward sensor)	2π **5π/6	
*Pyrgeometer	CNR 4	Upward long-wave radiation (facing-downward sensor) Downward long-wave radiation (facing-upward sensor)	2π 5π/6	

* The pyranometer and pyrgeometer are coupled in the CNR 4;
** To prevent illumination at low SZAs due to the lower sun shield.

The four radiometers consist of a pyranometer pair (facing upward and downward) to measure SW and a pyrgeometer pair (facing upward and downward) to measure LW. It was calibrated three times, as displayed in Table 2.5. From the first calibration to the last, the calibration coefficients have remained stable over time, suggesting a minimal instrumental drift and a reliable measurement performance.

Table 2.5. Calibration coefficients of the UPC CNR 4. Pm refers to the polynomials: Ts is the temperature of the sensors, Ts = Cc3x3 + Cc2x2 + Cc1x + Cc0, where Cc0-3 are the calibration coefficients; and Py and Pg = (1000/(sensor sensitivity))x, where the sensor sensitivity (μV/Wm^{-2}) is provided after the calibration, x is the experimental voltage (mV), Py$^{\downarrow}$ and Py$^{\uparrow}$ are the facing-upward and downward pyranometers, respectively, Pg$^{\downarrow}$ and Pg$^{\uparrow}$ are the facing-upward and downward pyrgeometers, respectively, ↑ stands for upward flux, and ↓ stands for downward flux. This table is adapted from Ref. [193].

P_m	1st calibration (Nov 2016)	2nd calibration (Feb 2020)	3rd cal.
Ts	$1.665e^{-8}x^3$-$5.576e^{-5}x^2$+0.0991x-44.42	$1.529e^{-8}x^3$-$5.168e^{-5}x^2$+0.0955x-43.52	*
Py$^{\downarrow}$	66.1813x	66.401x	65.7462x
Py$^{\uparrow}$	77.1605x	77.639x	77.101x
Pg$^{\downarrow}$	78.7402x	81.234x	80x
Pg$^{\uparrow}$	78.1861x	80.58x	78.064x

* The 3rd Ts-calibration coefficients remain the same as the 2nd one because there were no changes in the method to calculate temperature. The third one took place in December 2024.

The facing-upward and downward sensors allow the estimation of some parameters such as Albedo (A), Net Solar Radiation (NSR), Net Far Infrared Radiation (NFIR), Net (total) Radiation (NR), Ground Temperature (GT), and Sky Temperature (ST) [192]. The albedo is the ratio of downward-to-upward SW radiation, as equation below:

$$A = \frac{\mathrm{Py}^{\uparrow}}{\mathrm{Py}^{\downarrow}} \tag{2.45}$$

Usually, its values vary from 0 (completely absorbent surface) to 1 (completely reflective surface). The NSR is defined as the difference between the SW and the reflected solar radiation; hence, it only has positive values:

$$NSR = \mathrm{Py}^{\downarrow} - \mathrm{Py}^{\uparrow} \tag{2.46}$$

The NFIR is the part that contributes to heating or cooling the surface. In the CNR 4 operationality, it is calculated by:

$$NFIR = \mathrm{Pg}^{\downarrow} - \mathrm{Pg}^{\uparrow} \tag{2.47}$$

The NR is the difference between all incoming and reflected radiations:

$$NR = \mathrm{Py}^{\downarrow} + \mathrm{Pg}^{\downarrow} - \mathrm{Py}^{\uparrow} - \mathrm{Pg}^{\uparrow} \tag{2.48}$$

Furthermore, assuming that sky and ground behave like blackbodies (Subsection 2.2.2), it is possible to measure GT and ST with the pyrgeometer sensors:

$$GT = \left(\frac{\mathrm{Pg}^{\uparrow}}{5.67 \cdot 10^{-8}}\right)^{0.25} \tag{2.49}$$

$$ST = \left(\frac{\mathrm{Pg}^{\uparrow}}{5.67 \cdot 10^{-8}}\right)^{0.25} \tag{2.50}$$

The CM 21 model is part of the Solar Radiation Network (SolRad-Net, last access: May 28th, 2025) and it measures irradiance (Wm^{-2}) on a plane surface [194] at L1.5. Data Quality Assessment and Data Level Designations of NASA classifies the L1.5 <last access: May 28th, 2025> as level free of any operational problems like amplifier malfunctions, a contaminated or dirty dome, and a non-level sensor as examples, and it shows minimal sensor drift of less than 1%. The CM 21 has only one sensor facing upward to measure the SW. Table 2.6 shows the technical specifications of both radiometer models at the UPC.

Besides SolRad-Net, the SURFace RADiation Budget (SURFRAD) Network [195,196] and the World Radiation Monitoring Center - Baseline Surface Radiation Network (WRMC-BSRN) [197–199] are networks that detect and store solar radiation and other parameters. The GAW programme also manages radiation observations worldwide.

Table 2.6. Technical specifications of the UPC CNR 4 and the CM 21 sensors. This table was adapted from Refs. [192–194].

Characteristics	UPC CNR 4 SW*	UPC CNR 4 LW**	CM 21
Spectral range (nm)	300-2800 (50% points***)	4500-42000 (50% points)	305-2800 (50% points) 355-2200 (95% points)
Directional error (Wm^{-2})	< 20 (angles up to 80° with 1000 Wm^{-2} beam radiation). Combined zenith and azimuth error from 0° to 80° with 1000 Wm^{-2} beam radiation.		< ±10 (1000 Wm^{-2} beam radiation)
Sensitivity ($\mu V/Wm^{-2}$)	10-20	5-15	7-17
Irradiance (Wm^{-2})	0-2000	-250 to +250	0-4000
Cosine response	Max. sensitivity of 1 at 0º (SZA), zero at 90º (SZA), and between 90º and 0º, the sensitivity should be proportional to the cosine of the SZA.		Max. ±2% deviation from ideal at 60º (SZA) and max. ±6% at 80º (SZA) in any azimuth direction.
Sensor	Thermopile (absorber paint)	Thermopile (absorber paint) and silicon window	Thermal detector

* Pyranometers;
** Pyrgeometers;
*** 'Points' are the wavelengths where the output of the instrument is 50% or 95% reduced with 100% input (Kipp and Zonen, last access: May 28th, 2025).

The validation of the UPC CNR 4 facing-upward pyranometer is shown in Figure 2.14, where its instantaneous radiative fluxes are compared with those from the CM 21 [193]. Both pyranometers have an excellent correlation with a coefficient of determination (r^2) of 0.94, the linear regression (red line) has a crescent slope of 0.96, the Root Mean Square Error (RMSE) has a high value (69.18 Wm^{-2}), and the Normalized Mean Bias (NMB) shows a CNR 4 non-significant overestimation with a slight positive bias of 0.5%. The r^2 indicates that 94% of the variance of the UPC CNR 4 data is explained by the variance of the CM 21 data; thus, the UPC CNR 4 pyranometer properly measures the radiative fluxes. Additionally, the high RMSE value is expected because of the high dispersion of the points (dark blue dots) between 600 and 1200 Wm^{-2}.

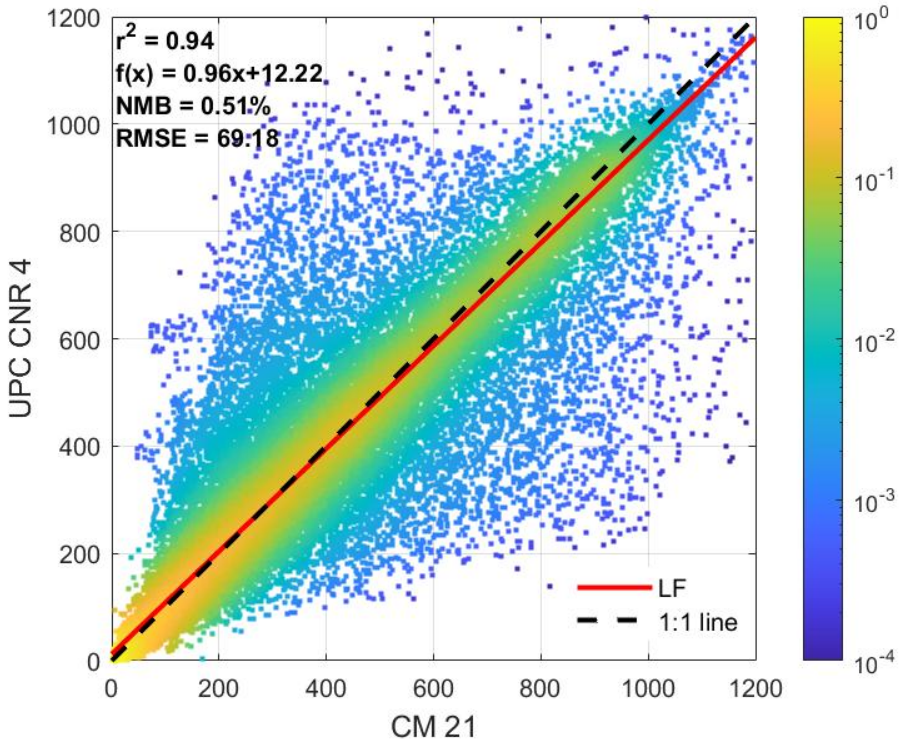

Figure 2.14. Instantaneous radiative fluxes in Wm-2 from the CM 21 (SolRad-Net) and the UPC CNR 4 from February 2021 to August 2023. LF is the linear fitting (red line) and the dashed black line (1:1 line) is the reference. The data density is represented in the color bar with a logarithmic scale varying from 0 to 1 (100%).

3 AEROSOL INVERSION ALGORITHMS

*I dedicate this chapter to Geremias Bristot, we are always in **synergy**, Nikki Diala Tagdulang, Sarah Cavalcanti Josuá, Roselena Rubino,* Ivan Zhou, *and all my PhD colleagues.*

Recycle!

This chapter discusses the major inversion algorithms employed to retrieve aerosol properties from ground-based remote sensing measurements, focusing on lidar systems and Sun photometers. The direct and inverse problems are introduced to better understand the remote-sensing interpretation of the scattered radiation from the interaction between a target and the light; then, some inversion methods are presented for each instrument (elastic lidar system and Sun photometer) and the synergy between them. More emphasis is given to the GARRLiC (Generalized Aerosol Retrieval from Radiometer and Lidar Combined data, [51]) code, owing to its use in developing this research. GARRLiC code is now a module in the GRASP (Generalized Retrieval of Atmosphere and Surface Properties) algorithm, in charge of retrieving aerosol characteristics by combining observations from radiometers and lidars.

3.1 GROUND-BASED REMOTE SENSING INVERSIONS

Remote sensing involves the interpretation and inversion of radiometric measurements of electromagnetic radiation [81], requiring scattered light (attenuated radiation) and radiative transfer theories, which were approached in Chapter II. Regarding the interpretation of the radiation-aerosol interaction, there are two types of problems: the direct problem and the inverse problem. An overview of both issues in remote sensing is illustrated in Figure 3.1. According to Ref. [81], an electromagnetic signal (Sg) as a function of an interaction target (Tg), such as molecules, particulates, and/or surfaces, can be written symbolically as a mathematical function:

$$Sg = J(Tg) \tag{3.1}$$

J is a function that governs the electromagnetic-radiation transfer. This function is not necessarily linear, and its inverse is given by:

$$Tg = J^{-1}(Sg) \tag{3.2}$$

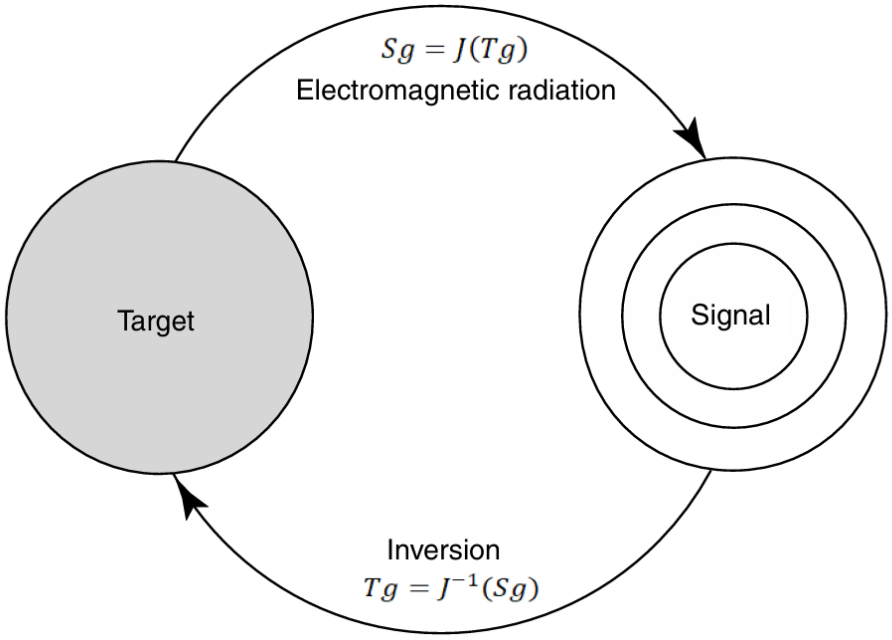

Figure 3.1. Symbolic representations of direct and inverse problems using mathematical function notation. This figure was adapted from Ref. [81].

On the one hand, the direct problem solves an equation system of a unique solution based on known parameters, initial conditions, and physical theories. Sometimes, the direct problem is called the forward problem because it can be used to predict the behavior of a given variable. For example, the forward problem is used in (i) calculations of light characteristics for a given ensemble of scatterings [131]; (ii) the modeling of atmospheric sky radiance by solving the radiative transfer equation for a plane-parallel atmosphere [45] in the case of photometer measurements; and (iii) the modeling of optical properties of aerosol ensembles with known microphysical properties [200].

On the other hand, the inversion problem determines the characteristics of particles from measured light extinction, scattering, or polarization as functions of wavelength and corresponding angles [131]. For example, backscattering radiation from a lidar signal can be used to classify the aerosols in the atmosphere. Figure 3.2 illustrates the direct and inverse problems applied to aerosol remote sensing.

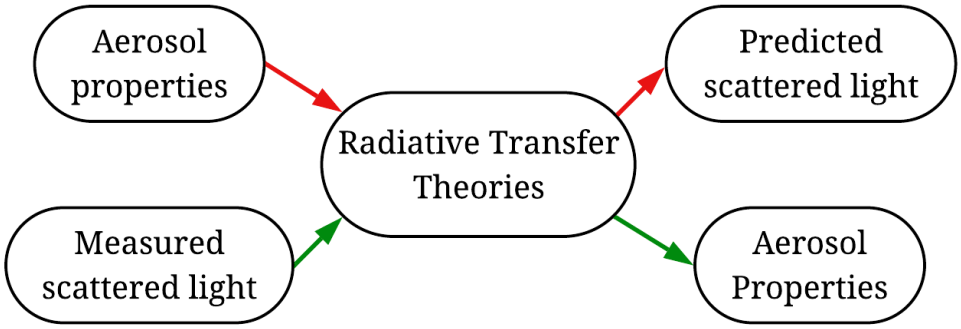

Figure 3.2. The direct and inverse problems applied to atmospheric aerosols. The red arrows refer to the direct problem, and the green arrows refer to the inverse problem.

The inverse problem is more complex than the direct one, which has a particular solution. The nonuniqueness of the solution of remote sensing inversion problems arises because the medium under investigation may be composed of many unknown parameters, a combination of which may lead to the same radiation signature [81]. Generally, a linearization procedure is applied to solve it by repeating to reach the convergence of the systems [131]. The errors of the inverse problem can be estimated in the procedure, and a condition is applied to perform the iterations of the convergence.

3.2 LIDAR INVERSIONS

The inversion of a measured elastic-lidar signal provides aerosol properties distributed in height. To achieve the most accurate inversion of the measured lidar signal, the range variations of the backscatter-to-extinction ratio along the examined atmospheric path should be considered [156]. Thus, a previous knowledge of the backscatter-to-extinction ratio, adopted here as the Lidar Ratio (LR), is required. This property reveals information regarding the size, shape, and absorption efficiency of the aerosol particles. The particle size is usually inversely related to the LR, and the particle absorption efficiency is directly related to the LR [201]. According to Ref. [67], typical desert dust values range from ~40 to ~75 sr. Figure 3.3 presents an LR comparison between CALIPSO and ground-based lidar retrievals. Its values range from ~20 to ~100 sr [152]. For lidar inversions, the LR has large variability according to the aerosol type. This variability can lead to large uncertainties in the retrieved

extinction profiles. Furthermore, the LRs are dependent on the laser wavelength, the aerosol particle chemical composition, the particle size distribution, and the atmospheric index of refraction [152,156].

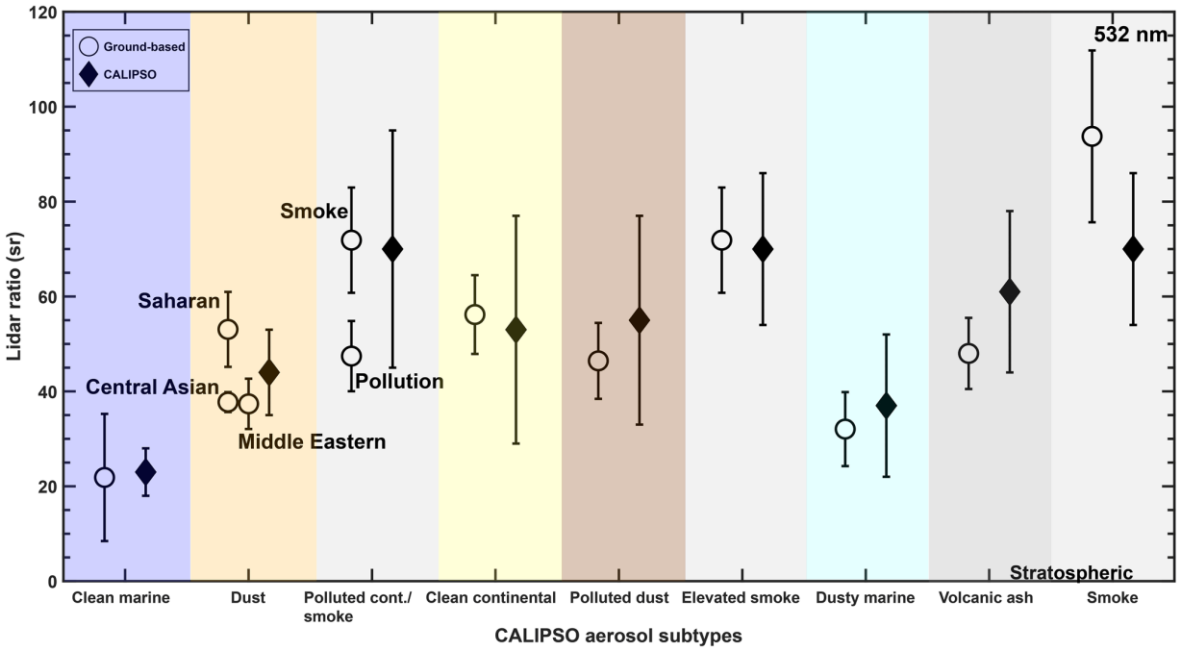

Figure 3.3. Aerosol classification and the LR comparison with data from CALIPSO [202,203], black rhombuses, and Ref. [201], empty circles, for stratospheric aerosols measured at 532 nm. This figure is available in Ref. [201].

Chapter II shows that an elastic-lidar equation (Equation 2.34) also depends on the backscatter coefficient (β(λ, R)) and the extinction coefficient (α(λ, R)), in which β(λ, R) has contributions of molecule and aerosol scatterings (Equation 2.35) and α(λ, R) is also constituted by molecules and aerosols (Equation 2.37). The LRs related to the aerosols and molecules are, respectively:

$$LR_{aer}(\lambda, R) = \frac{\alpha_{aer}(\lambda, R)}{\beta_{aer}(\lambda, R)} \tag{3.3}$$

$$LR_{mol}(\lambda, R) = \frac{\alpha_{mol}(\lambda, R)}{\beta_{mol}(\lambda, R)} = \frac{8\pi}{3} sr \tag{3.4}$$

It is worth mentioning that Equations 3.3 and 3.4 are governed by Mie and Rayleigh scattering theories (Subsection 2.3.3.1), respectively. Both optical coefficients are unknown values, making the elastic-lidar equation more complex to

solve. Nevertheless, it is possible to invert an elastic-lidar signal to find the coefficients by applying one or more *a priori* assumptions on the retrieval technique.

3.2.1 Elastic Inversion

The main inversion methods for obtaining α(λ, R) with the elastic technique are the slope method, the optical depth solution, and the Klett-Fernald-Sasano (KFS) inversion. These methods are used to calibrate lidar systems.

The slope method. The first method determines the mean extinction coefficient over an extended measurement range in a homogeneous atmosphere [156]. In general, the slope methods estimate the extinction at some point at a distance R along the lidar line by assuming the extinction is constant in an interval surrounding the point [204]. The elastic-lidar equation (Equation 2.34) can be rewritten as a function of the Range Corrected Signal (RCS), the lidar system constant (C), and the atmosphere transmission from a lidar system (Equation 2.36):

$$P(\lambda, R) = \frac{C}{R^2}\beta(\lambda, R)T_L^2(\lambda, R) \tag{3.5}$$

and

$$RCS(\lambda, R) = R^2P(\lambda, R) = C\beta(\lambda, R)T_L^2(\lambda, R) \tag{3.6}$$

where P(λ, R) is the optical return power corrected from the sky-background signal (Equation 2.34), and R is the range in m. Ref. [205] analyzed the RCS by applying a logarithmic range-adjusted power, which is a more convenient signal variable, and assuming the dependency of the lidar wavelength (ξ)[27] is equal to 1. Therefore, Equation 3.6 can be rearranged as follows:

$$\frac{d\ln[RCS(R)]}{dR} = \frac{1}{\beta(\lambda, R)}\frac{d\beta(\lambda, R)}{dR} - 2\alpha(\lambda, R) \tag{3.7}$$

In a homogenous atmosphere, β(λ, R) and α(λ, R) are assumed constants: $\beta_{ct}(\lambda)$ and $\alpha_{ct}(\lambda)$:

[27] Ref. [205] related the approximate backscatter and extinction coefficients by a power law: $\beta(\lambda, R) = \mathbb{c}\alpha^{\xi}(\lambda, R)$, in which $\mathbb{c}$ is a constant and ξ depends on the lidar wavelength and aerosol properties. Generally, ξ values are from 0.67 to 1. Therefore, a homogenous atmosphere $\mathbb{c}$ =1 and ξ = 1.

$$\alpha_{ct}(\lambda) = -\frac{1}{2}\frac{d\ln[RCS(R)]}{dR} \tag{3.8}$$

However, this inversion technique is not recommended to be applied to determine α(λ, R) at a local point in the atmospheric column because a small range increment is extremely sensitive to signal noise and to the presence of local heterogeneity, causing large errors in the $\alpha_{ct}(\lambda)$ [156].

The optical depth solution. The optical depth inversion requires a known or assumed total optical depth or transmittance over the lidar measurement range [156], which can be used in both homogeneous and inhomogeneous atmospheres. In this inversion, the LR is assumed to be range independent and the optical depth or transmittance (Equations 2.17-2.21) may be obtained from a Sun photometer for a clear or moderately turbid atmosphere [206]. Thus, the $\alpha_{ct}(\lambda)$ is estimated by:

$$\alpha_{ct}(\lambda) = \frac{0.5RCS(\lambda, R)}{\frac{I_{R,max}}{1 - T_{max}^2} - I_R(R_0, R)} \tag{3.9}$$

where $I_{(R,\,max)}(R_0, R_{max})$ is the integral of the RCS in the maximum range from R_0 to R_{max} and T_{max}^2 is the two-way total transmittance of the lidar maximum range that should be estimated, as mentioned previously, and it takes values between 0 and 1. This inversion is more useful (i) to determine extinction coefficient profiles in a thin atmospheric layer, (ii) when the atmospheric transmission can be obtained from an independent measurement, (iii) when the targets are available in the lidar path, and (iv) when the measurements are made in turbid atmospheres [156].

KFS inversion. The first version of the KFS [205–209] algorithm, the single-component algorithm, needed a hypothesis on the total (aerosols + molecules) lidar ratio. As this ratio has no physical meaning, the single-component algorithm is not used in practice [210].

The most common application of the KFS inversion is obtaining the extinction and backscattering coefficients in an inhomogeneous atmosphere from aerosol and molecule contributions separately by guessing the relation between both coefficients. It is called two-component inversion. *A priori* assumptions for this

algorithm are: a first guess of LR_{aer} considered independent of the range (LR(λ)) [206,207] and the profile reaches an aerosol-free region [206,207]. Bearing in mind Equations 3.3, 3.4, and 2.37, the extinction can be estimated as a function of the aerosol and molecule backscatters:

$$\alpha(\lambda, R) = LR_{aer}(\lambda, R)\beta_{aer}(\lambda, R) + \frac{8\pi}{3}\beta_{mol}(\lambda, R) \tag{3.10}$$

Considering (i) Klett's approach (Equation 3.7) and (ii) the dependencies of the propagation range and wavelength are omitted; a Bernoulli differential is found:

$$\frac{d\beta(R)}{dR} - \beta(R)\frac{d\ln[RCS(R)]}{dR} = 2LR_{aer}(R)\beta^2(R) \tag{3.11}$$

The solution of Equation 3.11 is achieved if β(R) is assumed known at a reference range (R_0), leading to a forward solution ($R^{28} > R_0$) for spaceborne lidars (not applied here) and a backward solution ($R < R_0$) for ground-based lidars:

$$\beta_{aer}(R) = \frac{\beta(R_0)RCS(R)}{RCS(R_0) + 2\beta(R_0)\int_{R_0}^{R} LR_{aer}(R)RCS(R)} - \beta_{mol}(R) \tag{3.12}$$

For this solution, $LR_{aer}(R)$ is assumed, and it is necessary to consider an aerosol-free range for β_{mol} estimation. Ref. [209] presented an optional formulation for those from Refs. [205,208] by introducing the normalized total extinction coefficient y(R) defined as below:

$$y(R) = \alpha_{aer}(R) + \frac{LR_{aer}(R)}{LR_{mol}(R)}\alpha_{mol}(R) \tag{3.13}$$

Additionally, the KFS inversion can be constrained by the AOD [206] from an independent instrument. As a result, lidar systems are collocated near photometers, e.g., the MPLs and AERONET Sun photometers [141]. This inversion method is based on guesses about the LR (an assumed constant $LR_{aer}(R) = LR_{aer}$), which is adjusted until the integral of the aerosol extinction of the n-iteration equals the AOD from a Sun photometer within acceptable limits. With these inversion techniques, it

[28] In this case, the attenuation occurs from the TOA or R until R_0. However, in the backward solution, the attenuation occurs from R to R_0.

is possible to retrieve the aerosol backscatter coefficient, aerosol microphysics, cloud properties, and the structure of the atmosphere.

3.2.2 Elastic-Raman Inversion

An important inversion method that uses two lidar techniques is the Elastic-Raman method. Raman lidar can provide the vertical profile of the aerosol backscatter coefficient without assuming a LR [82], which can be used to achieve a more accurate inverted LR [156]. The combination of two techniques was successfully applied by Refs. [211–214], among others. The Raman lidar (Subsection 2.4.1) has an additional signal from atmospheric gases in addition to the conventional elastic signal; hence, the scattering from atmospheric nitrogen, e.g., is used to determine attenuation coefficients [156]. According to Ref. [215], the molecular backscatter coefficient (β_{Ra}) is linked to the differential (Raman or Rayleigh) backscatter cross-section ($d\sigma/d\Omega$) of a molecule number density of the reference gas (N_{Ra}) at the lidar wavelength (λ) and the scattering angle Θ by the relation:

$$\beta_{Ra}(R,\lambda) = N_{Ra}(R)\frac{d\sigma(\Theta,\lambda)}{d\Omega} \tag{3.14}$$

According to Ref. [152], $\beta_{Ra}(\lambda)$ is identical with β_{mol} (Equation 2.35) if the Raman lidar equation describes a Rayleigh signal. Additionally, $N_{Ra}(R)$ is calculated from radiosonde observations or standard-atmosphere temperature and pressure profiles. The assumed scattered wavelength dependency (λ^{-ex}) of the aerosol extinction is:

$$\frac{\alpha_{aer}(\lambda,R)}{\alpha_{aer}(\lambda_{Ra},R)} = \left(\frac{\lambda}{\lambda_{Ra}}\right)^{-ex} \tag{3.15}$$

and

$$\alpha_{aer}(\lambda,R) = \frac{\frac{d}{dR}\left[\ln\frac{N_{Ra}(R)}{R^2 P_{\lambda_{Ra}}(R)}\right] - \alpha_{mol}(\lambda,R) - \alpha_{mol}(\lambda_{Ra},R)}{1+\left(\frac{\lambda}{\lambda_{Ra}}\right)^{-ex}} \tag{3.16}$$[29]

[29] Equation 3.16 was obtained by replacing Equations 3.14 and 3.15 in the Raman lidar equation. For more information about this lidar equation, see Refs. [211,215].

where the Raman wavelength of the reference gas is λ_{Ra} (Equation 2.39).

Despite the Raman-method overall limitation to nighttime measurements due to the weakness of Raman backscatter signals, which explains the reason why the cross-section for this process is smaller than the Rayleigh scattering cross-section by 3 orders of magnitude [204], both methods together (elastic and Raman) can efficiently retrieve the aerosol backscatter and aerosol extinction coefficients, the aerosol-microphysics properties, and the structure of the atmosphere.

3.2.3 Optical Depolarization Products

The depolarization ratio of backscattered laser light (Equation 2.38) is used to characterize the degree of nonsphericity of aerosol particles [131], and it has been used to distinguish water drops [216] and clouds [217]. The linear depolarization ratio $\delta(\lambda, R)$ is also called volume depolarization ratio ($\delta^v(\lambda, R)$), because $\delta^v \equiv \delta$, differentiating from the particle depolarization ratio ($\delta^p(\lambda, R)$), as in the following equations:

$$\delta^v(\lambda, R) = \frac{\beta_{\perp}^{aer} + \beta_{\perp}^{mol}(\lambda, R)}{\beta_{\parallel}^{aer} + \beta_{\parallel}^{mol}(\lambda, R)} \tag{3.17}$$

and

$$\delta^p(\lambda, R) = \frac{\beta_{\perp}^{aer}(\lambda, R)}{\beta_{\parallel}^{aer}(\lambda, R)} \tag{3.18}$$

The $\delta^p(\lambda, R)$ and LR measurements are useful for classifying aerosol [144], as in Figure 3.4, e.g., values ranging from 10 to 30% are typical for desert dust [67]. The overlaps of the aerosol types are attributed to the mixing state of the particles, requiring additional information (AE, geographical location, and others) to refine the classification. For instance, pollution and smoke overlap for LR between 40 and 70 sr and $\delta^p < 7\%$.

Some highlighted techniques were also developed to retrieve optical properties with depolarization channels. For instance, Refs. [218,219] used the particle depolarization ratio and the backscattering coefficient at 532 nm to estimate the contribution of dust to the total extinction coefficient. Both studies assumed a

heavy dust depolarization ratio of 0.35 in the extinction coefficient equation. While [218] determined an empirically free-dust depolarization ratio of 0.05, [219] determined a value of 0.02 for the same parameter. Their research obtained the dust backscattering coefficient as a function of height. Ref. [220] developed a simple two-component theory considering two types of aerosols (dust and spherical aerosols) and using the particle depolarization ratio and the backscatter coefficient at 532 and 1064 nm. This method derived the mixing ratio of dust and the backscatter-related Ångström exponents for dust and spherical aerosol by assuming dust depolarization ratios equal to 0.35 at both wavelengths.

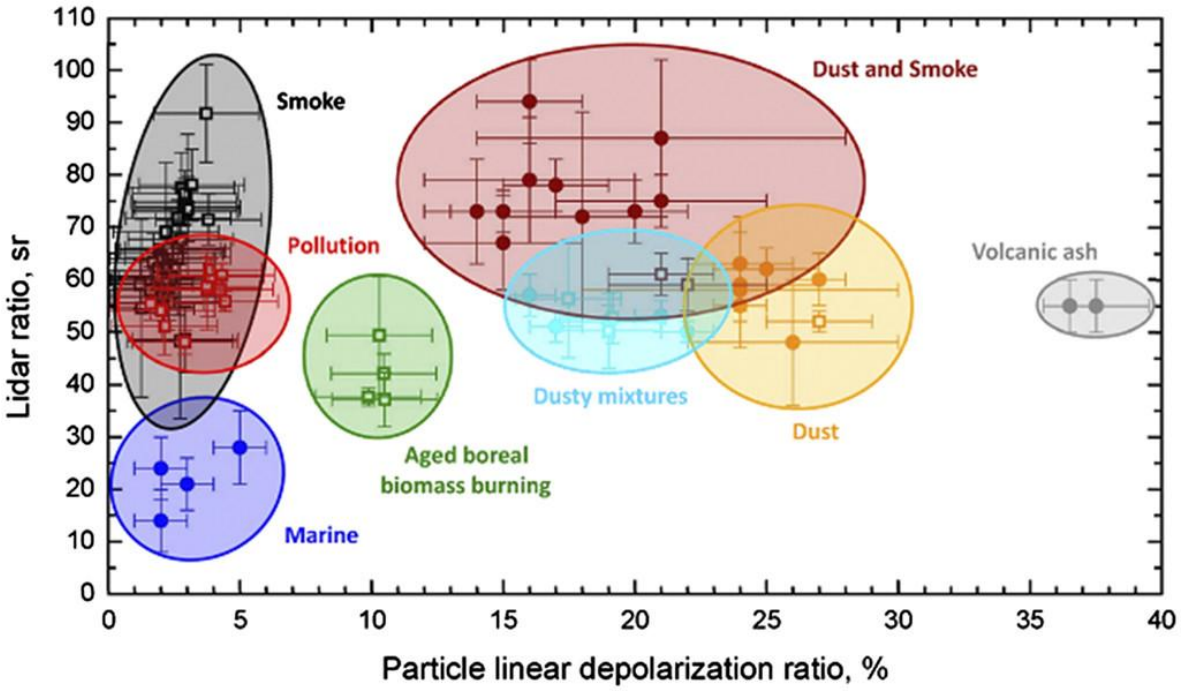

Figure 3.4. Aerosol classification based on the LR as a function of the δp at 355 nm. This figure is available in Ref. [144].

Ref. [221] demonstrated that a three-component atmosphere approach was able to solve the lidar equation by using a volume depolarization ratio calculated with three atmospheric components: Rayleigh scattering (molecular contribution), volcanic ash (depolarizing), and boundary-layer aerosols (assumed non-depolarizing), where the two aerosol types are assumed externally mixed. This solution combined backscatter and depolarization measurements to quantitatively distinguish two different aerosol types with different depolarization properties [221]

at 355 nm. They assumed lidar ratios and aerosol depolarization ratios for volcanic ash (82 sr and 0.34, respectively) and non-depolarizing aerosols (35 sr and 0, respectively), and they also assumed molecular coefficients (backscatter and extinction) to calculate the molecular depolarization ratio. They could estimate backscatter and extinction coefficients, AOD, and mass concentration.

Lastly, Ref. [222] presented a technique for estimating optical backscatter and extinction profiles by exploiting the difference between the δ^p at 355 nm and the corresponding expected aerosol-only depolarization ratio. However, this inversion procedure is applied when a single strongly depolarizing species (volcanic ash) is mixed with nondepolarizing aerosol, and the depolarizing particle is associated with the linear particulate depolarization ratio, which is assumed to be known.

3.2.4 Lidar Microphysical Inversions

In the last three decades, several algorithms have been developed using different lidar techniques (Raman and elastic, for example) to improve the retrievals of the aerosol microphysical properties. This subsection presents a class of methods to retrieve microphysical parameters that uses a rigorous mathematical approach based on multiwavelength lidar observations [152]. These methods need the spectral information contained in the backscatter and extinction information (from elastic and Raman lidars, respectively) at multiple wavelengths and their change with particle size [152]. Here, a few well-known algorithms are presented. To summarize the inversion methods, β stands for elastic channels, and α stands for Raman channels.

The ill-posed inverse problem [223] is a numerical solution process for a problem that does not satisfy any of the following conditions: (i) there is a solution for problems with (ii) a unique solution, and (iii) the solution is non-continuous, dependent on the input data. The regularization method with constraints [224] is one technique to deal with this kind of inverse problem. The regularization is also the standard method for microphysical-parameter retrievals of tropospheric particles

from multiwavelength lidar observations [152] by the solution of the following equation:

$$g_i(\lambda_z) = \int_{r_{min}}^{r_{max}} \mathrm{K}_i(r, N, \lambda_z, s)\, v(r)\, dr + \epsilon^{exp}(\lambda_z) \tag{3.19}$$

where i = α_{aer}, β_{aer}, z = 1 to nth-wavelength, $g_i(\lambda_z)$ is the optical data in a specific R, $\mathrm{K}_i(r, N, \lambda_z, s)$ is the kernel efficiencies, r is the radius of the particles[30], N is the complex refractive index, s is the shape of the particles, υ(r) volume concentration of particles per radius interval dr, and ϵ^{exp} is the data error.

Regarding inversion algorithms, Ref. [225] retrieved physical parameters of tropospheric particle size distributions (effective radius, volume, surface area, and number concentrations), as well as the mean complex refractive index by applying to lidar data (novelty) the regularization method performed by generalized cross-validation [226,227]. Refs. [53,228] also utilized the regularization method in their code. This method did not require knowledge of the shape of the particle size distribution and could handle measurement errors of the order of 20%. They retrieved aerosol properties at six elastic channels (355, 400, 532, 710, 800, and 1064 nm) and two Raman channels (387 and 607 nm), 6β + 2α, for simulations with monomodal and bimodal logarithmic-normal size distributions. In the same year, Ref. [229] performed a sensitivity study to investigate the stability properties of the algorithm for the sought parameters. Then, Ref. [230] presented the inversion results of the scanning six-wavelength aerosol lidar and cross-checked the performance characteristics of the algorithm concerning experimental data by comparison with results from a Sun photometer.

Ref. [53] retrieved particle volume distribution, mean refractive index, effective radius, volume, surface-area, and number concentration of tropospheric and stratospheric aerosols from optical data of multi-wavelength setups with six backscatter channels (355, 400, 532, 710, 800, and 1064 nm) and two extinction channels (355 and 532 nm), 6β + 2α, allowing also one extinction and three

[30] r_{min} is the radius down to which particles are optically efficient and r_{max} is the radius at which concentrations are so low that particles no longer contribute significantly to the signal [152]. In the troposphere, r_{max} < 10 μm.

backscatter coefficients setup (3β + α). Their hybrid regularization method combined regularization by discretization, variable higher-order B-spline functions, and a truncated singular-value decomposition, and it requires neither *a priori* knowledge of the analytical shape of the distribution nor an initial guess of the distribution. Furthermore, bimodal and multimodal distributions can be retrieved without advanced knowledge of the number of modes. Ref. [54] presented the continuation of the investigation of the so-called IMP (Institute of Mathematics of Potsdam University) method for two cases (6β + 2α and 3β + 2α), and they also retrieved SSA.

Ref. [228] presented an inversion algorithm for retrieving particle size distribution parameters (mean or effective radius, number, surface area, and volume concentration) and complex refractive index. Their code performs the averaging of solutions in the vicinity of the global minimum instead of the solution proposed by Tikhonov's method [231]. This averaging stabilized the underlying ill-posed inverse problem in their algorithm, but constraints were needed for retrieving particle size distributions. They combined three backscatter coefficients at 355, 532, and 1064 nm from elastic signals and two extinction coefficients at 355 and 532 nm from Raman signals, i.e., 3β + 2α inversion algorithm. Ref. [232] extended their previous code to be applied to a bimodal particle size distribution to retrieve properties from large particles.

Ref. [233] derived vertical profiles of aerosol physical parameters in the planetary boundary layer by performing their 3β + 2α inversion algorithm under varying relative humidity conditions. Furthermore, they demonstrated the potential of the multi-wavelength technique to study aerosol hygroscopic growth. Lastly, Ref. [234] incorporated the same concept of a spheroidal model [67] from AERONET into the lidar retrieval of aerosol physical properties. This model is a mixture of spherical and nonspherical components (an ensemble of randomly oriented spheroids with a size-independent shape distribution). Other applications with 3β + 2α inversion were performed by Refs. [235,236].

3.3 AERONET INVERSIONS

The AERONET [183] became an important worldwide network in which its inversion codes provide aerosol optical properties in the total atmospheric column derived from the direct and diffuse radiation [237] measured by Cimel Electronique Sun-sky photometers. Ref. [45][31] developed their first inversion code for retrieving an extended set of aerosol parameters from multangular and multispectral measurements of the atmospheric radiances. Their method was based on previous inversions as Refs. [238,239,242], which considered the aerosol particles as homogeneous spheres with assumed refractive indices. The first method inverts spectral measurements of optical thickness only; meanwhile, the second inverts the angular distribution of sky radiance in the presence or absence of optical thickness.

Ref. [45] also assumed homogeneous Mie-scattering spheres as the aerosol microstructure in the code. The algorithm retrieves the particle size distribution over a wide range of sizes (0.05-15 μm) with spectrally dependent N and SSA [45]. This code became the so-called Version 1. After the development of the described method, Ref. [46] tested it by perturbations in the inversion resulting from random errors, instrumental offsets (Sun or sky miscalibration, inaccurate azimuth angle pointing during sky radiance measurements, and inaccuracy in accounting for surface reflectance), and known uncertainties in the atmosphere radiation model. They found acceptable retrieval accuracy for most applications: polydisperse homogeneous spheres and externally and internally mixed spherical particles with different refractive indices.

Other implementations in the AERONET inversions were applied by Refs. [67,130,243]. Ref. [243] employed a method for the retrieval of the optical properties of non-spherical aerosol based on the model of a shape mixture of randomly oriented polydisperse spheroids, improving derived properties (phase functions, size distributions, and refractive indices) from dust observations. In this method, they

[31] Before this inversion method, AERONET employed other inversions as Refs. [238,239] to derive volume size distribution, Ref. [240] to derive the SSA, and Ref. [241] to derive the real part of the refractive index.

used the Kernel look-up tables for implementing quick and accurate simulations of spheroid phase functions. In the same year, Ref. [130] discussed the SSA as a parameter characterizing absorption. They also verified and enriched the aerosol properties derived from ground-based remote sensing by intercomparisons with available *in situ* aerosol information, hence creating a climatology of the microphysical-optical properties of key aerosol types[32]. Then, further developments were applied to modeling the entire scattering matrix of spheroids [67], which included retrieving the degree of aerosol nonsphericity and the multiterm Least Squares Method (LSM). They also used developed look-up tables in the validation of the spheroid model and considered a generalized aerosol model for representing spherical, nonspherical, and mixed aerosols in the atmospheric aerosol retrievals.

The application of those inversion codes for the almucantar retrievals and their quality controls originated the Version 2 [244], which remains valid in Version 3 (V3) [49,245] and kept the cloud screening of the direct-Sun AOD measurements [179]. In this version, the Bidirectional Reflectance Distribution Function (BRDF) models were utilized instead of an isotropic and invariant geographical reflectance [49]. More inversion methods were developed for AERONET retrievals; e.g., Ref. [246], who modified the algorithm developed by Ref. [45] to retrieve surface reflectance in addition to aerosol parameters with minimal assumptions by combining satellite observations with collocated ground-based measurements. The new properties are the bidirectional reflectance factor and surface albedo in addition to SD, N, and SSA.

The AERONET inversion also applies the Spectral Deconvolution Algorithm (SDA), developed by Refs. [48,247], to separate fine and coarse mode contributions to atmospheric AOD at a reference wavelength, typically taken at 500 nm [248]. The SDA methodology uses only AOD spectra to calculate fine and coarse parameters. Finally, Ref. [49] replaced the scalar discrete ordinate Radiative Transfer Code (RTC) of Ref. [249] by a polarized RTC Successive ORDers of scattering (SORD) [250,251] in the AERONET aerosol retrieval algorithm [49], allowing more accurate

[32] Other aerosol characteristics, such as absorption AOD, AF, lidar, and depolarization ratios, are calculated from the retrieved aerosol parameters [49].

simulations of atmospheric radiation in a wide spectral range (which includes the 380-nm channel) without truncation approximation. Additionally, new BRDF parameters for land sites, a new version of the extraterrestrial solar flux spectrum, and new temperature correction procedures of both AOD and sky measurements were implemented.

3.4 SYNERGIC LIDAR-PHOTOMETER INVERSION

Since the 2000s, efforts to improve the retrieval of the microphysical and optical properties of aerosols using combinations of remote sensing instruments have become more popular in the scientific community, which has led to the development of several algorithms to enhance the inversions of aerosol properties by combining synergistically photometer and lidar data [134]. Bear in mind that lidar and photometer observations are complementary, owing to the photometer's sensitivity to the optical-microphysical-radiative properties of the columnar aerosol and the lidar's sensitivity to the vertical distribution of the optical properties, but the microphysical information is limited.

This section explores and summarizes the main synergy codes developed to retrieve aerosol properties by combinations between both observations. First, LIRIC [252], POLIPHON [60,61], and other inversion synergy algorithms are presented; then the GRASP/GARRLiC Algorithm [51,63,64,253] is more detailed due to its relevance to the current research.

3.4.1 Overview of the Existing Lidar-Photometer Inversion Algorithms

LIRIC. One of the first ideas of synergy between a lidar system and a radiometer was proposed by Ref. [254], who presented the methodology to process data of combined experiments using a Sun-sky photometer and a multi-wavelength lidar system. This method retrieved vertical distributions of aerosol microstructure characteristics in an inhomogeneous aerosol layer. The method was enriched by Refs. [56,252,255]. In the frame of EARLINET projects, the algorithm was disseminated and named LIdar-Radiometer Inversion Code (LIRIC) for processing data of EARLINET measurements [252]. LIRIC processes the co-located data by a

two-step sequential inversion where the photometer data is derived according to the standard AERONET inversions (Subsection 3.3) and the results are used as *a priori* constraints on aerosol properties for lidar data processing [256].

The basic physics and math of LIRIC are described by Ref. [256] and consist of (i) parameterization of the target, i.e., development of the aerosol layer model; (ii) derivation of the equations that relate observed signals with specified parameters of the aerosol model (forward modeling); and (iii) inverse modeling or retrieval of the target parameters of the aerosol model that minimize discrepancies between the measured and the calculated input signals [256]. Via this method, it is possible to distinguish between fine and coarse spherical fractions or between spherical and non-spherical coarse particles. Additionally, Ref. [257] presented the first LIRIC retrievals, applied on combined lidar and Sun photometer data during a Saharan dust episode over Athens in Greece.

POLIPHON. The POLarization LIdar PHOtometer Networking (POLIPHON) method was first presented by Ref. [60] and it was consolidated by Ref. [61]. The first study presented a combined lidar-photometer method that retrieves the vertical profile of the fine and coarse modes of particle mass concentrations for ash and non-ash particles. Then, they extended this technique to dust observations in Ref. [61]. The instruments, retrieval methods, and uncertainties are also discussed by Refs. [258,259]. This technique uses the depolarization ratio at a single wavelength (532 nm) to identify layers with nonspherical particles and quantify their contribution to the profile of the particle backscatter coefficient, and it uses the coarse-mode optical thickness from the Sun photometer to convert the extinction coefficients into fine-mode particles and coarse-mode (dust and ash, nonspherical particles) mass concentrations.

The POLIPHON method is also described by Ref. [260] and some changes were applied to estimate the desert-dust ice nuclei profiles [261]; to profile ice and cloud nuclei profiles for other types of aerosols [262]; to extend the methodology for fine and coarse dust separation at 355 and 1064 nm, including Raman signals [263];

and to update the conversion factors for deriving number, surface area, volume, and ice and cloud nuclei parameters of the dust and smoke [264,265].

Other lidar-photometer inversions. Ref. [59] developed the Lidar and Almucantar (LidAlm) algorithm that combines information provided by standard elastic-backscatter lidar (backscatter coefficient profile at one or two wavelengths) and Sun photometer AERONET inversion of almucantar (column integrated aerosol size distribution and refractive index) to characterize the atmospheric column by its different aerosol layers. The following year, Ref. [62] demonstrated a method to derive the concentration of aerosol components from the spectral measurements of AOD, SSA, SD, and extinction profile available from AERONET and MPLNET stations. This technique finds the best combination of aerosol concentration by minimizing differences between measured and calculated values of the mentioned aerosol parameters.

Ref. [266] extended the retrieval approach based on the lidar-only retrieval scheme [200] by an improved model for aerosol ensembles and consideration of photometer measurements. Ref. [266] added AOD and almucantar retrievals to derive aerosol properties (mass-extinction conversion factor, aerosol mass concentration, and SSA) for two aerosol models (spheroid model and an advanced model that considers irregular particle shapes). Both approaches use the Monte-Carlo method for sampling the microphysical parameters of aerosol ensembles to find the solutions of the retrieval by comparing modeled results with measurement data.

Finally, Ref. [55] presented a project combining lidar, photometer, and particle counter data with a regularization software tool for a closure study of aerosol microphysical property retrieval. The microphysical properties of the aerosol were derived from optical data with a particularly developed software package via regularization [53,54]. In their inversion, the lidar data are used to retrieve the particle size distribution; then, the photometer data are added for a good consistency of the retrieved particle size distributions, which may be compared with the measured particle size distributions from a particle counter.

3.4.2 GRASP/GARRLiC Algorithm

GRASP algorithm. The GRASP code was introduced by Ref. [253] and is the first unified algorithm and a software package developed for retrieving atmospheric properties from a wide variety of remote sensing observations, including satellite, ground-based, and airborne passive and active measurements of atmospheric radiation and their combinations [267]. This powerful code has heritage on the AERONET retrieval advances [45,46,67,130,243], but its first concept was proposed by Ref. [64] to develop an algorithm to enhance aerosol retrieval by a statistically optimized multi-variable fitting of all available angular observations obtained by the POLarization and Directionality of the Earth's Reflectances (POLDER) sensor on board the Polarization and Anisotropy of Reflectances for Atmospheric Sciences coupled with Observations from a Lidar (PARASOL).

The GRASP software package has a component called the scientific GRASP core, which implements the inversion of remote sensing observations following the retrieval procedure assumed by the scientific core [267]. The scientific GRASP core is complemented by the control unit to optimize the processing of large volumes of data, e.g., satellite observations. The control unit manages the preparations of observations, the implementation of actual retrievals by scientific code, and the output of results [267]. The control unit requires setting files in YAML (YAML Ain't Markup Language) format due to its flexibility, easy-to-write and clear-to-read files, and self-explanatory names.

The code is composed of two main modules called Numerical Inversion and Forward Model (they are described further by focusing on the modification implemented by Ref. [51]. The first drives the retrievals (scientific GRASP core), and the second implements simulations of the inverted observations. The Numerical Inversion can retrieve properties by single-pixel and multi-pixel approaches, the first two *a priori* constraints of the inversions. The single-pixel retrieval is a conventional approach when the remote sensing observations over each single pixel are inverted completely independently, whereas the multiple-pixel retrieval, in which the observations of the satellite instrument over a group of pixels are inverted

simultaneously and extra *a priori* constraints on the inter-pixel variability of the retrieved parameters is applied [64]. The second approach improves retrieval consistency by using known limitations on the spatial and/or temporal variability of retrieved parameters [268].

The Forward Model carries out simulations of the inverted remote sensing observations to find iteratively the best inversion solution for the retrievals, or it also creates synthetic data. According to Ref. [268], it consists of several distinct modules: Multiple Scattering, Aerosol single scattering columnar/volume properties, Aerosol vertical profile, Surface reflectance, and Gas absorption calculations. These blocks are semi-independent in the sense that each block can be changed or entirely replaced with no or minimal effect on the other parts of the "forward model" routine [268].

The algorithm inputs are separated into two types of files. One of them is the setting files in YAML format. It is organized into three blocks: input, output, and retrieval. The largest block is the retrieval one, which requires an extensive setup:

- 'General' requires the path to internal data files;
- 'Mode': 'inversion' or 'forward' options define how the code is run. In the case of forward, the code can create synthetic data;
- 'Regime' specifies the single- or multi-pixel approaches;
- 'Convergence' defines the iterations of the modules, such as thresholds for stopping, maximum number of iterations, among others;
- 'Measurement fitting' defines the inversion regimes as the degree of polarization or the scattering angle for normalized P11[33];
- 'Noises' defines the standard deviation synthetic (weight of the synthetic random noise added to the corresponding inverted data[34]), the error type (defines the covariance matrices [268] used in measurement fitting and in

[33] The element of the phase matrix.

[34] If its value is 0, no synthetic random noise is added. This methodology is used for inversion mode.

modeling synthetic noise), the standard deviation[35] (weight of the expected random noise, which also defines the covariance matrix used in fitting), the measurement type (kind of measurements from the observations in Table 4.6 in Ref. [267] for applying the noise assumptions), and the indexes of involved wavelengths;

- 'Forward model' determines the scale of the binning of the SD, the phase matrix configurations, the minimum and maximum radius by modes in the bins, and the configuration of the radiative transfer;
- 'Products' sets the indices of Ångström's wavelengths, retrieved aerosol products, retrieved aerosol errors, forcing products, residuals, fittings, surface products, and others;
- 'Constraints' defines the characteristics by 'type' (Table 4.2 in Ref. [267]) and by 'mode', specifies if the characteristic will be retrieved or only used in forward model by 'retrieved', requires values, minimum, maximum and indexes of involved wavelengths for the initial guesses, and sets the smoothness constraints for single- and multi-pixel approaches (difference order and Lagrange multiplier[36]).

The other input is the SData (Sensor Data) file, which is read by a generic SData driver. The SData format was designed by the GRASP science team to allow a simple and flexible code. The SData contains the preprocessed measurements (Subsection 4.2.1) and is structured by the file header, segment header, an empty line, and a cell (group of neighboring pixels) of the segment. Additionally, GRASP software is an open-source code written in Fortran and C languages, and it is organized in folders, such as *build*, *doc*, *examples*, *libs*, and *src*. More details are found in Ref. [267].

[35] Noise in the data has a Gaussian distribution [268]; hence, the standard deviations are Gaussian distributed.

[36] The difference order is the order of the derivatives/differences used for applying *a priori* smoothness constraints for the retrieved characteristics and the Lagrange multiplier is the value of the Lagrange multiplier used for applying *a priori* smoothness constraints for the retrieved characteristics [267].

Currently, the approached algorithm is capable of retrieving a wide variety of properties, such as the optical-microphysical-radiative parameters of atmospheric aerosols and surface properties (nearly 50 parameters). Table 3.1 details some direct products[37] (GRASP outputs) and those calculated from the direct products, called here derived products. Both products are retrieved for fine and coarse modes.

It is worth mentioning that the aerosol components are modeled as a mixture of randomly oriented spheres and spheroids with retrievable SF [63,67,130,243]; the set of aerosol microphysical properties allows retrieving the N of both aerosol modes without assumptions; and a retrievable lidar calibration coefficient[38] was introduced in case of the reference altitude of the backscattered light is not provided by only molecular scattering.

Figure 3.5 shows the structure of the algorithm and the iteration between the two independent modules. The Numerical Inversion inverts a set of measurements (f*) by a statistically optimized fitting called Multi-Term LSM [64,268,269] to deduce the inputs of the Forward Model (a^p). Then, new simulated observations ($f(a^p)$) are obtained in the Forward Model to be inverted in the Numerical Inversion again until a "best" convergence is achieved in the p-th[39] iteration ($a^{p\text{-final}}$), i.e., there is an iteration procedure[40]. This method considers the errors in the observations, the inversion of multi-source data with different levels of accuracy, and *a priori* and ancillary information [63].

The a^p contains the microphysical properties (SD, N, SF, and Aerosol Vertical Profile, AVP, for fine and coarse modes) plus the lidar calibration coefficient, and through the inversion, it could be retrieved from f* [63]. Therefore, the Multi-Term LSM solves the system of equations below:

[37] Direct and derived are used here as nomenclatures for GRASP outputs.

[38] This parameter is defined for the number of lidar wavelengths [63].

[39] The initial guess in the setting file is used as the first array of characteristics to be retrieved when p = 0, i.e., the iterative procedure starts from $a^{p=0}$ until it obtains a result array at p-final.

[40] This convergence can be assessed by the residual. According to Ref. [64], the residual is a useful tool for diagnostics of the retrieval dynamics, where the final residual value should be close to the level of the expected measurement noise. However, at early iterations, the residual has a value much higher than the level of the expected measurement noise due to the linearization errors. Thus, the weight of the *a priori* term should be increased, improving the convergence of nonlinear fitting. The right solution of the Multi-Term LSM should be very small, achieved after the n-th iteration.

$$\begin{cases} f^* = f(a) + \Delta f^* \\ 0^* = (\Delta a)^* = Ma + \Delta(\Delta a) \\ a^* = a + \Delta a^* \end{cases} \tag{3.20}$$

where the first equation is the observation fitting and f* stands for the vector of the independent measurements with different accuracy levels, i.e., different covariance matrices (weight matrix)[41]. In this case, f* has five components[42]: radiances, optical thickness, and three lidar observations. Generally, the variances in the measurement errors are 3% for radiances, 0.005 in absolute level for optical thickness [45], 20% for 355 nm, 15% for 532 nm, and 10% for 1064 nm (lidar channels) [51].

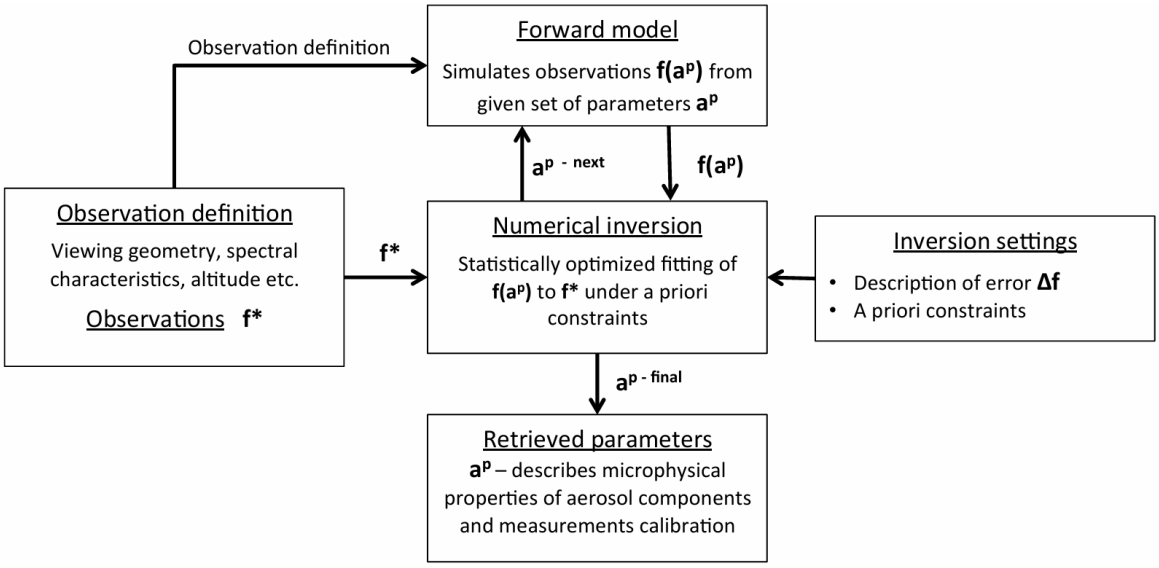

Figure 3.5. The general structure of the inversion algorithm developed by Ref. [64] and applied by Ref. [51] in the GARRLiC code. f* is the vector of the measurements of physical characteristics, a^p is the vector of unknowns at the p-th iteration, $f(a^p)$ is the vector of fitted simulated measurements at the p-th iteration, and Δf is the vector of measurement errors. This figure is available in Ref. [51].

[41] More details about the covariance matrix can be found in Refs. [46,64,268].
[42] Nowadays, it is possible to put more measurements in f*. See Table 4.6 in Ref. [267].

Table 3.1. Main direct and derived products from the GRASP algorithm. This table was adapted from Refs. [134,270].

	Products			
	Name	**Acronyms**	**Equation**	
Direct *	Vertical distribution of the aerosol concentration or Aerosol Vertical Profile	AVP(R)	These parameters are direct outputs from the GRASP code. So, their equations are not listed (except for NAF and AFE).	
	Size Distribution	SD		
	Spectral Real Refractive Index	RRI(λ)		
	Spectral Imaginary Refractive Index	IRI(λ)		
	Spectral Ångström Exponent	AE(λ)		
	Spectral Aerosol Optical Depth	AOD(λ)		
	Spectral Single Scattering Albedo	SSA(λ)		
	Spectral Absorption AOD	AAOD(λ)		
	Spectral Lidar Ratio	LR(λ)		
	Sphere Fraction	SF		
	Effective radius	r_{eff}		
	Volume mean radius	r_v		
	Aerosol Volume Concentration	AVC		
	Fittings, relative errors, and bias of all properties			
	Upward Broadband Flux without Aerosol**	$UBFA_0(R)$		
	Downward Broadband Flux without Aerosol	$DBFA_0(R)$		
	Upward Broadband Flux with Aerosol	UBFA(R)		
	Downward Broadband Flux with Aerosol	DBFA(R)		
	Net Aerosol Forcing	NAF(R)	$(DBFA(R) - UBFA(R)) - (DBFA_0(R) - UBFA_0(R))$	(3.21)
	Aerosol Forcing Efficiency	AFE(R)	$\mathrm{NAF(R)}/AOD(550\,nm)$	(3.22)
Derived	Volume Concentration Profile	VC(R)	$AVC_1 \cdot AVP_1(R) + AVC_2 \cdot AVP_2(R)$	(3.23)
	Extinction profile	α(λ, R)	$AOD_1(\lambda) \cdot AVP_1(R) + AOD_2(\lambda) \cdot AVP_2(R)$	(3.24)
	Backscatter profile	β(λ, R)	$AOD_1(\lambda) \cdot AVP_1(R)/LR_1(\lambda) + AOD_2(\lambda) \cdot AVP_2(R)/LR_2(\lambda)$	(3.25)
	Ångström Exponent Profile	AEP(λ, R)	$-\log(\beta(\lambda_1,R)/\beta(\lambda_2,R))/\log(\lambda_1/\lambda_2)$**	(3.26)
	Lidar Ratio Profile	LRP(λ, R)	$\alpha(\lambda,R)/\beta(\lambda,R)$	(3.27)
	Absorption coefficient profile	σ_{abs}(λ, R)	$AOD_1(\lambda) \cdot AVP_1(R) \cdot (1 - SSA_1(\lambda)) + AOD_2(\lambda) \cdot AVP_2(R) \cdot (1 - SSA_2(\lambda))$	(3.28)
	Scattering coefficient profile	σ_{sca}(λ, R)	$AOD_1(\lambda) \cdot AVP_1(R) \cdot SSA_1(\lambda) + AOD_2(\lambda) \cdot AVP_2(R) \cdot SSA_2(\lambda)$	(3.29)
	Single Scattering Albedo Profile	SSAP(λ, R)	$(\alpha(\lambda,R) - \sigma_{abs}(\lambda,R))/\alpha(\lambda,R)$	(3.30)

* The surface parameters and the aerosol chemical composition are not shown here (see Ref. [267]), and the optical-microphysical properties are retrieved for fine (1) and coarse (2) modes;
** Subscript 0 stands for aerosol-free, while subscripts 1 and 2 stand for initial and final λ.

The second equation stands for the *a priori* smoothness assumptions to constrain the microphysical properties, 0* stands for the vector of zeros, M stands for the matrix of coefficients of the derivatives, and Δ(Δa) stands for the vector of the uncertainties characterizing the deviations of the differences from the zeros [63]. The matrices M have different dimensions and represent differences of different orders, e.g., 3 for SD, 1 for N, 2 for the vertical profile of aerosol concentration, and no smoothness constraints for SF and lidar calibration coefficient [63].

The third part of the system of equations incorporates a* (vector of *a priori* estimates) and Δa* (vector of the uncertainties in *a priori* estimates). The errors (Δ) presented in the system of equations are assumed to be normally distributed. Thus, the Numerical Inversion is organized by the general organization of observation fitting with error estimation and the *a priori* data representation [63].

GARRLiC versus LIRIC. The GARRLiC and the LIRIC algorithms have heritage from the AERONET inversion code, such as the statistically optimized inversion approach. They have been developed in the framework of ACTRIS. Both methods utilize AERONET and lidar systems observations to retrieve aerosol properties. Furthermore, the LIRIC uses the identical AERONET model of aerosol microphysics and the lidar retrievals adopt some elements of the AERONET inversions [51], while GARRLiC was developed by direct modification of AERONET and PARASOL algorithms [64] together to include lidar measurements in the Numerical Inversion.

Figure 3.6 depicts the comparison between the inversion methods. Some differences between the codes are related to the inputs and outputs of GARRLiC. The inputs from radiometers are optical thickness or AOD, scattered radiances, and their viewing geometry. In contrast, LIRIC requires columnar inverted properties from AERONET for fine and coarse modes (LR, volume concentration, and optical thickness). Regarding the outputs, the GARRLiC method has more retrievals than LIRIC, including SD, N, and SF for fine and coarse modes at all wavelengths.

According to Ref. [271]: (i) both algorithms work well for individual aerosol components or mixtures of fine and coarse particles (e.g., pollution and dust,

respectively), but they should not be able to fully characterize the mixture components in the case of more than one fine or coarse modes in the mixture (e.g., smoke-pollution or dust-marine); and (ii) LIRIC code provides an effective characterization for the volume concentration profiles, because it derives the coarse spherical particles and the non-spherical particles, but not satisfactory for the particle microphysical properties. For the microphysical characterization of the particles, the GARRLiC algorithm is more complete.

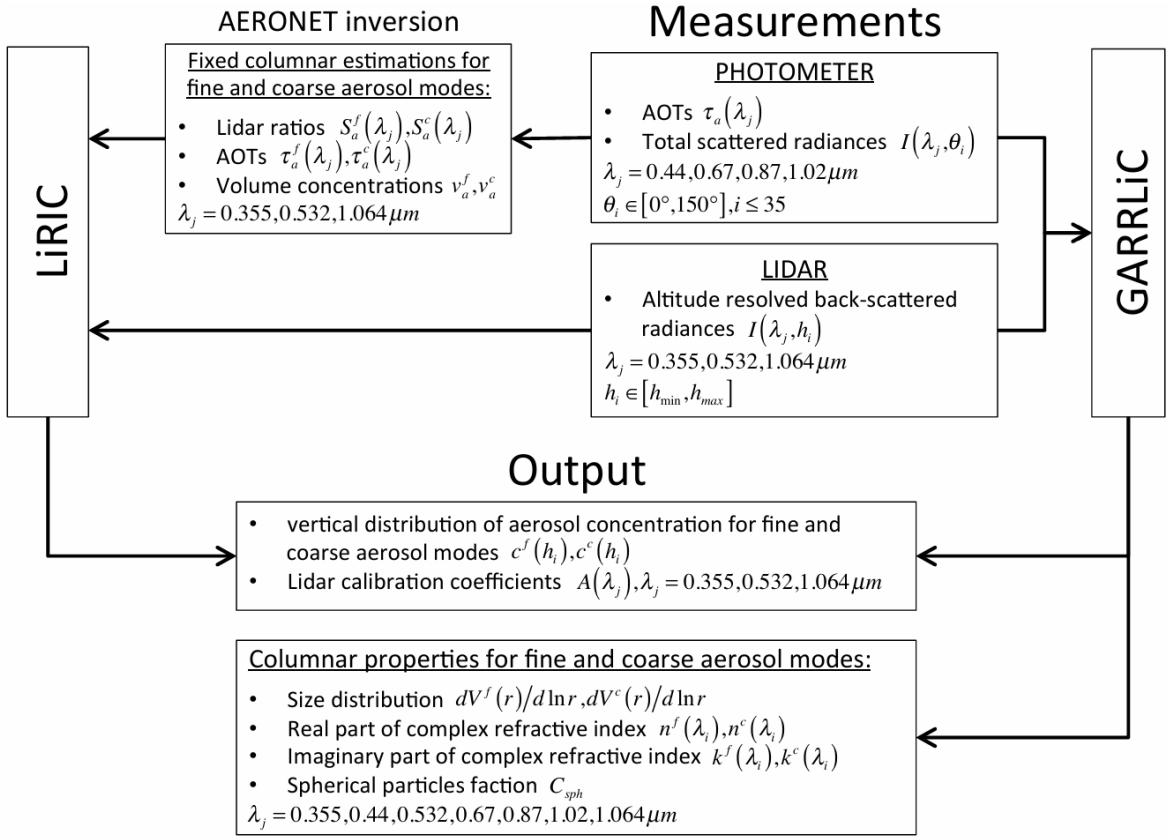

Figure 3.6. Algorithm comparison. This figure is available in Ref. [51].

Regarding GRASP enhancements and applications, the algorithm has allowed many researches about synergy retrievals between ground-based remote-sensing instruments: Ref. [51] implemented and developed the GARRLiC code in GRASP to retrieve aerosol properties from coincident lidar and radiometer observations; Ref. [272] integrated a tool for calculation of radiative fluxes and demonstrated the importance of detailed representation of aerosol and surface to retrieve radiative properties; Ref. [273] provided a complete analysis and illustration

of AOD inversion using GRASP approaches; Ref. [274] used the mentioned algorithm to investigate the potential of retrieving aerosol properties from combined photometer and ceilometer data; Ref. [275] explored the aerosol retrieval synergies from diverse combinations of ground-based passive Sun photometric data with collocated active lidar ground-based (MPL) and radiosonde (Compact Optical Backscatter AerosoL Detector - COBALD) observations; Ref. [276] described the generation of the dynamic error estimates of GRASP retrieval and evaluated the reliability of the error estimations in the presence of random and systematic uncertainties for aerosol retrievals from radiometer observations alone and with lidar; Ref. [277] included in GRASP an SOS-based RT approach (Successive Orders of Scattering Radiative Transfer) code which enables its application from the UV to the thermal infrared parts of the electromagnetic spectrum; Ref. [134] evaluated the GRASP accuracy for retrieving aerosol properties from synergy polarized Sun-sky-lunar photometer and three-wavelengths elastic lidar; and Ref. [278] compared the diurnal aerosol products (AOD, LR, and vertical profiles of aerosol extinction and backscatter at 532 nm) from GRASP and MPLNET approaches.

Furthermore, indirect contributions to the GRASP algorithm were performed by adapting the AERONET inversion code, such as Ref. [190], who investigated the dependency of aerosol retrieval on the geometry used in the sky radiance measurements, and Ref. [69], who included the polarimetric data to the routine inversion (adapted AERONET code) of the radiometric ground-based measurements for characterization of the atmospheric aerosols.

All algorithms to perform lidar-photometer inversions discussed in this manuscript are summarized in Table 3.2.

Table 3.2. Summary of the main algorithms for the inversion of atmospheric aerosol properties by combining lidar and Sun photometer data.

Algorithm	Retrieved Parameters	References
LIRIC	Fine-coarse vertical distribution of the aerosol concentration and lidar calibration coefficients.	[56,57,252,254,256,257]
LidAlm	Fine-coarse vertical profile of the particle mass concentrations, ice and cloud nuclei profiles, number, surface area, and volume concentrations	[59]

Continuation of Table 3.2.

GARRLiC	AVP, RRI, IRI, SD, SF (bimodal), lidar calibration coefficients, and other parameters.	[51]
Minimization method *	AOD, SSA, SD, and extinction profile.	[62]
POLIPHON	Fine-coarse vertical profile of the particle mass concentrations, ice and cloud nuclei profiles, number, surface area, and volume concentrations.	[60,61,260–262]
Unnamed	Mass-extinction conversion factor, aerosol mass concentration, and SSA for spheroid and nonspheroid models.	[266]
Unnamed	Particle size distributions, r_{eff}, and N.	[55]

* The authors used this name in one of their plots.

4 METHODOLOGY

I dedicate this chapter to the Universitat Politècnica de Catalunya, the Department of Signal Theory and Communications (including IT and laboratory staff), the School of Doctorate in Signal Theory and Communications, the Autonomous Community of Catalunya, and the Government of Spain. I had to follow their ***methodology****. I also dedicate it to Waldyr Guimarães Araújo de Souza.*

Save water!

This chapter describes the methodology applied in this research to achieve the objectives proposed in Chapter I. The methodology was executed in two stages: the first refers to the retrieving of aerosol properties by sensitivity test of the GRASP code, owing the synergy between Sun photometer (including linear polarization) and lidar data, and the second refers to the estimation of the radiative effects of aerosols with observations from Sun photometers and pyranometers (long-term analysis), and from retrievals of some combinations (Sun photometers + lidar) presented in the first stage of the methodology for case studies. This chapter was adapted from the methods applied in Refs. [134,279].

4.1 MEASUREMENT SITE

Barcelona (41.384N, 2.120E, 115 m a.s.l.) is located in the northeast of Spain in a large coastal metropolitan area (more than 5 million inhabitants) between the Mediterranean Sea and the Collserola Mountains. Its climate changes at a fast pace [280] and is characterized by four seasonal patterns. The measurement site is highly affected by urban and marine particles, local aerosols, transported desert dust outbreaks, and biomass burning from forest fires in the summer due to vegetation dryness [281]. Additionally, Barcelona is affected by European pollution episodes [282] and contributions of pollen and spores [283,284].

Table 4.1 shows AOD(440 nm) monthly averages and AE(440-870 nm), measured by Sun photometers during 17 years of AERONET direct observations at L2 [49,179,244] in Barcelona. Over the whole period, the AOD average is 0.18 and the AE average is 1.31, i.e., small particles are predominant. These results are typical of an urban-industrialized area, according to Ref. [285].

Table 4.1. AOD(440 nm) monthly average and AE(440-870 nm), from 2004 to 2021, at L2. The standard deviations (std) are in italic.

AP	Winter			Spring			Summer			Autumn		
	Dec	**Jan**	**Feb**	**Mar**	**Apr**	**May**	**Jun**	**Jul**	**Aug**	**Sep**	**Oct**	**Nov**
AOD	0.10	0.11	0.16	0.16	0.2	0.18	0.23	0.25	0.23	0.21	0.16	0.11
std	*0.07*	*0.08*	*0.12*	*0.12*	*0.12*	*0.09*	*0.11*	*0.11*	*0.11*	*0.12*	*0.11*	*0.08*
AE	1.37	1.35	1.36	1.27	1.25	1.28	1.34	1.30	1.32	1.34	1.23	1.33
std	*0.34*	*0.38*	*0.36*	*0.34*	*0.38*	*0.34*	*0.39*	*0.37*	*0.36*	*0.32*	*0.35*	*0.31*

4.2 PARAMETRIZATION AND SENSITIVITY OF GRASP/GARRLIC ALGORITHM

The GRASP/GARRLiC algorithm performs the synergetic retrievals proposed in this study. The GRASP code needs two input files, as mentioned in Subsection 3.4.2: the SData file contains the observed data and the setting file contains all the retrieval settings information. To run the GRASP code, it is necessary to prepare some of the observational data and configure the setting files, as detailed in the following subsections. In routine, the code is set in its Numerical Inversion module (Figure 4.1a) to perform real data inversions. For this mode to be optimum, the setting parameters have to be optimized. This is assessed by a sensitivity test (Figure 4.1b), which requires the user to use both the Forward Model and Numerical Inversion modules of the code. The explanation of both modules is also in Subsection 3.4.2, and a detailed description of GRASP inputs is found in Ref. [267].

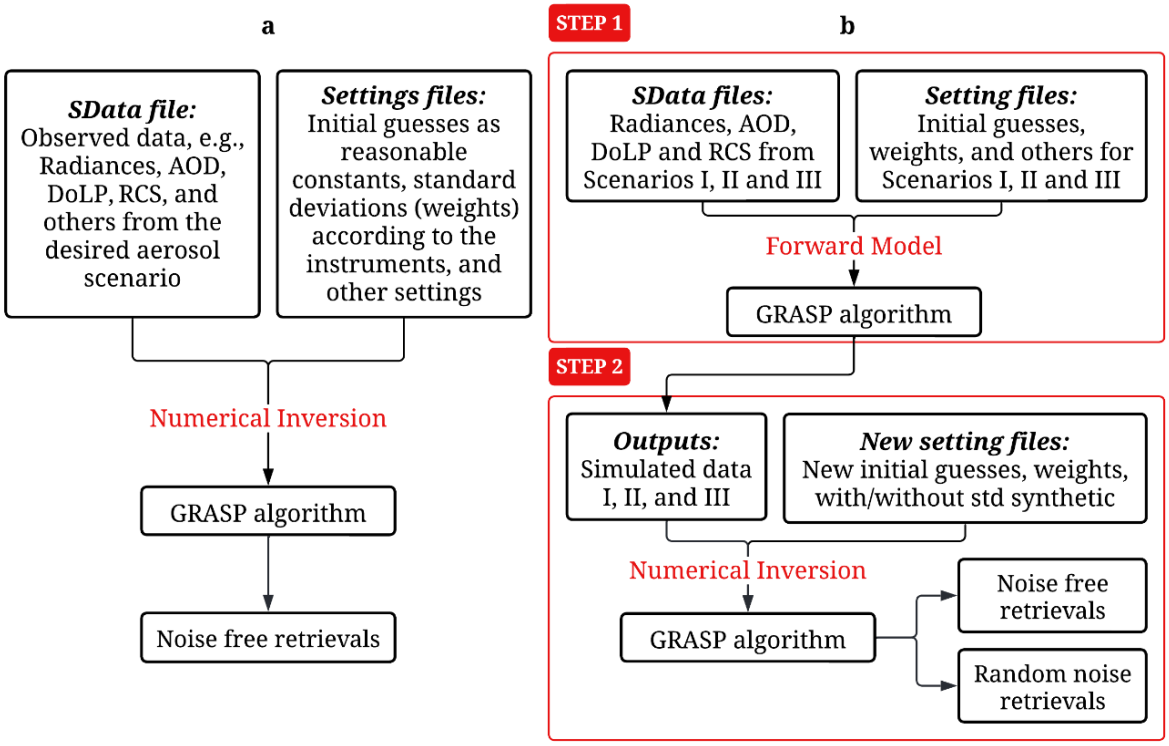

Figure 4.1. Methodology flowchart for the sensitivity tests. **a** is the usual procedure for inverting data in the GARSP code, and **b** is the procedure for performing the sensitivity test.

4.2.1 GRASP Input Data: SData File

The measurements are organized in the SData file, which contains information about viewing geometry, altitude, spectral characteristics such as AOD and radiation, type of measurements and their quantities, coordinates of the measurement place, date, pixel number, and others. However, to run the GRASP algorithm properly, the photometer and lidar data need to be prepared before being arranged in the SData file, i.e., a specific preparation is required. Figure 4.2 illustrates the data preparation to fill the SData file. The normalization of the radiances and RCS, and symmetry-check, angle-conversion, and logarithmic-profile procedures are explained in the following subsection.

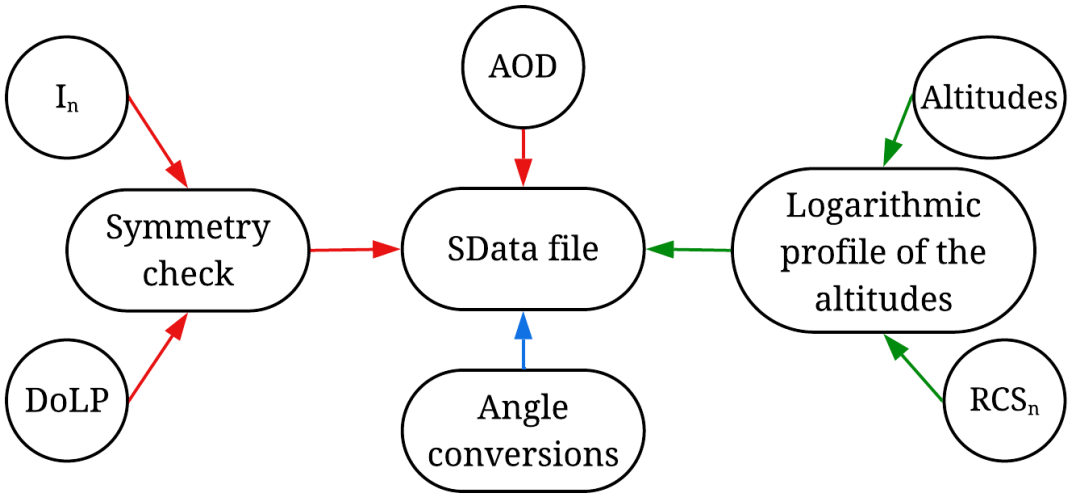

Figure 4.2. Flowchart for the SData preparation.

4.2.1.1 Photometer data

In the case of photometer observations, the raw data are already calibrated by the Langley method, intercomparison procedure with a reference instrument, and sphere-calibration procedure [44]. The sphere-calibration procedure and an intercomparison procedure with a reference polarized light [68,69] are also

performed for the linearly polarized light. Furthermore, the absolute radiances[43] from the almucantar scan (Subsection 2.4.2) must be reduced and normalized as follows:

$$I_n(\lambda) = \frac{I(\lambda)\pi ESD}{I_0(\lambda)100} \tag{4.1}$$

where $I_n(\lambda)$ is the spectral normalized radiances[44], in $mWm^{-2}sr^{-1}nm^{-1}$, $I(\lambda)$ is the spectral absolute radiance provided by AERONET inversion products (almucantar extension file, 'alm', columns 12 to 88), in $\mu Wcm^{-2}sr^{-1}nm^{-1}$, $I_0(\lambda)$ is the spectral extraterrestrial solar irradiance computed by Ref. [286], in $Wm^{-2}nm^{-1}$, and shown in Table 4.2, 100 is the conversion factor. ESD is the Earth-Sun Distance, which depends on the Day Angle (DA):

$$ESD = \frac{1}{1.00011 + 0.034221\cos DA + 0.00128\sin DA + 0.000719\cos 2DA + 0.000077\sin 2DA} \tag{4.2}$$

and

$$DA = \frac{2\pi(day\ of\ the\ year - 1)}{365} \tag{4.3}$$

the day of the year varies from 1 (January 1st) to 365.

Table 4.2. Spectral extraterrestrial irradiance according to Ref. [286].

λ (nm)	**I_0 ($Wm^{-2}nm^{-1}$)**
380	1.325
440	1.848
500	1.932
675	1.492
870	0.989
1020	0.697
1640	0.221

Once radiances were normalized, they were averaged and the symmetry between right and left almucantar scans was checked for each Azimuth Angle (AA) by the following condition:

[43] This first part of the methodology used the L1.5, the only one available when the research was performed. This level applies the cloud screening criterion [179] from Version 3 [49,245], guaranteeing any cloud contamination.

[44] The GRASP range for normalized radiances is from $1e^{-11}$ to $1e^{2}$ mWm^{-2}.

$$\frac{I_{n,right}(\lambda, AA) - I_{n,left}(\lambda, AA)}{(I_{n,right}(\lambda, AA) + I_{n,left}(\lambda, AA))/2} < 0.2 \quad (4.4)$$

which values equal or greater than 20% were eliminated to assure data uniformity by eliminating sky inhomogeneities and reducing some of the possible instrumental biases [190].

Regarding the DoLP (Subsection 2.2.3.2), the symmetry check was also applied on the polarization data [69] from the polarized almucantar scan in the AERONET inversion products (extension file, 'alp', columns 12 to 41). The principal plane scan was not chosen, owing to its many limitations: horizon obstructions, inexact optical mass computation, and the maximum scattering angle is typically smaller than stated theoretically [190]. Furthermore, the almucantar scan is already well validated and the hybrid scan is still under validation [287].

Other data preparation is the definition of zenithal and azimuthal angles inside the code because the GRASP algorithm uses the satellite as the reference for the angle system. The angle conversions from photometer to GRASP algorithm are:

$$ZA_G = 180° - ZA_P \quad (4.5)$$

$$AA_G = 180° + AA_P \quad (4.6)$$

where ZA_G and AA_G are the converted zenith and azimuth angles of GRASP, respectively, and ZA_P and AA_P are the zenith and azimuth angles of the photometer, respectively, available on the AERONET network. Furthermore, zenith and azimuth angles for the AOD and the lidar system are zero, owing to their vertical optical path.

4.2.1.2 Lidar data

The input data from the lidar system are its spectral measurements[45] (elastic signal, Raman signal, volume depolarization ratio[46], and extinction or backscatter profiles), including their altitudes in meters. The RCS were processed by the ACTRIS/EARLINET Single Calculus Chain (SCC) [288–290] in which background

[45] The choice of the lidar products will depend on each lidar system and the purpose of the research. In this study the RCS and the δ^v were used.

[46] The volume depolarization ratio has to be in the percentage range from $1e^{-9}$ to 100%.

subtraction, range correction, trigger delay, overlap correction, dead-time correction, and gluing analog and photon-counting signals were applied to the lidar signals, being the minimum recommendations to run the GRASP algorithm with lidar data. Besides those corrections, all profiles were scaled logarithmically equidistant in 60 points to avoid an excessively high number of retrieved parameters [51]. According to the same authors, a logarithmic profile can represent the aerosol profiles because of its similarity with the air density, i.e., it decreases exponentially as a function of height, averting noise interference on the lidar signals at higher altitudes. The calculation of the logarithmical profiles was done as follows:

$$R_i = \mathrm{e}^{(\log R_{\min} + (i-1)R_{stp})} \tag{4.7}$$

where R_i is the same logarithmic altitude from i = 1 to 60 for all lidar wavelengths, R_{min} is the initial altitude from the selected range (R_{min} to R_{max}, in meters), and R_{stp} is the altitude step:

$$R_{stp} = \frac{(\log R_{max} - \log R_{min})}{60} \tag{4.8}$$

which R_{min} was influenced by the overlap correction and R_{max} was chosen considering acceptable noise levels and the presence of aerosols at this atmospheric height. Then, the lidar signals were interpolated (RCS_{interp}) using the logarithmic altitude (R_i) as the reference profile. Finally, the RCSs were normalized to 1 according to the simple Equation 4.9:

$$RCS_n(\lambda, R) = \frac{RCS_{interp}(\lambda, R)}{\int_{R_{min}}^{R_{max}} RCS_{interp}\, dR} \tag{4.9}$$

where RCS_n is the normalized lidar profile for each channel. Bear in mind that all AERONET inversions with less than 3% of sky error[47] were selected. To guarantee the coincidence of both instrument measurements, the lidar profiles were averaged over 60 minutes centered on the time of the AERONET inversions. Assuming a homogeneous and continuous atmosphere, the AOD and sky-polarized radiances were chosen in the closest possible time, i.e., a 16 min interval centered on

[47] It is the error in sky radiance measurements and is found in AERONET inversion products (almucantar extension file, 'all', columns 123).

almucantar inversion time, the same interval chosen by Ref. [287]. An example of the SData file with the UPC observations is in Appendix A.

4.2.2 GRASP Input Data: Setting File

The main configurations of the setting file are the GRASP noises[48] and the initial guesses (Subsection 3.4.2). The first is the definition of the noises associated with the data in the SData file, which are used to arrange an optimum set of noise constraints for the UPC instruments. The second is the values that the GRASP algorithm will use as "starting points" to invert data.

4.2.2.1 GRASP noises

The noises configured in the GRASP synergy were the normalized radiances, aerosol optical depth, linear polarization, and lidar signal with their respective error types: relative, absolute, absolute, and relative. The standard deviation synthetic, a Gaussian-distributed noise, adds a random perturbation, which depends on each instrument. In this research, the standard deviation synthetics were selected according to previous studies: 0.05 for radiances [274,276], 0.005 for AOD [51,183,291], 0.01 for DoLP [64,68,69], 0.2 for 355 nm, 0.15 for 532 nm, and 0.1 for 1064 nm [51,276]. The standard deviation, a Gaussian-distributed weight associated with an observation or synthetic data, was filled according to the uncertainties of the UPC instruments to achieve the best convergence (minimum residuals). Table 4.3 shows the noise configuration used to generate the simulated data and add noise to it. More details are in Subsection 4.2.4.

Table 4.3. GRASP noise configuration applied in this research. Std stands for standard deviation.

GRASP Noises	Error Type	Std *	Std Synthetic **
I	Relative	0.03	0.05
AOD	Absolute	0.01	0.005
DoLP	Absolute	0.1	0.01

[48] In this manuscript, GRASP noises refer to the 'noises', a GRASP concept of the setting file that configure (i) the addition of random noises by the standard deviation synthetic, (ii) error type of the measurement, (iii) standard deviation (weight associated with the observations), and (iv) the measurement type for each observation put in the SData file (Subsection 4.2.1). Additionally, an explanation about 'noises' is found in Ref. [267].

Continuation of Table 4.3.

RCS (355 nm)	Relative		0.2
RCS (532 nm)	Relative	0.2	0.15
RCS (1064 nm)	Relative		0.1

* These values were applied to create the synthetic data by activating the Forward Model;
** These values were applied to add random noises to the synthetic data.

4.2.2.2 Initial guesses

Subsection 3.4.2 explained that the initial guesses are an array that evolves in each iteration until getting the result array [267], i.e., they are some constraints of GRASP characteristics (SD, RRI, IRI, SF, AVP, and others[49]). Once an initial guess is loaded in the code, it becomes the first array of characteristics to be retrieved by the iteration process until it gets the results. Then, the GRASP Forward Model is called, using this result array to obtain the rest of the results [267].

The initial guesses of each mentioned characteristic were obtained from AERONET inversion data for Barcelona and Ref. [130] by following the recommendations of previous studies, such as Refs. [51,190,273]. All characteristics were set for three aerosol scenarios. Another constraint is the smoothness applied to each characteristic. The difference order and the Lagrange multiplier composed the smoothness (Subsection 3.4.2).

The first initial guess is the SD (obtained from AERONET retrievals for Barcelona), a bimodal lognormal function corresponding to a mixture of aerosols with 22 log-spaced triangle bins, in which the first 10 bins (0.05 to 0.576 μm) correspond to the fine mode while the last 15 bins (0.335 to 15 μm) were assigned for the coarse mode, i.e., three bins overlap by distributing both modes.

The second initial guess is the RRI and IRI. They were adapted from the aerosol models reported by Ref. [130], in which data from Mexico City and Bahrain were used for the fine and coarse modes, respectively, because they have values closer to those from Barcelona. Furthermore, the AERONET inversion products do

[49] See Table 4.2 in Ref. [267].

not provide the refractive indices by modes; thus, it was necessary to obtain refractive values for both modes. The RRI-IRI missing values from the new photometer and lidar wavelengths (380, 500, 532, 1064, and 1640 nm) were interpolated or extrapolated [51,273], assuming that both components of the refractive index have a very weak spectral dependence [130,190,273].

The third is the SF [67], whose values were obtained from AERONET inversions of Barcelona data. Concerning the aerosol shape, the GRASP algorithm considers each aerosol component as a mixture of polydisperse spheres and spheroids [51,63].

The last initial guess is the AVP, which describes the variability of aerosols at all altitudes from ground to space, being normalized to unity [51]. The fine and coarse modes of the AVP were obtained following the approach of Refs. [51,276], in which the aerosol modes were represented in two different layers: an exponential distribution from the ground to maximum height for the fine mode and a Gaussian distribution for the coarse mode at a higher altitude. The heights of the layers were placed according to the aerosol layers from the local lidar signal. The vertical concentrations were multiplied by the fine-mode fraction at 500 nm from the SDA [48], part of the AERONET inversions (Subsection 3.3), to simulate the contribution of fine AOD to the fine-mode profile. Finally, the AVP[50] was normalized to unity according to Equation 16a in Ref. [64] and after Equation 8 in Ref. [51]. Table 4.4 summarizes the properties used as characteristics.

Table 4.4. Initial guesses used in this research. Diff stands for difference, Lag stands for Lagrange, and Modes stands for the parameter modes.

Initial Guesses	Modes	Diff. Order	Lag. Multiplier
SD	fine and coarse	3	0.3
RRI	fine and coarse	1	500
IRI	fine and coarse	1	500
SF	total	0	0
Vertical profile	fine and coarse	3	$1x10^{-5}$
Surface land BRDF Ross-Li	isotropic, volumetric, and geometric	0	0

[50] An attempt to use a hybrid profile was proposed in this research. It is approached in Appendix B.

Continuation of Table 4.4.

Surface land polarized Maignan-Breon	only one mode	0	0

4.2.2.3 BRDF-BPDF characteristics

The GRASP/GARRLiC algorithm (Subsection 3.4.2) can also retrieve aerosol forcing and surface properties. For this purpose, it needs radiance and polarization measurements and requires accurate models for the Bidirectional Reflectance Distribution Function (BRDF) and the Bidirectional Polarization Distribution Function (BPDF), for example, the Ross-Li model [292–294] and Maignan-Breon model [295,296], respectively. Both reflectance parameters were validated and extensively compared with the POLDER data by Ref. [296,297]. The Ross-Li model is a linear combination of three-surface scatterings (isotropic, volumetric, and geometric optical), while the Maignan-Breon model is a linear one-parameter BPDF.

Regarding the methodology in Subsection 4.2.1, the BRDF-BPDF characteristics were included as a dark surface, although they were considered for retrievals of realistic measurements (Subsection 4.3.3). A dark surface does not interfere with the aerosol property retrievals from synthetic data (with and without DoLP) because the goal is to assess the GRASP capability of retrieving synergic data from ground-based measurements, not surface measurements.

Regarding the inversions in Subsection 4.3.3, this study obtained the BRDF-BPDF surface values from the POLDER satellite [298] climatology over Barcelona. The BRDF isotropic values were interpolated for the photometer channels. In contrast, the volumetric, geometric, and BPDF surface values are considered spectrally independent in the visible and infrared regions [299]. After configuring these initial guesses, the broadband solar flux and aerosol radiative effect calculations at the BOA were conducted using the code and principles described in Ref. [272] and their implementation in the GRASP algorithm [64,253,268]. The

radiative code [272] also assumed nonspherical-spherical particles, as the GARRLiC code [51].

4.2.3 Procedure for GRASP Tests

This subsection reports the methodology to perform the sensitivity tests for the combinations flagged in Table 4.5. Notably, the GRASP algorithm can simulate synthetic data, activating the 'forward' option in the setting file. Figure 4.1b describes the steps for generating synthetic data and retrieving it with and without added noise. Once 'noises' (Subsection 4.2.2.1) and 'initial guesses' (Subsection 4.2.2.2) were defined, the GRASP code was run to create the synthetic data[51] (Step 1 in Figure 4.1b) and to retrieve aerosol properties under two conditions (Step 2 in Figure 4.1b): (i) added random noises (RN) and (ii) noise-free (NF). The simulated data was created to be as similar as possible to the atmospheric conditions in Barcelona, Spain.

As mentioned above, in the first step, the simulated data were created with the GRASP Forward Model based on (i) a prepared SData file (Subsection 4.2.1) with some real observations (SD, RRI, IRI, and SF) and built AVPs, (ii) configurations of the GRASP noises (Table 4.3), and (iii) initial guesses (Table 4.4) from aerosol observations with dominant fine and coarse modes.

The simulations were performed for three aerosol scenarios in Barcelona, where:

- Scenario I was a dominant coarse mode with high aerosol load, AOD(440 nm) = 0.64;
- Scenario II was a dominant coarse mode with low aerosol load, AOD(440 nm) = 0.26; and
- Scenario III was a dominant fine mode with high aerosol load, AOD(440 nm) = 0.33.

[51] Simulated and synthetic data are considered synonyms in this manuscript.

In all scenarios, the radiance uncertainties are less than or equal to 3% of the sky error uncertainties (Subsection 4.2.1.1). Even though the lidar contributions already provide maximum benefits in the synergy for retrievals with low aerosol loading [51], it is a better option to use AERONET retrievals with a load greater than 0.3 [46,190][52], i.e., Scenarios I and III. As recommended by Ref. [273] and confirmed by Ref. [287], the lower limit of AOD(440 nm) is 0.2 for the bimodal log-normal size distribution parameters to assure the quality retrievals of aerosol particles since the uncertainty in the parameters dramatically increases as the aerosol load decreases [273,276]. Therefore, the synthetic data contains created radiations, DoLP, AOD, and RCS for each aerosol scenario.

The second step was to invert the synthetic data under NF-RN conditions in the GRASP code. Two new setting files were set to invert the mentioned conditions. Both files had new initial guesses, generally with reasonable constant values (no real observations). The NF data was inverted to test the stability of the GRASP inversions to minor noise [69], i.e., neither systematic nor random errors were introduced in this approach, and the RN data was inverted to estimate the sensitivity [51] of GRASP inversions. Note that NF inversions are the routine for retrieving aerosol observations when the 'inversion' mode is activated. The NF-RN inversions were carried out for the flagged combinations in Table 4.5 by three aerosol scenarios; thus, 15 retrievals were performed for the NF condition (5 combinations by 3 scenarios by 1 NF retrieval), and 1500 retrievals were performed for RN the condition (5 combinations by 3 scenarios by 100 RN retrievals).

4.2.4 Data Combinations

The GRASP algorithm retrieved a set of aerosol properties by several combinations between a Sun-sky-polarized photometer and the UPC/EARLINET multi-wavelength lidar system to compare the improvements from the simple one (D0) to the most complex one (D1P+L+δ^v). D0 was defined using the standard photometer (limited to 4λ), and the combinations became more complex as further

[52] In this manuscript, an aerosol load is considered high when AOD ≥ 0.3.

information was introduced, e.g, the addition of DoLP, RCS, and δ^v. Table 4.5 presents the possible combinations of both instruments. D0P+L, D1+L, D1P+L, and D1P+L+δ^v combinations were inverted for the first time, consolidating this study as pioneering.

Table 4.5. Daytime combinations (D) between the UPC/EARLINET multi-wavelength lidar system and the new Sun-sky-lunar multispectral polarized photometer. The standard photometer (4-channels) is notated with 0, and the new one (7-channels) is notated with 1, P refers to the polarized data (DoLP), L refers to the RCS_n, and δv refers to the volume depolarization ratio.

Notation	Input Data
D0 (AERONET-Like)*	[AOD + I_n] (4λ)
D0P	[AOD + I_n + DoLP] (4λ)
D0+L*	[AOD + I_n] (4λ) + RCS_n (3λ)
D0P+L*	[AOD + I_n + DoLP] (4λ) + RCS_n (3λ)
D1	[AOD + I_n] (7λ)
D1P	[AOD + I_n + DoLP] (7λ)
D1+L*	[AOD + I_n] (7λ) + RCS_n (3λ)
D1P+L*	[AOD + I_n + DoLP] (7λ) + RCS_n (3λ)
D1P+L+δ^v **	[AOD + I_n + DoLP] (7λ) + RCS_n (3λ) + δ^v(2λ)

* The GRASP code inverted them in both stages of this research;
** This combination was also inverted for the first time, but it is not the focus of this research.

4.2.5 Statistical Indicators

Afterward, the results of the NF-RN inversions were compared with the reference data (simulated data). Some statistical indicators were calculated to quantify the comparisons. The first one is the correlation coefficient (corr) to quantify the intensity of the linear relationship between the reference and the RN averaged inversions, that is, the capability of RN averaged inversions to reproduce the shape of the VC(R). The second statistical indicator is the Fractional Bias (F_B), which expresses the underestimation or overestimation caused by only the systematic errors [165] between the reference and RN averaged inversions. The F_B was computed by the following equation in Ref. [300]:

$$F_B = \frac{2}{i}\left(\sum_1^i \frac{M_{ref} - O_{RN}}{M_{ref} + O_{RN}}\right) \quad (4.10)$$

where *i* is the sample size, M_{ref} is the reference, and O_{RN} is the averaged profile of the RN inversions. When $F_B = 0$, it indicates perfect overlapping between the profiles, i.e., free from bias, while $F_B = 2$ indicates an extreme underestimation and $F_B = 2$ indicates an extreme overestimation. F_B and corr were calculated in the main aerosol layer from each VC profile to avoid a distorted estimation caused by too small values in the ratio (Equation 4.10) or by another aerosol layer in the same profile.

The last indicator, calculated for the other aerosol parameters, is the RMSE. It assesses the dispersion of the RN inversions concerning reference data. The RMSE was calculated by the equation below:

$$\mathrm{RMSE} = \sqrt{\frac{1}{i}\sum_{1}^{i}\left|M_{ref} - O_{RN}\right|^2} \tag{4.11}$$

If RMSE values are equal to 0, there is an optimum fit between the RN averaged inversions and the reference, i.e., a correlation coefficient equal to 1.

4.3 AEROSOL FORCING ESTIMATION

This part of the methodology focuses on the aerosol forcing estimation by applying a simple mathematical method: the direct method [71]. Furthermore, the parametrization of the GRASP code for retrieving aerosol forcing is detailed here.

4.3.1 Clear-sky Selection

This methodology required a differentiation between all-skies and clear-sky days. The all-skies radiative fluxes were provided by the SolRad-Net at L1.5 from 2009 to 2023. The observations were selected by (i) diurnal cycles with 80% of measurements during hours of sunshine, ensuring more complete diurnal cycles, and (ii) radiative flux values at a minimum SZA ± 1° (nearest to the zenith). The data from the pandemic year (2020) are not included in this work because there are not enough measurements from the instruments in Barcelona.

Before calculating the aerosol forcing, a selection of the cloudless sky conditions was performed by a quadratic fitting [301–304]. This simple approach

identifies only clear-sky days during a whole day by a regression equation, ax^2+bx+c, where a, b, and c are its coefficients. The quadratic fitting was applied to the radiative fluxes on the surface and their respective SZA cosine (x-axis), which greatly influences the radiative fluxes [305]. Figure 4.3 is an example of a day classified as a clear-sky day by the quadratic fitting.

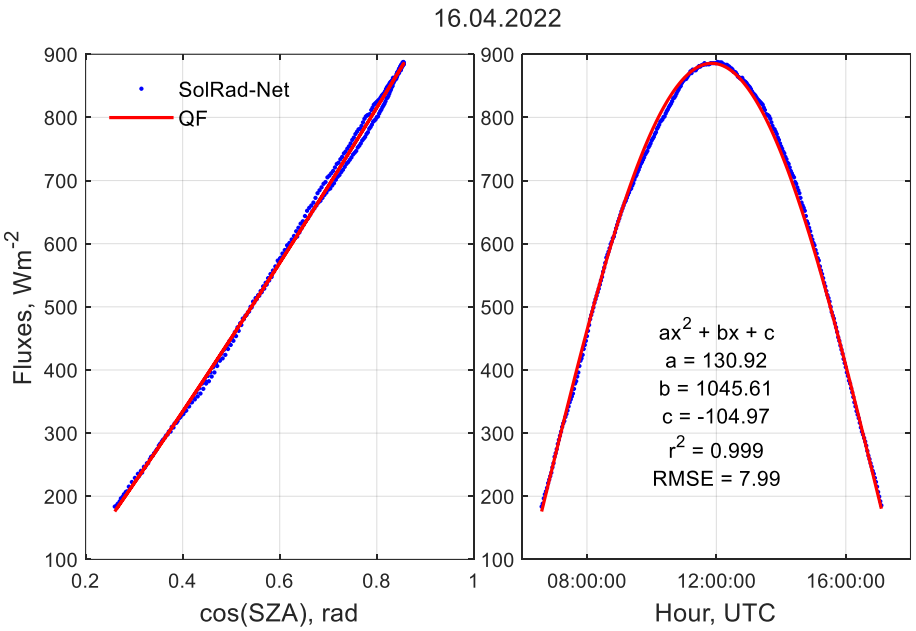

Figure 4.3. Example of a selected clear-sky day (16 April 2022) employing the quadratic fitting (QF) in red and the SolRad-Net measurements in blue as a function of cos(SZA), left plot, and UTC, right plot.

To execute the fitting and to guarantee a homogenous atmosphere (i.e., the symmetry between morning and afternoon fluxes) and ensure less variability in the fluxes caused by possible clouds in the morning or afternoon period, the following criteria were applied to the diurnal cycles: (i) selection of diurnal cycles with 80% of measurements during hours of sunshine, ensuring more complete diurnal cycles; (ii) elimination of SZAs greater than 75° to avoid interferences from surrounding reliefs and to avoid errors from the cosine response on the measurements [80]; (iii) application of r^2 greater than 0.98 for the best fit between cosines of the SZA and radiative fluxes; and (iv) application of a seasonal adaptive RMSE (i.e., winter factor of 1, spring factor of 1.18, summer factor of 2.1, and autumn factor of 1.1) by obtaining the rates between the period average of all winter solstices (maximum flux

values around noon) and the period averages of all summer solstices and autumn-spring equinoxes (maximum flux values around noon). Figure 4.3 shows a classification with an r^2 of 0.999 and an RMSE of 7.99 Wm^{-2}.

4.3.2 Direct Method

The ARF is the difference between the net irradiance on the surface (I_{net}) and the net irradiance without aerosol contribution ($I_{net,0}$), i.e., the ARF is the change in the net flux due to variations in the aerosol properties regarding an aerosol-free atmosphere. The ARF can be calculated by the equation below:

$$ARF = I_{net} - I_{net,0} \tag{4.12}$$

The I_{net} component is computed as follows:

$$I_{net} = (1 - A)I \tag{4.13}$$

where A is the surface albedo calculated as the period mean of the ratio between outgoing and incoming radiations from the UPC CNR 4 (Equation 2.45) by SZA, and I is the measured downward irradiance on the surface. To cover the greatest amount of SZA, six angle groups were fixed (20°, 30°, 40°, 50°, 60°, and 70°) with a range of ± 1° because larger angle ranges can have higher variation in irradiation. For Barcelona, A is the mean albedo over the 3-year CNR 4 observations at SZA ranges (20 ± 1°, 30 ± 1°, 40 ± 1°, 50 ± 1°, 60 ± 1°, and 70 ± 1°) with 0.104, 0.104, 0.106, 0.108, 0.115, and 0.124, respectively.

As aerosol forcing is strongly affected by the aerosol load [306], it can be assessed by the AFE, which is the change in the ARF per unit in AOD for a certain wavelength (λ) [31]:

$$AFE(SZA, \lambda) = \frac{dARF}{dAOD} \tag{4.14}$$

Equation 4.14 can be rewritten based on Equation 4.12:

$$AFE(SZA, \lambda) = \frac{d\left(I_{net} - I_{net,0}\right)}{dAOD} \tag{4.15}$$

This estimation avoids some errors due to the instrumental or model offsets, more common in other methods to compute the AFE; thus, the present study used the direct method determined by Ref. [71] to estimate it as the slope derived from the linear regression between the I_{net} and the coincident AOD at an established SZA (Equation 4.15) from the clear-sky condition (Subsection 4.3.1). The direct method was also well applied by Refs. [28,40,80,307,308], among others. Furthermore, the efficiency was calculated for the standard wavelengths of the AERONET inversions (440, 675, 870, and 1020 nm). It is important to mention that the outliers greater than three times the median were deleted from the database to remove possible residual contamination by clouds, and then the fitting was calculated.

The advantage of this method lies in direct estimates of the AFE from observations, without further assumptions about the radiative fluxes under aerosol-free conditions [28], i.e., there is no dependency on the aerosol load under aerosol-free conditions. Hence, the direct method is derived from Equation 4.15 without the $I_{net,0}$:

$$AFE(SZA, \lambda) = \frac{dI_{net}}{dAOD} \tag{4.16}$$

Once the AFE was estimated, the ARF was derived by multiplying the AFE by each AOD [28,80,307,308] at the corresponding SZA for each wavelength (440, 675, 870, and 1020 nm). Then, the final AFE is averaged by SZA and by year. Furthermore, the ARF was also estimated for three groups of aerosols at 440 nm: Mixed Aerosols (MA), Desert Dust (DD), and Urban/Industrial-Biomass Burning aerosols (UI-BB). To better determine the thresholds of the 'AOD *versus* AE' classifications, two aerosol types [108,309] were adopted, which fitted what was proposed in this study, even if there is no support for chemical speciation or other aerosol properties for ensuring the aerosol types in a mixed-source urban environment. Those classifications were chosen because (i) both sites, Lampedusa Island in Italy [108] and Huelva City in Spain [309], are strongly influenced by marine aerosols, desert dust, and local aerosols, as in Barcelona, allowing mixtures between them; (ii) both locations are in the Mediterranean region; and (iii) there is not such a complete kind of aerosol classification for Barcelona.

4.3.3 Aerosol Forcing Comparisons

Three case studies were used to compare the outputs from the GRASP inversions, the direct method (synergy between pyranometer and photometer data), and the AERONET inversions. The aerosol forcing from GRASP inversions was retrieved for clear-sky days with AOD, I_n, DoLP, and RCS_n (Subsection 4.2.1) as inputs[53] for the same combinations proposed by Table 4.5. The combinations are shaped by data from the UPC/EARLINET lidar system and the Sun-sky-lunar photometer for five combinations: D0, D0+L, D0P+L, D1+L, and D1P+L. The AERONET inversions had also less than 3% sky errors and AOD (440 nm) ≥ 0.2 to ensure good retrievals. The SCC [288–290] processed lidar signals. With this synergy, more complete information about the radiation attenuation (vertically distributed and column-integrated properties) by aerosols was provided for the forcing calculations. Additionally, improvement in the aerosol property retrievals (e.g., AOD and SSA) relevant to the forcing is expected by adding polarization data [65–67,69] to the synergy [134]. The fluxes from the pyranometer and the photometer over 14 years were also compared for 958 inversions under the clear-sky condition.

To simplify the comparison among the broadband fluxes from AERONET inversions and pyranometer observations, the parameters were plotted as a function of the SZA, in which only three angle groups were fixed with a range of ±1° (50°, 60°, and 70°) due to the AERONET inversions that do not perform measurements at small SZAs [44,46,237,310]. The Percentage Error (PE) was calculated to indicate the magnitude of the deviation between the inversions and the observations, as in Equation 4.17:

$$PE = \left(\frac{inverted\ value - observed\ value}{observed\ value}\right) 100\% \quad (4.17)$$

Therefore, with the proposed methodology, the present research is a pioneer for calculating aerosol radiative effects integrated from 305 to 2800 nm at 20° to 70°

[53] At this point, the AERONET L2 was available and used to retrieve the aerosol forcing.

during 14 years in Barcelona, Spain. Figure 4.4 summarizes the methodology applied to the aerosol forcing estimation.

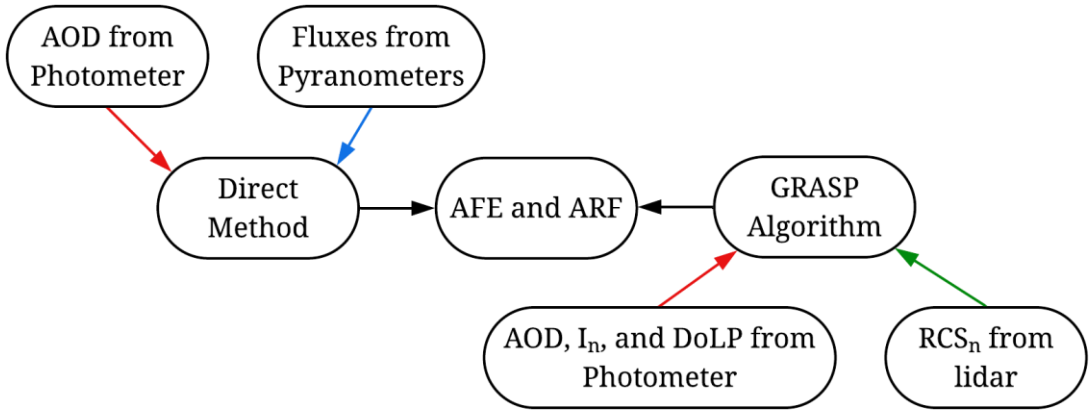

Figure 4.4. Flowchart for AFE-ARF estimation.

4.3.4 AOD and Radiative-Fluxes Trends

The period study from 2009 to 2023, availability of coincident AERONET and pyranometer observations, was analyzed with the Mann-Kendall (MK) test and Sen's slope. As indicated by Ref. [311], the MK test is used to identify increasing or decreasing long-term monotonic trends where the data are not serially correlated, and the Sen's slope estimator, which is less sensitive to outliers and extreme values, is based on the median of slopes calculated from all possible data pairs. The MK test considers seasonality and reduces the chances of falsely detecting a trend where one does not exist [311]. The MK test was applied with a 95% Confidence Interval (CI95) for the AOD and the all-skies radiative fluxes, and it was performed by [312,313]'s functions. Linear regressions fit the clear-sky fluxes by season with a CI95 and the slopes of the uncertainties were also estimated with a CI95.

5 GRASP SENSITIVITY TESTS WITH POLARIZATION INPUT

*I dedicate these **first results** to the GRASP team and the Laboratoire d'Optique Atmosphérique, Université de Lille, especially to Oleg Dubovik, Anton Lopatin, Milagros Estefania Herrera, Marcos Herreras-Giralda, Benjamin Torres, Pavel Litvinov, Yevgeny Derimian, Masahiro Momoi, Qiaoyun Hu, and David Fuertes.*

Save power!

The sensitivity tests of GRASP to the Degree of Linear Polarization (DoLP) parameter used as a new input in the synergy between a photometer and a lidar system are presented in this chapter. Then, several input data configurations with increasing complexity are tested to evaluate the impact on GRASP inversions and the possible improvements. These results were published in Remote Sensing and adapted for this chapter.

5.1 NOISE-FREE INVERSIONS

Subsection 4.2.3 explains how to proceed to retrieve the NF condition for each combination (Table 4.5) without any RN; hence, the simulated data can achieve the best inversion convergence with small residuals.

Table 5.1 shows the standard deviations used to retrieve the simulated data by aerosol scenario and combination, as well as the residual after the last GRASP iteration (Subsection 3.4.2), which should be less than 0.05 (5%) for good convergence [64]. For Scenario I, the convergence improves when the DoLP data is included (D0P+L and D1P+L), with the minimum of 0.0008 for D1P+L.

The standard deviation of the I_n for Scenario II was set at 5% to obtain smaller residuals equal to 0.00055 for D0P+L and D1P+L. However, the smallest residual (0.00043) is achieved when more photometer channels are added to the combination (D1+L). The last aerosol scenario has the best convergence for the D0P+L combination (residual of 0.00111), but the weights for DoLP and RCS_n had to be increased (0.05 and 25%, respectively). The weights (standard deviations in the setting files) in Table 5.1 are optimized for the UPC site.

5.2 RANDOM NOISE INVERSIONS

This subsection mostly focuses on the RN inversions, comparing combinations with DoLP (D0P+L and D1P+L) with those without it (D0+L and D1+L) for three aerosol scenarios (first column in Table 5.1). A perturbation with a Gaussian distribution is added to the simulated data[54] in the RN condition. The perturbation

[54] The simulated data are the references in the results.

values were selected according to previous studies: 0.005 for AOD [51,183,291], 0.05 for radiances [274,276], 0.01 for DoLP [64,68,69], 0.2 for 355 nm, 0.15 for 532 nm, and 0.1 for 1064 nm [51,276]. Each aerosol scenario is analyzed using descriptive statistics calculated from the RN inversions: the average represents the best-estimated retrieval, and the standard deviation represents the uncertainty around the average.

Table 5.1. Standard deviations and best residuals from the inverted simulated data for each combination (Comb.) and scenario.

Scenario	Comb.	I_n	AOD	DoLP	RCS_n	Residual (%)
I (high AOD and dominant coarse mode)	D0	3%	0.01	-	20%	0.04520
	D0+L			-		0.00435
	D0P+L			0.01		0.00183
	D1+L			-		0.00593
	D1P+L			0.01		0.00080
II (low AOD and dominant coarse mode)	D0	5%	0.01	-	20%	0.05149
	D0+L			-		0.00753
	D0P+L			0.01		0.00055
	D1+L			-		0.00043
	D1P+L			0.01		0.00055
III (high AOD and dominant fine mode)	D0	3%	0.01	-	25%	0.02581
	D0+L			-		0.00213
	D0P+L			0.05		0.00111
	D1+L			-		0.00148
	D1P+L			0.05		0.00121

Scenario I. This is characterized by a dominant coarse mode regime with AOD(440 nm) = 0.64 and AE(440-870 nm) = 0.29. Figures 5.1-5.3 show the microphysical and optical properties retrieved by the GRASP algorithm, as well as the comparison with the reference (simulated data), and the NF-RN inversions for D0, D0+L, D0P+L, D1+L, and D1P+L combinations. As in the figures, all the NF inversions have the best fits, compared with the reference, when the DoLP is added (D0P+L and D1P+L combinations) in the retrievals. The residuals in Table 5.1 also confirm the best fits.

Figure 5.1 displays SD, RRI, and IRI retrieved by NF and RN inversions. The photometer-only combination (D0) is presented in all cases because it is the basic inversion of the AERONET network that only uses direct and diffuse radiances and AOD to derive the microphysical and optical properties of the aerosols [64,273]. It is

important to emphasize that the D0 inversions compared to the ones from other combinations show some differences due to D0 being inverted as a one-component aerosol, while other combinations were inverted with contributions from fine and coarse particles, i.e., bi-component aerosol, as discussed in Ref. [51]. Their approach also provides two independent vertical profiles of aerosol concentrations (AVP).

The uncertainty in the inverted values for the coarse mode of the SD (first column of Figure 5.1) shows an increase of 2% and 3% when DoLP is included in the synergy (D0+L/D0P+L and D1+L/D1P+L comparisons[55], respectively), followed by a slight decrease in the underestimation of the reference (correlation coefficient values vary from 0.9794 to 0.9803 for D0+L and D0P+L and from 0.9790 to 0.9865 for D1+L and D1P+L). This change was not found in Ref. [69], as lidar channels were absent from their research. Nevertheless, the average of RN inversions overestimates the fine mode as compared with the reference and shift the peak of this mode to radius 0.066 μm in all the combinations, which could be attributed to (i) the lidar contributions at the shorter edge of the SD and (ii) the GRASP algorithm adjusting the dominant mode better in the retrieved properties [51]. The shifted peak is also observed in the next scenario. The overestimations of the fine mode are expected due to the low AOD in this mode, which decreases to values under 0.05 at longer wavelengths as the GRASP algorithm tends to fit better with the dominant mode [51].

[55] The D1+L/D1P+L comparison means the retrievals of the D1+L combination are being compared with those from the D1P+L combination. This explanation is extended for the other combinations.

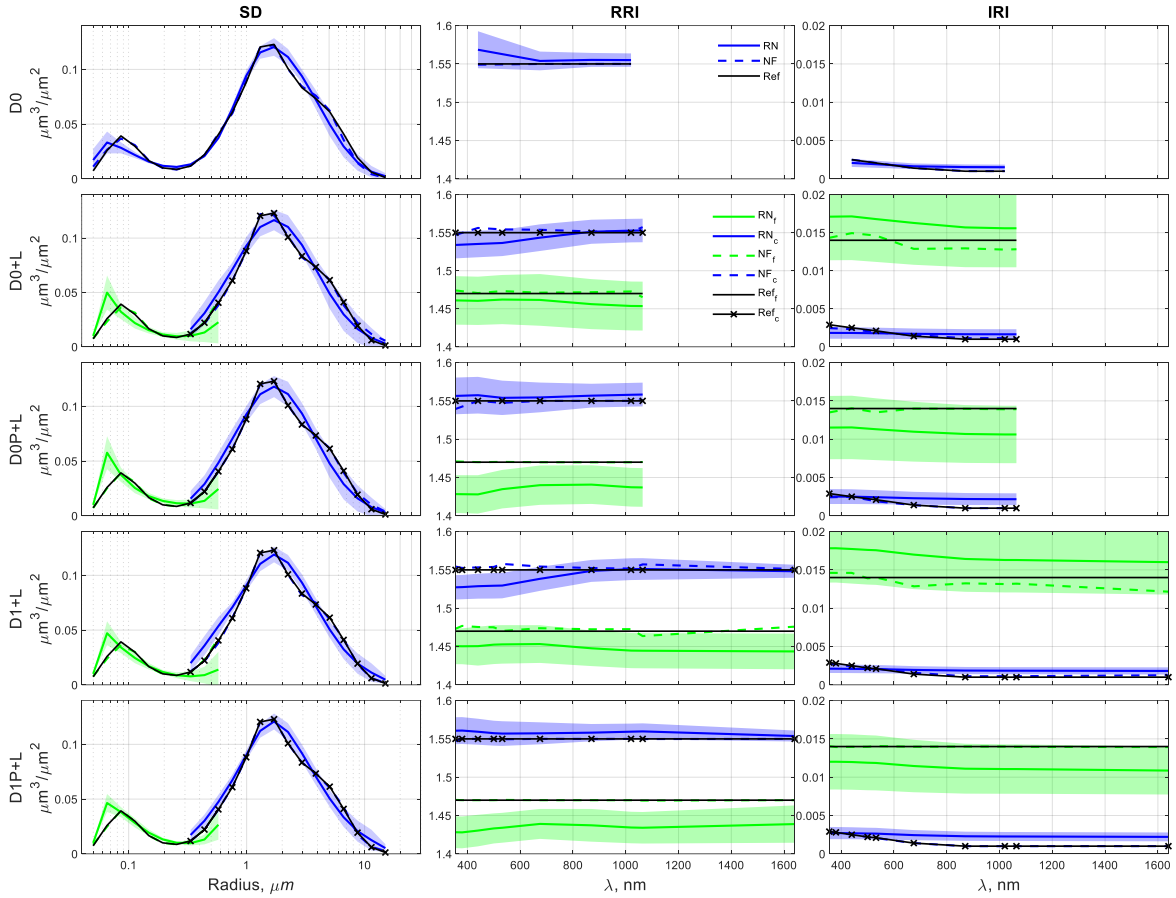

Figure 5.1. Microphysical properties of the aerosols retrieved from the simulated data. The columns from left to right refer to the SD, RRI, and IRI, while the rows from top to bottom refer to the combinations D0, D0+L, D0P+L, D1+L, and D1P+L. Green refers to the fine mode, and blue refers to the coarse mode (subscripts f and c, respectively) or one-component aerosol in the D0 case. Colorful solid lines are the averaged profiles of the RN retrievals, shaded areas are their standard deviations, dashed lines are the NF retrievals, and solid black lines are the reference (Ref). This is scenario I (high AOD, dominant coarse mode).

The GRASP algorithm improves the estimations of the coarse mode of the RRI at longer wavelengths while underestimating them at shorter wavelengths, as shown in the second column of Figure 5.1. For instance, the uncertainty values show a decrease of 21% at 870 nm, 26% at 1020 and 1064 nm, and 15% at 1640 nm for D1+L/D1P+L comparison. These RRI uncertainty reductions can be explained by the influence on the linear polarization of big particles, which is more noticeable at larger wavelengths for a dominant coarse-mode aerosol. The improvements with DoLP in the estimation of the coarse mode of the RRI at shorter wavelengths were also observed by Ref. [69]. Furthermore, the uncertainties in the fine mode of the

RRI estimation decrease when D0P+L, D1+L, and D1P+L combinations are inverted, achieving a reduction of 24% for D0+L/D0P+L comparison and 23% for D1P+L/D1+L comparison.

The third column of Figure 5.1 shows the IRI, in which the coarse mode of the reference is slightly overestimated with an increase in uncertainties at longer wavelengths, followed by a better adjustment at shorter wavelengths when DoLP is an input to the GRASP algorithm. Ref. [68] attributed the small change in the coarse-mode estimation to the low DoLP contribution from non-spherical particles. Although the estimation of the fine mode of the IRI has uncertainty reductions of 29% (D0+L/D0P+L comparison) and 26% (D1+L/D1P+L comparison), the under- and overestimation of the references remain in the retrievals when DoLP is included in the data.

The first column of Figure 5.2 displays the AOD spectrum derived with and without DoLP. The fine and coarse modes of the AOD have small changes when the linear polarization is considered in synergy, improving the estimation of both modes, especially for the D1+L/D1P+L comparison. Ref. [69] also found a small change in the AOD for inversions with DoLP. The second column of Figure 5.2 displays the spectral SSA. Higher accuracies are achieved in the retrievals with DoLP for the fine mode of the SSA (73% and 83% of error reductions for D0+L/D0P+L and D1+L/D1P+L comparisons, respectively, in Table 5.2). However, the coarse mode of the SSA only has improvements at shorter wavelengths, decreasing the underestimation of the reference. The fine mode has uncertainties reduced up to 26% (D0+L/D0P+L comparison) and 56% (D1+L/D1P+L comparison) at visible and infrared channels.

The last column of Figure 5.2 presents the LR as part of GRASP-output comparisons with and without DoLP. The addition of DoLP improves the accuracy in the retrievals, especially for the D1+L/D1P+L comparison for both modes (40% and 13% of error reductions for fine and coarse mode, respectively, in Table 5.2), but the average of the RN inversions slightly overestimates the reference of the LR for the

coarse mode. This overestimation is also present in the D1+L combination (without DoLP).

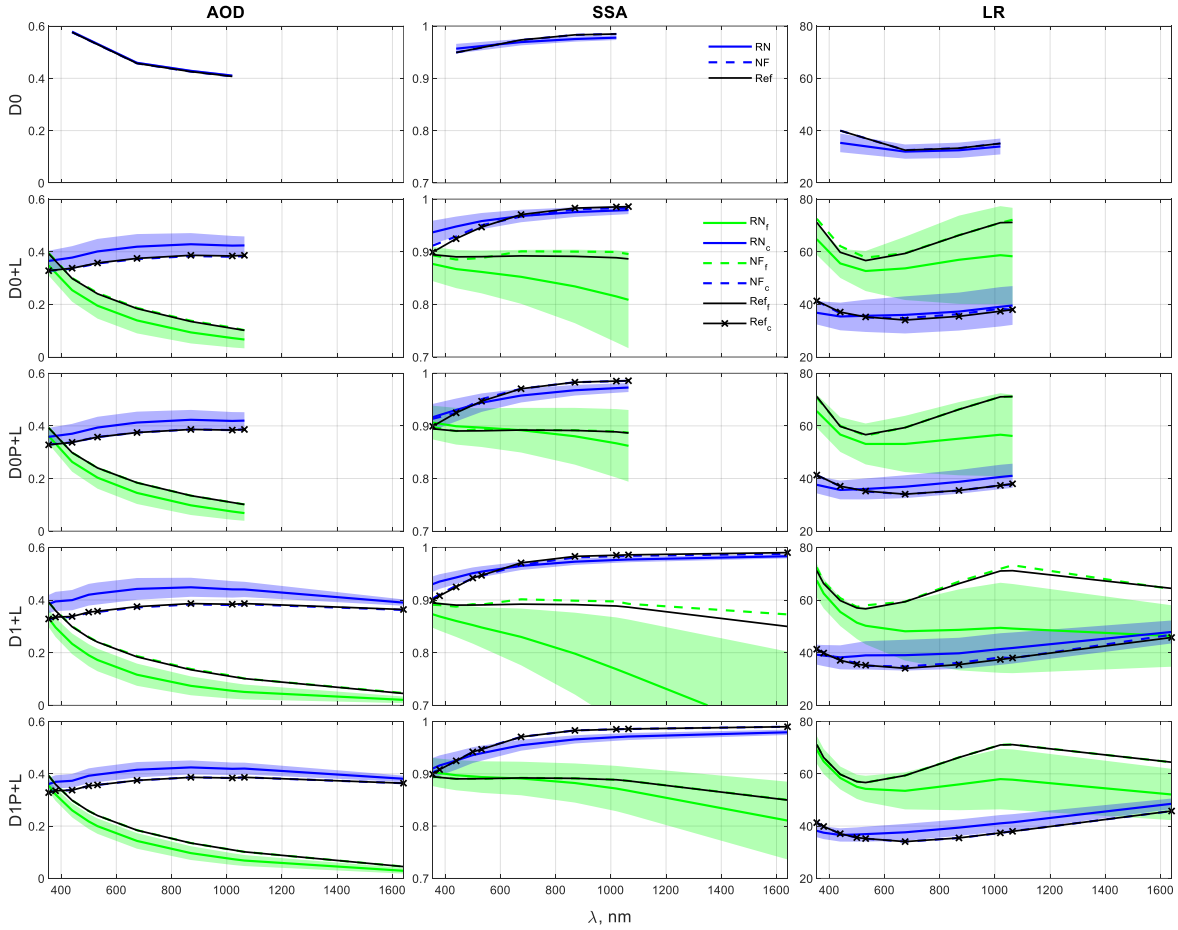

Figure 5.2. Optical properties of the aerosols retrieved from the simulated data. The columns from left to right refer to the AOD, SSA, and LR, while the rows from top to bottom refer to the combinations D0, D0+L, D0P+L, D1+L, and D1P+L. Green refers to the fine mode, and blue refers to the coarse mode (subscripts f and c, respectively) or one-component aerosol in the D0 case. Colorful solid lines are the averaged profiles of the RN retrievals, shaded areas are their standard deviations, dashed lines are the NF retrievals, and solid black lines are the reference (Ref). This is scenario I (high AOD, dominant coarse mode).

The maximum reductions in the uncertainties are 38% and 54% at longer wavelengths for D0+L/D0P+L and D1+L/D1P+L comparisons, respectively, in the coarse mode. The fine mode of the LR also has evident changes in retrieval accuracy, for instance, the DoLP insertion decreases the uncertainties by ~16% at the wavelengths, D0+L/D0P+L comparison, and a maximum reduction of 36% at longer wavelengths for the D1+L/D1P+L comparison. A similar tendency was

observed in the previous aerosol properties. In general, the results of the optical properties from Scenario I agree well with Refs. [46,51,190], who observed adequate retrievals of aerosol optical parameters for cases with high optical thickness.

The fine and coarse modes of the VC were computed by multiplying the AVP by the VC (Table 3.2), and they are displayed in Figure 5.3. In the fine mode, the RN inversions with DoLP (D0P+L and D1P+L) slightly overestimate the reference (negative F_B values become positive ones) in the layer below 2 km, followed by a nonsignificant change on the corr.

The coarse mode of the VC does not have a significant change in corr as well; however, the DoLP seems to slightly decrease the underestimation of the reference (reduction in F_B value), D0+L/D0P+L comparison. The slight overestimation of the fine mode and the underestimation of the coarse mode were pointed out by Ref. [51] for retrievals without DoLP, making the VC estimations expected. The small contribution of the DoLP in the concentration profiles can be related to the small differences between the aerosol loads for each combination (first column of Figure 5.2), in which the aerosol load is taken into consideration when estimating the AVP according to Equation (16a) in Ref. [64] and Equation (8) in Ref. [51].

In contrast with previous literature [69], who did not observe any advantages for adding DoLP in their retrievals of SD, IRI, and SSA, this study shows advantages in the retrieval of the dominant coarse-mode aerosol for those aerosol properties, plus SF, RRI, and LR. Nevertheless, the DoLP has the smallest contribution to retrieving SD, AOD, and VC. The observed improvements can also be related to the contribution from the lidar system in the synergy between the polarized Sun-sky-lunar multispectral photometer and the UPC/EARLINET lidar system.

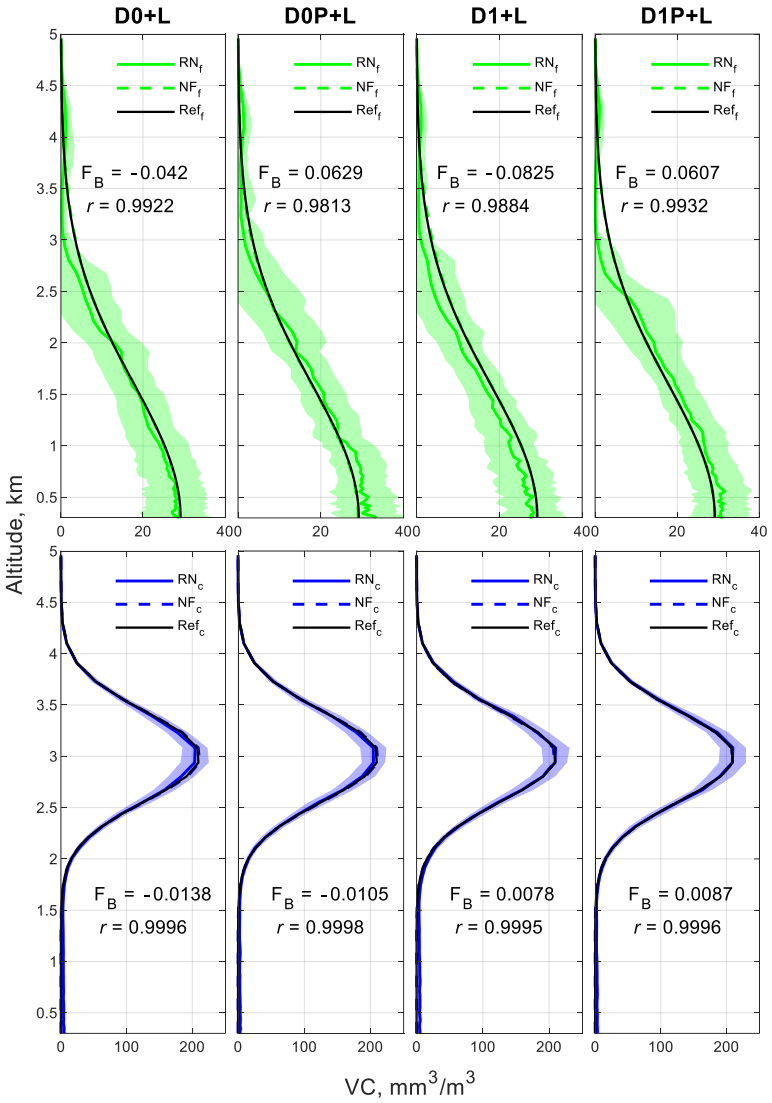

Figure 5.3. VC retrieved from the simulated data. The columns from left to right refer to the combinations D0+L, D0P+L, D1+L, and D1P+L. Green refers to the fine mode, and blue refers to the coarse mode (subscripts f and c, respectively). Colorful solid lines are the averaged profiles of the RN retrievals, shaded areas are their standard deviations, dashed lines are the NF retrievals, and solid black lines are the reference (Ref). This is scenario I (high AOD, dominant coarse mode).

Scenario II. The second aerosol scenario is a dominant coarse mode with low aerosol loading, AOD(440 nm) = 0.26, and AE(440-870 nm) = 0.43. Figure 5.4 shows the microphysical properties retrieved by NF and RN conditions for D0, D0+L, D0P+L, D1+L, and D1P+L combinations. The first column of Figure 5.4 shows the fine mode of the SD that overestimates the reference with a shifted peak, which was also observed in the previous aerosol scenario. The correlation between the average

of the RN inversions and the reference in the coarse mode of the SD slightly increases from 0.9939 to 0.9969 and from 0.9962 to 0.9971 (D0+L/D0P+L and D1+L/D1P+L comparisons, respectively). The increase in the correlation between D0+L and D0P+L is followed by an increase in the uncertainties (9%); however, the uncertainties are reduced by 53% when DoLP is added to the D1P+L combination.

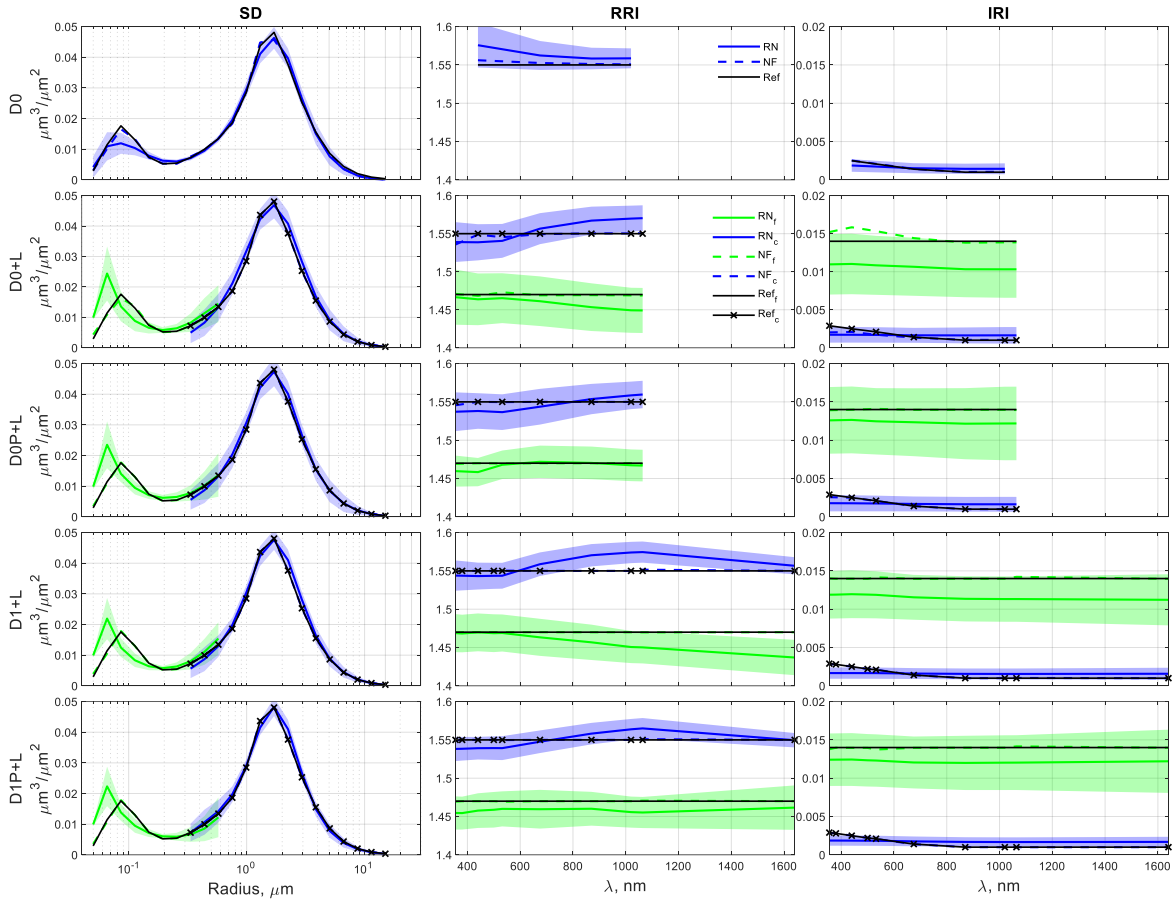

Figure 5.4. Idem as Figure 5.1 for Scenario II (low AOD, dominant coarse mode).

The RRI is depicted in the second column of Figure 5.4. The coarse mode decreases the overestimation of the reference at longer wavelengths, with a maximum uncertainty reduction of 16% at 1640 nm. At shorter wavelengths, where the underestimation of the reference continues when DoLP is added to the inversions, the uncertainties decrease up to ~20%. There is a decrease in the underestimation of the reference at longer wavelengths for the fine mode with DoLP, but maximum uncertainty reductions (46% and 13%) only occur at shorter wavelengths (D0P+L and D1P+L, respectively). On the one hand, in the third column

of Figure 5.4, the coarse mode of the IRI does not seem to have any improvements with DoLP. On the other hand, DoLP only decreases the underestimations of the reference in its fine mode.

Figure 5.5 presents AOD, SSA, and LR as retrievals with NF and RN conditions compared to the references. Both retrieved modes of AOD in the first column seem to adjust better to the reference with the DoLP (D0P+L and D1P+L combinations) in the GRASP inversions, mainly by reducing the RN uncertainties up to 8% in the fine mode and 7% in the coarse mode at longer wavelengths. Low sensitivity has also been observed in the AOD by Ref. [69].

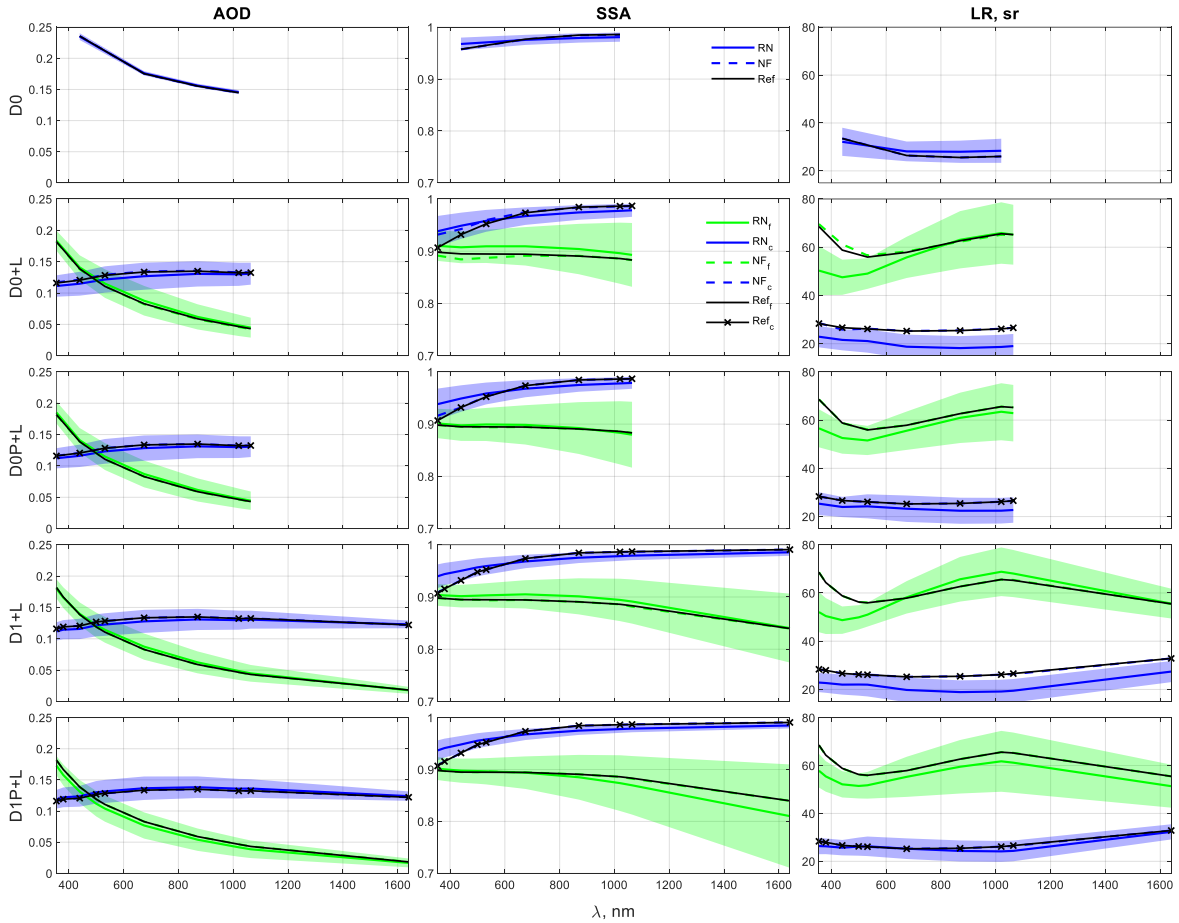

Figure 5.5. Idem as Figure 5.2 for Scenario II (low AOD, dominant coarse mode).

As in the previous aerosol scenario, SSA and LR have the most noticeable gains with DoLP in the GRASP retrievals. The coarse mode of the SSA reduces the RN uncertainties up to 10% (D0+L/D0P+L comparison) and 18% (D1+L/D1P+L

comparison) at longer wavelengths, but the average of the RN inversions remains underestimating the reference, as can be seen in the second column of Figure 5.5. The fine mode of the SSA reduces the uncertainties by 2.5% at shorter wavelengths, followed by a decrease in the overestimation of the reference when DoLP is inserted in the D0+L combination (error reductions of 77%, in Table 5.2).

The LR comparisons are shown in the third column of Figure 5.5. In the fine mode, there is a decrease in the underestimation of the reference at shorter wavelengths, which is observed in D0P+L and D1P+L with maximum uncertainty reductions of 22% and 16% at 355 nm, respectively. However, there are no changes at longer wavelengths when DoLP is considered in the inversions. For the coarse mode, the underestimation of the reference decreases for D0P+L and D1P+L combinations (error reductions of 54% and 76%, respectively), with a maximum uncertainty reduction of 28% at 1640 nm.

The simulated VC and its NF and RN inversions are plotted in Figure 5.6. The underestimation of the reference remains with DoLP (D0P+L and D1P+L combinations) in the fine mode, that is, no significant change in F_B and corr values. The use of DoLP seems to be sensitive to the mixing region between 2 and 3 km, overestimating the reference in this region. The coarse mode of the VC decreases the overestimation of the reference (reduction in the F_B value) for D1+L/D1P+L comparison. Finally, DoLP seems not to have made any important contributions to the RN inversions for both modes.

Scenario III. This scenario is described as a dominant fine mode with high aerosol loading, AOD(440 nm) = 0.33, and AE(440-870 nm) = 1.16, with a small contribution of coarse particles. The SD in the first column of Figure 5.7 does not show any changes with DoLP to the inversions. However, there is an accurate retrieval at the edges of the modes when lidar channels and more photometer channels are added to the synergy (comparison among D0, D0+L, and D1+L). The shift in the edge is expected at higher radii due to the use of lidar signals in the inversions, providing additional information at scattering angles of 180° [51,276,314].

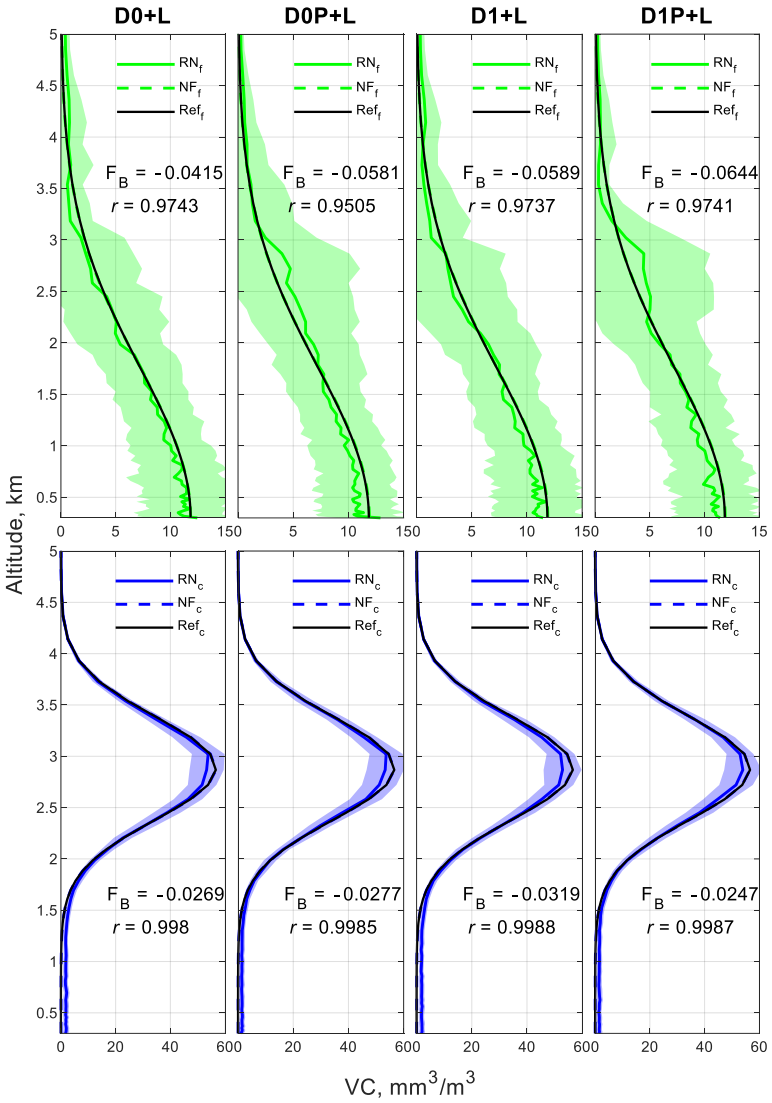

Figure 5.6. Idem as Figure 5.3 for Scenario II (low AOD, dominant coarse mode).

The RRI is shown in the second column of Figure 5.7. The reference is slightly overestimated in the fine mode with DoLP information in the retrievals (D0P+L and D1P+L combinations), followed by uncertainty reductions up to 30% (D0+L/D0P+L comparison) and 23% (D1+L/D1P+L comparison) at shorter wavelengths. The averages of the RN inversions slightly reduce the overestimation of the reference in the coarse mode for the D0P+L and D1P+L combinations, but the uncertainty reductions are observed only in the D1P+L combination, with maximum reduction at longer wavelengths (e.g., 36% at 1640 nm).

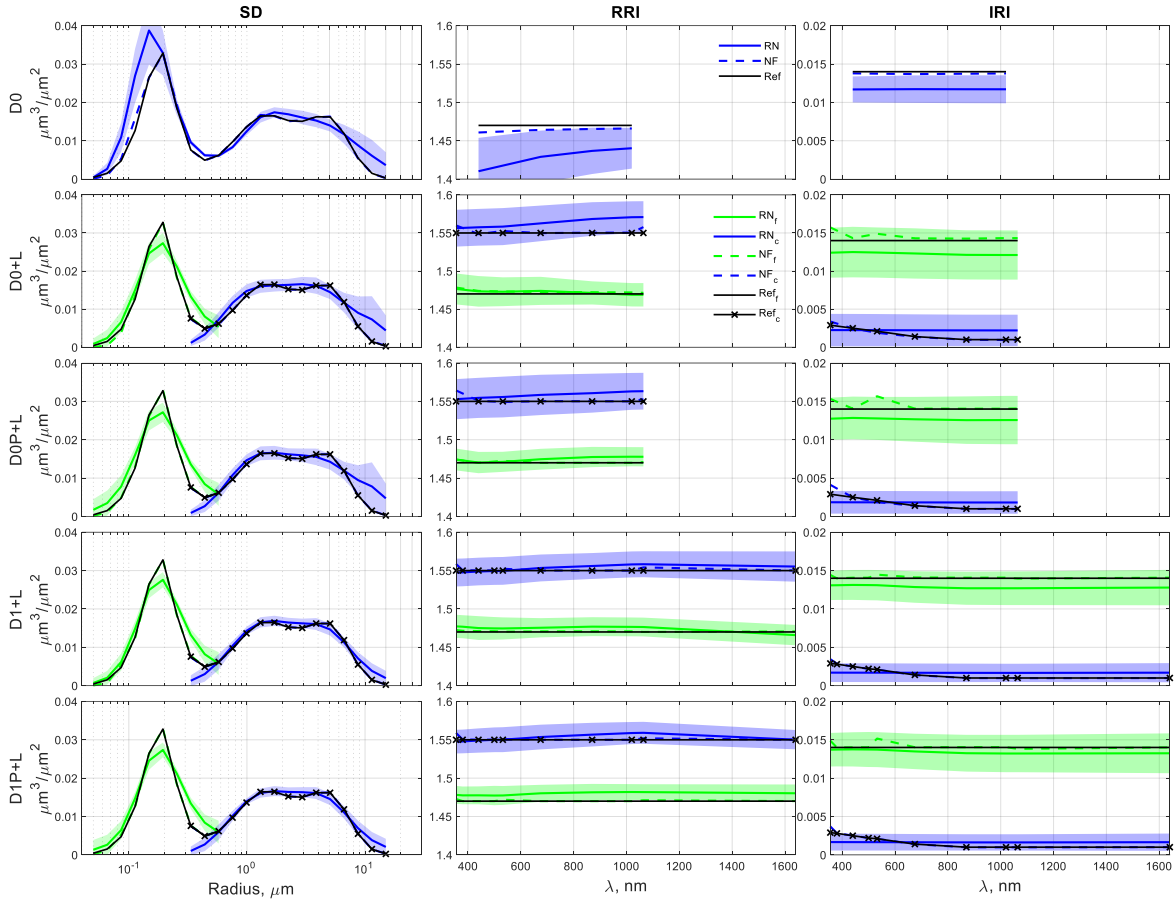

Figure 5.7. Idem as Figure 5.1 for Scenario III (high AOD, dominant fine mode).

The IRI in the third column of Figure 5.7 shows a decrease in the fine-mode underestimation of the reference for D0P+L and D1P+L combinations, followed by an uncertainty reduction of 16% at shorter wavelengths for D0P+L. The coarse mode of the IRI has uncertainty reductions of ~30% and ~10% at all wavelengths for the D0P+L and D1P+L combinations, respectively. The minor sensitivity to the addition of DoLP is consistent with the study of Ref. [69] for IRI in a dominant fine-mode aerosol. The results of the refractive indexes for this aerosol scenario agree with Ref. [68], who explained that polarization is more sensitive to RRI than IRI for particles with AE > 0.5.

Figure 5.8 shows the optical properties retrieved by the GRASP algorithm with and without DoLP. The retrieved AOD has no significant change when DoLP is inserted in the inversions for this aerosol scenario. The fine mode of the SSA has a maximum uncertainty reduction of 15% at shorter wavelengths (D0+L/D0P+L

comparison), and there is a slight decrease in the overestimation of the reference at shorter wavelengths for D0P+L and D1P+L combinations. In the coarse mode of the SSA, the DoLP also slightly decreases the underestimations of the reference, with a reduction in uncertainties of ~20% in all wavelengths (D0+L/D0P+L comparison), and the maximum reduction of 6% is observed for the D1P+L combination at longer wavelengths.

Figure 5.8 also presents LR in the third column, where the averaged fine mode slightly decreases the underestimation of the reference at shorter wavelengths when DoLP is added to the inversions. The uncertainty reduction for the D0P+L combination reaches a maximum of 18% at shorter wavelengths in this mode. The DoLP slightly decreases the underestimation of the reference for D0P+L and D1P+L combinations for the coarse mode of the LR, showing an uncertainty reduction up to 16% at 1640 nm for the D1P+L combination.

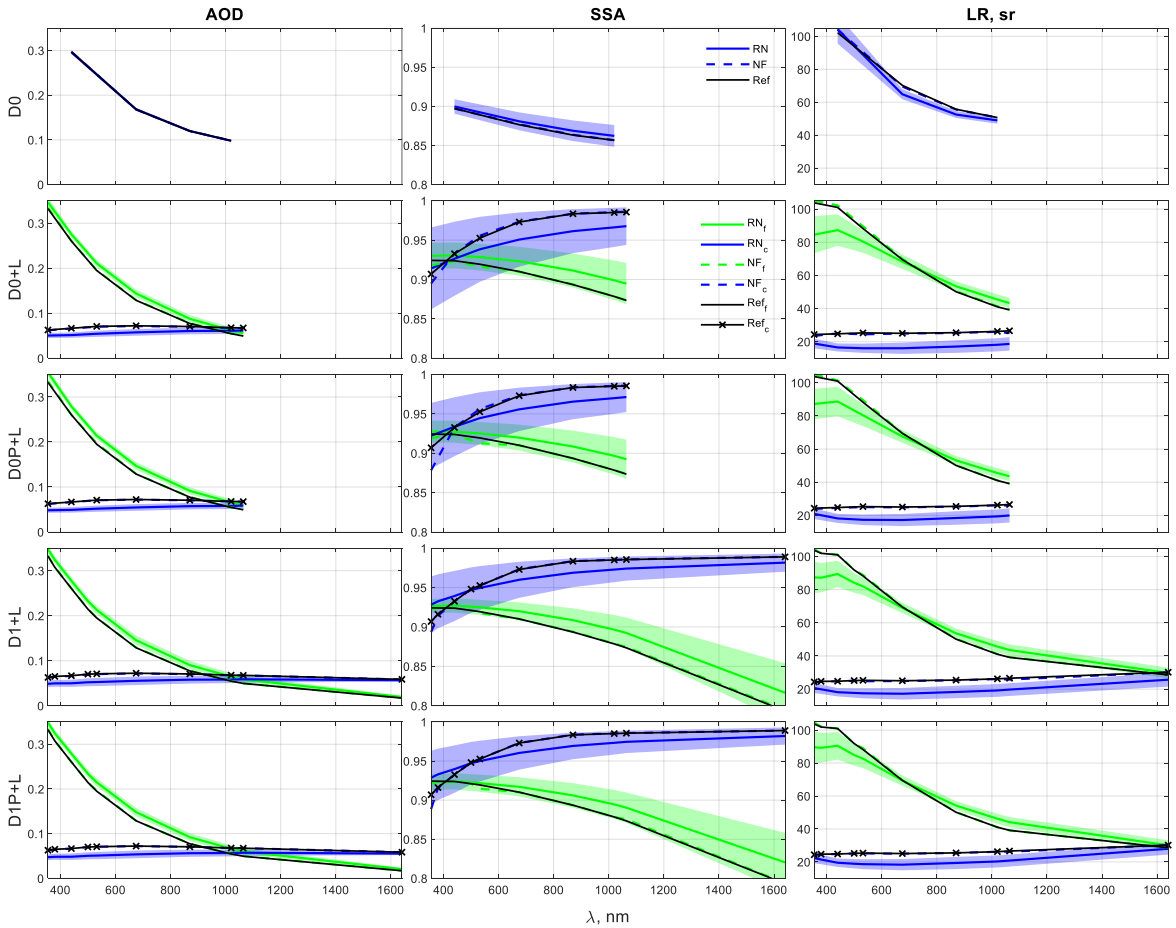

Figure 5.8. Idem as Figure 5.2 for Scenario III (high AOD, dominant fine mode).

The fine and coarse modes of the VC are shown in Figure 5.9. In the main layer of the fine mode (below 1 km), the DoLP addition to GRASP inversions slightly decreases the underestimation of the reference (reductions in the F_B value for D0P+L), followed by a small increase in the correlation (corr) between the averages of the RN inversions and the reference for D0P+L and D1P+L combinations. In the coarse mode of the VC, the DoLP also slightly decreases the underestimation of the reference, but it seems not to have any changes for the D1+L/D1P+L comparison. In general, the DoLP has minor improvements on the VC estimations for both modes in all aerosol scenarios.

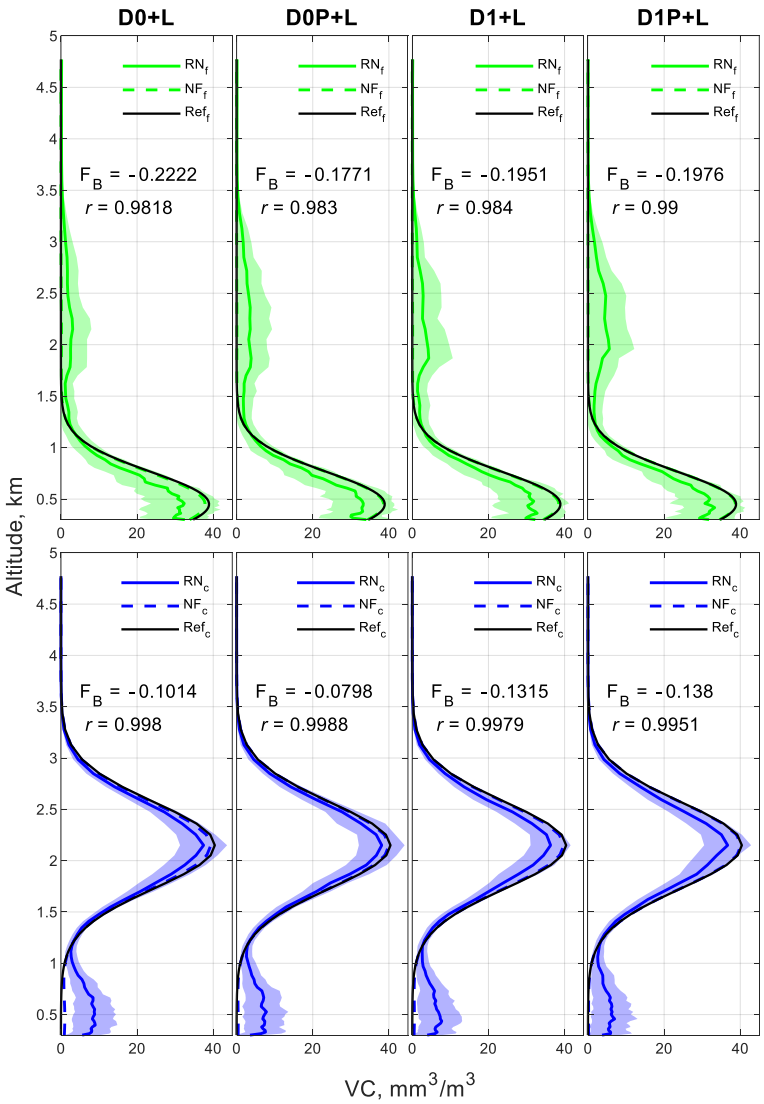

Figure 5.9. Idem as Figure 5.3 for Scenario III (high AOD, dominant fine mode).

5.3 ERROR ESTIMATION AND SF

The RMSE (Subsection 4.2.5) was calculated to assess the discrepancy between the averages of the RN inversions and the reference by the predicted errors. Furthermore, the last aerosol property of this research (SF) is also discussed. Both are shown in Table 5.2 below.

Table 5.2. RMSE calculated for fine (f) and coarse (c) modes of SD, RRI, IRI, AOD, SSA, LR, and SF with its standard deviation (std). They were retrieved from each combination (Comb.) and aerosol scenario (Sc.). Green highlights the RMSE reductions when DoLP is added in the synergy (D0P+L/D0+L and D1P+L/D1+L comparisons), and orange highlights the RMSE reductions for the D1+L/D0+L comparison.

Sc.	Comb.	SD		RRI		IRI		AOD		SSA		LR		SF *	
		f	c	f	c	f	c	f	c	f	c	f	c	Mean (std)	Total
I	D0+L	0.011	0.008	0.012	0.010	0.0024	0.0007	0.042	0.041	0.051	0.018	8.55	2.26	0.035 (0.055)	0.023
	D0P+L	0.012	0.008	0.035	0.007	0.0030	0.0009	0.035	0.035	0.014	0.012	9.61	2.80	0.010 (0.022)	0.001
	D1+L	0.012	0.009	0.021	0.016	0.0031	0.0007	0.060	0.059	0.096	0.016	13.54	3.28	0.024 (0.042)	0.013
	D1P+L	0.009	0.007	0.037	0.009	0.0025	0.0009	0.036	0.035	0.016	0.012	8.13	2.85	0.004 (0.010)	0.008
II	D0+L	0.005	0.002	0.014	0.015	0.0034	0.0007	0.003	0.005	0.013	0.015	8.55	6.42	0.360 (0.093)	0.164
	D0P+L	0.005	0.001	0.006	0.010	0.0016	0.0007	0.003	0.004	0.003	0.015	5.60	2.96	0.285 (0.068)	0.089
	D1+L	0.005	0.002	0.015	0.014	0.0024	0.0007	0.003	0.004	0.008	0.016	8.12	5.62	0.319 (0.076)	0.123
	D1P+L	0.005	0.001	0.013	0.011	0.0018	0.0007	0.007	0.003	0.011	0.015	5.85	1.34	0.232 (0.036)	0.036
III	D0+L	0.003	0.003	0.003	0.015	0.0017	0.0009	0.013	0.012	0.015	0.017	9.75	8.12	0.470 (0.176)	0.183
	D0P+L	0.003	0.003	0.006	0.009	0.0013	0.0007	0.017	0.015	0.012	0.014	8.77	6.75	0.400 (0.106)	0.113
	D1+L	0.003	0.002	0.006	0.005	0.0011	0.0008	0.014	0.014	0.013	0.012	8.78	6.53	0.427 (0.104)	0.140
	D1P+L	0.003	0.002	0.010	0.005	0.0006	0.0008	0.016	0.016	0.012	0.012	7.86	5.33	0.366 (0.083)	0.079

* The RMSE of the SF is calculated for one mode (total).

The RMSE reductions with DoLP are highlighted in green, and those reductions due to the new photometer channels (D1+L) are highlighted in orange in Table 5.2 to be compared with D0+L values. The 3rd and 4th columns in Table 5.2 show the RMSE of the SD. The averages of the RN inversions fit the reference better, hence, decrease the RMSE values only when DoLP is added to the D1+L combination for both SD modes in Scenario I (RMSE reductions of 25% and 22% for fine and coarse modes, respectively) and for coarse mode in Scenario II (RMSE reductions of 50% for D0P+L and D1P+L combinations).

Regarding the refractive indexes, the RRI is located in the 5th and 6th columns in Table 5.2. the DoLP reduces the RMSE in the coarse mode in Scenario I (30% and 44% for D0P+L and D1P+L, respectively), both modes of Scenario II (57% and13% in the fine mode of D0P+L and D1P+L, respectively, and 33% and 21% in

the coarse mode of D0P+L and D1P+L, respectively), and the coarse mode of Scenario III (40% in D0P+L). The IRI is shown in the 7th and 8th columns in Table 5.2. The reductions in RMSE values are observed in the fine modes of all scenarios, except for D0P+L in Scenario I, with the largest one for the fine mode of the IRI in Scenario II (53% for D0+L/D0P+L comparison). However, the only enhancement with DoLP in the coarse mode of the IRI is observed in Scenario III for D0P+L (22%).

The accuracy in the AOD retrievals with DoLP (9th and 10th columns in Table 5.2) is more pronounced in Scenario I for both aerosol modes (maximum reductions of 40% and 41% in the fine and coarse modes of D1P+L, respectively), in which the aerosol loading is almost 0.40. This agrees with Ref. [276], who noticed that the effect of AOD errors decreases with higher AOD. In opposition to Scenario I, Scenario II, low aerosol loading, has the smallest RMSE reductions for its coarse mode (20% and 25% for D0P+L and D1P+L, respectively).

The SSA and LR (from 11th to 14th columns in Table 5.2) are the most positively affected properties when DoLP is added in the GRASP retrievals because they are directly related to the scattered light and optical thickness. The higher RMSE reductions are in Scenario I (73% and 83% for the fine mode of D0P+L and D1P+L, respectively), followed by Scenario II (77% in the fine mode of D0P+L) and Scenario III, with an error reduction of 20% in the fine mode of D0P+L. The highest RMSE reductions of the LR are observed in Scenario I for the fine mode of D1P+L (40%), in the coarse mode of Scenario II with 54% and 76% (D0P+L and D1P+L, respectively), and in the coarse mode of Scenario III for the D1P+L combination (18%). The results of Scenarios I and III follow those found by Ref. [51], who pointed out that the LR errors for the non-dominant mode showed reductions when the photometer and lidar are put together.

The SF retrievals (16th column in Table 5.2) show significant reductions in the percentage of non-spherical particles of 71% (D0+L/D0P+L comparison) and 83% (D1+L/D1P+L comparison) for Scenario I, 21% (D0+L/D0P+L comparison) and 27% (D1+L/D1P+L comparison) for Scenario II, and 15% (D0+L/D0P+L comparison) and 14% (D1+L/D1P+L comparison) for Scenario III. In other words, the linear

polarization of scattered light is less sensitive to spherical particles in all dominant modes. The small reduction in the average of the SF with DoLP can be related to the coarse particle contribution in Scenario III. The advantage of adding polarized information to retrieve SF agrees with the study of Ref. [69], who observed that the non-sphericity is reproduced more correctly by inversion with DoLP for the dominant coarse mode.

More photometer channels (380, 500, and 1640 nm) with three-wavelength elastic lidar (D1+L) seem to supplement the information for retrieving some aerosol properties and reduce the RMSE for all aerosol scenarios. For instance, the coarse mode of the SSA (11%) and SF (43%) in Scenario I; the coarse mode of the RRI (7%), the fine mode of the IRI (29%), the coarse mode of the AOD (20%), the fine mode of the SSA (38%), both LR modes (5% and 12% in fine and coarse modes, respectively), and SF (25%) in Scenario II; and the coarse mode of the SD (33%), the coarse mode of the RRI (67%), both IRI modes (35% and 11% in fine and coarse modes, respectively), both SSA modes (13% and 29% in fine and coarse modes, respectively), both LR modes (10% and 20% in fine and coarse modes, respectively), and SF (23%) in Scenario III. The RMSE results reinforce the improvements with DoLP in the GRASP retrievals.

5.4 CASE STUDY OF THE NF RETRIEVALS USING LIDAR VOLUME DEPOLARIZATION RATIO AND SUN-PHOTOMETER DOLP IN THE GRASP ALGORITHM

This subsection adapts a case study that focuses on the description of the NF inversions as one of the GRASP sensitivity tests to verify the stability of the code for retrieving aerosol properties from the simulated data: three elastic and two depolarization channels from the UPC/EARLINET lidar system, and seven polarized Sun-photometer channels. This case study was presented at the 31st International Lidar Conference in 2024.

The case study is characterized by high aerosol loading, AOD(440 nm) = 0.36, and AE(440-870 nm) = 1.51 for a dust-urban scenario in Barcelona. The combinations inverted in the GRASP code are detailed in the 1st column of Table

5.3. The δ^v was measured at two wavelengths (355 and 532 nm), and its standard deviation (weight) was set at 20% (7th column in Table 5.3). The other weights were set according to Table 5.1 for NF inversions.

Table 5.3. Standard deviations for the input observations and the best residuals (Resid.) of the inverted simulated data for each combination.

Comb.	Input Data	I_n	AOD	DoLP	RCS_n	δ^v	Resid.
D0	[AOD + I_n] (4λ)			-	-	-	0.06%
D0+L	[AOD + I_n] (4λ) + RCS_n (3λ)			-	20%	-	0.10%
D1+L+δ^v	[AOD + I_n] (7λ) + RCS_n (3λ) + δ^v(2λ)	3%	0.01	-	20%	20%	0.09%
D1P+L+δ^v	[AOD + I_n + DoLP] (7λ) + RCS_n (3λ) + δ^v(2λ)			0.01	20%	20%	0.05%

Figures 5.10-5.15 show the comparisons between the reference (simulated data) and the NF inversions from the combinations in Table 5.3. The δ^v addition in the synergy seems not to improve the SD (Figure 5.10), mainly in the fine mode, where the reference is overestimated by D1+L+δ^v and underestimated by D1P+L+δ^v, while the coarse mode is overestimated at the largest radius by both combinations.

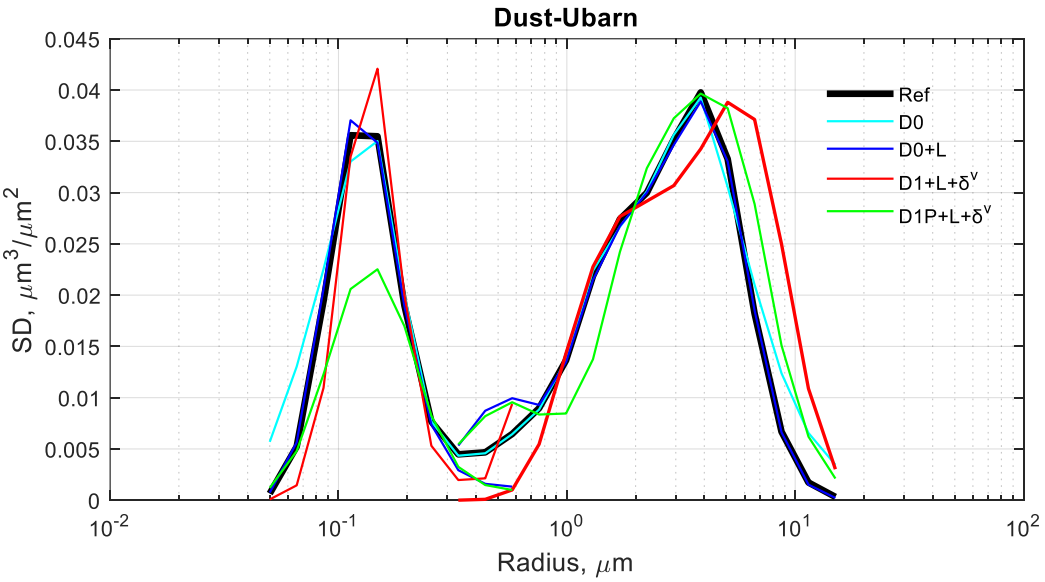

Figure 5.10. SD inverted from the combinations in Table 5.3. The solid black line is the reference (Ref).

The D0+L combination (Figure 5.10) has the best agreement with the simulated data compared with the other combinations, proving that the insertion of lidar signals to retrieve aerosol properties in the GRASP algorithm contributes essential information for the inversions.

The reference of the refractive indexes (RRI and IRI in Figure 5.11) is overestimated by all combinations. These estimations were also found in the previous results (Subsection 5.2) for dominant coarse modes.

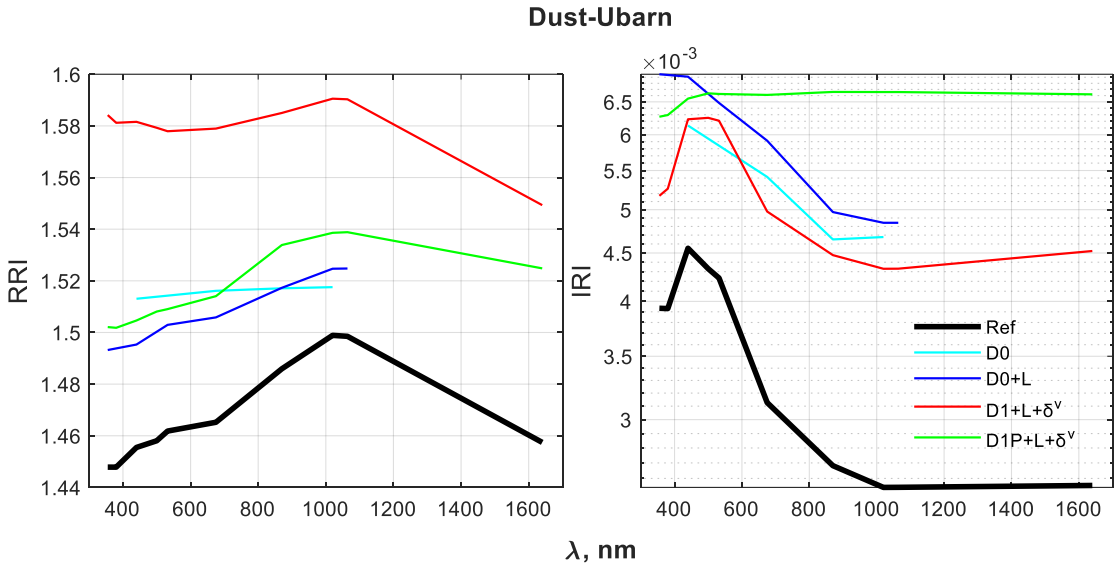

Figure 5.11. Refractive indices inverted from the combinations in Table 5.3. The solid black lines are the reference (Ref).

The AOD (Figure 5.12) retrieved from all combinations agrees well with the reference. However, it is slightly underestimated by D0, D0+L, and D1+L+δ^v combinations at the shortest wavelengths. In Figure 5.13, the simulated SSA is underestimated by all combinations where the photometer channels are run together with lidar signals (with and without δ^v). The previous results (Subsection 5.2) also pointed out the SSA underestimations in both aerosol modes.

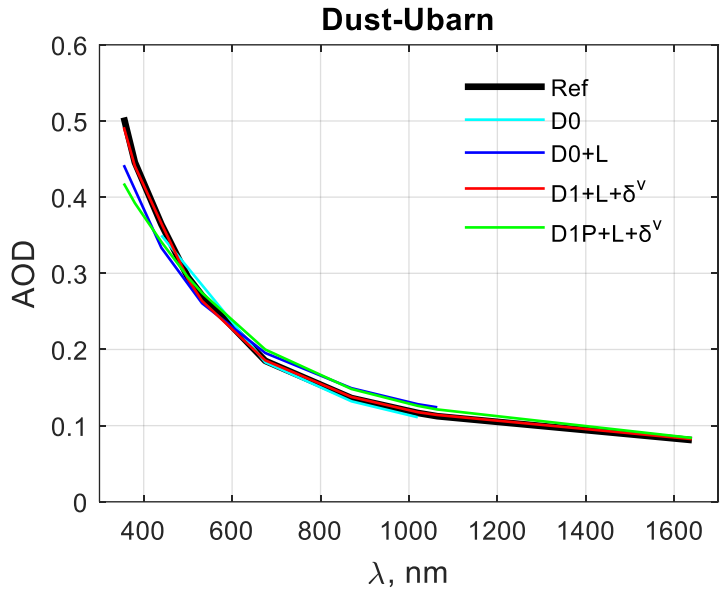

Figure 5.12. AOD inverted from the combinations in Table 5.3. The solid black line is the reference (Ref).

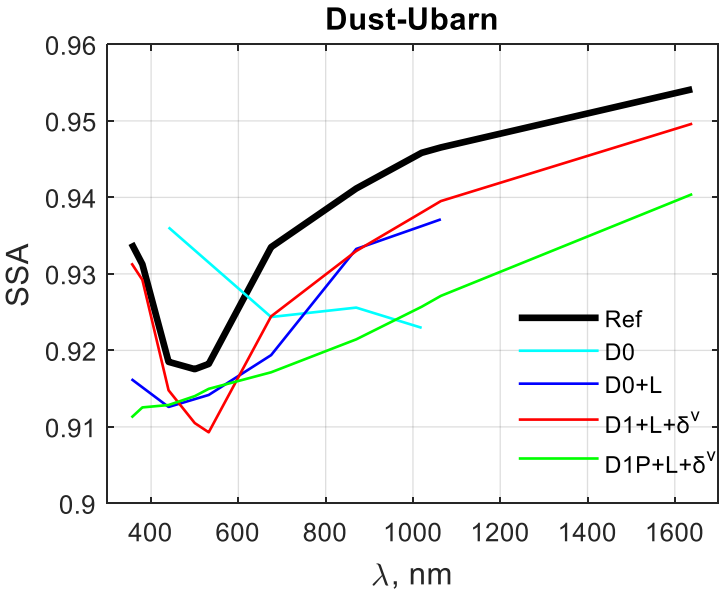

Figure 5.13. SSA inverted from the combinations in Table 5.3. The solid black line is the reference (Ref).

All combinations overestimate the simulated LR (Figure 5.14), but the D1+L+δ^v is the closest combination to the reference. The LR overestimations, mainly for the coarse mode, were also found in the previous results (Subsection 5.2).

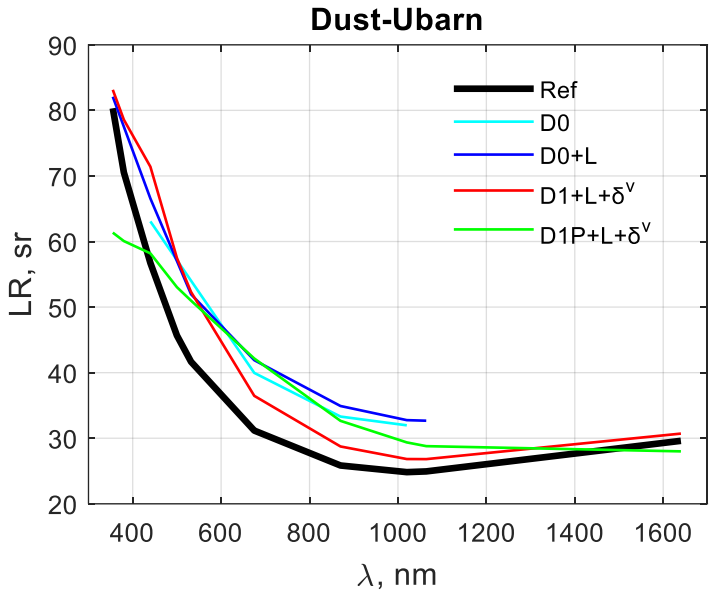

Figure 5.14. LR inverted from the combinations in Table 5.3. The solid black line is the reference (Ref).

Figure 5.15 shows the AVP and α from D0+L, D1+L+δ^v, and D1P+L+δ^v combinations, where the NF profiles are compared with their respective references. The initial guesses of the AVP in black lines are also plotted in Figure 5.15 to compare the shapes when the δ^v is introduced in D1+L+δ^v and D1P+L+δ^v. As shown in the 2nd and 3rd columns of Figure 5.15, the δ^v plays an important role in the shapes of the vertical distribution of the reference and AVPs of the NF, which is in opposition to the D0+L combination that keeps the shape of the initial guess profiles (IG). In the same figure, the α profiles are calculated according to Equation 3.23.

The α profiles from the NF retrievals agree very well with their respective reference profiles for D1+L+δ^v and D1P+L+δ^v combinations at the three fundamental wavelengths (355, 532, and 1064 nm). The simulated profiles are slightly overestimated at high heights and underestimated at low heights in the D0+L combination, probably owing to the constant LR as a function of the altitudes.

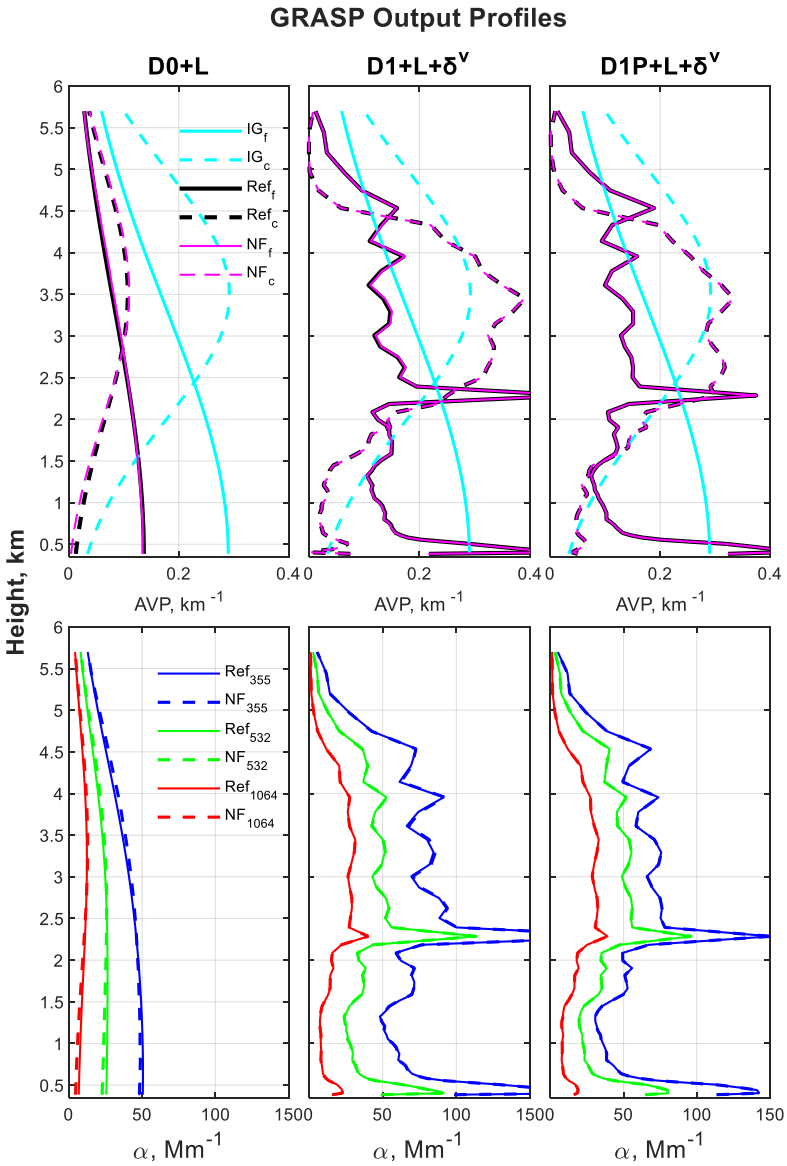

Figure 5.15. NF retrieval profiles of the AVP and α. IG is the initial guess used to build the simulated data (Ref) in the GRASP code for the fine (f) and coarse (c) modes.

5.5 CONCLUSIONS

This chapter evaluates the GRASP sensitivity to the DoLP addition as an input in aerosol retrievals from unique synergies with a polarized Sun-sky-lunar photometer and the UPC/EARLINET lidar system observations. Both noise-free and random-noise retrievals demonstrate that adding DoLP significantly improves the accuracy and stability of retrieved microphysical and optical properties of the

aerosols, particularly in scenarios dominated by coarse-mode particles (I and II). In the three distinct aerosol scenarios, DoLP consistently reduced uncertainties and the RMSE, especially for RRI, SSA, LR, and SF, with slight benefits for VC and SD in the fine-mode dominated case (Scenario III). Furthermore, the additional photometer channels combined with lidar data (D1+L combination) further enhanced the retrieval performance for the three aerosol scenarios, especially for optical properties.

The GRASP algorithm fitted the retrieved aerosol properties with linear polarization to the reference for the NF condition better than the retrievals without it. This is observed for all aerosol scenarios. Regarding the comparisons between the RN inversions (with and without DoLP) and the reference, some important conclusions are drawn and organized in sequence: i and ii are about each aerosol mode; iii and iv are attributed to conclusions of Scenario II and III, respectively; v is concerning the SD and VC properties; vi is about the SF; and vii is related to the contribution of the D1+L combination for the inversions. They are listed below:

i. GRASP retrievals with DoLP can significantly improve some microphysical and optical properties, even when the fine mode is the non-dominant (Scenarios I and II). For instance, maximum reductions are observed in the uncertainties: 29% (IRI from D0P+L in Scenario I), 8% (AOD from D0P+L in Scenario II), 56% (SSA from D1P+L in Scenario I), 36% (LR from D1P+L in Scenario I), 46% (RRI from D0P+L in Scenario II), and better adjustments of the average of RN inversions to the reference. Therefore, in coarse mode-dominated regimes, the DoLP inclusion in the GRASP inversions improves the retrieval of aerosol properties in the non-dominant, fine mode;
ii. The coarse mode of all scenarios presents gains with DoLP, mainly for D1P+L combination at longer wavelengths, which are expected because of the sensitivity of large particles to the polarized light when those particles are closer to their respective wavelengths (the same for small particles). The maximum reductions in the uncertainties are observed at 1020 and 1640 nm: 26% and 15% (RRI in Scenario I) respectively, 16% at 1640 nm (RRI in Scenario II), 28% at 1640 nm (LR in Scenario II), 36% at 1640 nm (RRI in

Scenario III), and 16% at 1640 nm (LR in Scenario III). Therefore, independently of the dominance or non-dominance of the coarse mode, the DoLP and 1640-channel inclusions in GRASP inversions improve the coarse mode of RRI and LR;

iii. The DoLP contributes to the accuracy of GRASP retrievals in Scenario II, dominant coarse mode with low aerosol loading, AOD(440 nm) = 0.26, decreasing the over-underestimations of the reference and reducing the uncertainties of the RN retrievals, with a maximum reduction of 46% (fine mode of the RRI), 20% (coarse mode of the RRI), 8% (fine mode of the AOD), 7% (coarse mode of the AOD), 3% (fine mode of the SSA), 18% (coarse mode of the SSA), 22% (fine mode of the LR), and 28% (coarse mode of the LR). These results showed an enhancement in the retrievals for low aerosol loading, in which better GRASP retrievals are expected for high aerosol loading [46,51,190,276];

iv. The use of DoLP in retrieving a dominant fine aerosol (Scenario III) shows an evident impact on the refractive indices. The uncertainties reduced up to 30% and 23% for RRI (D0P+L and D1P+L, respectively) and 16% for IRI (D0P+L) at shorter wavelengths. Furthermore, the coarse mode of the IRI has uncertainty reductions of 30% (D0P+L) and 10% (D1P+L), which is in opposition to the coarse mode of the IRI in Scenarios I and II (no enhancements), confirming that the linear polarization is more sensitive to RRI than IRI for small particles [68]. In addition to the improvements in Scenario III, the RN inversions fit well with the reference for the properties in the coarse mode. Once again, DoLP contributes to improving the estimations of the fine mode from GRASP inversions.

v. For all scenarios, the DoLP addition into the inversions has a minor contribution to the fine mode of the SD and the coarse mode of the VC.

vi. The SF accuracy is more notable for Scenarios I and II (dominant coarse aerosols), where the sensitivity of the non-spherical particles is more evident [69], decreasing the SF by 71% (D0P+L) and 83% (D1P+L) for Scenario I and 21% (D0P+L) and 27% (D1P+L) for Scenario II;

vii. The addition of more photometer channels in the synergy with three-wavelength elastic lidar (D1+L) shows good estimations, reducing the RMSE mostly in the fine mode of the RRI (29%) and coarse mode of the SSA (11%) in Scenario I, the coarse mode of the AOD (20%), fine mode of the SSA(38%) and coarse mode of the LR (12%) in Scenario II, the coarse mode of the SD (33%) and coarse mode of the RRI (67%), fine mode of the IRI (35%), coarse mode of the SSA (29%), and coarse mode of the LR (20%) in Scenario III, and the SF in Scenarios I, II, and III (43%, 25%, 23%, respectively). Therefore, the RMSE confirms the enhancements with the D1+L combination on GRASP retrievals, mainly for Scenarios II and III.

Lastly, the accuracy of the GRASP algorithm was also investigated by the RMSE calculations, using the average of RN inversions (with and without DoLP) and the reference for each aerosol property and their modes. The RMSE reductions agreed with the comparisons between the aerosol properties inversions and the reference, mainly for the optical parameters (SSA and LR) when DoLP is considered in the inversions.

Regarding the case study of a mixture aerosol (Dust-Urban), this study presented synergies between a new polarized Sun-photometer (7 channels), including the DoLP, and lidar signals (3 elastic channels), plus δ^v (2 channels): D1+L+δ^v and D1P+L+δ^v. The optical and microphysical properties of the simulated data were inverted for the NF conditions to verify the stability of the code when δ^v is added in the synergy. Furthermore, the reference was compared with the inversions from combinations of the standard one (D0, photometer only) to the most complex one (D1P+L+δ^v). The δ^v addition fitted the simulated data better than the other combinations without the δ^v for the optical properties; however, the microphysical properties, even with DoLP insertion, do not seem to improve. The NF inversions of the AVP and α profiles showed good fits to the simulated GRASP output profiles, which was expected, proving that the sensitivity of the GRASP code is stable for retrieving aerosol properties with δ^v and DoLP. Moreover, the δ^v insertion (D1+L+δ^v and D1P+L+δ^v) modulated the AVP shapes and their NF inversions.

6 AEROSOL RADIATIVE FORCING FROM GROUND-BASED SYNERGIES

*I dedicate these **second results** to my team: Michaël Sicard, Alejandro Rodríguez-Gómez, Adolfo Comerón, Constantino Muñoz-Porcar, Federico Dios, and Cristina Gil-Díaz.*

There is no Earth B!

This chapter focuses on aerosol forcing in Barcelona, Spain, using long-term and case-by-case approaches. The first approach applies the direct method between pyranometer and photometer observations to estimate the aerosol efficiency and forcing. The second compares the aerosol forcing from AERONET and GRASP inversions with that from the direct method. The results were published in Remote Sensing and adapted for this chapter.

The trends presented here correspond to the period study from 2009 to 2023, where AERONET and pyranometer observations (L2 and L1.5, respectively) are coincidental.

6.1 AOD TRENDS

Figure 6.1 depicts the AOD trends estimated by the MK test and the Sen's slope, for which the monthly means were calculated by the L2-V3 AERONET database <last access: June 6th, 2024>. The 2004-2023 period was decomposed into two trends to be compared: the black-trend line represents the whole L2-V3 AERONET period at Barcelona (2004-2023), and the red-trend line represents the study period (2009-2023).

The Sen's slopes for 2004-2023 and 2009-2023 trends computed with a CI95 from the MK test are also shown in Figure 6.1. The 2004-2023 trend (black line) has a Sen's slope of -0.0038 yr^{-1} with a change of -0.07 (312%) over the whole period (19 years). The 2009-2023 trend (red line) has a Sen's slope of -0.0015 yr^{-1} with a period change of -0.02 (11%) over 15 years. The downtrends are related to the air quality policies performed in Barcelona, hence, the drop in particulate matter (PM1, 2.5, and 10). However, an opposite relation was found between dust transportation and the annual AOD drop, given that dust frequency has increased through the years [315]. Therefore, the local aerosol sources have a dominant impact on the urban-environment AOD compared with dust events.

The first Barcelona's policy started in 2007 aiming to reduce the speed limit to 30 kmh^{-1} in 16 zones (Ajutament de Barcelona, last access: May 29th, 2025) followed by the Barcelona Urban Mobility Plans of 2006-2012 <last access: May 29th,

2025>, 2013-2018 <last access: May 29th, 2025>, and 2019-2024 <last access: May 29th, 2025> to reduce the environmental impacts and the contribution of mobility to climate change. Lastly, the Low Emission Zone policy was implemented in December 2020 <last access: May 29th, 2025> to protect areas where vehicles could not circulate without the environmental label from the General Directorate of Traffic.

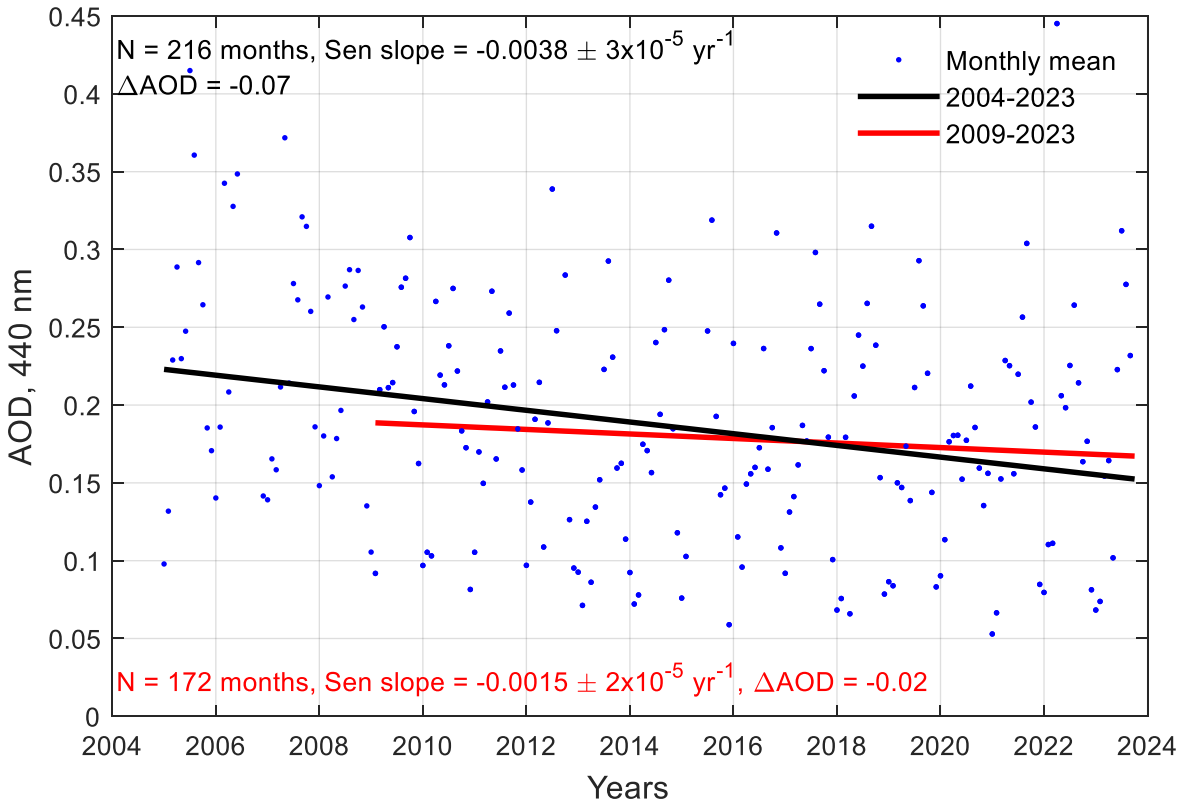

Figure 6.1. Time series of monthly AOD averages (blue dots) from the AERONET photometer at L2-V3 in all-skies conditions. The black line is the 2004-2023 trend, and the red line is this research trend (2009-2023), both with a CI95. N is the sample size, yr is an abbreviation for year, and ΔAOD is the AOD change over the period.

Therefore, the AOD drop is connected to the drop in PM1, 2.5, and 10 at Barcelona, improving the local air quality, which is supported by the following studies. Ref. [316] showed decreases in PM2.5 and 10 by applying the MK test and multi-exponential fit for the 2004-2014 trends at the urban background of Barcelona. They attributed the PM decreases to the effectiveness of pollution control measures implemented at European or regional/local levels. Ref. [317] also found a significant decrease in PM2.5 concentrations related to the success of mitigation strategies by

reducing the anthropogenic source contributions (heavy oil combustion, mixed combustion, industry, and secondary sulfate). Ref. [318] quantified the composition of PM2.5 and 10 and found contributions of dust (8% and 26%, respectively), marine (< 1% and 4%, respectively), and anthropogenic (73% and 54%, respectively). Ref. [319] found decreases in the PM1 trend (MK test) from 2012 to 2018 at the urban background, which is related to the pollutant-source reductions, the oxidation of the secondary precursors, and the local meteorological phenomena.

Furthermore, the 2000-2019 trends of PM2.5 and 10 dropped for the model and observations [320] in the western part of the European Monitoring and Evaluation Programme domain, including Barcelona. They also attributed the trend drops to the abatement strategies of anthropogenic gaseous precursors of secondary aerosols. Thus, the trend drop of the AOD is related to the efficiency of the air quality policies in reducing aerosol concentration in Barcelona in the last decades.

6.2 RADIATIVE-FLUX TRENDS

The trends in Figures 6.2 and 6.3 were calculated from monthly means of the daily solar noon (smallest SZA ± 1º) for all-skies days from 2019 to 2023 and clear-sky days by seasons at the same period, respectively. The seasonal trends were calculated better to represent the temporal evolution of the radiative fluxes, avoiding a biased tendency due to years with few clear-sky days. As shown in Figure 6.2, the radiative-fluxes uptrend, the red line, for the all-skies condition has an increase of +1.22 Wm^{-2} (+0.2%) and a crescent Sen's slope of +0.085 $Wm^{-2}yr^{-1}$, i.e., the radiative fluxes reaching the ground have increased over the years in Barcelona, which it is related to the AOD drop (2009-2023 trend in Figure 6.1) owing the less radiation attenuation by aerosol effects in the last 14 years and owing the scattering caused by clouds, which it interferes with the global radiation at the surface.

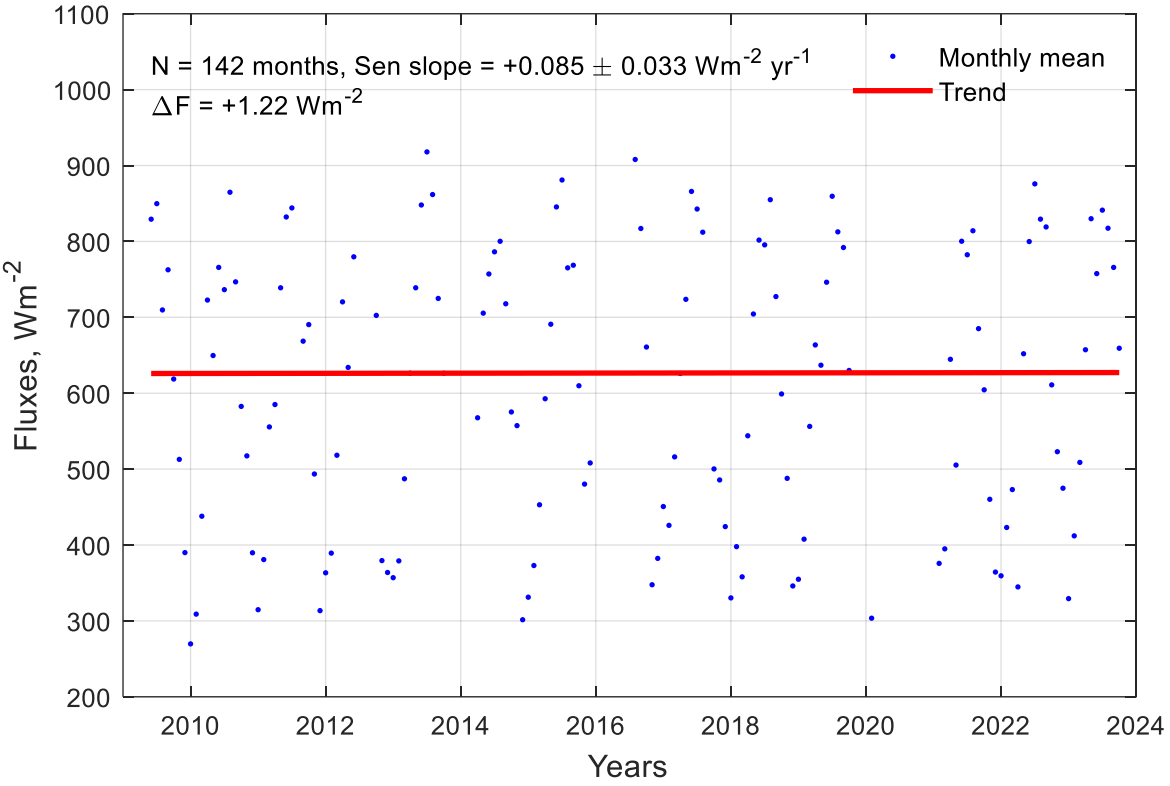

Figure 6.2. Time series of monthly radiative-fluxes averages (blue dots) from the SolRad-Net pyranometer at L1.5 (CM 21 model) in all-skies conditions. The black line is the trend with CI95 from 2009 to 2023. N is the sample size, yr is an abbreviation for year, and ΔF is the change in the radiative fluxes over the period.

The quadratic fitting as a clear-sky method could identify 614 days (17%) from the all-skies database (Subsection 4.3.1), which made it possible to verify the radiative fluxes and AOD trends for clear-sky days by season, as shown in Figure 6.3. The changes in winter trend have values of +11.85 Wm^{-2} (+2%) and -0.006 (-7%) with slopes of +1.18 $Wm^{-2}yr^{-1}$ and -0.0005 yr^{-1} for radiative fluxes and AOD, respectively. The spring trends have a flux change of -77.97 Wm^{-2} (-9%) with a slope of -6 $Wm^{-2}yr^{-1}$ and an AOD change of +0.02 (+14%) with a slope of +0.002 yr^{-1}. The summer trend presents a flux change of -3.63 Wm^{-2} (-0.4%) with a slope of -0.3 $Wm^{-2}yr^{-1}$ and an AOD change of +0.03 (+16%) with a slope of +0.0028 yr^{-1}. The last seasonal trends present a flux rise of +82.69 Wm^{-2} (+13%) with a slope of +6.89 $Wm^{-2}yr^{-1}$ and the largest AOD drop of -0.04 (-24%) with a slope of -0.0037 yr^{-1}.

On the one hand, the increase in the radiative fluxes is associated with a decrease in the AOD for winter and autumn from 2009 to 2023, i.e., the solar

radiation that reaches the ground is getting less attenuated over the years. The AOD decay can be related to the policies implemented since 2007 by Barcelona's government. On the other hand, the radiative flux decrease is associated with an AOD increase for spring and summer owing to the aerosol presence from local sources, as pollens, and from external sources, such as desert dust and biomass burning, which are common in these seasons [281–284]. The policies to reduce local pollution cannot control those aerosol types.

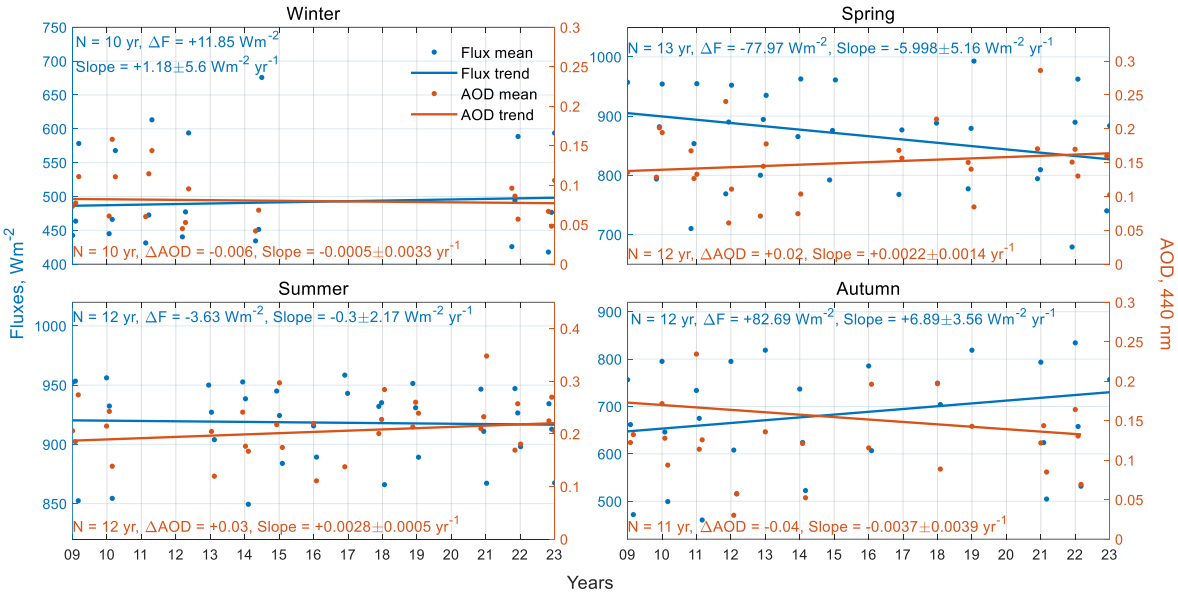

Figure 6.3. Seasonal clear-sky trends of radiative fluxes (blue dots) and AOD (orange dots) monthly averages from 2009 to 2023 with CI95. The continuous blue and orange lines are their respective trends, N is the sample size, yr is an abbreviation for year, Δ is the change in the radiative fluxes (F), and AOD over the period.

The seasonal diurnal cycles and daily variation of the radiative fluxes are presented in Figure 6.4. The continuous lines are the radiative-fluxes maximums, and the dashed lines are the radiative-fluxes averages, followed by their standard deviations (shaded areas). The blue color refers to all-skies days and the green color refers to clear-sky days. In all seasons, the peak flux is around noon for both sky conditions. For clear-sky, the maximums of sun hours reach 683.62, 1040.05, 1050.77, and 848.52 Wm^{-2} in winter, spring, summer, and autumn, respectively. Meanwhile, the all-skies maximums exceed 1000 Wm^{-2} in winter, reach 1200 Wm^{-2}

in autumn, and exceed 1200 Wm^{-2} in spring and summer due to the multiple scattering produced by fractional-cloud cover [321–324].

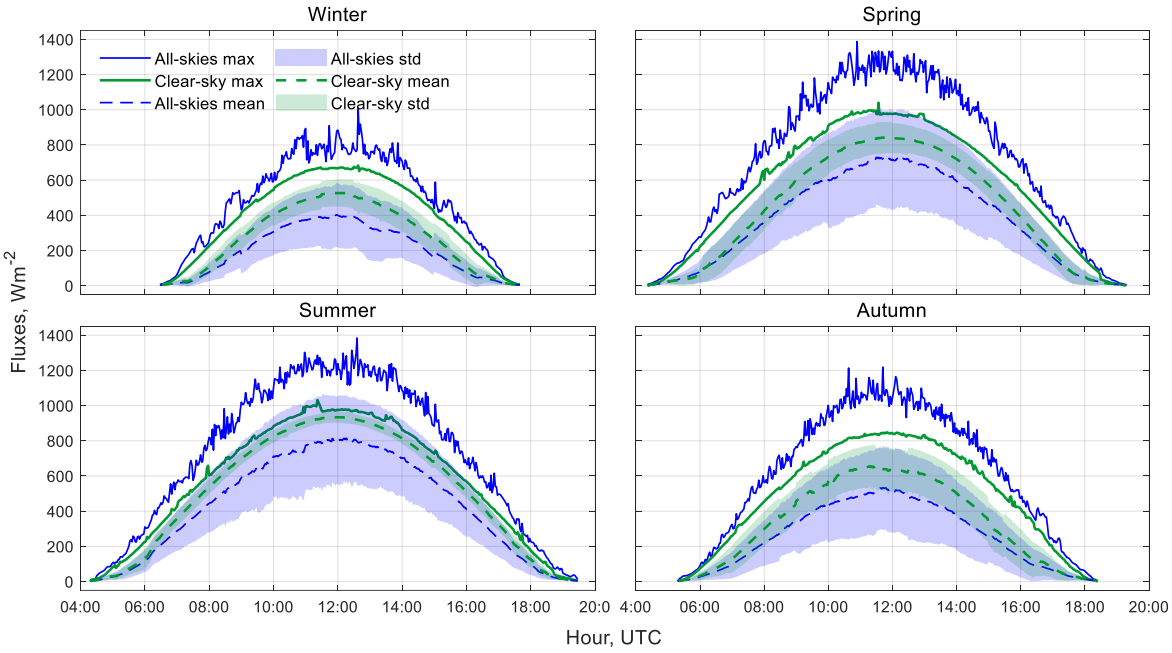

Figure 6.4. Diurnal cycle of radiative fluxes by seasons in Barcelona, including their maximum (max), mean, and standard deviations (std) for all-skies (blue lines) and clear-sky (green lines) conditions.

The clear-sky averages are higher than the all-skies ones for all seasons, followed by small variations (green shaded areas) because of the non-interference of the clouds; however, the cloud disturbances are visually expressive in the large variation of the all-skies standard deviations. For spring and summer, the solid green lines (maximums) show a few spikes due to the disturbances produced by fractional-cloud cover and the aerosol loads, which are more often in those seasons than in others. Pollen, desert dust outbreaks, biomass burning from forest fires, and European pollution episodes [321–324] are more common in spring and summer, scattering or absorbing the radiation that reaches the ground. Furthermore, aerosol fluxes are greater in summer [30] with a factor of 1.5 compared to winter.

6.3 AFE-ARF LONG-TERM

Figure 6.5 depicts the net radiance fluxes of the clear-skies days (2009-2023) as a function of the AOD(440 nm). Their linear fittings were calculated for each SZA

group (20 ± 1º, 30 ± 1º, 40 ± 1º, 50 ± 1º, 60 ± 1º, and 70 ± 1º) by year. The AFE-ARF long-term at 675, 870, and 1020 nm are in Appendix C, as additional information.

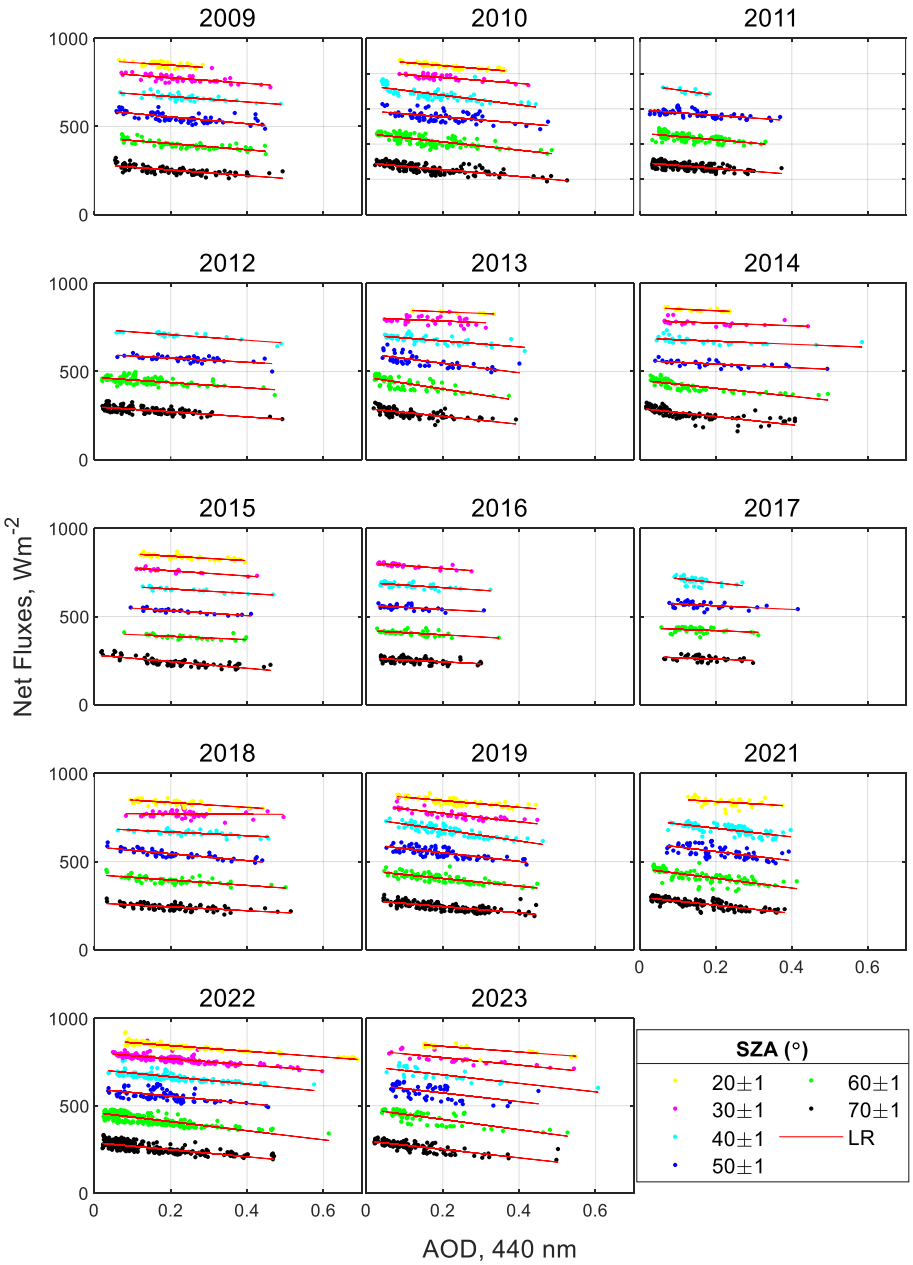

Figure 6.5. AFE Long-term from 2009 to 2023 for each SZA group at 440 nm. The LR slopes were estimated with a CI95.

All linear regressions (LR) have negative slopes varying between -331 and -10 $Wm^{-2}\tau^{-1}$, i.e., Barcelona has a dominant cooling effect in the analyzed period. The slopes are the AFE according to the direct method (Subsection 4.3.2). The AOD related to the AFEs varies from 0.016 to 0.690. These results follow Ref. [282] who

found high aerosol efficiencies at high SZA, -132.2 $Wm^{-2}\tau^{-1}$ (50º < SZA < 60º), in Mallorca Island, Spain; Ref. [325] who obtained -123 ± 11 $Wm^{-2}\tau^{-1}$ at 440 nm (SZA < 65º); and Ref. [41] who derived daily aerosol efficiencies varying from -188 ± 18 to -163 ± 16 $Wm^{-2}\tau^{-1}$ (SZAs from 32º to 73º), in Lampedusa Island, Italy.

Table 6.1 summarizes the AFEs and their CI95 by the fixed SZAs at 440 nm. The AFE tables of the other wavelengths (675, 870, and 1020 nm) are in Appendix C. The CI95 values decrease at higher SZAs (thicker atmosphere) owing to the larger data points than at lower SZAs, agreeing with Ref. [307]. For example, in 2009, the CI95 corresponded to 58% of the AFE at 20º, decreasing to 18% at 70º, and decaying from 84% to 11% in 2021 (Table 11.7). The seasonal variability of the fluxes also contributes to CI95 of the AFE, as shown in Figure 6.4, where summer and spring have maximum fluxes for the clear-sky days. On the one hand, the number of data points contributes to a large CI95 for years with fewer observations and fewer clear-sky days (Table 11.8) as occurred in 2015, 2016, and 2017, representing 4%, 4%, and 3% of the instantaneous observations, respectively, and ~4% of the clear-sky days in the same years. On the other hand, 2022 has the most observations (23%) in 72 clear-sky days (13%), Table 11.8, and has the smallest CI95, varying from 6% to 30% of the AFE.

Table 6.1. AFE with CI95 as a function of the AOD(440 nm) for each SZA group.

SZA / Yr	70 ± 1º	60 ± 1º	50 ± 1º	40 ± 1º	30 ± 1º	20 ± 1º
	AFE, $Wm^{-2}\,\tau^{-1}$					
2009	-158 ± 29	-175 ± 35	-195 ± 45	-153 ± 47	-159 ± 52	-145 ± 84
2010	-192 ± 27	-234 ± 39	-176 ± 64	-275 ± 57	-168 ± 49	-182 ± 30
2011	-168 ± 36	-190 ± 51	-153 ± 42	-305 ± 197	-	-
2012	-145 ± 26	-148 ± 40	-116 ± 43	-158 ± 37	-	-
2013	-224 ± 48	-331 ± 71	-270 ± 85	-170 ± 49	-86 ± 96	-91 ± 29
2014	-233 ± 42	-227 ± 42	-98 ± 41	-85 ± 52	-75 ± 68	-104 ± 45
2015	-188 ± 33	-96 ± 49	-140 ± 30	-127 ± 33	-148 ± 36	-127 ± 30
2016	-107 ± 46	-122 ± 58	-117 ± 63	-144 ± 52	-161 ± 43	-
2017	-76 ± 73	-80 ± 81	-102 ± 75	-235 ± 139	-	-
2018	-110 ± 29	-152 ± 41	-196 ± 37	-108 ± 42	-10 ± 67	-138 ± 48
2019	-179 ± 28	-218 ± 39	-242 ± 50	-319 ± 42	-243 ± 57	-190 ± 34
2021	-230 ± 25	-277 ± 46	-260 ± 77	-245 ± 52	-	-128 ± 107
2022	-202 ± 18	-260 ± 22	-208 ± 62	-210 ± 34	-174 ± 18	-163 ± 9
2023	-242 ± 32	-294 ± 53	-248 ± 112	-244 ± 81	-214 ± 62	-162 ± 43

Table 6.2 summarizes the ARF averages and their standard deviations for each SZA group at 440 nm by year. The ARF tables of the other wavelengths (675, 870, and 1020 nm) are in Appendix C. The ARF in Barcelona varies from -64 to -2 Wm^{-2} in the period. Ref. [282] found an ARF average of -26.4 Wm^{-2} at 50º < SZA < 60º and values ranging from -64 to -2 Wm^{-2} for Mallorca Island, Spain. The high standard deviations can be related to the direct method (Subsection 4.3.2), which directly depends on the aerosol load, i.e., high variability throughout the year for all aerosol types. This leads to an opposite angular dependency related to that in Table 6.1: at higher solar angles, thicker atmosphere, there is more AOD variability, increasing their standard deviations. For instance, the standard deviations rose from 26% to 49% of the ARF mean at 20º and 70º, respectively, in 2009, and from 27% at 20º to 61% of the ARF mean at 70º in 2021 (Table 11.7).

Table 6.2. ARF averages and their stds at 440 nm for each SZA group.

SZA / Yr	70 ± 1º	60 ± 1º	50 ± 1º	40 ± 1º	30 ± 1º	20 ± 1º
	AFE, $Wm^{-2}\,\tau^{-1}$					
2009	-33 ± 16	-41 ± 19	-41 ± 20	-36 ± 13	-36 ± 14	-27 ± 7
2010	-30 ± 19	-36 ± 22	-35 ± 16	-47 ± 27	-33 ± 13	-38 ± 15
2011	-21 ± 12	-26 ± 13	-22 ± 13	-39 ± 13	-	-
2012	-17 ± 13	-21 ± 14	-27 ± 10	-35 ± 18	-	-
2013	-25 ± 17	-35 ± 27	-41 ± 25	-27 ± 16	-14 ± 7	-21 ± 7
2014	-28 ± 24	-28 ± 25	-18 ± 11	-14 ± 11	-13 ± 8	-15 ± 6
2015	-41 ± 20	-23 ± 8	-31 ± 12	-30 ± 12	-30 ± 14	-30 ± 11
2016	-13 ± 7	-15 ± 8	-12 ± 7	-16 ± 10	-16 ± 11	-
2017	-12 ± 4	-12 ± 5	-17 ± 8	-34 ± 9	-	-
2018	-23 ± 11	-30 ± 15	-40 ± 20	-28 ± 10	-2 ± 1	-29 ± 11
2019	-36 ± 17	-44 ± 20	-48 ± 21	-64 ± 27	-57 ± 25	-42 ± 17
2021	-36 ± 22	-43 ± 26	-55 ± 21	-55 ± 21	-	-30 ± 8
2022	-28 ± 21	-34 ± 26	-38 ± 18	-42 ± 20	-35 ± 19	-35 ± 22
2023	-28 ± 21	-40 ± 28	-41 ± 21	-47 ± 31	-50 ± 28	-45 ± 22

In general, higher absolute values of AFE are found at intermediate SZAs because the atmosphere is optically thicker than at smaller SZAs, and, when the solar radiation path increases in the atmosphere, the attenuation increases [111], especially at shorter wavelengths, and then the AFE decreases [80]. The AFE drop at the highest SZA is associated with the decrease in the aerosol-scattered flux because the slant path is no longer optically thin [112]. This behavior is propagated in the ARF, as displayed in the first plot of Figure 6.6. The AFE varies between -200

and -175 $Wm^{-2}\tau^{-1}$ for SZA between 40º and 70º, at which the ARF decreases (in absolute value) from -37 Wm^{-2} to -27 Wm^{-2}. Similar angular dependences were found by Refs. [80,307,326–328]. While Ref. [326] associated the ARF decay at 70º with the slant path no longer being optically thin, Ref. [327] attributed the decay at larger SZA to the upscatter flux at sunset and sunrise being larger in comparison to the one at local noon.

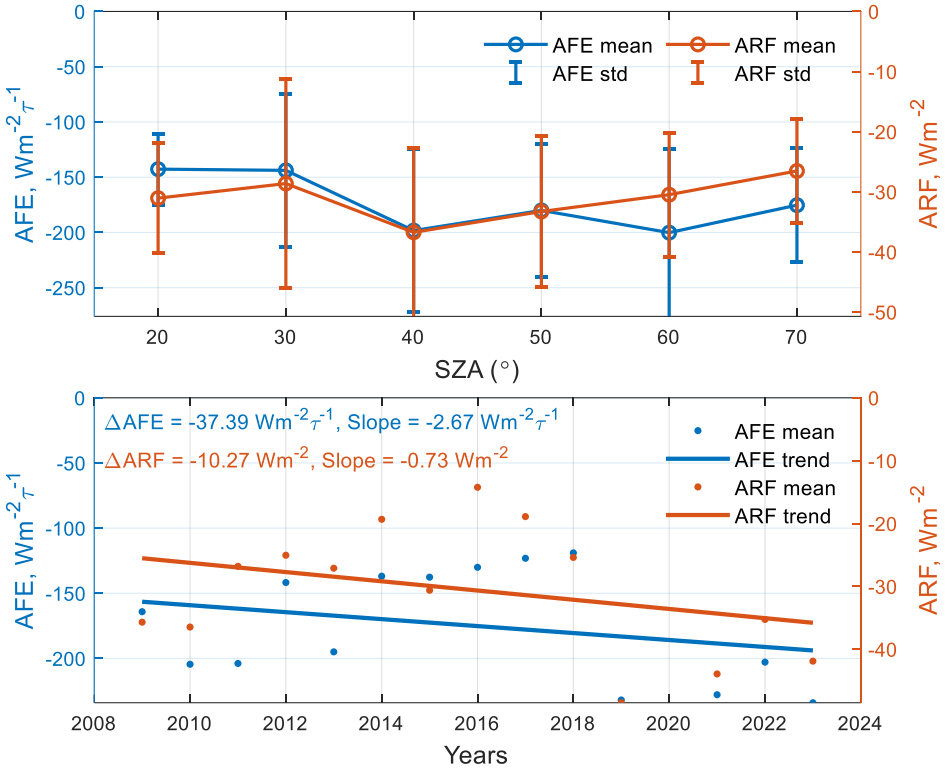

Figure 6.6. AFE-ARF angular dependency and their trends (2009-2023) for each SZA group at 440 nm. The LR slopes were estimated with a CI95. The continuous blue (AFE) and orange (ARF) lines are the trends, ΔAFE is the AFE change, and ΔARF is the ARF change over the period.

The second plot of Figure 6.6 displays the AFE-ARF trends at 20º-70º from 2009 to 2023. The AFE has a change of -37.39 $Wm^{-2}\tau^{-1}$ (-24%) and a slope of -2.67 $Wm^{-2}\tau^{-1}yr^{-1}$. The ARF change is -10.27 Wm^{-2} (-40%) with a slope of -0.73 $Wm^{-2}yr^{-1}$. Both trends increase in absolute values, indicating that the aerosol forcings throughout the analyzed period are getting stronger with time in Barcelona. Refs. [80,329] also pointed out this effect in Granada, Spain. The SSA of the period (0.94 ± 0.03) shows a considerable absorption aerosol according to Dubovik's climatology

[130]. However, AERONET inversions do not allow a robust analysis of the SSA and other parameters (e.g., AAOD and AF) for the corresponding clear-sky days owing to the few data available at L2. The relevance of the other aerosol parameters in this research is an open issue.

According to reports of the Ministry for Ecological Transition and the Demographic Challenge <last access: May 29th, 2025> and Ref. [315], dust episodes have increased by 5% to 15% from 2009 to 2023 in Spain and in the western Mediterranean for the 1948-2020 period, respectively. Table 11.8 shows that the number of dust days by year has increased. This fact contributes to the increase in the aerosol cooling effect owing to the dust upscattering, mainly for 2019 (second plot of Figure 6.6), with 19 days (Table 11.8).

6.4 AFE AND ARF FROM AEROSOL TYPES

This section quantifies the contribution of the aerosol types to the forcing in Barcelona. As indicated in Subsection 4.3.2, the aerosol in Barcelona was classified according to Refs. [108,309] and is displayed in Figure 6.7. Due to the complexity in determining the aerosol-classification thresholds for AOD-AE classifications, (i) the MA includes pure marine and marine polluted [108], mixed with continental or local-pollution aerosols [309], with AOD > 0 and 1.05 < AE < 1.5, AOD < 0.2 and AE ≤ 1.5, and AOD < 0.1 and AE > 1.5; (ii) the UI-BB includes local pollution and biomass burning [108] in the coast with AOD ≥ 0.1 and AE ≥ 1.5; and (iii) the DD includes dust and some mixture of dust and biomass-burning aerosols [309] with AOD ≥ 0.2 and AE ≤ 1.05. This classification shows a 61% predominance of MA, 29% of UI-BB, and 10% of DD in Barcelona for clear-sky days.

The graphical method proposed by Ref. [330] was applied to analyze the aerosol fine-mode size, the fractional contribution to the total AOD (η), and the AOD growth due to the increase in coarse particles. Their method depends on the AE difference, δAE = AE(440-675 nm) - AE(675-870 nm), as a function of the AE calculated between 440 and 870 nm for a bimodal lognormal size distribution with refractive index N = 1.4-0.001i. As stated by Ref. [330], the observations of the AOD(675 nm) > 0.15 were applied on all plots to avoid AOD error propagation larger

than ~30%; hence, the MA aerosol was reduced by 93%, the DD by 8%, and the UI-BB by 86%. It is worth mentioning that the MA and UI-BB contain marine aerosols (AOD < 0.2) that suffer drastic reductions when applying Gobbi's method. Furthermore, the AOD utilized in this analysis is observed at 440 nm. This particularity was well performed by Ref. [282]. For this research, the results in the graphical method are presented for the aerosol types by Ref. [108] in Figure 6.7.

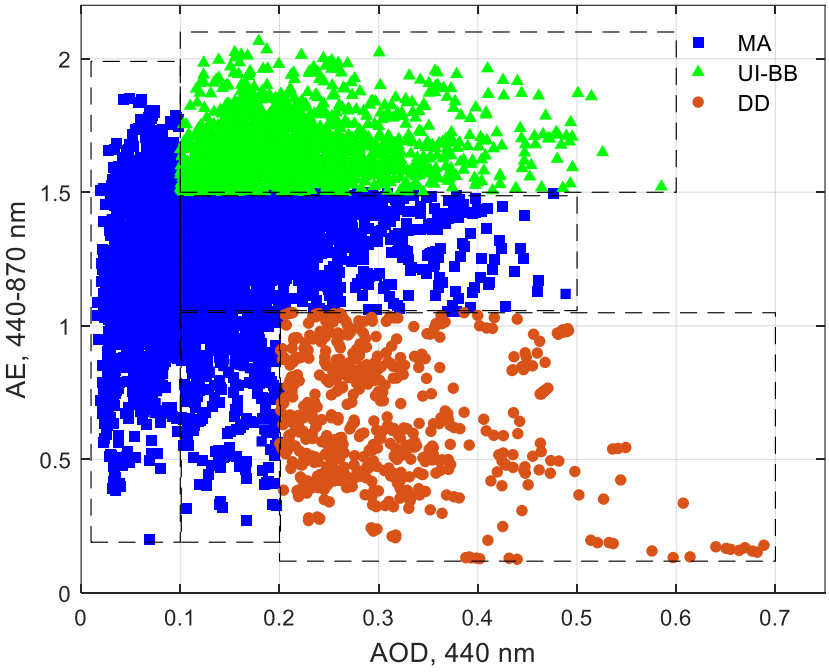

Figure 6.7. Scatter plot of the AOD(440 nm) from clear-sky days (2009-2023) according to the aerosol classifications of Refs. [108,309]. Colors and shapes refer to each aerosol type, and the rectangles delimit the classification regions.

Figure 6.8 depicts Gobbi's graphical method for the aerosol types by SZA in Barcelona. Most aerosols have positive δAE values (85%) with a δAE mean of 0.21 ± 0.11, indicating the presence of different aerosol modes [330,331]. The negative values of δAE have a mean of -0.13 ± 0.09. Regarding the AE, the coarse and fine modes are separated by 1.05 [309], in which the averages are 0.62 ± 0.23 and 1.47 ± 0.21, respectively.

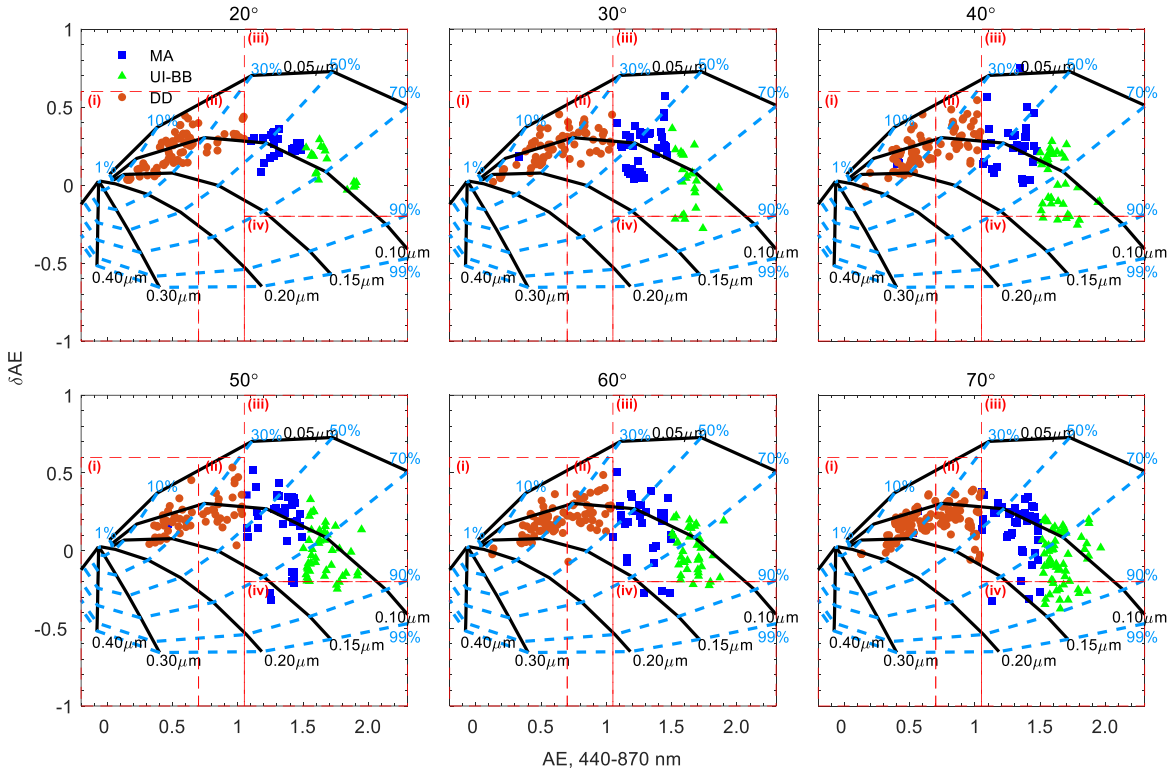

Figure 6.8. AE difference (δAE) as a function of the AE(440-870 nm) for the classification in Figure 6.7 and each SZA group. Colors and dot shapes refer to each aerosol type. The solid black lines are the aerosol radii, the dashed blue lines are the fine-mode fractions of the total AOD (η), and the dashed red lines are the aerosol clusters (i, ii, iii, and iv).

As expected, the aerosol amount increases from 17% at 20º to 24% of the total at 70º for DD, from 12% at 20º to 23% at 70º for MA, and from 8% at 20º to 28% at 70º for UI-BB at higher SZA. The Gobbi's method and aerosol classification (Figure 6.7) together characterized some aerosol clusters over Barcelona: (i) first coarse-mode cluster has an increase in the aerosol size from 0.05 to 0.20 μm, mainly for DD and a few MA, associated to a small fine fraction (η < 30%), and AE < 0.7 agreeing with Ref. [332], but, a δAE < 0.6 is divergent from theirs; (ii) second coarse-mode cluster has only DD with radii around 0.10 μm at lower SZA, exceeding 0.15 μm at higher SZA, AE between 0.7 and 1.05, δAE < 0.6 at lower SZA, some δAE < 0 at higher SZA, 30% < η < 45% at lower SZA, and η > 50% at higher SZA; (iii) first fine-mode cluster is a mixture of MA and UI-BB aerosols with radii centered in 0.10 μm varying from moderate to high fine fraction (35% < η < 80%) at lower SZA, exceeding 0.15 μm with high fine fraction (η > 80%) at higher SZA, δAE varyies from

-0.2 to 0.75, and AE > 1.05; Ref. [282] found similar values for fine-mode cluster from observation at insular sites in the western Mediterranean Basin; and (iv) second fine-mode cluster is a small cluster dominated by UI-BB at small SZAs and it is characterized by AE > 1.05, δAE < -0.2, 75% < η < 90%, and radii around 0.13 μm that agrees with Ref. [332] for polluted and continental aerosol in some sites in Iberian Peninsula and Western Mediterranean region, including Barcelona. These results reinforce that the angular dependency relies on the aerosol type, as was pointed out by Ref. [307].

Finally, the forcing contribution from each aerosol type is displayed in Figure 6.9 and summarized in Table 6.3. The DD has a cooling effect with negative AFE varying from -207 to -123 $Wm^{-2}\tau^{-1}$, increasing its absolute values at 40º and decreasing it at higher SZA. These results are close to -120 $Wm^{-2}\tau^{-1}$ (at 440 nm and 53º-75º) found by Ref. [333] during a strong dust event mixed with smoke in Granada; close to those found by Ref. [307], -185 to -81.7 $Wm^{-2}\tau^{-1}$ (at 495.7 nm and 20º-75º), in the Mediterranean island of Lampedusa; and following those found by Ref. [329] for two case studies (-124.4 and -149.1 $Wm^{-2}\tau^{-1}$ for the first case and -169.4, -178.9, and -198.9 $Wm^{-2}\tau^{-1}$ for the second case) within a dust transport episode in Granada, Spain.

The MA varies from -270 to -149 $Wm^{-2}\tau^{-1}$ and seems not to have a clear angular dependency because of the alternating drops and rises. This behavior can be related to the aerosol mixture that contains a large SSA variability [80]. The DD has the largest aerosol load (0.31 ± 0.09), and MA is the dominant aerosol (61%) with the largest AOD variability (0.13 ± 0.08), which can explain their angular dependence and their CI95s. The DD has the lowest CI95s, varying from 24% to 38% of the mean, while MA has the highest ones, ranging from 44% to 71% of the mean.

The AFE from UI-BB ranges from -190 to -94 $Wm^{-2}\tau^{-1}$ with an inflection point at 30º, which is also pointed out in the efficiencies calculated by Ref. [307]. The AOD of the UI-BB is quite variable, averaging 0.22 ± 0.08, leading to high CI95s (31-40%

of the mean). Thus, the AFE dependence on SZA changes according to the aerosol types, the optical thickness of the atmosphere, and its attenuation [80,307].

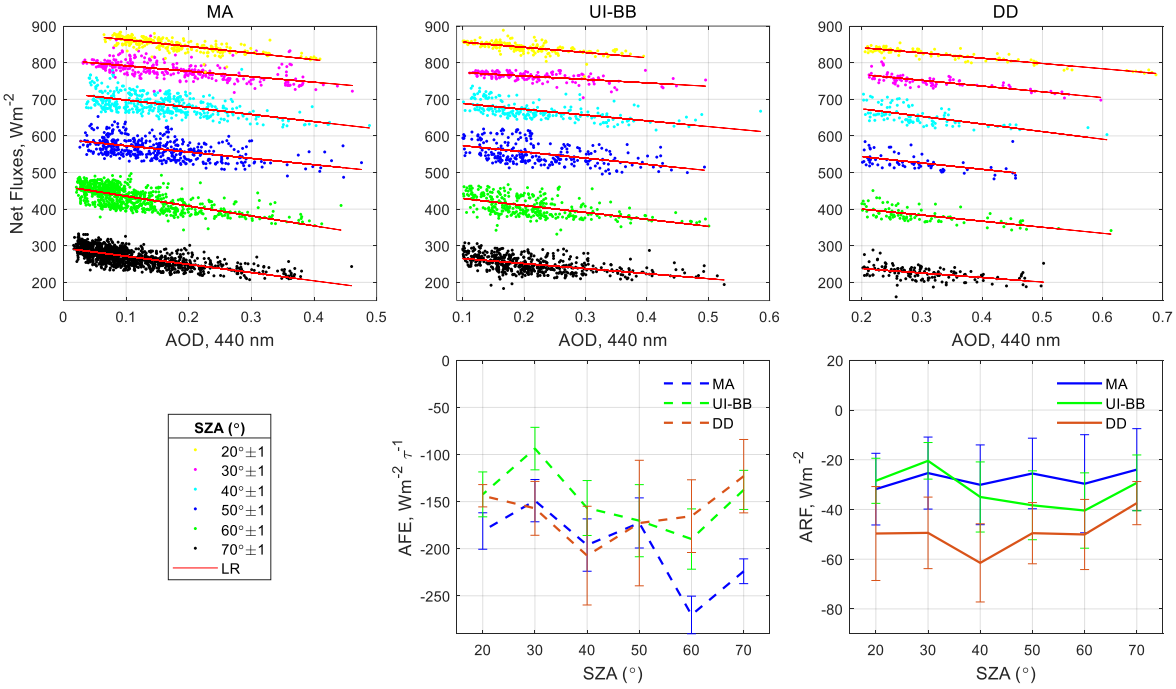

Figure 6.9. AFE-ARF averages by aerosol type from the classification in Figure 6.7 for each SZA group at 440 nm. LR slopes were estimated with a CI95. The vertical bars are the standard deviations.

Table 6.3. AFE and ARF by aerosol types and their standard deviation for each SZA group at 440 nm. AT stands for aerosol types, and All stands for all aerosols (first plot in Figure 6.6).

SZA / AT	70 ± 1º	60 ± 1º	50 ± 1º	40 ± 1º	30 ± 1º	20 ± 1º
	AFE, $Wm^{-2}\,\tau^{-1}$					
DD	-123 ± 39	-165 ± 39	-173 ± 67	-207 ± 52	-157 ± 29	-144 ± 12
MA	-224 ± 13	-270 ± 20	-173 ± 27	-196 ± 28	-149 ± 23	-181 ± 19
UI-BB	-138 ± 21	-190 ± 32	-170 ± 38	-157 ± 29	-94 ± 23	-142 ± 24
All	-175 ± 52	-200 ± 76	-180 ± 66	-198 ± 74	-144 ± 69	-143 ± 32
	ARF, Wm^{-2}					
DD	-37 ± 9	-50 ± 14	-50 ± 12	-62 ± 16	-49 ± 14	-50 ± 19
MA	-24 ± 17	-30 ± 20	-26 ± 14	-30 ± 16	-25 ± 15	-32 ± 14
UI-BB	-29 ± 11	-40 ± 15	-38 ± 14	-35 ± 14	-20 ± 7	-29 ± 9
All	-27 ± 9	-31 ± 10	-33 ± 13	-37 ± 14	-29 ± 17	-31 ± 9

As depicted in the last plot of Figure 6.9 (second row), the AFE angular dependencies are propagated to the ARF of the UI-BB and DD. The DD has the strongest cooling effect, and its forcing varies from -62 to -37 Wm^{-2}, increasing in

absolute value at 40º and then decreasing at higher SZA. These results are in the range of those estimated by Ref. [109] for instantaneous radiative forcing at 500 nm (-93.1 to -0.5 Wm^{-2}) during dust outbreaks in Barcelona. The DD has the largest ARF because of the largest AOD(440 nm). The ARF of UI-BB varies from -40 to -20 Wm^{-2} with an inflection point at 30º and increases (in absolute values) until 50º, followed by a decrease at 70º. However, the MA has the smallest ARF at 40º-70º, varying between -32 and -24 Wm^{-2}.

6.5 RADIATIVE PARAMETERS COMPARISONS

The comparison between the radiative fluxes from AERONET and the CM 21 pyranometer is plotted in Figure 6.10. The AERONET fluxes slightly overestimate those from CM 21 (on average, PE = 4 ± 1%), showing that both instruments measure comparable fluxes. A similar overestimation of the pyranometer by AERONET fluxes (4 ± 5.2%) was also found by Ref. [310], who attributed it to the combination of errors such as cosine response, calibration, and linearity in the pyranometer measurements.

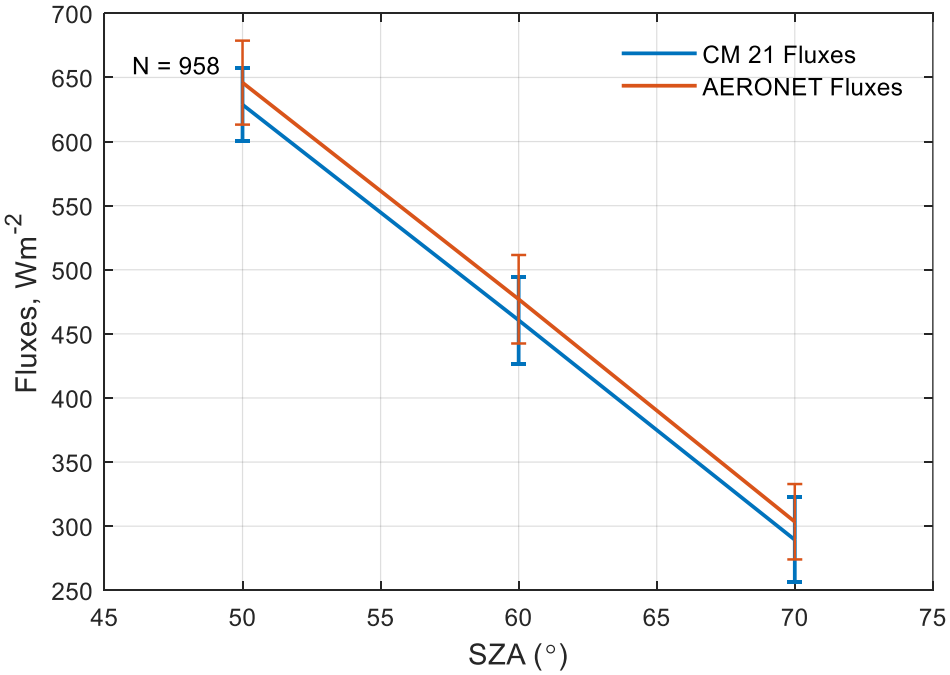

Figure 6.10. Comparison of the radiative fluxes between AERONET and CM 21 as a function of the SZA from 2009 to 2023. N is the number of observations, and the vertical bars are the standard deviations.

The comparisons among the radiative properties and fluxes from AERONET inversions, the direct method, and GRASP inversions are in Table 6.4. The AERONET fluxes slightly overestimate those from CM 21 in 1% and 3% (Cases I and II, respectively), which was expected according to Ref. [310], but it underestimates the CM 21 flux in 2% for Case III. The GRASP combinations (D0, D0+L, D0P+L, D1+L, and D1P+L) overestimate the CM 21 fluxes by ~7% for Cases I and II and ~1% for Case III. These overestimations can be related to the cosine response (greater SZAs, smaller PE) and due to the spectral range in which the GRASP code integrates the broadband solar flux from 200 to 4000 nm [272] and the CM 21 fluxes from 305 to 2800 nm (Table 2.6).

Table 6.4. Comparisons of the radiative fluxes, AFE, and ARF for three case studies.

Observations and inversions	Case I: AOD = 0.30 and SZA = 60º			Case II: AOD = 0.25 and SZA = 60º			Case III: AOD = 0.21 and SZA = 70º		
	Flux	AFE	ARF	Flux	AFE	ARF	Flux	AFE	ARF
CM 21 *	440	-260±22	-34±26	444	-260±22	-34±26	306	-202±18	-28±21
AERONET	445	-192	-39	456	-175	-35	301	-200	-30
D0	474	-187	-38	480	-166	-33	309	-187	-27
D0+L	472	-179	-39	476	-165	-36	310	-179	-27
D0P+L	474	-161	-37	476	-167	-36	308	-167	-27
D1+L	471	-177	-38	475	-164	-34	307	-173	-26
D1P+L	473	-165	-35	473	-171	-36	307	-167	-26

* The AFE and ARF are from 2022 (Tables 6.1 and 6.2, respectively), the year of the case studies.

The AFE-ARF comparison between GRASP combinations and the direct method shows (i) high underestimations of the AFE from the direct method in the three case studies (PE ≈ 32%, 35%, and 14% for Case I, II, and III, respectively), owing to the difference in estimating the aerosol efficiency (Appendix D and Subsection 4.3.2); (ii) ARF overestimations for high AOD (Case I and II) and ARF underestimations for low AOD (Case III) by GRASP combinations; (iii) the DoLP addition in GRASP combinations (D0P+L and D1P+L) increases the AFE underestimation of about 37% and 17% for Cases I and III, respectively, whereas it decreases the ARF overestimations caused by GRASP combinations. As the ARF depends directly on the AOD, any AOD variation will change the ARF observed when DoLP is added to the GRASP synergies. Refs. [69,311] pointed out adjustments in

the higher AODs when they were inverted with DoLP; and (iv) the DoLP insertion does not improve retrieved ARF in Cases II and III, probably owing to the low AOD.

Regarding the comparisons between the radiative fluxes, ARF, and AFE from GRASP combinations with those from AERONET inversions, (i) the flux overestimations by GRASP inversions decrease the PE to ~6% and ~4% in Cases I and II, respectively; (ii) the AFE underestimations also decrease PE to ~10%, ~5%, and ~13% for Case I, II, and III, respectively; (iii) the ARF varies according to GRASP combination, under- or overestimating the AERONET inversions (Cases I and II) and PE remains around 10% in Case III; and (iv) the GRASP inversions with DoLP show higher AFE underestimations to the direct method for Cases I and III: ΔAFE = -99 $Wm^{-2}\tau^{-1}$ (38%) for D0P+L and ΔAFE = -95 $Wm^{-2}\tau^{-1}$ (37%) for D1P+L in Case I, ΔAFE = -35 $Wm^{-2}\tau^{-1}$ (17%) for D0P+L and D1P+L in Case III. However, the DoLP addition keeps the ARF closer to that estimated by the direct method, mainly for Case I (high AOD).

The differences between the AERONET and GRASP inversions can be attributed to the AFE-ARF definitions, in which the GRASP code considers the upward fluxes (Equations 3.21). According to the Refs. [237,310], the ARF is the difference between the broadband fluxes with and without aerosols at the BOA, and the AFE is the rate at which the atmosphere is forced per unit of the AOD at 550 nm (Appendix D). However, the GRASP code retrieves the aerosol net radiative effect at the BOA, which is the difference between downwelling and upwelling fluxes at a given atmospheric layer in aerosol-free and aerosol-laden conditions [272]. The equations are in Appendix D.

6.6 CONCLUSIONS

The ARF and AFE were presented for the first time by long-term and case-by-case procedures over a decade in Barcelona, Spain. They were computed by the direct method, combining radiation measurements from the CM 21 pyranometer (L1.5) and AOD from the AERONET photometer (L2). The AFE was estimated from the slope between net fluxes and AOD at 440, 675, 870, and 1020 nm (AERONET fundamental wavelengths), and the ARF was calculated by multiplying the AFE by

the AOD. Both were estimated for six SZA groups (20º, 30º, 40º, 50º, 60º, and 70º). Clear-sky conditions were selected from all-skies conditions by a quadratic fitting with seasonal adaptive criteria. Moreover, the aerosol was characterized and classified to investigate the AFE-ARF contributions from each aerosol type.

The all-skies trend of the AOD showed a decrease in the last decade due to the local government's policies to reduce air pollution in Barcelona, whereas the flux trend increased for the same period. Additionally, the clear-sky seasonality showed decays in the flux trends, followed by increases in the AOD trends and *vice versa*. The AOD increases in spring and summer were expected because of the contributions of other aerosol types (e.g., dust and pollen). All trends highlight the influence of the aerosol load on global solar radiation that reaches the surface.

The AFE-ARF long-term revealed a cooling effect, which increases in absolute number over 14 years, 24% and 40% for AFE and ARF, respectively. The efficiencies varied from -331 and -10 $Wm^{-2}\tau^{-1}$ with an AOD varying from 0.16 to 0.69 and the ARF from -64 to -2 Wm^{-2}. Furthermore, the AFE-ARF angular dependency increased in absolute number at centered SZA (40º to 60º) because of the attenuation in a thicker atmosphere.

On the one hand, this research showed that a CI95 of the AFE depended mostly on the SZA, where smaller angles with fewer observations had higher CI95. The seasonal variability of the CI95 was also considered. The years with fewer clear-sky days (2015, 2016, and 2017) also contributed to a high CI95. On the other hand, standard deviations of the ARF were directly influenced by the aerosol load variability, according to the direct method.

Regarding the aerosol types, Barcelona had three main dominant aerosols for clear-sky days: MA (61%), UI-BB (29%), and DD (10%). This classification and Gobbi's method clustered the aerosols into four groups by AE analysis: two coarse modes and two fine modes. The contribution of the aerosol types to the forcing concluded that DD forcing had the greatest cooling effect, varying from -62 to -37 Wm^{-2}, followed by UI-BB (-40 to -20 Wm^{-2}) and MA (-32 to -24 Wm^{-2}).

Finally, comparisons between CM 21 observations and AERONET and GRASP inversions presented similar broadband-flux measurements for 958 inversions and three case studies. The AFE-ARF estimations had noticeable differences when the direct method was compared with GRASP retrievals; however, these differences decreased when GRASP outputs were compared with AERONET inversions, mostly for Cases I and II. The DoLP addition in GRASP synergy (D0P+L and D1P+L combinations) impacted the AFE by raising the underestimation of the direct method (38% with D0P+L and 37% with D1P+L in Case I, and 17% with both combinations in Case III) and reducing ARF overestimations in Case I (high AOD). Therefore, the GRASP code could retrieve the ARF satisfactorily, owing to the approximation between its ARF values and those from the direct method.

7 CONCLUSIONS AND FUTURE PERSPECTIVES

I dedicate this chapter to myself: to the one who accepted the challenge of leaving the country of his birth and embracing a new culture; who learned a new programming language, mastered new methods of analysis, handled (un)familiar instruments, ventured into new countries (Romania and France), and studied other languages in pursuit of better research.

Think about future generations!

This thesis was developed over four years, allowing authorship and co-authorship in some studies, e.g., Refs. [134,279], the most important publications, on which this manuscript is based. The complete list of studies is available in Appendix E. Understanding the GRASP inversion procedure, e.g., creating the SData file and configuring the setting file (GRASP inputs) according to the UPC instruments, was essential to achieve the first objective. Moreover, a challenging analysis of the 14-year observations was responsible for searching for methods to identify the largest number of clean-sky days and to present trends for all-skies and clean-sky conditions. This research also analyzed the properties and effects of the aerosols in Barcelona, Spain, by performing two distinct approaches connected by ground-based synergies, which were inverted by the GRASP algorithm. They were essential to achieve the second objective. The conclusions are organized from three main chapters (IV, V, and VI).

Chapter IV. This chapter described the methods to achieve the two objectives proposed by this PhD. In the first goal's methodology, GRASP sensitive tests were performed to evaluate the algorithm when the DoLP was inserted in the state-of-the-art synergy (lidar + photometer), requiring the preparation of the SData and the setting file with Barcelona's information, and creating a simulated SData based on the real observations and synthetic aerosol concentration profiles. The second goal's methodology estimated aerosol forcing and efficiency from the direct method (pyranometer and photometer observations) and presented how to obtain a comprehensive analysis of aerosol radiative effects over Barcelona for long-term, case-by-case, and aerosol type estimations. Moreover, GRASP retrievals were compared with AERONET and direct method values. The methodology of the synergies can be replicable or adaptable for various regions in the world, and support for international networks and field campaigns.

Chapter V. This research line evaluated the GRASP sensitivity to the DoLP. This analysis explored the improvements in aerosol properties when using synergy between a polarized Sun-sky-lunar photometer and a lidar system, the first time for specific combinations between both instruments (D0P+L, D1+L, and D1P+L). The aerosol parameters were retrieved, employing synthetic data from realistic

measurements (observations from the Optical Remote Sensing group at the Universitat Politècnica de Catalunya and Dubovik's climatology) and synthetic aerosol profiles. The inversions were carried out for (i) three different aerosol scenarios (I-high AOD with dominant coarse mode, II-low AOD with dominant coarse mode, and III-high AOD with dominant fine mode), (ii) seven synergy combinations (D0, D0+L, D0P+L, D1+L, D1P+L, D1+L+δ^v, and D1P+L+δ^v), and (iii) two conditions to be compared with the reference (simulated data): NF and RN inversions. The D1+L+δ^v and D1P+L+δ^v combinations were analyzed in a case study for the NF inversion only.

Overall, DoLP proved to be a valuable input for improving GRASP retrievals, particularly under higher aerosol load conditions. Retrieval improvements were most notable for the coarse mode of the optical properties, like SSA and LR, and for the coarse mode of the RRI. However, limited sensitivity is observed for the fine mode of VC and SD in all aerosol scenarios. Additional photometer channels significantly enhance the retrieved aerosol properties, as input to the GRASP code. RMSE reductions confirmed these gains in the retrievals with DoLP and additional photometer channels. Table 7.1 summarizes and highlights the gains with DoLP addition in the GRASP inversions.

Table 7.1. Improvements with DoLP and additional photometer channels to GRASP retrievals. The green color highlights the gains (✓) with new GRASP combinations.

Sc.	Comb.	SD		RRI		IRI		AOD		SSA		LR		SF
		f	c	f	c	f	c	f	c	f	c	f	c	Total
I	D0P+L	-	-	-	✓	-	-	✓	✓	✓	✓	-	-	✓
	D1+L	-	-	-	-	-	-	-	-	-	✓	-	-	✓
	D1P+L	✓	✓	-	✓	-	-	✓	✓	✓	✓	✓	-	✓
II	D0P+L	-	✓	✓	✓	✓	-	-	✓	✓	-	✓	✓	✓
	D1+L	-	-	-	✓	✓	-	-	✓	✓	-	✓	✓	✓
	D1P+L	-	✓	✓	✓	✓	-	-	✓	✓	-	✓	✓	✓
III	D0P+L	-	-	-	✓	✓	✓	-	-	✓	✓	✓	✓	✓
	D1+L	-	✓	-	✓	✓	✓	-	-	✓	✓	✓	✓	✓
	D1P+L	-	✓	-	✓	✓	✓	-	-	✓	✓	✓	✓	✓

Regarding the case study, simulating under a high aerosol loading scenario (dust-urban aerosol) in Barcelona, showed that the δ^{v} mainly influenced the vertical structure of aerosol profiles, and the DoLP addition did not seem to contribute to the retrievals.

Chapter VI. The second research line presented the long-term and case-by-case aerosol radiative effects over a decade in Barcelona, Spain, for the first time. This chapter estimated the efficiency and forcing of the aerosols in Barcelona under long-term and case-by-case analyses based on ground-based observations. The AOD and radiative-flux trends from 2009 to 2023 were examined, where the AOD trends have declined and solar fluxes have increased, particularly under clear-sky conditions, indicating reductions in the atmospheric aerosol attenuation. The AOD drops were attributed to local air quality policies, following the PM1, 2.5, and 10 drops. Seasonal trends revealed opposite AOD behaviors, with a decrease in winter and autumn and an increase in spring and summer due to aerosol natural sources (pollen and dust).

The AFE-ARF long-term was estimated using the direct method. AFE values range from -331 to -10 $Wm^{-2}\tau^{-1}$, and ARF values range from -64 to -2 Wm^{-2}, confirming a dominant cooling effect. The analysis by aerosol type revealed that DD produced the strongest cooling effect, followed by UI-BB and MA, with their angular dependencies influenced by the aerosol composition. The comparisons among fluxes and forcing retrieved by AERONET, GRASP code, and the direct method (three case studies) showed discrepancies owing to the differences in spectral ranges, cosine response, and algorithmic definitions. The GRASP combinations with DoLP (D0P+L and D1P+L) generally improve ARF, agreeing with that from the direct method in high-AOD cases (I and II), though they tend to underestimate the AFE in all case studies.

In conclusion, the scope of this PhD concerned two objectives, as described in Chapter I. The applied methodology (Chapter IV) and the results (Chapters V and VI) demonstrated that the inversions from the synergy between photometer and lidar, retrieved by the GRASP algorithm, are sensitive to the DoLP, which contributed

mainly to the high aerosol load, the refractive index, and the optical properties. The applied methodology and the results also demonstrated that the pyranometer/photometer observations and state-of-the-art synergy were able to retrieve aerosol radiative forcing adequately, mainly for high aerosol load. Moreover, the contribution of aerosols to the radiative forcing over Barcelona, Spain, showed a cooling effect over a decade, where the desert dust particles had the biggest influence on the forcing.

For future investigations with polarization information as GRASP input, the first research line can be applied (i) to invert microphysical and optical properties from real data and several aerosol scenarios; (ii) to validate satellite products; and (iii) to perform sensitivity tests to other instrumental parameters, e.g., Raman signal, extinction or backscatter profiles, and others (Table 4.6 in Ref. [267]), providing new combinations between them and DoLP. Moreover, the RN analysis needs to be performed to estimate the sensitivity of the GRASP code when the δ^{v} is inverted with and without DoLP, and to relate the δ^{v} to the AVP shapes and to relate the δ^{v} to the DoLP in the GRASP retrievals, as the combination of both variables does not seem to have good retrievals due to a possible incompatibility. This study could also help the GRASP team to optimize the GRASP code.

The second research line demonstrated that the combination of ground-based instruments improved the aerosol characterization since stand-alone instruments have limited capacity for a complete characterization, and the most robust retrievals (Table 7.1) provided more exactitude in the optical-microphysical properties of the aerosols. The results can support local or global climate modeling, air quality forecasting, validation of satellite products, as a ground-truth reference, climate-change policies, emissions inventories, and local observations and research.

Nevertheless, more complementary studies need to be performed to improve the understanding of aerosol-forcing contributions to the radiation budget, for instance, (i) investigating the influence of water vapor on the radiation budget [40,41,334] and the aerosol forcing; (ii) analyzing surface albedo and other aerosol

properties relevant to estimate the radiative effects, as single scattering albedo, asymmetry factor, phase function, and fine-mode fraction [335,336], which depend on the composition, size distribution, and shape of the particles, varying with wavelength and height [29]; (iii) characterizing the chemical speciation of the aerosol types; (iv) validating the radiative fluxes from GRASP code by retrieving aerosol radiative properties from a large database; and (v) validating the forcing with satellite observations.

BIBLIOGRAPHY

1. Carslaw, K.S. Introduction. In *Aerosols and Climate*; Elsevier, 2022; pp. 1–8 ISBN 978-0-12-819766-0.
2. Core Writing Team; Lee, H.; Romero, J. *IPCC, 2023: Climate Change 2023: Synthesis Report. Contribution of Working Groups I, II and III to the Sixth Assessment Report of the Intergovernmental Panel on Climate Change*; IPCC: Geneva, Switzerland, 2023; p. 184.
3. Intergovernmental Panel On Climate Change (IPCC) Technical Summary. In *Climate Change 2021: The Physical Science Basis. Working Group I Contribution to the Sixth Assessment Report of the Intergovernmental Panel on Climate Change*; Cambridge University Press: United Kingdom and New York, NY, USA, 2021; pp. 33–144 ISBN 978-1-009-15789-6.
4. Seinfeld, J.H.; Pandis, S.N. *Atmospheric Chemistry and Physics: From Air Pollution to Climate Change*; Third.; John Wiley & Sons: Hoboken, New Jersey, 2016; ISBN 978-1-119-22116-6.
5. Yang, B.-Y.; Guo, Y.; Morawska, L.; Bloom, M.S.; Markevych, I.; Heinrich, J.; Dharmage, S.C.; Knibbs, L.D.; Lin, S.; Yim, S.H.-L.; et al. Ambient PM1 Air Pollution and Cardiovascular Disease Prevalence: Insights from the 33 Communities Chinese Health Study. *Environ. Int.* **2019**, *123*, 310–317, doi:10.1016/j.envint.2018.12.012.
6. Canals-Angerri, A.; Via, M.; Lara, R.; Alastuey, A.; Minguillón, M.C.; Pandolfi, M.; Van Drooge, B.L.; Querol, X. Causes of the Unremitting High Ambient Levels of PM10 in a Suburban Background Site in NE Spain. *Environ. Pollut.* **2024**, *363*, 125113, doi:10.1016/j.envpol.2024.125113.
7. Shi, Y.; Chen, J.; Hu, D.; Wang, L.; Yang, X.; Wang, X. Airborne Submicron Particulate (PM1) Pollution in Shanghai, China: Chemical Variability, Formation/Dissociation of Associated Semi-Volatile Components and the Impacts on Visibility. *Sci. Total Environ.* **2014**, *473–474*, 199–206, doi:10.1016/j.scitotenv.2013.12.024.
8. Wang, J.; Wu, J.; Liu, B.; Liu, X.; Gao, H.; Zhang, Y.; Feng, Y.; Han, S.; Gong, X. Exploring the Sensitivity of Visibility to PM2.5 Mass Concentration and Relative Humidity for Different Aerosol Types. *Atmosphere* **2022**, *13*, 471, doi:10.3390/atmos13030471.
9. Meskhidze, N.; Chameides, W.L.; Nenes, A. Dust and Pollution: A Recipe for Enhanced Ocean Fertilization? *J. Geophys. Res. Atmospheres* **2005**, *110*, 2004JD005082, doi:10.1029/2004JD005082.
10. Mackey, K.R.M.; Buck, K.N.; Casey, J.R.; Cid, A.; Lomas, M.W.; Sohrin, Y.; Paytan, A. Phytoplankton Responses to Atmospheric Metal Deposition in the Coastal and Open-Ocean Sargasso Sea. *Front. Microbiol.* **2012**, *3*, doi:10.3389/fmicb.2012.00359.

11. Tang, W.; Llort, J.; Weis, J.; Perron, M.M.G.; Basart, S.; Li, Z.; Sathyendranath, S.; Jackson, T.; Sanz Rodriguez, E.; Proemse, B.C.; et al. Widespread Phytoplankton Blooms Triggered by 2019–2020 Australian Wildfires. *Nature* **2021**, *597*, 370–375, doi:10.1038/s41586-021-03805-8.

12. Hamilton, D.S.; Perron, M.M.G.; Bond, T.C.; Bowie, A.R.; Buchholz, R.R.; Guieu, C.; Ito, A.; Maenhaut, W.; Myriokefalitakis, S.; Olgun, N.; et al. Earth, Wind, Fire, and Pollution: Aerosol Nutrient Sources and Impacts on Ocean Biogeochemistry. *Annu. Rev. Mar. Sci.* **2022**, *14*, 303–330, doi:10.1146/annurev-marine-031921-013612.

13. Yuan, Z.; Achterberg, E.P.; Engel, A.; Wen, Z.; Zhou, L.; Zhu, X.; Dai, M.; Browning, T.J. Phytoplankton Community Response to Episodic Wet and Dry Aerosol Deposition in the Subtropical North Atlantic. *Limnol. Oceanogr.* **2023**, *68*, 2126–2140, doi:10.1002/lno.12410.

14. Jakovljević, T.; Marchetto, A.; Lovreškov, L.; Potočić, N.; Seletković, I.; Indir, K.; Jelić, G.; Butorac, L.; Zgrablić, Ž.; De Marco, A.; et al. Assessment of Atmospheric Deposition and Vitality Indicators in Mediterranean Forest Ecosystems. *Sustainability* **2019**, *11*, 6805, doi:10.3390/su11236805.

15. Wang, R.; Goll, D.; Balkanski, Y.; Hauglustaine, D.; Boucher, O.; Ciais, P.; Janssens, I.; Penuelas, J.; Guenet, B.; Sardans, J.; et al. Global Forest Carbon Uptake Due to Nitrogen and Phosphorus Deposition from 1850 to 2100. *Glob. Change Biol.* **2017**, *23*, 4854–4872, doi:https://doi.org/10.1111/gcb.13766.

16. Koren, I.; Kaufman, Y.J.; Washington, R.; Todd, M.C.; Rudich, Y.; Martins, J.V.; Rosenfeld, D. The Bodélé Depression: A Single Spot in the Sahara That Provides Most of the Mineral Dust to the Amazon Forest. *Environ. Res. Lett.* **2006**, *1*, 014005, doi:10.1088/1748-9326/1/1/014005.

17. Abouchami, W.; Näthe, K.; Kumar, A.; Galer, S.J.G.; Jochum, K.P.; Williams, E.; Horbe, A.M.C.; Rosa, J.W.C.; Balsam, W.; Adams, D.; et al. Geochemical and Isotopic Characterization of the Bodélé Depression Dust Source and Implications for Transatlantic Dust Transport to the Amazon Basin. *Earth Planet. Sci. Lett.* **2013**, *380*, 112–123, doi:10.1016/j.epsl.2013.08.028.

18. Rizzolo, J.A.; Barbosa, C.G.G.; Borillo, G.C.; Godoi, A.F.L.; Souza, R.A.F.; Andreoli, R.V.; Manzi, A.O.; Sá, M.O.; Alves, E.G.; Pöhlker, C.; et al. Soluble Iron Nutrients in Saharan Dust over the Central Amazon Rainforest. *Atmospheric Chem. Phys.* **2017**, *17*, 2673–2687, doi:10.5194/acp-17-2673-2017.

19. Checa-Garcia, R.; Balkanski, Y.; Albani, S.; Bergman, T.; Carslaw, K.; Cozic, A.; Dearden, C.; Marticorena, B.; Michou, M.; Van Noije, T.; et al. Evaluation of Natural Aerosols in CRESCENDO Earth System Models (ESMs): Mineral Dust. *Atmospheric Chem. Phys.* **2021**, *21*, 10295–10335, doi:10.5194/acp-21-10295-2021.

20. Boucher, O.; Randall, D.; Artaxo, P.; Bretherton, C.; Feingold, G.; Forster, P.; Kerminen, V.-M.; Kondo, Y.; Liao, H.; Lohmann, U.; et al. Clouds and Aerosols. In *Climate Change 2013: The Physical Science Basis. Contribution of Working*

Group I to the Fifth Assessment Report of the Intergovernmental Panel on Climate Change; Cambridge University Press: Cambridge, United Kingdom and New York, NY, USA, 2013.

21. Yamasoe, M.A.; Von Randow, C.; Manzi, A.O.; Schafer, J.S.; Eck, T.F.; Holben, B.N. Effect of Smoke and Clouds on the Transmissivity of Photosynthetically Active Radiation inside the Canopy. *Atmospheric Chem. Phys.* **2006**, *6*, 1645–1656, doi:10.5194/acp-6-1645-2006.
22. Albrecht, B.A. Aerosols, Cloud Microphysics, and Fractional Cloudiness. *Science* **1989**, *245*, 1227–1230, doi: 10.1126/science.245.4923.1227.
23. Twomey, S. Pollution and the Planetary Albedo. *Atmospheric Environ. 1967* **1974**, *8*, 1251–1256, doi:https://doi.org/10.1016/0004-6981(74)90004-3.
24. Hansen, J.; Sato, M.; Ruedy, R. Radiative Forcing and Climate Response. *J. Geophys. Res. Atmospheres* **1997**, *102*, 6831–6864, doi:10.1029/96JD03436.
25. Carslaw, K.S. Aerosol in the Climate System. In *Aerosols and Climate*; Elsevier, 2022; pp. 9–52 ISBN 978-0-12-819766-0.
26. Hartmann, D.L. *Global Physical Climatology*; International geophysics; Academic Press: San Diego, 1994; ISBN 978-0-12-328530-0.
27. Wang, Z.; Xue, L.; Liu, J.; Ding, K.; Lou, S.; Ding, A.; Wang, J.; Huang, X. Roles of Atmospheric Aerosols in Extreme Meteorological Events: A Systematic Review. *Curr. Pollut. Rep.* **2022**, *8*, 177–188, doi:10.1007/s40726-022-00216-9.
28. Foyo-Moreno, I.; Alados, I.; Antón, M.; Fernández-Gálvez, J.; Cazorla, A.; Alados-Arboledas, L. Estimating Aerosol Characteristics from Solar Irradiance Measurements at an Urban Location in Southeastern Spain. *J. Geophys. Res. Atmospheres* **2014**, *119*, 1845–1859, doi:https://doi.org/10.1002/2013JD020599.
29. Meloni, D.; Di Sarra, A.; Di Iorio, T.; Fiocco, G. Direct Radiative Forcing of Saharan Dust in the Mediterranean from Measurements at Lampedusa Island and MISR Space-borne Observations. *J. Geophys. Res. Atmospheres* **2004**, *109*, 2003JD003960, doi:10.1029/2003JD003960.
30. Charlson, R.J.; Langner, J.; Rodhe, H.; Leovy, C.B.; Warren, S.G. Perturbation of the Northern Hemisphere Radiative Balance by Backscattering from Anthropogenic Sulfate Aerosols. *Tellus A* **1991**, *43*, 152–163, doi:10.1034/j.1600-0870.1991.00013.x.
31. Bush, B.C.; Valero, F.P.J. Surface Aerosol Radiative Forcing at Gosan during the ACE-Asia Campaign. *J. Geophys. Res.* **2003**, *118*, doi:10.1029/2002JD003233, 2003.
32. Norris, J.R.; Wild, M. Trends in Aerosol Radiative Effects over Europe Inferred from Observed Cloud Cover, Solar “Dimming,” and Solar “Brightening.” *J. Geophys. Res. Atmospheres* **2007**, *112*, doi:10.1029/2006JD007794.

33. Carslaw, K.S.; Boucher, O.; Spracklen, D.V.; Mann, G.W.; Rae, J.G.L.; Woodward, S.; Kulmala, M. A Review of Natural Aerosol Interactions and Feedbacks within the Earth System. *Atmospheric Chem. Phys.* **2010**, *10*, 1701–1737, doi:10.5194/acp-10-1701-2010.

34. López-Cayuela, M.-Á.; Herreras-Giralda, M.; Córdoba-Jabonero, C.; Lopatin, A.; Dubovik, O.; Guerrero-Rascado, J.L. Vertical Assessment of the Mineral Dust Optical and Microphysical Properties as Retrieved from the Synergy between Polarized Micro-Pulse Lidar and Sun/Sky Photometer Observations Using GRASP Code. *Atmospheric Res.* **2021**, *264*, 105818, doi:10.1016/j.atmosres.2021.105818.

35. Charlson, R.J.; Schwartz, S.E.; Hales, J.M.; Cess, R.D.; Coakley, J.A.; Hansen, J.E.; Hofmann, D.J. Climate Forcing by Anthropogenic Aerosols. *Science* **1992**, *255*, 423–430, doi:10.1126/science.255.5043.423.

36. Iqbal, M. *An Introduction to Solar Radiation*; Academic Press: Toronto; New York, 1983; ISBN 978-0-12-373750-2.

37. Bergstrom, R.W.; Pilewskie, P.; Russell, P.B.; Redemann, J.; Bond, T.C.; Quinn, P.K.; Sierau, B. Spectral Absorption Properties of Atmospheric Aerosols. *Atmos Chem Phys* **2007**.

38. Bellouin, N.; Yu, H. Aerosol–Radiation Interactions. In *Aerosols and Climate*; Elsevier, 2022; pp. 445–487 ISBN 978-0-12-819766-0.

39. Zhang, X.; Jiang, H.; Mao, M.; Yin, Y. Does Optically Effective Complex Refractive Index of Internal-Mixed Aerosols Have a Physically-Based Meaning? *Opt. Express* **2019**, *27*, A1216, doi:10.1364/OE.27.0A1216.

40. Di Sarra, A.; Pace, G.; Meloni, D.; De Silvestri, L.; Piacentino, S.; Monteleone, F. Surface Shortwave Radiative Forcing of Different Aerosol Types in the Central Mediterranean. *Geophys. Res. Lett.* **2008**, *35*, 2007GL032395, doi:10.1029/2007GL032395.

41. Di Sarra, A.; Fuà, D.; Meloni, D. Estimate of Surface Direct Radiative Forcing of Desert Dust from Atmospheric Modulation of the Aerosol Optical Depth. *Atmospheric Chem. Phys.* **2013**, *13*, 5647–5654, doi:10.5194/acp-13-5647-2013.

42. IPCC Summary for Policymakers. In *Climate Change 2021: The Physical Science Basis. Contribution of Working Group I to the Sixth Assessment Report of the Intergovernmental Panel on Climate Change*; Switzerland, 2021 ISBN 978-92-9169-158-6.

43. Forster, P.; Ramaswamy, V.; Artaxo, P.; Berntsen, T.; Betts, R.; Fahey, D.W.; Haywood, J.; Lean, J.; Lowe, D.C.; Raga, G.; et al. Changes in Atmospheric Constituents and in Radiative Forcing. In *Climate Change 2007: The Physical Science Basis. Contribution of Working Group I to the Fourth Assessment Report of the Intergovernmental Panel on Climate Change*; Cambridge: United Kingdom and New York, NY, USA, 2007.

44. Holben, B.N.; Eck, T.F.; Slutsker, I.; Tanré, D.; Buis, J.P.; Setzer, A.; Vermote, E.; Reagan, J.A.; Kaufman, Y.J.; Nakajima, T.; et al. AERONET—A Federated Instrument Network and Data Archive for Aerosol Characterization. *Remote Sens. Environ.* **1998**, *66*, 1–16, doi:10.1016/S0034-4257(98)00031-5.

45. Dubovik, O.; King, M.D. A Flexible Inversion Algorithm for Retrieval of Aerosol Optical Properties from Sun and Sky Radiance Measurements. *J. Geophys. Res. Atmospheres* **2000**, *105*, 20673–20696, doi:10.1029/2000JD900282.

46. Dubovik, O.; Smirnov, A.; Holben, B.N.; King, M.D.; Kaufman, Y.J.; Eck, T.F.; Slutsker, I. Accuracy Assessments of Aerosol Optical Properties Retrieved from Aerosol Robotic Network (AERONET) Sun and Sky Radiance Measurements. *J. Geophys. Res. Atmospheres* **2000**, *105*, 9791–9806, doi:10.1029/2000JD900040.

47. O'Neill, N.T.; Ignatov, A.; Holben, B.N.; Eck, T.F. The Lognormal Distribution as a Reference for Reporting Aerosol Optical Depth Statistics; Empirical Tests Using Multi-year, Multi-site AERONET Sunphotometer Data. *Geophys. Res. Lett.* **2000**, *27*, 3333–3336, doi:10.1029/2000GL011581.

48. O'Neill, N.T.; Eck, T.F.; Smirnov, A.; Holben, B.N.; Thulasiraman, S. Spectral Discrimination of Coarse and Fine Mode Optical Depth. *J. Geophys. Res.* **2003**, *108*, 4559, doi:10.1029/2002JD002975.

49. Sinyuk, A.; Holben, B.N.; Eck, T.F.; Giles, D.M.; Slutsker, I.; Korkin, S.; Schafer, J.S.; Smirnov, A.; Sorokin, M.; Lyapustin, A. The AERONET Version 3 Aerosol Retrieval Algorithm, Associated Uncertainties and Comparisons to Version 2. *Atmospheric Meas. Tech.* **2020**, *13*, 3375–3411, doi:10.5194/amt-13-3375-2020.

50. Takayabu, Y.N.; Ueno, T.; Nakajima, T.; Matsui, I.; Tsushima, Y.; Aoki, K.; Sugimoto, N.; Uno, I. Estimate of the Cloud and Aerosol Effects on the Surface Radiative Flux Based on the Measurements and the Transfer Model Calculations Part I: Shortwave Forcing at Tateno, Japan. *J. Meteorol. Soc. Jpn.* **1999**, *77*, 1007–1021, doi:10.2151/jmsj1965.77.5_1007.

51. Lopatin, A.; Dubovik, O.; Chaikovsky, A.; Goloub, P.; Lapyonok, T.; Tanré, D.; Litvinov, P. Enhancement of Aerosol Characterization Using Synergy of Lidar and Sun-Photometer Coincident Observations: The GARRLiC Algorithm. *Atmospheric Meas. Tech.* **2013**, *6*, 2065–2088, doi:10.5194/amt-6-2065-2013.

52. Chaikovsky, A.P.; O. Dubovik; Brent N. Holben; Andrey I. Bril Methodology to Retrieve Atmospheric Aerosol Parameters by Combining Ground-Based Measurements of Multiwavelength Lidar and Sun Sky-Scanning Radiometer.; February 28, 2002; Vol. 4678, pp. 257–268.

53. Böckmann, C. Hybrid Regularization Method for the Ill-Posed Inversion of Multiwavelength Lidar Data in the Retrieval of Aerosol Size Distributions. *Appl. Opt.* **2001**, *40*, 1329, doi:10.1364/AO.40.001329.

54. Böckmann, C.; Mironova, I.; Müller, D.; Schneidenbach, L.; Nessler, R. Microphysical Aerosol Parameters from Multiwavelength Lidar. *J. Opt. Soc. Am. A* **2005**, *22*, 518, doi:10.1364/JOSAA.22.000518.

55. Böckmann, C.; Ritter, C.; Cappelletti, D. Mathematical Tool for a Closure Study of Aerosol Microphysical Property Retrieval Using Lidar and Photometer Data. In Proceedings of the IGARSS 2018 - 2018 IEEE International Geoscience and Remote Sensing Symposium; IEEE: Valencia, July 2018; pp. 5575–5578.

56. Chaikovsky; A. I. Bril; Vladimir V. Barun; O. Dubovik; Brent N. Holben; Philippe Goloub; P. Sobolewski Methodology and Sample Results of Retrieving Aerosol Parameters by Combined Multiwavelength Lidar and Sun-Sky Scanning Measurements.; February 23, 2004; Vol. 5397, pp. 146–157.

57. Chaikovsky, A.; Dubovik, O.; Goloub, P.; Tanre, D.; Lopatsin, A.; Denisov, S.; Lapyonok, T.; Karol, Y. THE RETRIEVAL OF AEROSOL MICROPHYSICAL PROPERTIES IN THE VERTICAL COLUMN USING COMBINED LIDAR/PHOTOMETER DATA: A STEP TO INTEGRATING PHOTOMETER AND LIDAR NETWORKS. In Proceedings of the Curran Associates, Inc.; Curran Associates: Red Hook, NY, 2010.

58. Chaikovsky, A.; Dubovik, O.; Holben, B.; Bril, A.; Goloub, P.; Tanré, D.; Pappalardo, G.; Wandinger, U.; Chaikovskaya, L.; Denisov, S.; et al. Lidar-Radiometer Inversion Code (LIRIC) for the Retrieval of Vertical Aerosol Properties from Combined Lidar/Radiometer Data: Development and Distribution in EARLINET. *Atmospheric Meas. Tech.* **2016**, *9*, 1181–1205, doi:10.5194/amt-9-1181-2016.

59. Cuesta, J.; Flamant, P.H.; Flamant, C. Synergetic Technique Combining Elastic Backscatter Lidar Data and Sunphotometer AERONET Inversion for Retrieval by Layer of Aerosol Optical and Microphysical Properties. *Appl. Opt.* **2008**, *47*, 4598, doi:10.1364/AO.47.004598.

60. Ansmann, A.; Tesche, M.; Seifert, P.; Groß, S.; Freudenthaler, V.; Apituley, A.; Wilson, K.M.; Serikov, I.; Linné, H.; Heinold, B.; et al. Ash and Fine-Mode Particle Mass Profiles from EARLINET-AERONET Observations over Central Europe after the Eruptions of the Eyjafjallajökull Volcano in 2010. *J. Geophys. Res.* **2011**, *116*, doi:10.1029/2010jd015567.

61. Ansmann, A.; Seifert, P.; Tesche, M.; Wandinger, U. Profiling of Fine and Coarse Particle Mass: Case Studies of Saharan Dust and Eyjafjallajökull/Grimsvötn Volcanic Plumes. *Atmospheric Chem. Phys.* **2012**, *12*, 9399–9415, doi:10.5194/acp-12-9399-2012.

62. Ganguly, D.; Ginoux, P.; Ramaswamy, V.; Dubovik, O.; Welton, J.; Reid, E.A.; Holben, B.N. Inferring the Composition and Concentration of Aerosols by Combining AERONET and MPLNET Data: Comparison with Other Measurements and Utilization to Evaluate GCM Output. *J. Geophys. Res.* **2009**, *114*, D16203, doi:10.1029/2009JD011895.

63. Lopatin, A. Enhanced Remote Sensing of Atmospheric Aerosol by Joint Inversion of Active and Passive Remote Sensing Observations. PhD Thesis, Université de Lille: Lille, France, 2013.

64. Dubovik, O.; Herman, M.; Holdak, A.; Lapyonok, T.; Tanré, D.; Deuzé, J.L.; Ducos, F.; Sinyuk, A.; Lopatin, A. Statistically Optimized Inversion Algorithm for Enhanced Retrieval of Aerosol Properties from Spectral Multi-Angle Polarimetric Satellite Observations. *Atmospheric Meas. Tech.* **2011**, *4*, 975–1018, doi:10.5194/amt-4-975-2011.

65. Mishchenko, M.I.; Travis, L.D. Satellite Retrieval of Aerosol Properties over the Ocean Using Polarization as Well as Intensity of Reflected Sunlight. *J. Geophys. Res. Atmospheres* **1997**, *102*, 16989–17013, doi:10.1029/96JD02425.

66. Li, Z.; Goloub, P.; Devaux, C.; Gu, X.; Deuzé, J.-L.; Qiao, Y.; Zhao, F. Retrieval of Aerosol Optical and Physical Properties from Ground-Based Spectral, Multi-Angular, and Polarized Sun-Photometer Measurements. *Remote Sens. Environ.* **2006**, *101*, 519–533, doi:10.1016/j.rse.2006.01.012.

67. Dubovik, O.; Sinyuk, A.; Lapyonok, T.; Holben, B.N.; Mishchenko, M.; Yang, P.; Eck, T.F.; Volten, H.; Muñoz, O.; Veihelmann, B.; et al. Application of Spheroid Models to Account for Aerosol Particle Nonsphericity in Remote Sensing of Desert Dust. *J. Geophys. Res.* **2006**, *111*, D11208, doi:10.1029/2005JD006619.

68. Li, Z.; Goloub, P.; Dubovik, O.; Blarel, L.; Zhang, W.; Podvin, T.; Sinyuk, A.; Sorokin, M.; Chen, H.; Holben, B.; et al. Improvements for Ground-Based Remote Sensing of Atmospheric Aerosol Properties by Additional Polarimetric Measurements. *J. Quant. Spectrosc. Radiat. Transf.* **2009**, *110*, 1954–1961, doi:10.1016/j.jqsrt.2009.04.009.

69. Fedarenka, A.; Dubovik, O.; Goloub, P.; Li, Z.; Lapyonok, T.; Litvinov, P.; Barel, L.; Gonzalez, L.; Podvin, T.; Crozel, D. Utilization of AERONET Polarimetric Measurements for Improving Retrieval of Aerosol Microphysics: GSFC, Beijing and Dakar Data Analysis. *J. Quant. Spectrosc. Radiat. Transf.* **2016**, *179*, 72–97, doi:10.1016/j.jqsrt.2016.03.021.

70. Sekera, Z. Introduction. In *Polarization of skylight*; Springer, Berlin, Heidelberg: Berlin, Germany, 1957; Vol. 10/48, pp. 288–328, ISBN 978-3-642-45881-1.

71. Satheesh, S.K.; Ramanathan, V. Large Differences in Tropical Aerosol Forcing at the Top of the Atmosphere and Earth's Surface. *Nature* **2000**, *405*, 60–63, doi:10.1038/35011039.

72. Yıldız, İ. Solar Energy. In *Comprehensive Energy Systems*; Elsevier, 2018; pp. 638–664 ISBN 978-0-12-814925-6.

73. Jones, H.G.; Vaughan, R.A. *Remote Sensing of Vegetation: Principles, Techniques, and Applications*; Oxford University Press: Oxford, United Kingdom, 2010; ISBN 978-0-19-920779-4.

74. Jones, H.G. *Plants and Microclimate: A Quantitative Approach to Environmental Plant Physiology*; Third edition; Cambridge University Press: Cambridge, United Kingdom, 2014; ISBN 978-0-521-27959-8.

75. Gallagher, R.P.; Lee, T.K. Adverse Effects of Ultraviolet Radiation: A Brief Review. *Prog. Biophys. Mol. Biol.* **2006**, *92*, 119–131, doi:10.1016/j.pbiomolbio.2006.02.011.

76. Narayanan, D.L.; Saladi, R.N.; Fox, J.L. Review: Ultraviolet Radiation and Skin Cancer. *Int. J. Dermatol.* **2010**, *49*, 978–986, doi:10.1111/j.1365-4632.2010.04474.x.

77. Häder, D.-P.; Helbling, E.W.; Williamson, C.E.; Worrest, R.C. Effects of UV Radiation on Aquatic Ecosystems and Interactions with Climate Change. *Photochem. Photobiol. Sci.* **2011**, *10*, 242–260, doi:10.1039/c0pp90036b.

78. Barnes, P.W.; Robson, T.M.; Zepp, R.G.; Bornman, J.F.; Jansen, M.A.K.; Ossola, R.; Wang, Q.-W.; Robinson, S.A.; Foereid, B.; Klekociuk, A.R.; et al. Interactive Effects of Changes in UV Radiation and Climate on Terrestrial Ecosystems, Biogeochemical Cycles, and Feedbacks to the Climate System. *Photochem. Photobiol. Sci.* **2023**, *22*, 1049–1091, doi:10.1007/s43630-023-00376-7.

79. Austin, A.T.; Ballaré, C.L. Photodegradation in Terrestrial Ecosystems. *New Phytol.* **2024**, *244*, 769–785, doi:10.1111/nph.20105.

80. Lozano, I.L.; Sánchez-Hernández, G.; Guerrero-Rascado, J.L.; Alados, I.; Foyo-Moreno, I. Aerosol Radiative Effects in Photosynthetically Active Radiation and Total Irradiance at a Mediterranean Site from an 11-Year Database. *Atmospheric Res.* **2021**, *255*, 105538, doi:10.1016/j.atmosres.2021.105538.

81. Liou, K.N. *An Introduction to Atmospheric Radiation*; INTERNATIONAL GEOPHYSICS SERIES; 2nd ed.; Academic Press: San Diego, California, 2002; Vol. 84; ISBN 0-12-451451-0.

82. *Guide to Meteorological Instruments and Methods of Observation*; World Meteorological Organization: Geneva, 2023; ISBN 978-92-63-10008-5.

83. Solar Radiation Measurement: Progress in Radiometry for Improved Modeling. In *Modeling solar radiation at the earth's surface: recent advances*; Badescu, V., Ed.; Springer: Berlin, 2008; pp. 1–28, ISBN 978-3-540-77454-9.

84. Stephens, G.L.; Li, J.; Wild, M.; Clayson, C.A.; Loeb, N.; Kato, S.; L'Ecuyer, T.; Stackhouse, P.W.; Lebsock, M.; Andrews, T. An Update on Earth's Energy Balance in Light of the Latest Global Observations. *Nat. Geosci.* **2012**, *5*, 691–696, doi:10.1038/ngeo1580.

85. Ahrens, C.D. *Essentials of Meteorology: An Invitation to the Atmosphere*; Essentials of Meteorology: An Invitation to the Atmosphere; Thomson Brooks/Cole, 2008; ISBN 978-0-495-11558-8.

86. Schmauß, A. Kolloidchemie and Meteorologie. *Meteorologische Zeitschrift* **1920**, *37*, 1–8.

87. Schmauss, A. Kolloidchemie Und Meteorologie. *Kolloid-Z.* **1922**, *31*, 266–269, doi:10.1007/BF01423586.

88. Junge, C.E. 2 Aerosols. In *International Geophysics*; Academic Press, 1963; Vol. 4, pp. 111–208, ISBN 978-0-12-392150-5.

89. Bellouin, N.; Quaas, J.; Gryspeerdt, E.; Kinne, S.; Stier, P.; Watson-Parris, D.; Boucher, O.; Carslaw, K.S.; Christensen, M.; Daniau, A. -L.; et al. Bounding Global Aerosol Radiative Forcing of Climate Change. *Rev. Geophys.* **2020**, *58*, e2019RG000660, doi:10.1029/2019RG000660.

90. Carslaw, K.S.; Pringle, K. Global Aerosol Properties. In *Aerosols and Climate*; Elsevier, 2022; pp. 101–133 ISBN 978-0-12-819766-0.

91. Hoesly, R.M.; Smith, S.J.; Feng, L.; Klimont, Z.; Janssens-Maenhout, G.; Pitkanen, T.; Seibert, J.J.; Vu, L.; Andres, R.J.; Bolt, R.M.; et al. Historical (1750–2014) Anthropogenic Emissions of Reactive Gases and Aerosols from the Community Emissions Data System (CEDS). *Geosci. Model Dev.* **2018**, *11*, 369–408, doi:10.5194/gmd-11-369-2018.

92. Carslaw, K.S. Aerosol Processes. In *Aerosols and Climate*; Elsevier, 2022; pp. 135–185 ISBN 978-0-12-819766-0.

93. Buseck, P.R.; Adachi, K. Nanoparticles in the Atmosphere. *Elements* **2008**, *4*, 389–394, doi:10.2113/gselements.4.6.389.

94. Alves, C. Aerossóis atmosféricos: perspectiva histórica, fontes, processos químicos de formação e composição orgânica. *Quím. Nova* **2005**, *28*, 859–870, doi:10.1590/S0100-40422005000500025.

95. O'Dowd, C.D.; De Leeuw, G. Marine Aerosol Production: A Review of the Current Knowledge. *Philos. Trans. R. Soc. Math. Phys. Eng. Sci.* **2007**, *365*, 1753–1774, doi:10.1098/rsta.2007.2043.

96. Hu, R. -M.; Blanchet, J. -P.; Girard, E. Evaluation of the Direct and Indirect Radiative and Climate Effects of Aerosols over the Western Arctic. *J. Geophys. Res. Atmospheres* **2005**, *110*, 2004JD005043, doi:10.1029/2004JD005043.

97. Quinn, P.K.; Bates, T.S.; Baum, E.; Doubleday, N.; Fiore, A.M.; Flanner, M.; Fridlind, A.; Garrett, T.J.; Koch, D.; Menon, S.; et al. Short-Lived Pollutants in the Arctic: Their Climate Impact and Possible Mitigation Strategies. *Atmos Chem Phys* **2008**.

98. Zender, C.S.; Miller, R.L.R.L.; Tegen, I. Quantifying Mineral Dust Mass Budgets: Terminology, Constraints, and Current Estimates. *Eos Trans. Am. Geophys. Union* **2004**, *85*, 509–512, doi:10.1029/2004EO480002.

99. Gallisai, R.; Peters, F.; Volpe, G.; Basart, S.; Baldasano, J.M. Saharan Dust Deposition May Affect Phytoplankton Growth in the Mediterranean Sea at Ecological Time Scales. *PLoS ONE* **2014**, *9*, e110762, doi:10.1371/journal.pone.0110762.

100. Zhao, C.; Li, Y.; Zhou, Z.; Wu, R.; Su, M.; Song, H. Simulated Wind Erosion and Local Dust Deposition Affect Soil Micro-Food Web by Changing Resource Availability. *Ecol. Process.* **2025**, *14*, 7, doi:10.1186/s13717-024-00574-w.

101. Richardson, S.C.; Mytilinaios, M.; Foskinis, R.; Kyrou, C.; Papayannis, A.; Pyrri, I.; Giannoutsou, E.; Adamakis, I.D.S. Bioaerosol Detection over Athens, Greece Using the Laser Induced Fluorescence Technique. *Sci. Total Environ.* **2019**, *696*, 133906, doi:10.1016/j.scitotenv.2019.133906.

102. Weikl, F.; Radl, V.; Munch, J.C.; Pritsch, K. Targeting Allergenic Fungi in Agricultural Environments Aids the Identification of Major Sources and Potential Risks for Human Health. *Sci. Total Environ.* **2015**, *529*, 223–230, doi:10.1016/j.scitotenv.2015.05.056.

103. Whitehead, J.D.; Darbyshire, E.; Brito, J.; Barbosa, H.M.J.; Crawford, I.; Stern, R.; Gallagher, M.W.; Kaye, P.H.; Allan, J.D.; Coe, H.; et al. Biogenic Cloud Nuclei in the Central Amazon during the Transition from Wet to Dry Season. *Atmospheric Chem. Phys.* **2016**, *16*, 9727–9743, doi:10.5194/acp-16-9727-2016.

104. Ariya, P.A.; Amyot, M. New Directions: The Role of Bioaerosols in Atmospheric Chemistry and Physics. *Atmos. Environ.* **2004**, *38*, 1231–1232, doi:10.1016/j.atmosenv.2003.12.006.

105. Prenni, A.J.; Petters, M.D.; Kreidenweis, S.M.; Heald, C.L.; Martin, S.T.; Artaxo, P.; Garland, R.M.; Wollny, A.G.; Pöschl, U. Relative Roles of Biogenic Emissions and Saharan Dust as Ice Nuclei in the Amazon Basin. *Nat. Geosci.* **2009**, *2*, 402–405, doi:10.1038/ngeo517.

106. Koren, I.; Kaufman, Y.J.; Remer, L.A.; Martins, J.V. Measurement of the Effect of Amazon Smoke on Inhibition of Cloud Formation. *Science* **2004**, *303*, 1342–1345, doi:10.1126/science.1089424.

107. Bond, T.C.; Doherty, S.J.; Fahey, D.W.; Forster, P.M.; Berntsen, T.; DeAngelo, B.J.; Flanner, M.G.; Ghan, S.; Kärcher, B.; Koch, D.; et al. Bounding the Role of Black Carbon in the Climate System: A Scientific Assessment. *J. Geophys. Res. Atmospheres* **2013**, *118*, 5380–5552, doi:10.1002/jgrd.50171.

108. Pace, G.; di Sarra, A.; Meloni, D.; Piacentino, S.; Chamard, P. Aerosol Optical Properties at Lampedusa (Central Mediterranean). 1. Influence of Transport and Identification of Different Aerosol Types. *Atmos Chem Phys* **2006**.

109. Sicard, M.; Bertolín, S.; Mallet, M.; Dubuisson, P.; Comerón, A. Estimation of Mineral Dust Long-Wave Radiative Forcing: Sensitivity Study to Particle Properties and Application to Real Cases in the Region of Barcelona. *Atmospheric Chem. Phys.* **2014**, *14*, 9213–9231, doi:10.5194/acp-14-9213-2014.

110. Keil, A.; Haywood, J.M. Solar Radiative Forcing by Biomass Burning Aerosol Particles during SAFARI 2000: A Case Study Based on Measured Aerosol and Cloud Properties. *J. Geophys. Res. Atmospheres* **2003**, *108*, 2002JD002315, doi:10.1029/2002JD002315.

111. Meloni, D.; Di Sarra, A.; Di Iorio, T.; Fiocco, G. Influence of the Vertical Profile of Saharan Dust on the Visible Direct Radiative Forcing. *J. Quant. Spectrosc. Radiat. Transf.* **2005**, *93*, 397–413, doi:10.1016/j.jqsrt.2004.08.035.

112. Boucher, O.; Schwartz, S.E.; Ackerman, T.P.; Anderson, T.L.; Bergstrom, B.; Bonnel, B.; Chýlek, P.; Dahlback, A.; Fouquart, Y.; Fu, Q.; et al. Intercomparison of Models Representing Direct Shortwave Radiative Forcing by Sulfate Aerosols. *J. Geophys. Res. Atmospheres* **1998**, *103*, 16979–16998, doi:10.1029/98JD00997.

113. Mateos, D.; Antón, M.; Valenzuela, A.; Cazorla, A.; Olmo, F.J.; Alados-Arboledas, L. Short-Wave Radiative Forcing at the Surface for Cloudy Systems at a Midlatitude Site. *Tellus B Chem. Phys. Meteorol.* **2013**, *65*, 21069, doi:10.3402/tellusb.v65i0.21069.

114. Wu, Y.; Cheng, T.; Zheng, L.; Chen, H. Black Carbon Radiative Forcing at TOA Decreased during Aging. *Sci. Rep.* **2016**, *6*, 38592, doi:10.1038/srep38592.

115. Xie, Y.; Li, Z.; Li, L.; Wagener, R.; Abboud, I.; Li, K.; Li, D.; Zhang, Y.; Chen, X.; Xu, H. Aerosol Optical, Microphysical, Chemical and Radiative Properties of High Aerosol Load Cases over the Arctic Based on AERONET Measurements. *Sci. Rep.* **2018**, *8*, 9376, doi:10.1038/s41598-018-27744-z.

116. Bohren, C.F.; Huffman, D.R. *Absorption and Scattering of Light by Small Particles*; A Wiley-Interscience publication; Wiley-CH Verlag GmbH & Co KGaA: New York, 2004; ISBN 978-0-471-29340-8.

117. Mie, G. Beiträge zur Optik trüber Medien, speziell kolloidaler Metallösungen. *Ann. Phys.* **1908**, *330*, 377–445, doi:10.1002/andp.19083300302.

118. Denjean, C.; Cassola, F.; Mazzino, A.; Triquet, S.; Chevaillier, S.; Grand, N.; Bourrianne, T.; Momboisse, G.; Sellegri, K.; Schwarzenbock, A.; et al. Size Distribution and Optical Properties of Mineral Dust Aerosols Transported in the Western Mediterranean. *Atmospheric Chem. Phys.* **2016**, *16*, 1081–1104, doi:10.5194/acp-16-1081-2016.

119. Hänel, G. The Properties of Atmospheric Aerosol Particles as Functions of the Relative Humidity at Thermodynamic Equilibrium with the Surrounding Moist Air. In *Advances in Geophysics*; Elsevier, 1976; Vol. 19, pp. 73–188 ISBN 978-0-12-018819-2.

120. Kanakidou, M.; Seinfeld, J.H.; Pandis, S.N.; Barnes, I.; Dentener, F.J.; Facchini, M.C.; Dingenen, R.V.; Ervens, B.; Nenes, A.; Nielsen, C.J.; et al. Organic Aerosol and Global Climate Modelling: A Review. *Atmos Chem Phys* **2005**.

121. Rudich, Y.; Donahue, N.M.; Mentel, T.F. Aging of Organic Aerosol: Bridging the Gap Between Laboratory and Field Studies. *Annu. Rev. Phys. Chem.* **2007**, *58*, 321–352, doi:10.1146/annurev.physchem.58.032806.104432.

122. Kasten, F. Visibility Forecast in the Phase of Pre-Condensation. *Tellus* **1969**, *21*, 631–635, doi:10.1111/j.2153-3490.1969.tb00469.x.

123. Sheridan, P.J.; Jefferson, A.; Ogren, J.A. Spatial Variability of Submicrometer Aerosol Radiative Properties over the Indian Ocean during INDOEX. *J. Geophys. Res. Atmospheres* **2002**, *107*, doi:10.1029/2000JD000166.

124. Skupin, A.; Ansmann, A.; Engelmann, R.; Seifert, P.; Müller, T. Four-Year Long-Path Monitoring of Ambient Aerosol Extinction at a Central European Urban Site: Dependence on Relative Humidity. *Atmospheric Chem. Phys.* **2016**, *16*, 1863–1876, doi:10.5194/acp-16-1863-2016.

125. Titos, G.; Cazorla, A.; Zieger, P.; Andrews, E.; Lyamani, H.; Granados-Muñoz, M.J.; Olmo, F.J.; Alados-Arboledas, L. Effect of Hygroscopic Growth on the Aerosol Light-Scattering Coefficient: A Review of Measurements, Techniques and Error Sources. *Atmos. Environ.* **2016**, *141*, 494–507, doi:10.1016/j.atmosenv.2016.07.021.

126. Haarig, M.; Ansmann, A.; Althausen, D.; Klepel, A.; Groß, S.; Freudenthaler, V.; Toledano, C.; Mamouri, R.-E.; Farrell, D.A.; Prescod, D.A.; et al. Triple-Wavelength Depolarization-Ratio Profiling of Saharan Dust over Barbados during SALTRACE in 2013 and 2014. *Atmospheric Chem. Phys.* **2017**, *17*, 10767–10794, doi:10.5194/acp-17-10767-2017.

127. Bedoya-Velásquez, A.E.; Navas-Guzmán, F.; Granados-Muñoz, M.J.; Titos, G.; Román, R.; Casquero-Vera, J.A.; Ortiz-Amezcua, P.; Benavent-Oltra, J.A.; De Arruda Moreira, G.; Montilla-Rosero, E.; et al. Hygroscopic Growth Study in the Framework of EARLINET during the SLOPE I Campaign: Synergy of Remote Sensing and in Situ Instrumentation. *Atmospheric Chem. Phys.* **2018**, *18*, 7001–7017, doi:10.5194/acp-18-7001-2018.

128. Dawson, K.W.; Ferrare, R.A.; Moore, R.H.; Clayton, M.B.; Thorsen, T.J.; Eloranta, E.W. Ambient Aerosol Hygroscopic Growth From Combined Raman Lidar and HSRL. *J. Geophys. Res. Atmospheres* **2020**, *125*, e2019JD031708, doi:10.1029/2019JD031708.

129. Sicard, M.; Fortunato Dos Santos Oliveira, D.C.; Muñoz-Porcar, C.; Gil-Díaz, C.; Comerón, A.; Rodríguez-Gómez, A.; Dios Otín, F. Measurement Report: Spectral and Statistical Analysis of Aerosol Hygroscopic Growth from Multi-Wavelength Lidar Measurements in Barcelona, Spain. *Atmospheric Chem. Phys.* **2022**, *22*, 7681–7697, doi:10.5194/acp-22-7681-2022.

130. Dubovik, O.; Holben, B.; Eck, T.F.; Smirnov, A.; Kaufman, Y.J.; King, M.D.; Tanré, D.; Slutsker, I. Variability of Absorption and Optical Properties of Key Aerosol Types Observed in Worldwide Locations. *J. Atmospheric Sci.* **2002**, *59*, 590–608, doi:10.1175/1520-0469(2002)059<0590:VOAAOP>2.0.CO;2.

131. Kokhanovsky, A.A. Aerosol Optics: Light Absorption and Scattering by Particles in the Atmosphere. *Choice Rev. Online* **2008**, *46*, 46-1543-46–1543, doi:10.5860/CHOICE.46-1543.

132. Kasten, F.; Young, A.T. Revised Optical Air Mass Tables and Approximation Formula. *Appl. Opt.* **1989**, *28*, 4735, doi:10.1364/AO.28.004735.

133. Ångström, A. On the Atmospheric Transmission of Sun Radiation and on Dust in the Air. *Geogr. Ann.* **1929**, *11*, 156, doi:10.2307/519399.

134. Oliveira, D.C.F. dos S.; Sicard, M.; Rodríguez-Gómez, A.; Comerón, A.; Muñoz-Porcar, C.; Gil-Díaz, C.; Lolli, S.; Dubovik, O.; Lopatin, A.; Herrera, M.E.; et al. Evaluation of the Accuracy of the Aerosol Optical and Microphysical Retrievals by the GRASP Algorithm from Combined Measurements of a Polarized Sun-Sky-Lunar Photometer and a Three-Wavelength Elastic Lidar. *Remote Sens.* **2023**, *15*, 5010, doi:10.3390/rs15205010.

135. Gorchakov, G.I. Light scattering matrices of atmospheric air. *Izv. Akad. Nauk SSSR Fiz. Atmos. Okeana* **1966**, *2*, 595–605.

136. Stokes, G.G. *Mathematical and Physical Papers*; 1st ed.; Cambridge University Press, 1852; Vol. 9; ISBN 978-1-108-00264-6.

137. Knobelspiesse, K.; van Diedenhoven, B.; Marshak, A.; Dunagan, S.; Holben, B.; Slutsker, I. Cloud Thermodynamic Phase Detection with Polarimetrically Sensitive Passive Sky Radiometers. *Atmospheric Meas. Tech.* **2015**, *8*, 1537–1554, doi:10.5194/amt-8-1537-2015.

138. Kokhanovsky, A.A. *Polarization of Light in the Atmosphere and Ocean*; Springer Berlin Heidelberg: Berlin, Heidelberg, 2016; ISBN 978-3-662-46761-9.

139. Chandrasekhar, S. *Radiative Transfer*; Dover Publications: New York, NY, USA, 1960; ISBN 978-0-486-60590-6.

140. Gassó, S.; Knobelspiesse, K.D. Circular Polarization in Atmospheric Aerosols. *Atmospheric Chem. Phys.* **2022**, *22*, 13581–13605, doi:10.5194/acp-22-13581-2022.

141. Kahn, R.; Samset, B.H. Remote Sensing Measurements of Aerosol Properties. In *Aerosols and Climate*; Elsevier, 2022; pp. 395–444 ISBN 978-0-12-819766-0.

142. Winker, D.M.; Hunt, W.H.; McGill, M.J. Initial Performance Assessment of CALIOP. *Geophys. Res. Lett.* **2007**, *34*, 2007GL030135, doi:10.1029/2007GL030135.

143. Winker, D.M.; Vaughan, M.A.; Omar, A.; Hu, Y.; Powell, K.A.; Liu, Z.; Hunt, W.H.; Young, S.A. Overview of the CALIPSO Mission and CALIOP Data Processing Algorithms. *J. Atmospheric Ocean. Technol.* **2009**, *26*, 2310–2323, doi:10.1175/2009JTECHA1281.1.

144. Illingworth, A.J.; Barker, H.W.; Beljaars, A.; Ceccaldi, M.; Chepfer, H.; Clerbaux, N.; Cole, J.; Delanoë, J.; Domenech, C.; Donovan, D.P.; et al. The EarthCARE Satellite: The Next Step Forward in Global Measurements of Clouds, Aerosols, Precipitation, and Radiation. *Bull. Am. Meteorol. Soc.* **2015**, *96*, 1311–1332, doi:10.1175/BAMS-D-12-00227.1.

145. Donovan, D.P. The Expected Impact of Multiple Scattering on ATLID Signals. *EPJ Web Conf.* **2016**, *119*, 01006, doi:10.1051/epjconf/201611901006.

146. Donovan, D.; Zadelhoff, G.-J.V.; Daou, D.; Wandinger, U. Earthcare Atlid Extinction and Backscatter Retrieval Algorithms. *EPJ Web Conf.* **2018**, *176*, 02022, doi:10.1051/epjconf/201817602022.

147. Andrews, E.; Sheridan, P.J.; Ogren, J.A.; Hageman, D.; Jefferson, A.; Wendell, J.; Alástuey, A.; Alados-Arboledas, L.; Bergin, M.; Ealo, M.; et al. Overview of the NOAA/ESRL Federated Aerosol Network. *Bull. Am. Meteorol. Soc.* **2019**, *100*, 123–135, doi:10.1175/BAMS-D-17-0175.1.

148. Petzold, A.; Thouret, V.; Gerbig, C.; Zahn, A.; Brenninkmeijer, C.A.M.; Gallagher, M.; Hermann, M.; Pontaud, M.; Ziereis, H.; Boulanger, D.; et al. Global-Scale Atmosphere Monitoring by in-Service Aircraft – Current Achievements and Future Prospects of the European Research Infrastructure IAGOS. *Tellus B Chem. Phys. Meteorol.* **2015**, *67*, 28452, doi:10.3402/tellusb.v67.28452.

149. Reddington, C.L.; Carslaw, K.S.; Stier, P.; Schutgens, N.; Coe, H.; Liu, D.; Allan, J.; Browse, J.; Pringle, K.J.; Lee, L.A.; et al. The Global Aerosol Synthesis and Science Project (GASSP): Measurements and Modeling to Reduce Uncertainty. *Bull. Am. Meteorol. Soc.* **2017**, *98*, 1857–1877, doi:10.1175/BAMS-D-15-00317.1.

150. Pappalardo, G.; Amodeo, A.; Apituley, A.; Comeron, A.; Freudenthaler, V.; Linné, H.; Ansmann, A.; Bösenberg, J.; D'Amico, G.; Mattis, I.; et al. EARLINET: Towards an Advanced Sustainable European Aerosol Lidar Network. *Atmospheric Meas. Tech.* **2014**, *7*, 2389–2409, doi:10.5194/amt-7-2389-2014.

151. MIDDLETON, W.E.K.; SPILHAUS, A.F. *Meteorological Instruments: Third Edition*; 3rd ed.; University of Toronto Press, 1953; ISBN 978-1-4875-7229-7.

152. *Lidar: Range-Resolved Optical Remote Sensing of the Atmosphere*; Weitkamp, C., Ed.; Springer series in optical sciences; Springer: New York, 2005; ISBN 978-0-387-40075-4.

153. Maiman, T.H. Stimulated Optical Radiation in Ruby. *Nature Publishing Group* **1960**, *187*, 493–494.

154. McClung, F.J.; Hellwarth, R.W. Giant Optical Pulsations from Ruby.

155. Silfvast, W.T. *Laser Fundamentals*; Second edition published 2004, first paperback edition 2008.; Cambridge University Press: Cambridge, 2004; ISBN 978-0-521-83345-5.

156. Kovalev, V.A.; Eichinger, W.E. *Elastic Lidar: Theory, Practice, and Analysis Methods*; 1st ed.; Wiley, 2004; ISBN 978-0-471-20171-7.

157. PHOTON COUNTING: Using Photomultiplier Tubes 1998.

158. Freudenthaler, V.; Esselborn, M.; Wiegner, M.; Heese, B.; Tesche, M.; Ansmann, A.; Müller, D.; Althausen, D.; Wirth, M.; Fix, A.; et al. Depolarization Ratio Profiling at Several Wavelengths in Pure Saharan Dust during SAMUM

2006. *Tellus B Chem. Phys. Meteorol.* **2009**, *61*, 165, doi:10.1111/j.1600-0889.2008.00396.x.

159. Saito, Y.; Hosokawa, T.; Shiraishi, K. Collection of Excitation-Emission-Matrix Fluorescence of Aerosol-Candidate-Substances and Its Application to Fluorescence Lidar Monitoring. *Appl. Opt.* **2022**, *61*, 653, doi:10.1364/AO.445507.

160. Pan, Y.-L. Detection and Characterization of Biological and Other Organic-Carbon Aerosol Particles in Atmosphere Using Fluorescence. *J. Quant. Spectrosc. Radiat. Transf.* **2015**, *150*, 12–35, doi:10.1016/j.jqsrt.2014.06.007.

161. Sugimoto, N.; Nishizawa, T.; Shimizu, A.; Jin, Y. The Asian Dust and Aerosol Lidar Observation Network (AD-Net). In Proceedings of the Light, Energy and the Environment; OSA: Leipzig, 2016; p. EW2A.1.

162. Nishizawa, T.; Sugimoto, N.; Matsui, I.; Shimizu, A.; Higurashi, A.; Jin, Y. The Asian Dust and Aerosol Lidar Observation Network (AD-NET): Strategy and Progress. *EPJ Web Conf.* **2016**, *119*, 19001, doi:10.1051/epjconf/201611919001.

163. Chaikovsky, A.; Ivanov, A.; Balin, Yu.; Elnikov, A.; Tulinov, G.; Plusnin, I.; Bukin, O.; Chen, B. Lidar Network CIS-LiNet for Monitoring Aerosol and Ozone in CIS Regions.; Zherebtsov, G.A., Matvienko, G.G., Eds.; February 14 2006; pp. 616035-616035–616039.

164. Rocadenbosch, F.; Mattis, I.; Ansmann, A.; Wandinger, U.; Bockmann, C.; Pappalardo, G.; Amodeo, A.; Bosenberg, J.; Alados-Arboledas, L.; Apituley, A.; et al. The European Aerosol Research Lidar Network (EARLINET): An Overview. In Proceedings of the IGARSS 2008 - 2008 IEEE International Geoscience and Remote Sensing Symposium; IEEE: Boston, MA, USA, 2008; p. II-410-II–413.

165. Sicard, M.; D'Amico, G.; Comerón, A.; Mona, L.; Alados-Arboledas, L.; Amodeo, A.; Baars, H.; Baldasano, J.M.; Belegante, L.; Binietoglou, I.; et al. EARLINET: Potential Operationality of a Research Network. *Atmospheric Meas. Tech.* **2015**, *8*, 4587–4613, doi:10.5194/amt-8-4587-2015.

166. Guerrero-Rascado, J.L.; Landulfo, E.; Antuña, J.C.; De Melo Jorge Barbosa, H.; Barja, B.; Bastidas, Á.E.; Bedoya, A.E.; Da Costa, R.F.; Estevan, R.; Forno, R.; et al. Latin American Lidar Network (LALINET) for Aerosol Research: Diagnosis on Network Instrumentation. *J. Atmospheric Sol.-Terr. Phys.* **2016**, *138–139*, 112–120, doi:10.1016/j.jastp.2016.01.001.

167. Antuña-Marrero, J.C.; Landulfo, E.; Estevan, R.; Barja, B.; Robock, A.; Wolfram, E.; Ristori, P.; Clemesha, B.; Zaratti, F.; Forno, R.; et al. LALINET: The First Latin American–Born Regional Atmospheric Observational Network. *Bull. Am. Meteorol. Soc.* **2017**, *98*, 1255–1275, doi:10.1175/BAMS-D-15-00228.1.

168. Welton, E.J.; Campbell, J.R.; Berkoff, T.A.; Valencia, S.; Spinhirne, J.D.; Holben, B.; Tsay, S.-C. THE NASA MICRO-PULSE LIDAR NETWORK

(MPLNET): CO-LOCATION OF LIDARS WITH AERONET SUNPHOTOMETERS AND RELATED EARTH SCIENCE APPLICATIONS.; Huelva, Spain, January 1, 2004.

169. De Mazière, M.; Thompson, A.M.; Kurylo, M.J.; Wild, J.D.; Bernhard, G.; Blumenstock, T.; Braathen, G.O.; Hannigan, J.W.; Lambert, J.-C.; Leblanc, T.; et al. The Network for the Detection of Atmospheric Composition Change (NDACC): History, Status and Perspectives. *Atmospheric Chem. Phys.* **2018**, *18*, 4935–4964, doi:10.5194/acp-18-4935-2018.

170. Rocadenbosch, F.; Sicard, M.; Comerón, A.; Baldasano, J.M.; Agishev, R.; Muñoz, C.; López, M.A.; García-Vizcaino, D. The UPC Scanning Raman Lidar: An Engineering Overview. In Proceedings of the Proceeding; 2002; Vol. 1, pp. 19–70.

171. Kumar, D.; Rocadenbosch, F.; Sicard, M.; Comeron, A.; Muñoz, C.; Lange, D.; Tomás, S.; Gregorio, E. Six-Channel Polychromator Design and Implementation for the UPC Elastic/Raman Lidar.; Singh, U.N., Pappalardo, G., Eds.; Prague, Czech Republic, October 6 2011; p. 81820W.

172. Rodríguez-Gómez, A.; Sicard, M.; Granados-Muñoz, M.-J.; Chahed, E.B.; Muñoz-Porcar, C.; Barragán, R.; Comerón, A.; Rocadenbosch, F.; Vidal, E. An Architecture Providing Depolarization Ratio Capability for a Multi-Wavelength Raman Lidar: Implementation and First Measurements. *Sensors* **2017**, *17*, 2957, doi:10.3390/s17122957.

173. Comerón, A.; Rodríguez-Gómez, A.; Sicard, M.; Barragán, R.; Muñoz-Porcar, C.; Rocadenbosch, F.; Granados-Muñoz, M. Considerations about the Determination of the Depolarization Calibration Profile of a Two-Telescope Lidar and Its Implications for Volume Depolarization Ratio Retrieval. *Sensors* **2018**, *18*, 1807, doi:10.3390/s18061807.

174. Zenteno-Hernández, J.A.; Comerón, A.; Rodríguez-Gómez, A.; Muñoz-Porcar, C.; D'Amico, G.; Sicard, M. A Comparative Analysis of Aerosol Optical Coefficients and Their Associated Errors Retrieved from Pure-Rotational and Vibro-Rotational Raman Lidar Signals. *Sensors* **2021**, *21*, 1277, doi:10.3390/s21041277.

175. Veselovskii, I.; Whiteman, D.N.; Korenskiy, M.; Suvorina, A.; Pérez-Ramírez, D. Use of Rotational Raman Measurements in Multiwavelength Aerosol Lidar for Evaluation of Particle Backscattering and Extinction. *Atmospheric Meas. Tech.* **2015**, *8*, 4111–4122, doi:10.5194/amt-8-4111-2015.

176. Rodríguez-Gómez, A.; Muñoz-Porcar, C.; Zenteno-Hernández, J.-A.; Comerón, A.; Dios, F.; Sicard, M.; Gil-Díaz, C.; Oliveira, D.C.F.S.; Mandal, C. Use of Pure Rotational Raman Channels for Lidar Measurement of Aerosol Extinction Coefficient: The EARLINET/ACTRIS Barcelona Station Experience. In Proceedings of the Remote Sensing of Clouds and the Atmosphere XXVII; Comerón, A., Kassianov, E.I., Schäfer, K., Picard, R.H., Weber, K., Singh, U.N., Eds.; SPIE: Berlin, Germany, October 28, 2022; p. 13.

177. SALOMONSON, V.V.; BARNES, W.L.; MAYMON, P.W.; MONTGOMERY, H.E.; OSTROW, H. MODIS: Advanced Facility Instrument for Studies of the Earth as a System. *IEEE Trans. Geosci. REMOTE Sens.* **1989**, *27*, 145–153.

178. Diner, D.J.; Beckert, J.C.; Reilly, T.H.; Bruegge, C.J.; Conel, J.E.; Kahn, R.A.; Martonchik, J.V.; Ackerman, T.P.; Davies, R.; Gerstl, S.A.W.; et al. Multi-Angle Imaging SpectroRadiometer (MISR) Instrument Description and Experiment Overview. *IEEE Trans. Geosci. Remote Sens.* **1998**, *36*, 1072–1087, doi:10.1109/36.700992.

179. Smirnov, A.; Holben, B.N.; Eck, T.F.; Dubovik, O.; Slutsker, I. Cloud-Screening and Quality Control Algorithms for the AERONET Database. *Remote Sens. Environ.* **2000**, *73*, 337–349, doi:10.1016/S0034-4257(00)00109-7.

180. Takamura, T.; Nakajima, T. Overview of SKYNET and Its Activities. *ÓPTICA PURA Apl.* **2004**, *37*, 3303–3308.

181. Nakajima, T.; Yoon, S.; Ramanathan, V.; Shi, G.; Takemura, T.; Higurashi, A.; Takamura, T.; Aoki, K.; Sohn, B.; Kim, S.; et al. Overview of the Atmospheric Brown Cloud East Asian Regional Experiment 2005 and a Study of the Aerosol Direct Radiative Forcing in East Asia. *J. Geophys. Res. Atmospheres* **2007**, *112*, 2007JD009009, doi:10.1029/2007JD009009.

182. Herman, J.; Cede, A.; Spinei, E.; Mount, G.; Tzortziou, M.; Abuhassan, N. NO_2 Column Amounts from Ground-based Pandora and MFDOAS Spectrometers Using the Direct-sun DOAS Technique: Intercomparisons and Application to OMI Validation. *J. Geophys. Res. Atmospheres* **2009**, *114*, 2009JD011848, doi:10.1029/2009JD011848.

183. Holben, B.N.; Eck, T.F.; Slutsker, I.; Tanré, D.; Buis, J.P.; Setzer, A.; Vermote, E.; Reagan, J.A.; Kaufman, Y.J.; Nakajima, T.; et al. AERONET—A Federated Instrument Network and Data Archive for Aerosol Characterization. *Remote Sens. Environ.* **1998**, *66*, 1–16, doi:10.1016/S0034-4257(98)00031-5.

184. Barreto, Á.; Cuevas, E.; Granados-Muñoz, M.-J.; Alados-Arboledas, L.; Romero, P.M.; Gröbner, J.; Kouremeti, N.; Almansa, A.F.; Stone, T.; Toledano, C.; et al. The New Sun-Sky-Lunar Cimel CE318-T Multiband Photometer – a Comprehensive Performance Evaluation. *Atmospheric Meas. Tech.* **2016**, *9*, 631–654, doi:10.5194/amt-9-631-2016.

185. Li, Z.; Goloub, P.; Devaux, C.; Gu, X.; Qiao, Y.; Zhao, F.; Chen, H. Aerosol Polarized Phase Function and Single-Scattering Albedo Retrieved from Ground-Based Measurements. *Atmospheric Res.* **2004**, *71*, 233–241, doi:10.1016/j.atmosres.2004.06.001.

186. Barreto, A.; Cuevas, E.; Damiri, B.; Guirado, C.; Berkoff, T.; Berjón, A.J.; Hernández, Y.; Almansa, F.; Gil, M. A New Method for Nocturnal Aerosol Measurements with a Lunar Photometer Prototype. *Atmospheric Meas. Tech.* **2013**, *6*, 585–598, doi:10.5194/amt-6-585-2013.

187. Barreto, A.; Cuevas, E.; Damiri, B.; Romero, P.M.; Almansa, F. Column Water Vapor Determination in Night Period with a Lunar Photometer Prototype. *Atmospheric Meas. Tech.* **2013**, *6*, 2159–2167, doi:10.5194/amt-6-2159-2013.

188. Barreto, Á.; Román, R.; Cuevas, E.; Berjón, A.J.; Almansa, A.F.; Toledano, C.; González, R.; Hernández, Y.; Blarel, L.; Goloub, P.; et al. Assessment of Nocturnal Aerosol Optical Depth from Lunar Photometry at the Izaña High Mountain Observatory. *Atmospheric Meas. Tech.* **2017**, *10*, 3007–3019, doi:10.5194/amt-10-3007-2017.

189. CIMEL Multiband Photometer CE318-T: User's Manual 2021.

190. Torres, B.; Dubovik, O.; Toledano, C.; Berjon, A.; Cachorro, V.E.; Lapyonok, T.; Litvinov, P.; Goloub, P. Sensitivity of Aerosol Retrieval to Geometrical Configuration of Ground-Based Sun/Sky Radiometer Observations. *Atmospheric Chem. Phys.* **2014**, *14*, 847–875, doi:10.5194/acp-14-847-2014.

191. Elias, T.; Piketh, S.J.; Burger, R.; Silva, A.M. Exploring the Potential of Combining Column-integrated Atmospheric Polarization with Airborne in Situ Size Distribution Measurements for the Retrieval of an Aerosol Model: A Case Study of a Biomass Burning Plume during SAFARI 2000. *J. Geophys. Res. Atmospheres* **2003**, *108*, 2002JD002426, doi:10.1029/2002JD002426.

192. Kipp & Zonen CNR4 Net Radiometer: Instruction Manual 2014.

193. Oliveira, D.C.F.D.S.; Sicard, M.; Rodríguez-Gómez, A.; Comerón, A.; Muñoz-Porcar, C.; Gil-Díaz, C.; Dubovik, O.; Derimian, Y.; Momoi, M.; Lopatin, A. Aerosol Forcing from Ground-Based Synergies over a Decade in Barcelona, Spain. *Remote Sens.* **2025**, *17*, 1439, doi:10.3390/rs17081439.

194. Kipp & Zonen CM 21: INSTRUCTION MANUAL 2004.

195. Augustine, J.A.; DeLuisi, J.J.; Long, C.N. SURFRAD—A National Surface Radiation Budget Network for Atmospheric Research. *Bull. Am. Meteorol. Soc.* **2000**, *81*, 2341–2357, doi:10.1175/1520-0477(2000)081<2341:SANSRB>2.3.CO;2.

196. Augustine, J.A.; Hodges, G.B.; Cornwall, C.R.; Michalsky, J.J.; Medina, C.I. An Update on SURFRAD—The GCOS Surface Radiation Budget Network for the Continental United States. *J. Atmospheric Ocean. Technol.* **2005**, *22*, 1460–1472, doi:10.1175/JTECH1806.1.

197. McArthur, L.J.B. BASELINE SURFACE RADIATION NETWORK (BSRN): Operations Manual Version 2.1 2005.

198. König-Langlo, G.; Sieger, R.; Schmithüsen, H.; Bücker, A.; Richter, F.; Dutton, E.G. *The Baseline Surface Radiation Network and Its World Radiation Monitoring Centre at the Alfred Wegener Institute*; World Meteorological Organization, 2013;

199. Driemel, A.; Augustine, J.; Behrens, K.; Colle, S.; Cox, C.; Cuevas-Agulló, E.; Denn, F.M.; Duprat, T.; Fukuda, M.; Grobe, H.; et al. Baseline Surface

Radiation Network (BSRN): Structure and Data Description (1992–2017). *Earth Syst. Sci. Data* **2018**, *10*, 1491–1501, doi:10.5194/essd-10-1491-2018.

200. Gasteiger, J.; Groß, S.; Freudenthaler, V.; Wiegner, M. Volcanic Ash from Iceland over Munich: Mass Concentration Retrieved from Ground-Based Remote Sensing Measurements. *Atmospheric Chem. Phys.* **2011**, *11*, 2209–2223, doi:10.5194/acp-11-2209-2011.

201. Floutsi, A.A.; Baars, H.; Engelmann, R.; Althausen, D.; Ansmann, A.; Bohlmann, S.; Heese, B.; Hofer, J.; Kanitz, T.; Haarig, M.; et al. DeLiAn – a Growing Collection of Depolarization Ratio, Lidar Ratio and Ångström Exponent for Different Aerosol Types and Mixtures from Ground-Based Lidar Observations. *Atmospheric Meas. Tech.* **2023**, *16*, 2353–2379, doi:10.5194/amt-16-2353-2023.

202. Kim, M.-H.; Omar, A.H.; Tackett, J.L.; Vaughan, M.A.; Winker, D.M.; Trepte, C.R.; Hu, Y.; Liu, Z.; Poole, L.R.; Pitts, M.C.; et al. The CALIPSO Version 4 Automated Aerosol Classification and Lidar Ratio Selection Algorithm. *Atmospheric Meas. Tech.* **2018**, *11*, 6107–6135, doi:10.5194/amt-11-6107-2018.

203. Tackett, J.L.; Kar, J.; Vaughan, M.A.; Getzewich, B.J.; Kim, M.-H.; Vernier, J.-P.; Omar, A.H.; Magill, B.E.; Pitts, M.C.; Winker, D.M. The CALIPSO Version 4.5 Stratospheric Aerosol Subtyping Algorithm. *Atmospheric Meas. Tech.* **2023**, *16*, 745–768, doi:10.5194/amt-16-745-2023.

204. Lu, X.; Jiang, Y.; Zhang, X.; Wang, X.; Spinelli, N. Two-Wavelength Lidar Inversion Algorithm for Determination of Aerosol Extinction-to-Backscatter Ratio and Its Application to CALIPSO Lidar Measurements. *J. Quant. Spectrosc. Radiat. Transf.* **2011**, *112*, 320–328, doi:10.1016/j.jqsrt.2010.07.013.

205. Klett, J.D. Stable Analytical Inversion Solution for Processing Lidar Returns. *Appl. Opt.* **1981**, *20*, 211, doi:10.1364/AO.20.000211.

206. Fernald, F.G.; Herman, M.; Reagan, J.A. Determination of Aerosol Height Distributions by Lidar. *J. Appl. Meteorol.* **1972**, *11*, 482–489.

207. Klett, J.D. Lidar Inversion with Variable Backscatter/Extinction Ratios. *Appl. Opt.* **1985**, *24*, 1638, doi:10.1364/AO.24.001638.

208. Fernald, F.G. Analysis of Atmospheric Lidar Observations: Some Comments. *Appl. Opt.* **1984**, *23*, 652, doi:10.1364/AO.23.000652.

209. Sasano, Y.; Browell, E.V.; Ismail, S. Error Caused by Using a Constant Extinction/Backscattering Ratio in the Lidar Solution. *Appl. Opt.* **1985**, *24*, 3929, doi:10.1364/AO.24.003929.

210. Sicard, M.; Comerón, A.; Rocadenbosch, F.; Rodríguez, A.; Muñoz, C. Quasi-Analytical Determination of Noise-Induced Error Limits in Lidar Retrieval of Aerosol Backscatter Coefficient by the Elastic, Two-Component Algorithm. *Appl. Opt.* **2009**, *48*, 176, doi:10.1364/AO.48.000176.

211. Ansmann, A.; Riebesell, M.; Wandinger, U.; Weitkamp, C.; Voss, E.; Lahmann, W.; Michaelis, W. Combined Raman Elastic-Backscatter LIDAR for Vertical Profiling of Moisture, Aerosol Extinction, Backscatter, and LIDAR Ratio. *Appl. Phys. B Photophysics Laser Chem.* **1992**, *55*, 18–28, doi:10.1007/BF00348608.

212. Reichardt, J. Combined Raman Lidar for Aerosol, Ozone, and Moisture Measurements. *Opt. Eng.* **1996**, *35*, 1457, doi:10.1117/1.600681.

213. Donovan, D.P.; Carswell, A.I. Principal Component Analysis Applied to Multiwavelength Lidar Aerosol Backscatter and Extinction Measurements. *Appl. Opt.* **1997**, *36*, 9406, doi:10.1364/AO.36.009406.

214. Behrendt, A.; Nakamura, T.; Onishi, M.; Baumgart, R.; Tsuda, T. Combined Raman Lidar for the Measurement of Atmospheric Temperature, Water Vapor, Particle Extinction Coefficient, and Particle Backscatter Coefficient. *Appl. Opt.* **2002**, *41*, 7657, doi:10.1364/AO.41.007657.

215. Ansmann, A.; Riebesell, M.; Weitkamp, C. Measurement of Atmospheric Aerosol Extinction Profiles with a Raman Lidar. *Opt. Lett.* **1990**, *15*, 746, doi:10.1364/OL.15.000746.

216. Schotland, R.M.; Sassen, K.; Stone, R. Observations by Lidar of Linear Depolarization Ratios Of Hydrometeors. *J. Appl. Meteorol.* **1971**, 1011–1017.

217. Pal, S.R.; Carswell, A.I. Polarization Properties of Lidar Backscattering from Clouds. *Appl. Opt.* **1973**, *12*, 1530, doi:10.1364/AO.12.001530.

218. Sugimoto, N.; Uno, I.; Nishikawa, M.; Shimizu, A.; Matsui, I.; Dong, X.; Chen, Y.; Quan, H. Record Heavy Asian Dust in Beijing in 2002: Observations and Model Analysis of Recent Events. *Geophys. Res. Lett.* **2003**, *30*, 2002GL016349, doi:10.1029/2002GL016349.

219. Shimizu, A.; Sugimoto, N.; Matsui, I.; Arao, K.; Uno, I.; Murayama, T.; Kagawa, N.; Aoki, K.; Uchiyama, A.; Yamazaki, A. Continuous Observations of Asian Dust and Other Aerosols by Polarization Lidars in China and Japan during ACE-Asia. *J. Geophys. Res. Atmospheres* **2004**, *109*, 2002JD003253, doi:10.1029/2002JD003253.

220. Sugimoto, N.; Lee, C.H. Characteristics of Dust Aerosols Inferred from Lidar Depolarization Measurements at Two Wavelengths. *Appl. Opt.* **2006**, *45*, 7468, doi:10.1364/AO.45.007468.

221. Marenco, F.; Hogan, R.J. Determining the Contribution of Volcanic Ash and Boundary Layer Aerosol in Backscatter Lidar Returns: A Three-Component Atmosphere Approach. *J. Geophys. Res.* **2011**, *116*, D00U06, doi:10.1029/2010JD015415.

222. Donovan, D.P.; Apituley, A. Practical Depolarization-Ratio-Based Inversion Procedure: Lidar Measurements of the Eyjafjallajökull Ash Cloud over the Netherlands. *Appl. Opt.* **2013**, *52*, 2394, doi:10.1364/AO.52.002394.

223. Hadamard, J. Sur Les Problèmes Aux Dérivées Partielles et Leur Signification Physique. *Princet. Univ. Bull.* **1902**, *13*, 49–52.

224. Willoughby, R.A. Solutions of Ill-Posed Problems (A. N. Tikhonov and V. Y. Arsenin). *SIAM Rev.* **1979**, *21*, 266–267, doi:10.1137/1021044.

225. Müller, D.; Wandinger, U.; Ansmann, A. Microphysical Particle Parameters from Extinction and Backscatter Lidar Data by Inversion with Regularization: Theory. *Appl. Opt.* **1999**, *38*, 2346, doi:10.1364/AO.38.002346.

226. Craven, P.; Wahba, G. Smoothing Noisy Data with Spline Functions. *Numer. Math.* **1978**, *31*, 377–403, doi:10.1007/BF01404567.

227. Golub, G.H.; Heath, M. Generalized Cross-Validation as a Method for Choosing a Good Ridge Parameter.

228. Veselovskii, I.; Kolgotin, A.; Griaznov, V.; Müller, D.; Wandinger, U.; Whiteman, D.N. Inversion with Regularization for the Retrieval of Tropospheric Aerosol Parameters from Multiwavelength Lidar Sounding. *Appl. Opt.* **2002**, *41*, 3685, doi:10.1364/AO.41.003685.

229. Müller, D.; Wandinger, U.; Ansmann, A. Microphysical Particle Parameters from Extinction and Backscatter Lidar Data by Inversion with Regularization: Simulation. *Appl. Opt.* **1999**, *38*, 2358, doi:10.1364/AO.38.002358.

230. Müller, D.; Wagner, F.; Wandinger, U.; Ansmann, A.; Wendisch, M.; Althausen, D.; Von Hoyningen-Huene, W. Microphysical Particle Parameters from Extinction and Backscatter Lidar Data by Inversion with Regularization: Experiment. *Appl. Opt.* **2000**, *39*, 1879, doi:10.1364/AO.39.001879.

231. Tikhonov, A.N.; Arsenin, V.Y. *Solutions of Ill-Posed Problems*; Winston, 1977; ISBN 0-470-99124-0.

232. Veselovskii, I.; Kolgotin, A.; Griaznov, V.; Müller, D.; Franke, K.; Whiteman, D.N. Inversion of Multiwavelength Raman Lidar Data for Retrieval of Bimodal Aerosol Size Distribution. *Appl. Opt.* **2004**, *43*, 1180, doi:10.1364/AO.43.001180.

233. Veselovskii, I.; Whiteman, D.N.; Kolgotin, A.; Andrews, E.; Korenskii, M. Demonstration of Aerosol Property Profiling by Multiwavelength Lidar under Varying Relative Humidity Conditions. *J. Atmospheric Ocean. Technol.* **2009**, *26*, 1543–1557, doi:10.1175/2009JTECHA1254.1.

234. Veselovskii, I.; Dubovik, O.; Kolgotin, A.; Lapyonok, T.; Di Girolamo, P.; Summa, D.; Whiteman, D.N.; Mishchenko, M.; Tanré, D. Application of Randomly Oriented Spheroids for Retrieval of Dust Particle Parameters from Multiwavelength Lidar Measurements. *J. Geophys. Res. Atmospheres* **2010**, *115*, 2010JD014139, doi:10.1029/2010JD014139.

235. Veselovskii, I.; Dubovik, O.; Kolgotin, A.; Korenskiy, M.; Whiteman, D.N.; Allakhverdiev, K.; Huseyinoglu, F. Linear Estimation of Particle Bulk Parameters from Multi-Wavelength Lidar Measurements. *Atmospheric Meas. Tech.* **2012**, *5*, 1135–1145, doi:10.5194/amt-5-1135-2012.

236. Veselovskii, I.; Whiteman, D.N.; Korenskiy, M.; Suvorina, A.; Kolgotin, A.; Lyapustin, A.; Wang, Y.; Chin, M.; Bian, H.; Kucsera, T.L.; et al. Characterization of Forest Fire Smoke Event near Washington, DC in Summer 2013 with Multi-Wavelength Lidar. *Atmospheric Chem. Phys.* **2015**, *15*, 1647–1660, doi:10.5194/acp-15-1647-2015.

237. AERONET DOCUMENT AERONET Inversion Products (Version 3).

238. Nakajima, T.; Tanaka, M.; Yamauchi, T. Retrieval of the Optical Properties of Aerosols from Aureole and Extinction Data. *Appl. Opt.* **1983**, *22*, 2951, doi:10.1364/AO.22.002951.

239. Nakajima, T.; Tonna, G.; Rao, R.; Boi, P.; Kaufman, Y.; Holben, B. Use of Sky Brightness Measurements from Ground for Remote Sensing of Particulate Polydispersions. *Appl. Opt.* **1996**, *35*, 2672, doi:10.1364/AO.35.002672.

240. Dubovik, O.; Holben, B.N.; Kaufman, Y.J.; Yamasoe, M.; Smirnov, A.; Tanré, D.; Slutsker, I. Single-scattering Albedo of Smoke Retrieved from the Sky Radiance and Solar Transmittance Measured from Ground. *J. Geophys. Res. Atmospheres* **1998**, *103*, 31903–31923, doi:10.1029/98JD02276.

241. Yamasoe, M.A.; Kaufman, Y.J.; Dubovik, O.; Remer, L.A.; Holben, B.N.; Artaxo, P. Retrieval of the Real Part of the Refractive Index of Smoke Particles from Sun/Sky Measurements during SCAR-B. *J. Geophys. Res. Atmospheres* **1998**, *103*, 31893–31902, doi:10.1029/98JD01211.

242. King, M.D.; Byrne, D.M.; Herman, B.M.; Reagan, J.A. Aerosol Size Distribution Obtained by Inversion of Spectral Optical Depth Measurements. *J. Atmospheric Sci.* **1978**, *35*, 2153–2167.

243. Dubovik, O.; Holben, B.N.; Lapyonok, T.; Sinyuk, A.; Mishchenko, M.I.; Yang, P.; Slutsker, I. Non-Spherical Aerosol Retrieval Method Employing Light Scattering by Spheroids: NON-SPHERICAL AEROSOL RETRIEVAL METHOD. *Geophys. Res. Lett.* **2002**, *29*, 54-1-54–4, doi:10.1029/2001GL014506.

244. Holben, B.N.; Eck, T.F.; Slutsker, I.; Smirnov, A.; Sinyuk, A.; Schafer, J.; Giles, D.; Dubovik, O. Aeronet's Version 2.0 Quality Assurance Criteria.; Tsay, S.-C., Nakajima, T., Singh, R.P., Sridharan, R., Eds.; Goa, India, December 1, 2006; p. 64080Q.

245. Giles, D.M.; Sinyuk, A.; Sorokin, M.G.; Schafer, J.S.; Smirnov, A.; Slutsker, I.; Eck, T.F.; Holben, B.N.; Lewis, J.R.; Campbell, J.R.; et al. Advancements in the Aerosol Robotic Network (AERONET) Version 3 Database – Automated near-Real-Time Quality Control Algorithm with Improved Cloud Screening for Sun Photometer Aerosol Optical Depth (AOD) Measurements. *Atmospheric Meas. Tech.* **2019**, *12*, 169–209, doi:10.5194/amt-12-169-2019.

246. Sinyuk, A.; Dubovik, O.; Holben, B.; Eck, T.F.; Breon, F.-M.; Martonchik, J.; Kahn, R.; Diner, D.J.; Vermote, E.F.; Roger, J.-C.; et al. Simultaneous Retrieval of Aerosol and Surface Properties from a Combination of AERONET

and Satellite Data. *Remote Sens. Environ.* **2007**, *107*, 90–108, doi:10.1016/j.rse.2006.07.022.

247. O'Neill, N.T.; Eck, T.F.; Holben, B.N.; Smirnov, A.; Dubovik, O.; Royer, A. Bimodal Size Distribution Influences on the Variation of Angstrom Derivatives in Spectral and Optical Depth Space. *J. Geophys. Res. Atmospheres* **2001**, *106*, 9787–9806, doi:10.1029/2000JD900245.

248. Kaku, K.C.; Reid, J.S.; O'Neill, N.T.; Quinn, P.K.; Coffman, D.J.; Eck, T.F. Verification and Application of the Extended Spectral Deconvolution Algorithm (SDA+) Methodology to Estimate Aerosol Fine and Coarse Mode Extinction Coefficients in the Marine Boundary Layer. *Atmospheric Meas. Tech.* **2014**, *7*, 3399–3412, doi:10.5194/amt-7-3399-2014.

249. Nakajima, T.; Tanaka, M. Matrix Formulations for the Transfer of Solar Radiation in a Plane-Parallel Scattering Atmosphere. *J. Quant. Spectrosc. Radiat. Transf.* **1986**, *35*, 13–21, doi:10.1016/0022-4073(86)90088-9.

250. Korkin, S.; Lyapustin, A.; Sinyuk, A.; Holben, B. A New Code SORD for Simulation of Polarized Light Scattering in the Earth Atmosphere.; Chenault, D.B., Goldstein, D.H., Eds.; Baltimore, Maryland, United States, May 4 2016; p. 985305.

251. Korkin, S.; Lyapustin, A.; Sinyuk, A.; Holben, B.; Kokhanovsky, A. Vector Radiative Transfer Code SORD: Performance Analysis and Quick Start Guide. *J. Quant. Spectrosc. Radiat. Transf.* **2017**, *200*, 295–310, doi:10.1016/j.jqsrt.2017.04.035.

252. Chaikovsky, A.; Dubovik, O.; Goloub, P.; Tanré, D.; Pappalardo, G.; Wandinger, U.; Chaikovskaya, L.; Denisov, S.; Grudo, Y.; Lopatin, A.; et al. ALGORITHM AND SOFTWARE FOR THE RETRIEVAL OF VERTICAL AEROSOL PROPERTIES USING COMBINED LIDAR/RADIOMETER DATA: DISSEMINATION IN EARLINET.; Porto Heli, Greece, 2012; pp. 399–402.

253. Dubovik, O.; Lapyonok, T.; Litvinov, P.; Herman, M.; Fuertes, D.; Ducos, F.; Torres, B.; Derimian, Y.; Huang, X.; Lopatin, A.; et al. GRASP: A Versatile Algorithm for Characterizing the Atmosphere. *SPIE Newsroom* **2014**, doi:10.1117/2.1201408.005558.

254. Chaikovsky, A.P.; Dubovik, O.; Holben, B.N.; Bril, A.I. Methodology to Retrieve Atmospheric Aerosol Parameters by Combining Ground-Based Measurements of Multiwavelength Lidar and Sun Sky-Scanning Radiometer.; Zherebtsov, G.A., Matvienko, G.G., Banakh, V.A., Koshelev, V.V., Eds.; Irkutsk, Russia, February 28, 2002; p. 257.

255. *25th International Laser Radar Conference 2010: (ILRC 25) : St. Petersburg, 5-9 July 2010. Monograph*; Curran Associates: Red Hook, N.Y., 2010; ISBN 978-1-61782-614-6.

256. Chaikovsky, A.; Dubovik, O.; Holben, B.; Bril, A.; Goloub, P.; Tanré, D.; Pappalardo, G.; Wandinger, U.; Chaikovskaya, L.; Denisov, S.; et al. Lidar-Radiometer Inversion Code (LIRIC) for the Retrieval of Vertical Aerosol

Properties from Combined Lidar/Radiometer Data: Development and Distribution in EARLINET. *Atmospheric Meas. Tech.* **2016**, *9*, 1181–1205, doi:10.5194/amt-9-1181-2016.

257. Tsekeri, A. Application of a Synergetic Lidar and Sunphotometer Algorithm for the Characterization of a Dust Event Over Athens, Greece. *Br. J. Environ. Clim. Change* **2013**, *3*, doi:10.9734/BJECC/2013/2615.

258. Tesche, M.; Ansmann, A.; Müller, D.; Althausen, D.; Engelmann, R.; Freudenthaler, V.; Groß, S. Vertically Resolved Separation of Dust and Smoke over Cape Verde Using Multiwavelength Raman and Polarization Lidars during Saharan Mineral Dust Experiment 2008. *J. Geophys. Res.* **2009**, *114*, D13202, doi:10.1029/2009JD011862.

259. Tesche, M.; Müller, D.; Gross, S.; Ansmann, A.; Althausen, D.; Freudenthaler, V.; Weinzierl, B.; Veira, A.; Petzold, A. Optical and Microphysical Properties of Smoke over Cape Verde Inferred from Multiwavelength Lidar Measurements. *Tellus B Chem. Phys. Meteorol.* **2011**, *63*, 677, doi:10.1111/j.1600-0889.2011.00549.x.

260. Mamouri, R.E.; Ansmann, A. Fine and Coarse Dust Separation with Polarization Lidar. *Atmospheric Meas. Tech.* **2014**, *7*, 3717–3735, doi:10.5194/amt-7-3717-2014.

261. Mamouri, R.E.; Ansmann, A. Estimated Desert-Dust Ice Nuclei Profiles from Polarization Lidar: Methodology and Case Studies. *Atmospheric Chem. Phys.* **2015**, *15*, 3463–3477, doi:10.5194/acp-15-3463-2015.

262. Mamouri, R.-E.; Ansmann, A. Potential of Polarization Lidar to Provide Profiles of CCN- and INP-Relevant Aerosol Parameters. *Atmospheric Chem. Phys.* **2016**, *16*, 5905–5931, doi:10.5194/acp-16-5905-2016.

263. Mamouri, R.-E.; Ansmann, A. Potential of Polarization/Raman Lidar to Separate Fine Dust, Coarse Dust, Maritime, and Anthropogenic Aerosol Profiles. *Atmospheric Meas. Tech.* **2017**, *10*, 3403–3427, doi:10.5194/amt-10-3403-2017.

264. Ansmann, A.; Mamouri, R.-E.; Hofer, J.; Baars, H.; Althausen, D.; Abdullaev, S.F. Dust Mass, Cloud Condensation Nuclei, and Ice-Nucleating Particle Profiling with Polarization Lidar: Updated POLIPHON Conversion Factors from Global AERONET Analysis. *Atmospheric Meas. Tech.* **2019**, *12*, 4849–4865, doi:10.5194/amt-12-4849-2019.

265. Ansmann, A.; Ohneiser, K.; Mamouri, R.-E.; Knopf, D.A.; Veselovskii, I.; Baars, H.; Engelmann, R.; Foth, A.; Jimenez, C.; Seifert, P.; et al. Tropospheric and Stratospheric Wildfire Smoke Profiling with Lidar: Mass, Surface Area, CCN, and INP Retrieval. *Atmospheric Chem. Phys.* **2021**, *21*, 9779–9807, doi:10.5194/acp-21-9779-2021.

266. Gasteiger, J.; Wiegner, M.; Toledano, C.; Groß, S.; Freudenthaler, V. Case Study on Combined Lidar-Photometer Retrieval of Volcanic ASH Properties. *EPJ Web Conf.* **2016**, *119*, 07004, doi:10.1051/epjconf/201611907004.

267. Dubovik, O.; Ducos, F.; Fuertes, D. The GRASP Package. An Overview. - Generalized Retrieval of Atmosphere and Surface Properties 2024.

268. Dubovik, O.; Fuertes, D.; Litvinov, P.; Lopatin, A.; Lapyonok, T.; Doubovik, I.; Xu, F.; Ducos, F.; Chen, C.; Torres, B.; et al. A Comprehensive Description of Multi-Term LSM for Applying Multiple a Priori Constraints in Problems of Atmospheric Remote Sensing: GRASP Algorithm, Concept, and Applications. *Front. Remote Sens.* **2021**, *2*, 706851, doi:10.3389/frsen.2021.706851.

269. Dubovik, O. Optimization of Numerical Inversion in Photopolarimetric Remote Sensing.; Springer, Dordrecht, 2004; Vol. 161.

270. Benavent-Oltra, J.A. Synergetic Use of Active and Passive Remote Sensing Techniques to Retrieve Vertical Profiles of Atmospheric Aerosol Properties during Day- and Night-Time. PhD Thesis, Universidad de Granada: Granada, Spain, 2019.

271. Tsekeri, A.; Lopatin, A.; Amiridis, V.; Marinou, E.; Igloffstein, J.; Siomos, N.; Solomos, S.; Kokkalis, P.; Engelmann, R.; Baars, H.; et al. GARRLiC and LIRIC: Strengths and Limitations for the Characterization of Dust and Marine Particles along with Their Mixtures. *Atmospheric Meas. Tech.* **2017**, *10*, 4995–5016, doi:10.5194/amt-10-4995-2017.

272. Derimian, Y.; Dubovik, O.; Huang, X.; Lapyonok, T.; Litvinov, P.; Kostinski, A.B.; Dubuisson, P.; Ducos, F. Comprehensive Tool for Calculation of Radiative Fluxes: Illustration of Shortwave Aerosol Radiative Effect Sensitivities to the Details in Aerosol and Underlying Surface Characteristics. *Atmospheric Chem. Phys.* **2016**, *16*, 5763–5780, doi:10.5194/acp-16-5763-2016.

273. Torres, B.; Dubovik, O.; Fuertes, D.; Schuster, G.; Cachorro, V.E.; Lapyonok, T.; Goloub, P.; Blarel, L.; Barreto, A.; Mallet, M.; et al. Advanced Characterisation of Aerosol Size Properties from Measurements of Spectral Optical Depth Using the GRASP Algorithm. *Atmospheric Meas. Tech.* **2017**, *10*, 3743–3781, doi:10.5194/amt-10-3743-2017.

274. Román, R.; Benavent-Oltra, J.A.; Casquero-Vera, J.A.; Lopatin, A.; Cazorla, A.; Lyamani, H.; Denjean, C.; Fuertes, D.; Pérez-Ramírez, D.; Torres, B.; et al. Retrieval of Aerosol Profiles Combining Sunphotometer and Ceilometer Measurements in GRASP Code. *Atmospheric Res.* **2018**, *204*, 161–177, doi:10.1016/j.atmosres.2018.01.021.

275. Lopatin, A.; Dubovik, O.; Fuertes, D.; Stenchikov, G.; Lapyonok, T.; Veselovskii, I.; Wienhold, F.G.; Shevchenko, I.; Hu, Q.; Parajuli, S. Synergy Processing of Diverse Ground-Based Remote Sensing and in Situ Data Using the GRASP Algorithm: Applications to Radiometer, Lidar and Radiosonde Observations. *Atmospheric Meas. Tech.* **2021**, *14*, 2575–2614, doi:10.5194/amt-14-2575-2021.

276. Herrera, M.E.; Dubovik, O.; Torres, B.; Lapyonok, T.; Fuertes, D.; Lopatin, A.; Litvinov, P.; Chen, C.; Benavent-Oltra, J.A.; Bali, J.L.; et al. Estimates of Remote Sensing Retrieval Errors by the GRASP Algorithm: Application to

Ground-Based Observations, Concept and Validation. *Atmospheric Meas. Tech.* **2022**, *15*, 6075–6126, doi:10.5194/amt-15-6075-2022.

277. Herreras-Giralda, M.; Litvinov, P.; Dubovik, O.; Derimian, Y.; Lapyonok, T.; Fuertes, D.; Sourdeval, O.; Preusker, R.; Fischer, J. Thermal Emission in the Successive Orders of Scattering (SOS) Radiative Transfer Approach. *J. Quant. Spectrosc. Radiat. Transf.* **2022**, *291*, 108327, doi:10.1016/j.jqsrt.2022.108327.
278. Lopatin, A.; Dubovik, O.; Stenchikov, G.; Welton, E.J.; Shevchenko, I.; Fuertes, D.; Herreras-Giralda, M.; Lapyonok, T.; Smirnov, A. Comparison of Diurnal Aerosol Products Retrieved from Combinations of Micro-Pulse Lidar and Sun Photometer Observations over the KAUST Observation Site. *Atmospheric Meas. Tech.* **2024**, *17*, 4445–4470, doi:10.5194/amt-17-4445-2024.
279. Oliveira, D.C.F.D.S.; Sicard, M.; Rodríguez-Gómez, A.; Comerón, A.; Muñoz-Porcar, C.; Gil-Díaz, C.; Dubovik, O.; Derimian, Y.; Momoi, M.; Lopatin, A. Aerosol Forcing from Ground-Based Synergies over a Decade in Barcelona, Spain. *Remote Sens.* **2025**, *17*, 1439, doi:10.3390/rs17081439.
280. Landi, T.; Bonasoni, P.; Brunetti, M.; Campbell, J.; Marquis, J.; Di Girolamo, P.; Lolli, S. Aerosol Direct Radiative Effects under Cloud-Free Conditions over Highly-Polluted Areas in Europe and Mediterranean: A Ten-Years Analysis (2007–2016). *Remote Sens.* **2021**, *13*, 2933, doi:10.3390/rs13152933.
281. Sicard, M.; Rocadenbosch, F.; Reba, M.N.M.; Comerón, A.; Tomás, S.; García-Vízcaino, D.; Batet, O.; Barrios, R.; Kumar, D.; Baldasano, J.M. Seasonal Variability of Aerosol Optical Properties Observed by Means of a Raman Lidar at an EARLINET Site over Northeastern Spain. *Atmospheric Chem. Phys.* **2011**, *11*, 175–190, doi:10.5194/acp-11-175-2011.
282. Sicard, M.; Barragan, R.; Dulac, F.; Alados-Arboledas, L.; Mallet, M. Aerosol Optical, Microphysical and Radiative Properties at Regional Background Insular Sites in the Western Mediterranean. *Atmospheric Chem. Phys.* **2016**, *16*, 12177–12203, doi:10.5194/acp-16-12177-2016.
283. Sicard, M.; Izquierdo, R.; Alarcón, M.; Belmonte, J.; Comerón, A.; Baldasano, J.M. Near-Surface and Columnar Measurements with a Micro Pulse Lidar of Atmospheric Pollen in Barcelona, Spain. *Atmospheric Chem. Phys.* **2016**, *16*, 6805–6821, doi:10.5194/acp-16-6805-2016.
284. Sicard, M.; Jorba, O.; Ho, J.J.; Izquierdo, R.; De Linares, C.; Alarcón, M.; Comerón, A.; Belmonte, J. Measurement Report: Characterization of the Vertical Distribution of Airborne Pinus Pollen in the Atmosphere with Lidar-Derived Profiles – a Modeling Case Study in the Region of Barcelona, NE Spain. *Atmospheric Chem. Phys.* **2021**, *21*, 17807–17832, doi:10.5194/acp-21-17807-2021.
285. Mallet, M.; Dubovik, O.; Nabat, P.; Dulac, F.; Kahn, R.; Sciare, J.; Paronis, D.; Léon, J.F. Absorption Properties of Mediterranean Aerosols Obtained from

Multi-Year Ground-Based Remote Sensing Observations. *Atmospheric Chem. Phys.* **2013**, *13*, 9195–9210, doi:10.5194/acp-13-9195-2013.

286. Gueymard, C.A. The Sun's Total and Spectral Irradiance for Solar Energy Applications and Solar Radiation Models. *Sol. Energy* **2004**, *76*, 423–453, doi:10.1016/j.solener.2003.08.039.
287. Torres, B.; Fuertes, D. Characterization of Aerosol Size Properties from Measurements of Spectral Optical Depth: A Global Validation of the GRASP-AOD Code Using Long-Term AERONET Data. *Atmospheric Meas. Tech.* **2021**, *14*, 4471–4506, doi:10.5194/amt-14-4471-2021.
288. D'Amico, G.; Amodeo, A.; Baars, H.; Binietoglou, I.; Freudenthaler, V.; Mattis, I.; Wandinger, U.; Pappalardo, G. EARLINET Single Calculus Chain – Overview on Methodology and Strategy. *Atmospheric Meas. Tech.* **2015**, *8*, 4891–4916, doi:10.5194/amt-8-4891-2015.
289. D'Amico, G.; Amodeo, A.; Mattis, I.; Freudenthaler, V.; Pappalardo, G. EARLINET Single Calculus Chain – Technical – Part 1: Pre-Processing of Raw Lidar Data. *Atmospheric Meas. Tech.* **2016**, *9*, 491–507, doi:10.5194/amt-9-491-2016.
290. Mattis, I.; D'Amico, G.; Baars, H.; Amodeo, A.; Madonna, F.; Iarlori, M. EARLINET Single Calculus Chain – Technical – Part 2: Calculation of Optical Products. *Atmospheric Meas. Tech.* **2016**, *9*, 3009–3029, doi:10.5194/amt-9-3009-2016.
291. Eck, T.F.; Holben, B.N.; Reid, J.S.; Dubovik, O.; Smirnov, A.; O'Neill, N.T.; Slutsker, I.; Kinne, S. Wavelength Dependence of the Optical Depth of Biomass Burning, Urban, and Desert Dust Aerosols. *J. Geophys. Res. Atmospheres* **1999**, *104*, 31333–31349, doi:10.1029/1999JD900923.
292. Ross, J. *The Radiation Regime and Architecture of Plant Stands*; Tasks for Vegetation Science; Springer Dordrecht, 1981; ISBN 978-90-6193-607-7.
293. Li, X.; Strahler, A.H. Geometric-Optical Bidirectional Reflectance Modeling of the Discrete Crown Vegetation Canopy: Effect of Crown Shape and Mutual Shadowing. *IEEE Trans. Geosci. Remote Sens.* **1992**, *30*, 276–292, doi:10.1109/36.134078.
294. Wanner, W.; Li, X.; Strahler, A.H. On the Derivation of Kernels for Kernel-driven Models of Bidirectional Reflectance. *J. Geophys. Res. Atmospheres* **1995**, *100*, 21077–21089, doi:10.1029/95JD02371.
295. Nadal, F.; Breon, F.-M. Parameterization of Surface Polarized Reflectance Derived from POLDER Spaceborne Measurements. *IEEE Trans. Geosci. Remote Sens.* **1999**, *37*, 1709–1718, doi:10.1109/36.763292.
296. Maignan, F.; Bréon, F.-M.; Fédèle, E.; Bouvier, M. Polarized Reflectances of Natural Surfaces: Spaceborne Measurements and Analytical Modeling. *Remote Sens. Environ.* **2009**, *113*, 2642–2650, doi:10.1016/j.rse.2009.07.022.

297. Maignan, F.; Bréon, F.-M.; Lacaze, R. Bidirectional Reflectance of Earth Targets: Evaluation of Analytical Models Using a Large Set of Spaceborne Measurements with Emphasis on the Hot Spot. *Remote Sens. Environ.* **2004**, *90*, 210–220, doi:10.1016/j.rse.2003.12.006.

298. Deschamps, P.-Y.; Breon, F.-M.; Leroy, M.; Podaire, A.; Bricaud, A.; Buriez, J.-C.; Seze, G. The POLDER Mission: Instrument Characteristics and Scientific Objectives. *IEEE Trans. Geosci. Remote Sens.* **1994**, *32*, 598–615, doi:10.1109/36.297978.

299. Litvinov, P.; Hasekamp, O.; Cairns, B. Models for Surface Reflection of Radiance and Polarized Radiance: Comparison with Airborne Multi-Angle Photopolarimetric Measurements and Implications for Modeling Top-of-Atmosphere Measurements. *Remote Sens. Environ.* **2011**, *115*, 781–792, doi:10.1016/j.rse.2010.11.005.

300. Emery, C.; Liu, Z.; Russell, A.G.; Odman, M.T.; Yarwood, G.; Kumar, N. Recommendations on Statistics and Benchmarks to Assess Photochemical Model Performance. *J. Air Waste Manag. Assoc.* **2017**, *67*, 582–598, doi:10.1080/10962247.2016.1265027.

301. Karim, S.A.A.; Singh, B.S.M. Global Solar Radiation Modeling Using Polynomial Fitting. *Appl. Math. Sci.* **2014**, *8*, 367–378, doi:10.12988/ams.2014.39516.

302. Bayrakçı, H.C.; Demircan, C.; Keçebaş, A. The Development of Empirical Models for Estimating Global Solar Radiation on Horizontal Surface: A Case Study. *Renew. Sustain. Energy Rev.* **2018**, *81*, 2771–2782, doi:10.1016/j.rser.2017.06.082.

303. Nethwadzi, L.C.; Winkler, H. Calculation of Direct and Diffuse Solar Irradiance Components Using a Slob Algorithm Model in Gauteng Conditions. In Proceedings of the Proceedings of SAIP2017; December 31 2018; pp. 361–366.

304. Kaplan, A.G.; Kaplan, Y.A. Developing of the New Models in Solar Radiation Estimation with Curve Fitting Based on Moving Least-Squares Approximation. *Renew. Energy* **2020**, *146*, 2462–2471, doi:10.1016/j.renene.2019.08.095.

305. Alados-Arboledas, L.; Olmo, F.J.; Alados, I.; Pérez, M. Parametric Models to Estimate Photosynthetically Active Radiation in Spain. *Agric. For. Meteorol.* **2000**, *101*, 187–201, doi:10.1016/S0168-1923(99)00163-X.

306. García, O.E.; Díaz, A.M.; Expósito, F.J.; Díaz, J.P.; Redondas, A.; Sasaki, T. Aerosol Radiative Forcing and Forcing Efficiency in the UVB for Regions Affected by Saharan and Asian Mineral Dust. *J. Atmospheric Sci.* **2009**, *66*, 1033–1040, doi:10.1175/2008JAS2816.1.

307. Di Biagio, C.; Di Sarra, A.; Meloni, D.; Monteleone, F.; Piacentino, S.; Sferlazzo, D. Measurements of Mediterranean Aerosol Radiative Forcing and Influence of the Single Scattering Albedo. *J. Geophys. Res. Atmospheres* **2009**, *114*, 2008JD011037, doi:10.1029/2008JD011037.

308. Di Biagio, C.; Di Sarra, A.; Meloni, D. Large Atmospheric Shortwave Radiative Forcing by Mediterranean Aerosols Derived from Simultaneous Ground-based and Spaceborne Observations and Dependence on the Aerosol Type and Single Scattering Albedo. *J. Geophys. Res. Atmospheres* **2010**, *115*, 2009JD012697, doi:10.1029/2009JD012697.

309. Toledano, C.; Cachorro, V.E.; Berjon, A.; De Frutos, A.M.; Sorribas, M.; De La Morena, B.A.; Goloub, P. Aerosol Optical Depth and Ångström Exponent Climatology at El Arenosillo AERONET Site (Huelva, Spain). *Q. J. R. Meteorol. Soc.* **2007**, *133*, 795–807, doi:10.1002/qj.54.

310. García, O.E.; Díaz, A.M.; Expósito, F.J.; Díaz, J.P.; Dubovik, O.; Dubuisson, P.; Roger, J. -C.; Eck, T.F.; Sinyuk, A.; Derimian, Y.; et al. Validation of AERONET Estimates of Atmospheric Solar Fluxes and Aerosol Radiative Forcing by Ground-based Broadband Measurements. *J. Geophys. Res. Atmospheres* **2008**, *113*, 2008JD010211, doi:10.1029/2008JD010211.

311. Lolli, S.; Sicard, M.; Amato, F.; Comeron, A.; Gíl-Diaz, C.; Landi, T.C.; Munoz-Porcar, C.; Oliveira, D.C.F.S.; Dios Otin, F.; Rocadenbosch, F.; et al. Climatological Assessment of the Vertically Resolved Optical and Microphysical Aerosol Properties by Lidar Measurements, Sun Photometer, and in Situ Observations over 17 Years at Universitat Politècnica de Catalunya (UPC) Barcelona. *Atmospheric Chem. Phys.* **2023**, *23*, 12887–12906, doi:10.5194/acp-23-12887-2023.

312. Burkey, J. Seasonal Kendall Test with Slope for Serial Dependent Data 2024.

313. Burkey, J. Mann-Kendall Tau-b with Sen's Method (Enhanced) 2024.

314. Benavent-Oltra, J.A.; Román, R.; Granados-Muñoz, M.J.; Pérez-Ramírez, D.; Ortiz-Amezcua, P.; Denjean, C.; Lopatin, A.; Lyamani, H.; Torres, B.; Guerrero-Rascado, J.L.; et al. Comparative Assessment of GRASP Algorithm for a Dust Event over Granada (Spain) during ChArMEx-ADRIMED 2013 Campaign. *Atmospheric Meas. Tech.* **2017**, *10*, 4439–4457, doi:10.5194/amt-10-4439-2017.

315. Salvador, P.; Pey, J.; Pérez, N.; Querol, X.; Artíñano, B. Increasing Atmospheric Dust Transport towards the Western Mediterranean over 1948–2020. *Npj Clim. Atmospheric Sci.* **2022**, *5*, 34, doi:10.1038/s41612-022-00256-4.

316. Pandolfi, M.; Alastuey, A.; Pérez, N.; Reche, C.; Castro, I.; Shatalov, V.; Querol, X. Trends Analysis of PM Source Contributions and Chemical Tracers in NE Spainduring 2004–2014: A Multi-Exponential Approach. *Atmospheric Chem. Phys.* **2016**, *16*, 11787–11805, doi:10.5194/acp-16-11787-2016.

317. Veld, M.I. 'T; Alastuey, A.; Pandolfi, M.; Amato, F.; Pérez, N.; Reche, C.; Via, M.; Minguillón, M.C.; Escudero, M.; Querol, X. Compositional Changes of PM2.5 in NE Spain during 2009–2018: A Trend Analysis of the Chemical Composition and Source Apportionment. *Sci. Total Environ.* **2021**, *795*, 148728, doi:10.1016/j.scitotenv.2021.148728.

318. Querol, X. PM10 and PM2.5 Source Apportionment in the Barcelona Metropolitan Area, Catalonia, Spain. *Atmos. Environ.* **2001**, *35*, 6407–6419, doi:10.1016/S1352-2310(01)00361-2.

319. Via, M.; Minguillón, M.C.; Reche, C.; Querol, X.; Alastuey, A. Increase in Secondary Organic Aerosol in an Urban Environment. *Atmospheric Chem. Phys.* **2021**, *21*, 8323–8339, doi:10.5194/acp-21-8323-2021.

320. Aas, W.; Fagerli, H.; Alastuey, A.; Cavalli, F.; Degorska, A.; Feigenspan, S.; Brenna, H.; Gliß, J.; Heinesen, D.; Hueglin, C.; et al. Trends in Air Pollution in Europe, 2000–2019. *Aerosol Air Qual. Res.* **2024**, *24*, 230237, doi:10.4209/aaqr.230237.

321. Sabburg, J.; Wong, J. The Effect of Clouds on Enhancing UVB Irradiance at the Earth's Surface: A One Year Study. *Geophys. Res. Lett.* **2000**, *27*, 3337–3340, doi:10.1029/2000GL011683.

322. Badosa, J.; Calbó, J.; Mckenzie, R.; Liley, B.; González, J.; Forgan, B.; Long, C.N. Two Methods for Retrieving UV Index for All Cloud Conditions from Sky Imager Products or Total SW Radiation Measurements. *Photochem. Photobiol.* **2014**, *90*, 941–951, doi:10.1111/php.12272.

323. Lamy, K.; Portafaix, T.; Brogniez, C.; Lakkala, K.; Pitkänen, M.R.A.; Arola, A.; Forestier, J.-B.; Amelie, V.; Toihir, M.A.; Rakotoniaina, S. UV-Indien Network: Ground-Based Measurements Dedicated to the Monitoring of UV Radiation over the Western Indian Ocean. *Earth Syst. Sci. Data* **2021**, *13*, 4275–4301, doi:10.5194/essd-13-4275-2021.

324. Lamy, K.; Portafaix, T.; Brogniez, C.; Godin-Beekmann, S.; Bencherif, H.; Morel, B.; Pazmino, A.; Metzger, J.M.; Auriol, F.; Deroo, C.; et al. Ultraviolet Radiation Modelling from Ground-Based and Satellite Measurements on Reunion Island, Southern Tropics. *Atmospheric Chem. Phys.* **2018**, *18*, 227–246, doi:10.5194/acp-18-227-2018.

325. Antón, M.; Valenzuela, A.; Cazorla, A.; Gil, J.E.; Fernández-Gálvez, J.; Lyamani, H.; Foyo-Moreno, I.; Olmo, F.J.; Alados-Arboledas, L. Global and Diffuse Shortwave Irradiance during a Strong Desert Dust Episode at Granada (Spain). *Atmospheric Res.* **2012**, *118*, 232–239, doi:10.1016/j.atmosres.2012.07.007.

326. Valenzuela, A.; Olmo, F.J.; Lyamani, H.; Antón, M.; Quirantes, A.; Alados-Arboledas, L. Aerosol Radiative Forcing during African Desert Dust Events (2005–2010) over Southeastern Spain. *Atmospheric Chem. Phys.* **2012**, *12*, 10331–10351, doi:10.5194/acp-12-10331-2012.

327. Markowicz, K.M.; Flatau, P.J.; Remiszewska, J.; Witek, M.; Reid, E.A.; Reid, J.S.; Bucholtz, A.; Holben, B. Observations and Modeling of the Surface Aerosol Radiative Forcing during UAE2. *J. Atmospheric Sci.* **2008**, *65*, 2877–2891, doi:10.1175/2007JAS2555.1.

328. Guan, H.; Schmid, B.; Bucholtz, A.; Bergstrom, R. Sensitivity of Shortwave Radiative Flux Density, Forcing, and Heating Rate to the Aerosol Vertical

Profile. *J. Geophys. Res. Atmospheres* **2010**, *115*, 2009JD012907, doi:10.1029/2009JD012907.

329. Granados-Muñoz, M.J.; Sicard, M.; Román, R.; Benavent-Oltra, J.A.; Barragán, R.; Brogniez, G.; Denjean, C.; Mallet, M.; Formenti, P.; Torres, B.; et al. Impact of Mineral Dust on Shortwave and Longwave Radiation: Evaluation of Different Vertically Resolved Parameterizations in 1-D Radiative Transfer Computations. *Atmospheric Chem. Phys.* **2019**, *19*, 523–542, doi:10.5194/acp-19-523-2019.
330. Gobbi, G.P.; Kaufman, Y.J.; Koren, I.; Eck, T.F. Classification of Aerosol Properties Derived from AERONET Direct Sun Data. *Atmos Chem Phys* **2007**.
331. Kaufman, Y.J. Aerosol Optical Thickness and Atmospheric Path Radiance. *J. Geophys. Res. Atmospheres* **1993**, *98*, 2677–2692, doi:10.1029/92JD02427.
332. Basart, S.; Perez, C.; Cuevas, E.; Baldasano, J.M.; Gobbi, G.P. Aerosol Characterization in Northern Africa, Northeastern Atlantic, Mediterranean Basin and Middle East from Direct-Sun AERONET Observations. *Atmos Chem Phys* **2009**.
333. Cachorro, V.E.; Toledano, C.; Prats, N.; Sorribas, M.; Mogo, S.; Berjón, A.; Torres, B.; Rodrigo, R.; De La Rosa, J.; De Frutos, A.M. The Strongest Desert Dust Intrusion Mixed with Smoke over the Iberian Peninsula Registered with Sun Photometry. *J. Geophys. Res. Atmospheres* **2008**, *113*, 2007JD009582, doi:10.1029/2007JD009582.
334. Obregón, M.A.; Costa, M.J.; Silva, A.M.; Serrano, A. Spatial and Temporal Variation of Aerosol and Water Vapour Effects on Solar Radiation in the Mediterranean Basin during the Last Two Decades. *Remote Sens.* **2020**, *12*, 1316, doi:10.3390/rs12081316.
335. Logothetis, S.-A.; Salamalikis, V.; Kazantzidis, A. The Impact of Different Aerosol Properties and Types on Direct Aerosol Radiative Forcing and Efficiency Using AERONET Version 3. *Atmospheric Res.* **2021**, *250*, 105343, doi:10.1016/j.atmosres.2020.105343.
336. Chen, A.; Zhao, C.; Shen, L.; Fan, T. Influence of Aerosol Properties and Surface Albedo on Radiative Forcing Efficiency of Key Aerosol Types Using Global AERONET Data. *Atmospheric Res.* **2023**, *282*, 106519, doi:10.1016/j.atmosres.2022.106519.
337. Horvath, H.; Alados Arboledas, L.; Olmo, F.J.; Jovanović, O.; Gangl, M.; Kaller, W.; Sánchez, C.; Sauerzopf, H.; Seidl, S. Optical Characteristics of the Aerosol in Spain and Austria and Its Effect on Radiative Forcing. *J. Geophys. Res. Atmospheres* **2002**, *107*, doi:10.1029/2001JD001472.
338. Lyamani, H.; Olmo, F.J.; Alcántara, A.; Alados-Arboledas, L. Atmospheric Aerosols during the 2003 Heat Wave in Southeastern Spain II: Microphysical Columnar Properties and Radiative Forcing. *Atmos. Environ.* **2006**, *40*, 6465–6476, doi:10.1016/j.atmosenv.2006.04.047.

APPENDIX A – AN UPC SDATA

Figure 9.1 contains an example of the UPC SData file and its structure.

```
SDATA version 2.0                                                    File header
1 1 1 : NX NY NT                                                     Segment header
Empty line                                                                          Cell
1 2022-04-30T07:46:31Z 0.000000  0 0 : NPIXELS TIMESTAMP HOBS NSURF IFGAS                    Cell header
1 1 1 0 0 2.112060 41.389250 0.000000 100.000000                                           Values of the
7      0.355 0.440 0.532 0.675 0.870 1.02 1.064                                            pixel structure
1 3 1 3 3 3 1
31 12 41 46 31 12 41 46 12 41 46 12 41 46 31
60 1 27 15 60 1 27 14 1 27 15 1 24 12 60
0.000000 52.489177 0.000000 52.680138 52.871271 53.257088 0.000000
9430.983624   8907.706771   8413.463865   7946.643959   7505.725492   7089.271327
       6695.924065   6324.401623   5973.493053   5642.054598   5329.005961
       5033.326785   4754.053328   4490.275322   4241.133002   4005.814310
       3783.552244   3573.622359   3375.340405   3188.060099   3011.171015
RCSn   2844.096598   2686.292282   2537.243718   2396.465093   2263.497551
heights2137.907695   2019.286176   1907.246355   1801.423049   1701.471334
at 355 1607.065427   1517.897619   1433.677275   1354.129885   1278.996171
nm     1208.031241   1141.003791   1077.695350   1017.899569   961.421549
       908.077204    857.692663    810.103701    765.155207    722.700674
       682.601724    644.727660    608.955033    575.167245    543.254168
       513.111784    484.641846    457.751559    432.353275    408.364212
       385.706179    364.305324    344.091892    325.000000
0.000000 AOD ZA at 440 nm
127.510823    127.510823    127.510823    127.510823    127.510823    127.510823
       127.510823    127.510823    127.510823    127.510823    127.510823
In ZA  127.510823    127.510823    127.510823    127.510823    127.510823
at 440 127.510823    127.510823    127.510823    127.510823    127.510823
nm     127.510823    127.510823    127.510823    127.510823    127.510823
       127.510823
127.510823    127.510823    127.510823    127.510823    127.510823    127.510823
       127.510823    127.510823    127.510823    127.510823    127.510823
       127.510823    127.510823    127.510823    127.510823 DoLP ZA at 440 nm
9430.983624   8907.706771   8413.463865   7946.643959   7505.725492   7089.271327
       6695.924065   6324.401623   5973.493053   5642.054598   5329.005961
       5033.326785   4754.053328   4490.275322   4241.133002   4005.814310
       3783.552244   3573.622359   3375.340405   3188.060099   3011.171015
RCSn   2844.096598   2686.292282   2537.243718   2396.465093   2263.497551
heights2137.907695   2019.286176   1907.246355   1801.423049   1701.471334
at 532 1607.065427   1517.897619   1433.677275   1354.129885   1278.996171
nm     1208.031241   1141.003791   1077.695350   1017.899569   961.421549
       908.077204    857.692663    810.103701    765.155207    722.700674
       682.601724    644.727660    608.955033    575.167245    543.254168
       513.111784    484.641846    457.751559    432.353275    408.364212
       385.706179    364.305324    344.091892    325.000000
0.000000 AOD ZA at 675 nm
127.319862    127.319862    127.319862    127.319862    127.319862    127.319862
       127.319862    127.319862    127.319862    127.319862    127.319862
In ZA  127.319862    127.319862    127.319862    127.319862    127.319862
at 675 127.319862    127.319862    127.319862    127.319862    127.319862
nm     127.319862    127.319862    127.319862    127.319862    127.319862
       127.319862
127.319862    127.319862    127.319862    127.319862    127.319862    127.319862
       127.319862    127.319862    127.319862    127.319862    127.319862
       127.319862    127.319862    127.319862 P ZA at 675 nm
0.000000 AOD ZA at 870 nm
```

127.128729 127.128729 127.128729 127.128729 127.128729 127.128729
127.128729 127.128729 127.128729 127.128729 127.128729
I_n ZA 127.128729 127.128729 127.128729 127.128729 127.128729
at 870 127.128729 127.128729 127.128729 127.128729 127.128729
nm 127.128729 127.128729 127.128729 127.128729 127.128729
127.128729
127.128729 127.128729 127.128729 127.128729 127.128729 127.128729
127.128729 127.128729 127.128729 127.128729 127.128729
127.128729 127.128729 127.128729 127.128729 **DoLP ZA at 870 nm**
0.000000 **AOD ZA at 1020 nm**
126.742912 126.742912 126.742912 126.742912 126.742912 126.742912
I_n ZA 126.742912 126.742912 126.742912 126.742912 126.742912
at 126.742912 126.742912 126.742912 126.742912 126.742912
1020nm 126.742912 126.742912 126.742912 126.742912 126.742912
126.742912 126.742912 126.742912
126.742912 126.742912 126.742912 126.742912 126.742912 126.742912
126.742912 126.742912 126.742912 126.742912 126.742912
126.742912 **DoLP ZA at 1020 nm**
9430.983624 8907.706771 8413.463865 7946.643959 7505.725492 7089.271327
6695.924065 6324.401623 5973.493053 5642.054598 5329.005961
5033.326785 4754.053328 4490.275322 4241.133002 4005.814310
3783.552244 3573.622359 3375.340405 3188.060099 3011.171015
RCS_n 2844.096598 2686.292282 2537.243718 2396.465093 2263.497551
heights 2137.907695 2019.286176 1907.246355 1801.423049 1701.471334
at 1064 1607.065427 1517.897619 1433.677275 1354.129885 1278.996171
nm 1208.031241 1141.003791 1077.695350 1017.899569 961.421549
908.077204 857.692663 810.103701 765.155207 722.700674
682.601724 644.727660 608.955033 575.167245 543.254168
513.111784 484.641846 457.751559 432.353275 408.364212
385.706179 364.305324 344.091892 325.000000
0.000000 0.000000 0.000000 0.000000 0.000000 0.000000
0.000000 0.000000 0.000000 0.000000 0.000000 0.000000
0.000000 0.000000 0.000000 0.000000 0.000000 0.000000
Lidar 0.000000 0.000000 0.000000 0.000000 0.000000 0.000000
AA at 0.000000 0.000000 0.000000 0.000000 0.000000 0.000000
355 nm 0.000000 0.000000 0.000000 0.000000 0.000000 0.000000
0.000000 0.000000 0.000000 0.000000 0.000000 0.000000
0.000000 0.000000 0.000000 0.000000 0.000000 0.000000
0.000000 0.000000 0.000000 0.000000 0.000000 0.000000
0.000000 **AOD AA at 440 nm**
183.500000 184.000000 185.000000 186.000000 187.000000 188.000000
190.000000 192.000000 194.000000 196.000000 198.000000
I_n AA 200.000000 205.000000 210.000000 215.000000 220.000000
at 440 225.000000 230.000000 240.000000 250.000000 260.000000
nm 270.000000 280.000000 300.000000 320.000000 340.000000
360.000000
205.000000 210.000000 215.000000 220.000000 225.000000 230.000000
240.000000 250.000000 260.000000 270.000000 280.000000
290.000000 300.000000 320.000000 340.000000 **DoLP AA at 440 nm**
0.000000 0.000000 0.000000 0.000000 0.000000 0.000000
0.000000 0.000000 0.000000 0.000000 0.000000 0.000000
0.000000 0.000000 0.000000 0.000000 0.000000 0.000000
0.000000 0.000000 0.000000 0.000000 0.000000 0.000000
Lidar 0.000000 0.000000 0.000000 0.000000 0.000000 0.000000
AA at 0.000000 0.000000 0.000000 0.000000 0.000000 0.000000
532 nm 0.000000 0.000000 0.000000 0.000000 0.000000 0.000000
0.000000 0.000000 0.000000 0.000000 0.000000 0.000000
0.000000 0.000000 0.000000 0.000000 0.000000 0.000000
0.000000 **AOD AA at 675 nm**
183.500000 184.000000 185.000000 186.000000 187.000000 188.000000
I_n AA 190.000000 192.000000 194.000000 196.000000 198.000000
at 675
nm

```
       200.000000    205.000000    210.000000    215.000000    220.000000
       225.000000    230.000000    240.000000    250.000000    260.000000
       270.000000    280.000000    300.000000    320.000000    340.000000
       360.000000
205.000000    215.000000    220.000000    225.000000    230.000000    240.000000
       250.000000    260.000000    270.000000    280.000000    290.000000
       300.000000    320.000000    340.000000 DoLP AA at 675 nm
0.000000 AOD AA at 870 nm
183.500000    184.000000    185.000000    186.000000    187.000000    188.000000
       190.000000    192.000000    194.000000    196.000000    198.000000
In AA  200.000000    205.000000    210.000000    215.000000    220.000000
at 870 225.000000    230.000000    240.000000    250.000000    260.000000
nm     270.000000    280.000000    300.000000    320.000000    340.000000
       360.000000
205.000000    210.000000    215.000000    220.000000    225.000000    230.000000
       240.000000    250.000000    260.000000    270.000000    280.000000
       290.000000    300.000000    320.000000    340.000000 DoLP AA at 870 nm
0.000000 AOD AA at 1020 nm
183.500000    184.000000    185.000000    186.000000    187.000000    188.000000
In AA  190.000000    192.000000    194.000000    196.000000    198.000000
at 1020200.000000    205.000000    210.000000    215.000000    220.000000
nm     240.000000    260.000000    270.000000    280.000000    300.000000
       320.000000    340.000000    360.000000
220.000000    225.000000    230.000000    240.000000    250.000000    260.000000
       270.000000    280.000000    290.000000    300.000000    320.000000
       340.000000 DoLP AA at 1020 nm
0.000000      0.000000      0.000000      0.000000      0.000000      0.000000
       0.000000      0.000000      0.000000      0.000000      0.000000      0.000000
       0.000000      0.000000      0.000000      0.000000      0.000000      0.000000
       0.000000      0.000000      0.000000      0.000000      0.000000      0.000000
Lidar  0.000000      0.000000      0.000000      0.000000      0.000000      0.000000
AA at  0.000000      0.000000      0.000000      0.000000      0.000000      0.000000
1064 nm0.000000      0.000000      0.000000      0.000000      0.000000      0.000000
       0.000000      0.000000      0.000000      0.000000      0.000000      0.000000
       0.000000      0.000000      0.000000      0.000000      0.000000      0.000000
       0.000000      0.000000      0.000000      0.000000      0.000000      0.000000
3.235205e-05 3.499456e-05 3.859648e-05 3.859729e-05 3.991340e-05 4.207303e-05
       4.553849e-05 4.661853e-05 4.853324e-05 5.114994e-05 5.371119e-05
       5.805997e-05 6.698741e-05 7.770562e-05 7.686882e-05 9.661808e-05
       1.122156e-04 1.241233e-04 1.353509e-04 1.421623e-04 1.510042e-04
       1.600424e-04 1.717111e-04 1.599290e-04 1.658003e-04 1.739839e-04
RCSn at 1.855721e-04 1.802826e-04 1.994135e-04 2.116139e-04 2.172807e-04
355 nm 2.211827e-04 2.257470e-04 2.309687e-04 2.370463e-04 2.422007e-04
       2.500208e-04 2.590184e-04 2.660435e-04 2.717006e-04 2.777479e-04
       2.834905e-04 2.878183e-04 2.911195e-04 2.920016e-04 2.930536e-04
       2.945489e-04 2.972082e-04 3.009704e-04 3.059760e-04 3.165599e-04
       3.291426e-04 3.426283e-04 3.559684e-04 3.635189e-04 3.658417e-04
       3.680357e-04 3.603527e-04 3.527815e-04 3.456305e-04
0.536883 AOD observation at 440 nm
5.366891      4.662807      3.614139      2.889670      2.353154      1.958590
       1.444725      1.130672      0.933216      0.801121      0.710760      0.637282
In at  0.511021      0.436356      0.384308      0.337609      0.299189      0.269268
440 nm 0.223041      0.190992      0.167025      0.150659      0.139526      0.128013
       0.123423      0.121727      1.230702e-01
0.021617      0.029316      0.039272      0.052213      0.067382      0.085183
       0.126782      0.174152      0.225500      0.274100      0.316593      0.344776
       0.365598      0.366406      3.557395e-01 DoLP observations at 440 nm
2.459130e-05 2.507059e-05 3.324104e-05 3.650624e-05 3.495119e-05 3.448266e-05
       3.815608e-05 4.100255e-05 3.965893e-05 3.971782e-05 4.298917e-05
       4.842567e-05 7.563348e-05 1.070116e-04 8.605613e-05 1.526457e-04
RCSn at 2.008720e-04 2.224746e-04 2.384552e-04 2.371968e-04 2.416190e-04
532 nm 2.443148e-04 2.598499e-04 1.749496e-04 1.693961e-04 1.725413e-04
       1.769207e-04 1.490977e-04 1.677289e-04 1.779517e-04 1.786975e-04
```

```
       1.802183e-04  1.833770e-04  1.865774e-04  1.901106e-04  1.859299e-04
       1.857340e-04  1.878158e-04  1.892320e-04  1.901221e-04  1.917422e-04
       1.917202e-04  1.896035e-04  1.877685e-04  1.842765e-04  1.826490e-04
       1.828070e-04  1.842544e-04  1.878782e-04  1.939217e-04  2.092479e-04
       2.279711e-04  2.516178e-04  2.761963e-04  2.962250e-04  3.121081e-04
       3.271100e-04  3.276721e-04  3.277644e-04  0.000328
0.446374 AOD observation at 675 nm
5.885860      5.274572      4.379156      3.706371      3.173550      2.748756
       2.108651      1.655447      1.331485      1.108891      0.958236      0.822129
In at  0.587559      0.460526      0.379700      0.314032      0.264109      0.230511
675 nm 0.181165      0.146842      0.122164      0.104731      0.094502      0.081441
       0.077209      0.073332      0.072782
0.008210      0.015221      0.021519      0.029929      0.041302      0.069529
       0.102620      0.133327      0.166354      0.193553      0.213024      0.230321
       0.225099      0.221607 DoLP observations at 675 nm
0.416922 AOD observation at 870 nm
4.825468      4.352220      3.719187      3.261325      2.888356      2.586890
       2.080620      1.676083      1.370012      1.135802      0.974125      0.827364
In at  0.594971      0.463497      0.374635      0.298663      0.245801      0.212365
870 nm 0.160078      0.129251      0.106025      0.090991      0.081156      0.071724
       0.068540      0.065434      0.064745
0.008667      0.009972      0.012630      0.017016      0.022961      0.030569
       0.049579      0.075286      0.098344      0.122698      0.140682      0.149452
       0.160166      0.158220      0.148447 DoLP observations at 870 nm
0.403245 AOD observation at 1020 nm
4.829884      4.406103      3.816737      3.341514      2.945067      2.618198
       2.074897      1.692037      1.415938      1.209644      1.051851      0.896121
In at  0.665296      0.524751      0.409734      0.325453      0.170400      0.107612
1020 nm0.087794      0.077687      0.069025      0.065857      0.063186      0.065507
0.015662      0.020978      0.027439      0.044995      0.066311      0.090502
DoLP   0.110530      0.127330      0.137381      0.140974      0.144848      0.129960
6.511948e-06  4.278355e-06  8.072752e-06  1.399703e-05  7.805442e-06  7.621685e-06
       1.023370e-05  1.748777e-05  9.167527e-06  1.183153e-05  1.164166e-05
       2.201345e-05  6.979745e-05  1.261664e-04  8.500791e-05  2.165947e-04
       3.130975e-04  3.511906e-04  3.745582e-04  3.633200e-04  3.638522e-04
       3.650901e-04  3.870495e-04  1.944810e-04  1.826550e-04  1.861181e-04
       1.811351e-04  1.338408e-04  1.598426e-04  1.674082e-04  1.673745e-04
RCSn at1.731250e-04  1.791271e-04  1.869784e-04  1.912551e-04  1.756125e-04
1064 nm1.686104e-04  1.644821e-04  1.616742e-04  1.584787e-04  1.558195e-04
       1.502622e-04  1.414473e-04  1.332441e-04  1.250702e-04  1.194549e-04
       1.160769e-04  1.141459e-04  1.142125e-04  1.164705e-04  1.259739e-04
       1.382050e-04  1.496375e-04  1.603906e-04  1.630935e-04  1.585480e-04
       1.542548e-04  1.418972e-04  1.299577e-04  1.186807e-04
0 0 0 0 0 0 0 0 0 0 0 0 0 0 0 }  Two control
0 0 0 0 0 0 0 0 0 0 0 0 0 0 0 }  rows with zeros
```

Figure 9.1. Example of a UPC SData file and its structure for the D0P+L combination (Table 4.5). ZA refers to Zenith Angle. More details about the SData structure are in Ref. [267].

APPENDIX B – HYBRID AVP

Figure 10.1 displays an attempt to build AVP hybrid profiles for fine and coarse modes. The initial idea was based on the layer separation of aerosols, corresponding to the fine and coarse modes of the particles, and completing them with a Gaussian distribution. The hybrid profile was designed to represent the aerosol structure by modes as similar as possible to the observed atmosphere in Barcelona.

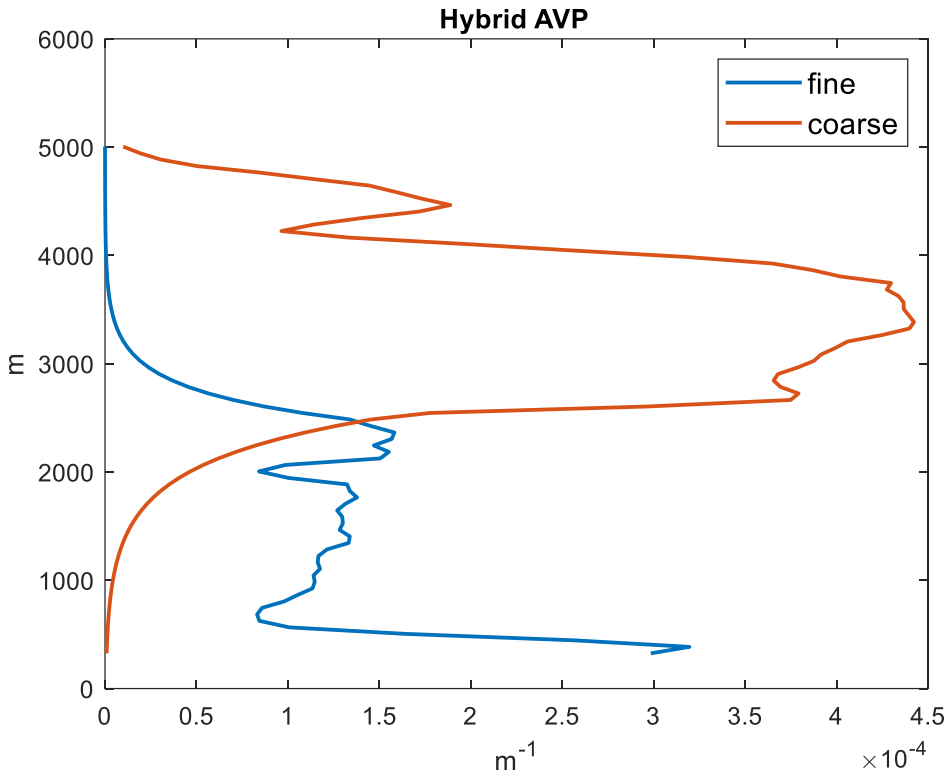

Figure 10.1. AVP hybrid profiles to create simulated data for Barcelona.

The AVP profiles were calculated with α(λ, R) from the UPC/EARLINET lidar system to be used as one of GRASP's initial guesses (Subsection 4.2.2.2). The following equations demonstrate how AVP profiles were calculated:

$$AC(\lambda, \mathrm{R}) = \frac{\alpha(\lambda, \mathrm{R})}{AOD(\lambda)} \tag{10.1}$$

where the AC is the aerosol concentration, as indicated by Equation 8 in Ref. [51], and the AOD is estimated according to Equation 2.20 from a chosen R_{min} to R_{max} at λ = 532 nm. Note that the RCS needs to have at least distinguished aerosol layers. Then:

$$AVP_f = AC(\lambda, \mathrm{R}) * FMF \tag{10.2}$$

$$AVP_c = AC(\lambda, \mathrm{R}) * (1 - FMF) \tag{10.3}$$

where f and c stand for fine and coarse modes, respectively, and FMF stands for Fine Mode Fraction from AERONET retrievals [248]. The FMF is used to obtain the contribution from fine-mode only and coarse-mode only, and it is calculated at 500 nm; thus, the difference between 532 nm in Equation 10.1 and 500 nm was neglected.

However, this approach was not carried forward due to the approach of Ref. [51] already being validated and applied. Therefore, the AVP hybrid calculation can be an initial-guess option and validated in future studies.

APPENDIX C – SPECTRAL FORCING

The AFEs at 675, 870, and 1020 nm are plotted in Figures 11.1-11.3 and summarized in Tables 11.1, 11.3, and 11.5, consecutively. The ARFs are summarized in Tables 11.2, 11.4, and 11.6 at the same wavelengths. All AFE ≥ 600 $Wm^{-2}\tau^{-1}$ (in absolute value) were deleted from this research to avoid efficiencies that are not documented in the literature. The AOD spectral dependence is propagated to the AFE-ARF spectral dependence because the direct method uses the AOD for estimating the forcing (Subsection 4.3.2). According to Ref. [40], the larger fraction of diffuse radiation concerning the total is found at larger SZAs, and when the SZA increases, radiation at the shorter wavelengths is reduced more strongly than at long wavelengths.

The AFE-ARF time series at 675 nm and 20º vary from -343 to -118 $Wm^{-2}\tau^{-1}$ (Table 11.1) and from -35 to -10 Wm^{-2} (Table 11.2), respectively. The AOD varies from 0.04 to 0.63. These results follow those found by Ref. [337], whose integrated radiative forcing was 43 Wm^{-2} at 670 nm and 20º in Almería, Spain; by Ref. [338], who obtained a forcing of -30 Wm^{-2} and an efficiency of -73 $Wm^{-2}\tau^{-1}$ at 670 nm and 20º in Granada, Spain, during the 2003 heat wave; and by Ref. [28], who calculated efficiency of 279 ± 21 $Wm^{-2}\tau^{-1}$ and radiative forcing of 23 ± 7 Wm^{-2} at 675 nm and 15º in Granada as well. The AFE and ARF vary from -524 to -11 $Wm^{-2}\tau^{-1}$ and -53 to -2 Wm^{-2} in the entire SZA range, respectively. These results are similar to those found by Ref. [80], where the AFE varied from -450 to -9 $Wm^{-2}\tau^{-1}$ and the ARF varied from -40 to -1 Wm^{-2} at 675 nm in Granada. Ref. [325] also calculated an efficiency of 115 ± 11 $Wm^{-2}\tau^{-1}$ at 675 nm and SZA < 65º in Granada.

The AFE and ARF at 870 nm (Tables 11.3 and 11.4, respectively) have variations from -560 to -39 $Wm^{-2}\tau^{-1}$ and from -47 to -5 Wm^{-2} associated with AOD, which varies from 0.007 to 0.61. These values are similar to those found by Refs. [307,325], the first one obtained 116 ± 10 $Wm^{-2}\tau^{-1}$ and the second one obtained daily efficiencies varying from -116.6 to -56.0 $Wm^{-2}\tau^{-1}$ at 868.7 nm and an SZA of 60º, even though the efficiency values have a large variability over the years for this

study. Lastly, the AFE and ARF at 1020 nm (Tables 11.5 and 11.6, respectively) show variations from -599 to -58 $Wm^{-2}\tau^{-1}$ and from -44 to -7 Wm^{-2}, with AOD varying from 0.003 to 0.60.

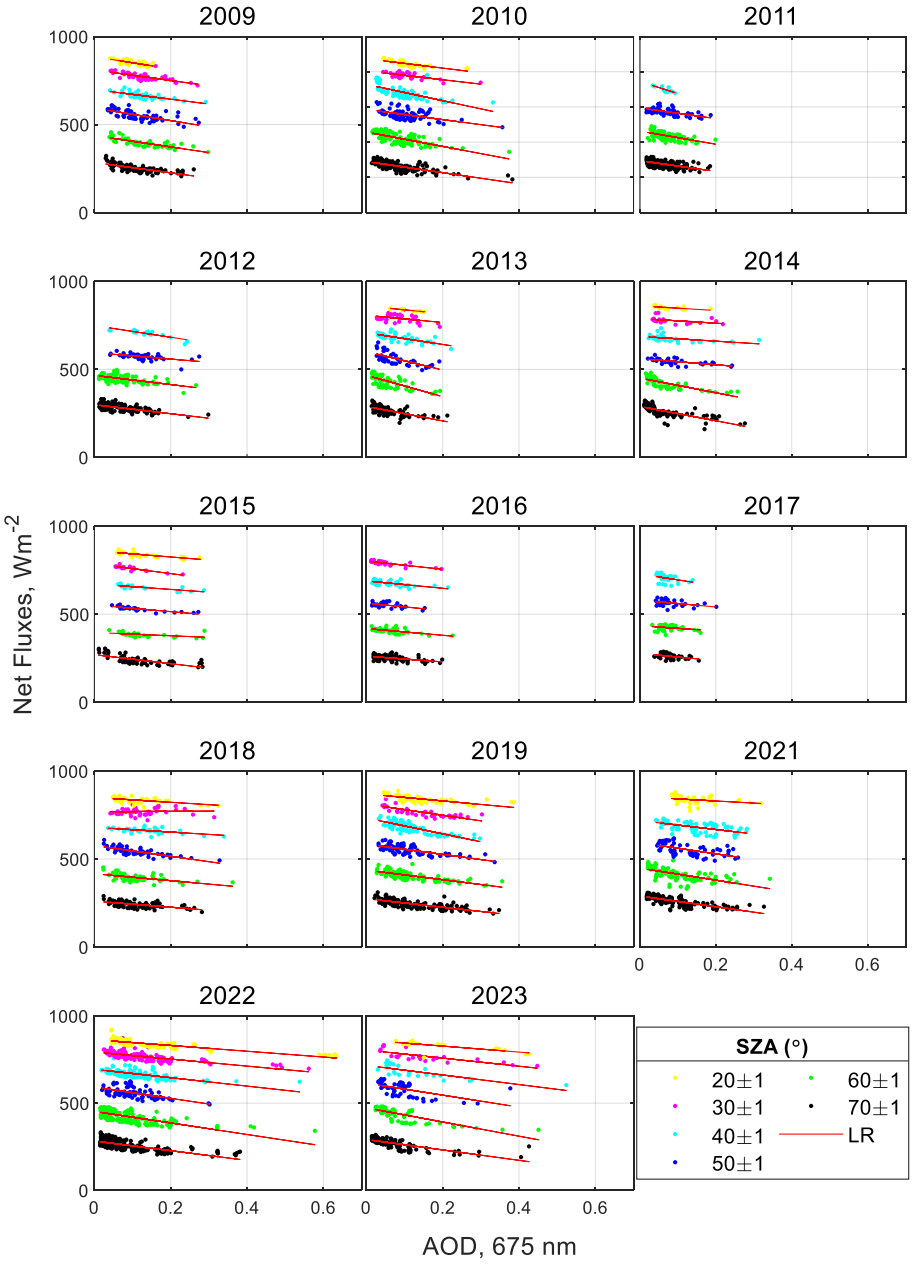

Figure 11.1. AFE Long-term from 2009 to 2023 for each SZA group at 675 nm. The LR slopes were estimated with a CI95.

Table 11.1. AFE with CI95 as a function of the AOD(675 nm) for each SZA group.

SZA / Yr	70 ± 1º	60 ± 1º	50 ± 1º	40 ± 1º	30 ± 1º	20 ± 1º
	AFE, $Wm^{-2}\,\tau^{-1}$					
2009	-295 ± 55	-323 ± 63	-355 ± 88	-274 ± 82	-300 ± 83	-343 ± 120
2010	-316 ± 47	-409 ± 69	-288 ± 112	-464 ± 109	-251 ± 89	-266 ± 58
2011	-305 ± 71	-372 ± 101	-302 ± 91	-	-	-
2012	-256 ± 47	-261 ± 75	-182 ± 87	-332 ± 86	-	-
2013	-411 ± 93	-	-524 ± 170	-330 ± 101	-203 ± 165	-216 ± 62
2014	-407 ± 70	-420 ± 80	-172 ± 76	-134 ± 94	-131 ± 130	-132 ± 85
2015	-255 ± 60	-93 ± 68	-186 ± 47	-156 ± 59	-282 ± 77	-175 ± 40
2016	-163 ± 73	-190 ± 86	-210 ± 104	-210 ± 79	-233 ± 62	-
2017	-204 ± 146	-148 ± 165	-194 ± 154	-331 ± 287	-371 ± 1845	-
2018	-172 ± 51	-195 ± 75	-306 ± 73	-134 ± 70	-	-137 ± 64
2019	-242 ± 35	-273 ± 52	-294 ± 66	-450 ± 63	-318 ± 85	-199 ± 46
2021	-306 ± 41	-341 ± 77	-319 ± 111	-253 ± 71	-11 ± 117	-119 ± 126
2022	-277 ± 30	-331 ± 37	-325 ± 102	-241 ± 56	-201 ± 26	-166 ± 15
2023	-298 ± 45	-406 ± 67	-344 ± 143	-275 ± 95	-232 ± 82	-172 ± 53

Table 11.2. ARF averages and their stds at 675 nm for each SZA group.

SZA / Yr	70 ± 1º	60 ± 1º	50 ± 1º	40 ± 1º	30 ± 1º	20 ± 1º
	AFE, $Wm^{-2}\,\tau^{-1}$					
2009	-33 ± 16	-41 ± 19	-41 ± 19	-34 ± 13	-38 ± 15	-35 ± 10
2010	-27 ± 19	-34 ± 22	-31 ± 15	-43 ± 26	-26 ± 12	-30 ± 14
2011	-20 ± 11	-26 ± 13	-22 ± 12	-	-	-
2012	-17 ± 13	-20 ± 13	-23 ± 9	-44 ± 17	-	-
2013	-25 ± 16	-	-42 ± 25	-27 ± 16	-17 ± 9	-24 ± 7
2014	-27 ± 24	-29 ± 25	-17 ± 11	-13 ± 10	-12 ± 8	-10 ± 5
2015	-29 ± 17	-12 ± 6	-22 ± 12	-20 ± 11	-28 ± 14	-22 ± 11
2016	-11 ± 7	-12 ± 8	-11 ± 7	-13 ± 9	-12 ± 11	-
2017	-16 ± 5	-11 ± 4	-16 ± 7	-24 ± 7	-24 ± 3	-
2018	-19 ± 10	-21 ± 12	-34 ± 18	-19 ± 8	-	-16 ± 9
2019	-31 ± 18	-34 ± 20	-35 ± 20	-53 ± 26	-47 ± 23	-28 ± 15
2021	-27 ± 20	-32 ± 22	-39 ± 19	-36 ± 17	-2 ± 1	-18 ± 7
2022	-23 ± 19	-25 ± 23	-34 ± 18	-27 ± 17	-23 ± 17	-21 ± 19
2023	-21 ± 20	-33 ± 29	-33 ± 22	-37 ± 30	-36 ± 27	-33 ± 21

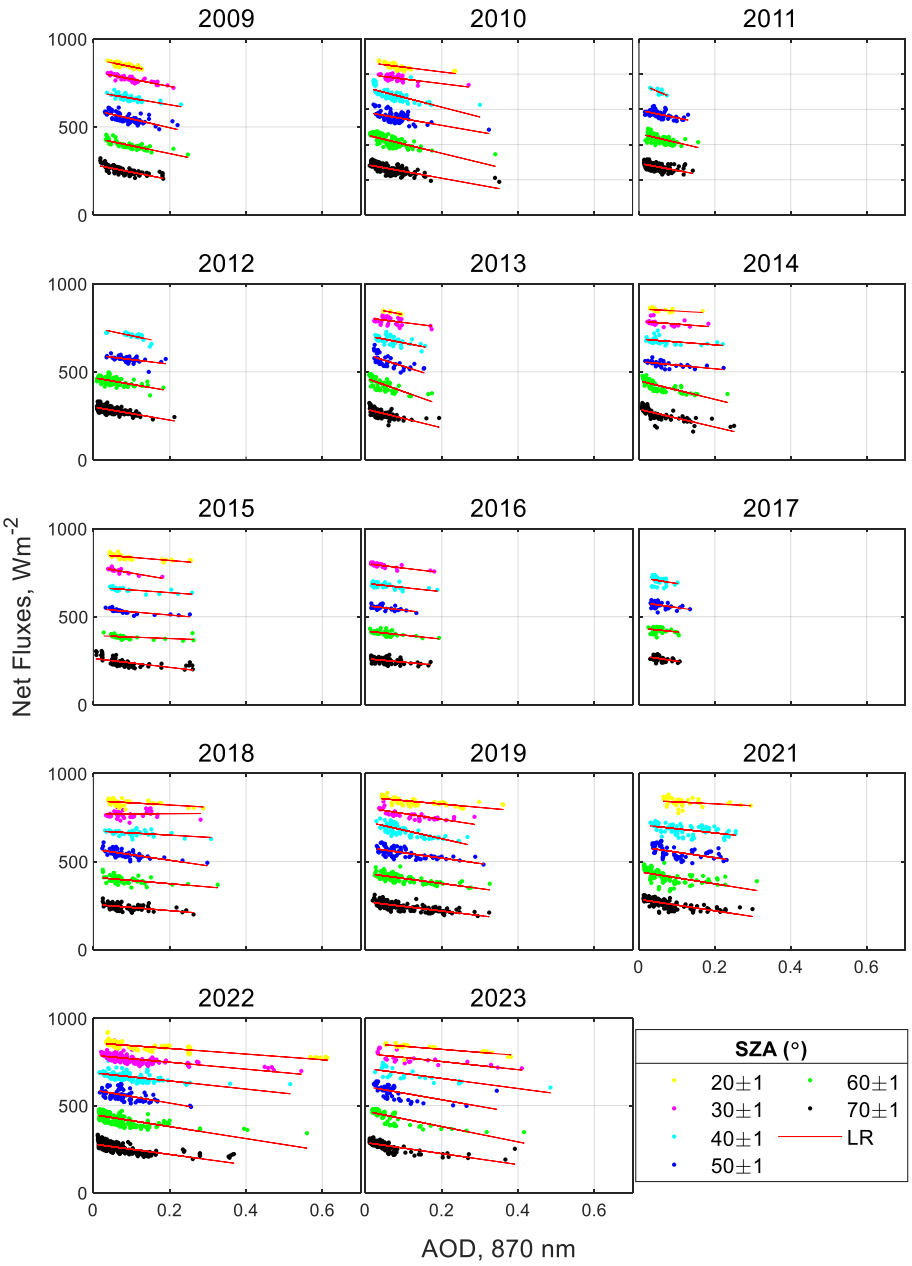

Figure 11.2. AFE Long-term from 2009 to 2023 for each SZA group at 870 nm. The LR slopes were estimated with a CI95.

Table 11.3. AFE with CI95 as a function of the AOD(870 nm) for each SZA group.

SZA / Yr	70 ± 1º	60 ± 1º	50 ± 1º	40 ± 1º	30 ± 1º	20 ± 1º
	AFE, $Wm^{-2}\,\tau^{-1}$					
2009	-426 ± 76	-448 ± 86	-503 ± 122	-366 ± 103	-417 ± 103	-437 ± 118
2010	-392 ± 61	-527 ± 90	-377 ± 139	-560 ± 144	-267 ± 115	-271 ± 81
2011	-406 ± 104	-508 ± 147	-431 ± 154	-	-	-
2012	-371 ± 67	-375 ± 109	-261 ± 140	-458 ± 184	-	-
2013	-534 ±124	-	-	-420 ± 155	-270 ± 202	-407 ± 113
2014	-505 ± 89	-527 ± 112	-205 ± 103	-164 ± 128	-168 ± 180	-127 ± 111
2015	-252 ± 74	-84 ± 74	-186 ± 61	-154 ± 75	-371 ± 120	-179 ± 48
2016	-200 ± 89	-229 ± 98	-261 ± 130	-236 ± 93	-259 ± 73	-
2017	-321 ± 209	-217 ± 244	-304 ± 229	-347 ± 390	-	-
2018	-179 ± 66	-183 ± 95	-314 ± 103	-124 ± 82	-	-123 ± 71
2019	-263 ± 41	-288 ± 62	-304 ± 77	-489 ± 83	-332 ± 106	-194 ± 52
2021	-324 ± 50	-342 ± 95	-314 ± 127	-237 ± 80	-39 ± 122	-109 ± 129
2022	-297 ± 36	-344 ± 45	-378 ± 123	-233 ± 65	-199 ± 29	-161 ± 17
2023	-316 ± 51	-440 ± 79	-381 ± 155	-290 ± 104	-233 ± 94	-175 ± 58

Table 11.4. ARF averages and their stds at 870 nm for each SZA group.

SZA / Yr	70 ± 1º	60 ± 1º	50 ± 1º	40 ± 1º	30 ± 1º	20 ± 1º
	AFE, $Wm^{-2}\,\tau^{-1}$					
2009	-34 ± 16	-42 ± 19	-44 ± 20	-35 ± 13	-41 ± 16	-35 ± 11
2010	-25 ± 18	-32 ± 22	-30 ± 16	-39 ± 25	-21 ± 11	-23 ± 12
2011	-19 ± 10	-26 ± 12	-23 ± 11	-	-	-
2012	-17 ± 13	-21 ± 13	-24 ± 8	-46 ± 15	-	-
2013	-24 ± 16	-	-	-26 ± 14	-17 ± 10	-30 ± 7
2014	-24 ± 24	-27 ± 24	-15 ± 10	-11 ± 9	-11 ± 7	-7 ± 4
2015	-21 ± 15	-8 ± 5	-16 ± 11	-15 ± 10	-26 ± 13	-17 ± 10
2016	-11 ± 7	-12 ± 8	-12 ± 7	-13 ± 9	-12 ± 10	-
2017	-18 ± 6	-12 ± 4	-18 ± 8	-18 ± 5	-	-
2018	-15 ± 9	-16 ± 10	-27 ± 16	-13 ± 7	-	-12 ± 8
2019	-27 ± 17	-29 ± 19	-30 ± 19	-47 ± 25	-40 ± 22	-24 ± 14
2021	-23 ± 19	-24 ± 19	-30 ± 18	-27 ± 16	-5 ± 2	-13 ± 6
2022	-19 ± 18	-21 ± 21	-31 ± 17	-21 ± 15	-17 ± 16	-17 ± 18
2023	-17 ± 19	-27 ± 29	-28 ± 22	-34 ± 30	-30 ± 25	-29 ± 20

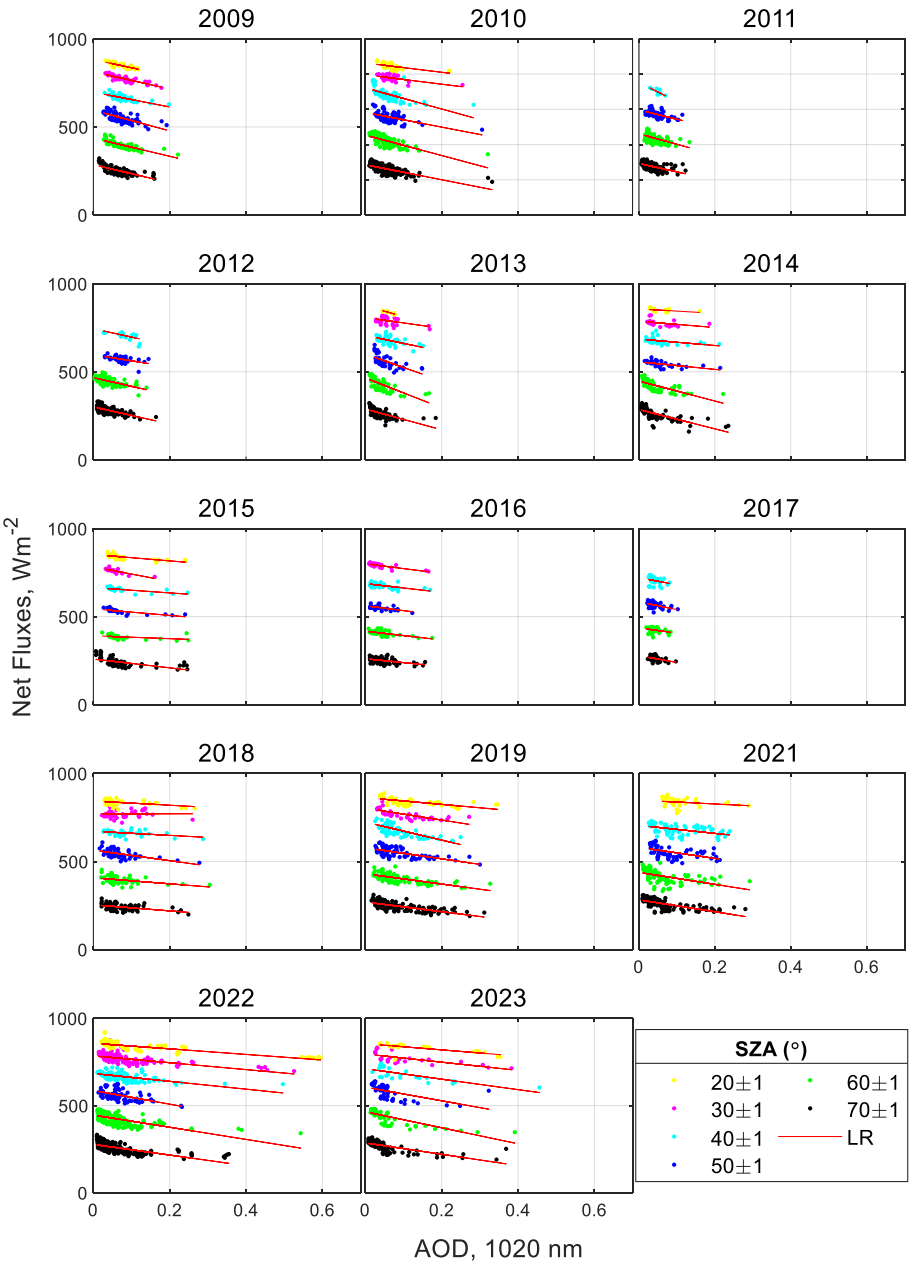

Figure 11.3. AFE Long-term from 2009 to 2023 for each SZA group at 1020 nm. The LR slopes were estimated with a CI95.

Table 11.5. AFE with CI95 as a function of the AOD(1020 nm) for each SZA group.

SZA / Yr	70 ± 1º	60 ± 1º	50 ± 1º	40 ± 1º	30 ± 1º	20 ± 1º
	AFE, $Wm^{-2}\,\tau^{-1}$					
2009	-512 ± 93	-513 ± 104	-585 ± 150	-421 ± 116	-487 ± 118	-461 ± 122
2010	-426 ± 70	-580 ± 104	-418 ± 154	-599 ± 166	-268 ± 129	-263 ± 93
2011	-476 ± 118	-592 ± 167	-525 ± 192	-	-	-
2012	-484 ± 83	-493 ± 128	-343 ± 183	-475 ± 251	-	-
2013	-589 ± 143	-	-	-453 ± 190	-303 ± 220	-588 ± 177
2014	-548 ± 100	-567 ± 132	-215 ± 117	-181 ± 148	-175 ± 202	-125 ± 121
2015	-249 ± 82	-81 ± 77	-186 ± 68	-151 ± 82	-412 ± 149	-181 ± 52
2016	-218 ± 98	-248 ± 104	-277 ± 149	-248 ± 101	-273 ± 80	-
2017	-382 ± 253	-296 ± 303	-442 ± 285	-408 ± 444	-	-
2018	-172 ± 74	-172 ± 104	-299 ± 119	-118 ± 87	-	-120 ± 74
2019	-273 ± 44	-292 ± 66	-315 ± 81	-513 ± 90	-338 ± 115	-193 ± 55
2021	-338 ± 55	-339 ± 104	-314 ± 134	-228 ± 85	-58 ± 126	-108 ± 131
2022	-305 ± 40	-348 ± 49	-392 ± 138	-224 ± 70	-197 ± 31	-160 ± 19
2023	-326 ± 55	-459 ± 81	-392 ± 164	-300 ± 111	-235 ± 101	-178 ± 62

Table 11.6. ARF averages and their stds at 1020 nm for each SZA group.

SZA / Yr	70 ± 1º	60 ± 1º	50 ± 1º	40 ± 1º	30 ± 1º	20 ± 1º
	AFE, $Wm^{-2}\,\tau^{-1}$					
2009	-34 ± 16	-40 ± 18	-43 ± 19	-34 ± 13	-41 ± 16	-32 ± 11
2010	-23 ± 18	-30 ± 22	-28 ± 16	-36 ± 23	-18 ± 10	-19 ± 11
2011	-18 ± 11	-25 ± 13	-24 ± 11	-	-	-
2012	-18 ± 13	-21 ± 14	-25 ± 8	-39 ± 13	-	-
2013	-24 ± 15	-	-	-26 ± 13	-18 ± 10	-38 ± 7
2014	-23 ± 24	-26 ± 23	-13 ± 9	-11 ± 9	-10 ± 7	-7 ± 4
2015	-18 ± 14	-7 ± 5	-14 ± 10	-13 ± 9	-24 ± 13	-15 ± 10
2016	-10 ± 7	-11 ± 8	-11 ± 7	-11 ± 9	-11 ± 10	-
2017	-17 ± 6	-13 ± 5	-20 ± 9	-17 ± 6	-	-
2018	-12 ± 8	-12 ± 9	-21 ± 14	-11 ± 6	-	-10 ± 7
2019	-25 ± 17	-27 ± 18	-28 ± 18	-44 ± 24	-37 ± 21	-21 ± 14
2021	-21 ± 18	-21 ± 18	-26 ± 17	-23 ± 14	-7 ± 4	-12 ± 6
2022	-17 ± 17	-18 ± 20	-28 ± 16	-17 ± 13	-16 ± 15	-14 ± 18
2023	-15 ± 19	-24 ± 29	-24 ± 22	-32 ± 29	-27 ± 24	-27 ± 20

Table 11.7 summarizes the percentages of the CI95s to their AFEs and the percentages of the standard deviations to their ARF averages. Table 11.8 shows the number of clear-sky days and dust days, and sample sizes of net fluxes as a function of the AOD for each SZA and year presented in Figure 6.5.

Table 11.7. Ratio between CI95s and AFEs and between standard deviations and ARF averages by SZA and years at 440 nm. The ratios were calculated from Tables 6.1 and 6.2.

SZA / Yr	20 ± 1º	30 ± 1º	40 ± 1º	50 ± 1º	60 ± 1º	70 ± 1º
	CI95/AFE (%), Standard Deviation/ARF (%)					
2009	58, 26	33, 39	31, 36	23, 49	0.2, 46	18, 49
2010	17, 40	29, 39	21, 58	36, 46	17, 61	14, 63
2011	-	-	65, 33	28, 59	27, 50	21, 57
2012	-	-	23, 51	37, 37	27, 67	18, 77
2013	33, 33	112, 50	29, 59	32, 61	22, 77	21, 68
2014	43, 40	91, 62	61, 79	42, 61	19, 89	18, 86
2015	24, 37	24, 47	26, 40	21, 39	51, 35	18, 49
2016	-	27, 69	36, 63	54, 58	48, 53	43, 54
2017	-	-	59, 27	74, 47	101, 42	96, 33
2018	35, 38	670, 50	39, 36	19, 50	27, 50	26, 48
2019	18, 41	24, 44	13, 42	21, 44	18, 46	16, 47
2021	84, 27	-	21, 38	30, 38	17, 61	11, 61
2022	6, 63	10, 54	16, 48	30, 47	9, 77	9, 75
2023	27, 49	29, 56	33, 66	45, 51	18, 70	13, 75

Table 11.8. Number of clear-sky days, including dust days, and sample size of the net fluxes as a function of the AOD(440 nm) for each SZA group by year, as shown in Figure 6.5.

SZA / Yr	20 ± 1º	30 ± 1º	40 ± 1º	50 ± 1º	60 ± 1º	70 ± 1º	Total*	Dust Days
	Number of Days, Sample Sizes							
2009	10, 40	20, 52	23, 44	23, 74	31, 62	34, 104	35, 376	4
2010	13, 50	18, 37	29, 79	35, 74	52, 122	56, 161	58, 523	1
2011	-	-	4, 10	23, 69	32, 103	50, 148	51, 330	3
2012	-	-	6, 24	17, 46	33, 95	45, 146	45, 311	1
2013	4, 12	14, 33	23, 48	24, 45	29, 67	32, 104	35, 309	1
2014	7, 21	14, 21	16, 30	17, 33	25, 69	31, 103	32, 277	3
2015	15, 44	13, 18	16, 20	15, 27	15, 28	19, 76	19, 213	3
2016	-	13, 31	19, 43	18, 34	21, 42	21, 73	21, 223	2
2017	-	-	18, 40	21, 33	23, 41	21, 42	23, 156	-
2018	13, 44	20, 51	22, 37	28, 53	28, 55	27, 89	28, 329	5
2019	19, 71	26, 40	39, 90	45, 80	48, 87	45, 147	49, 515	19
2021	10, 40	-	25, 85	27, 69	34, 114	42, 164	42, 472	11
2022	22, 209	37, 209	40, 150	35, 84	59, 298	70, 337	72, 1287	9
2023	8, 28	13, 24	14, 25	19, 54	30, 86	35, 144	36, 361	6

* The total does not include repeated days.

APPENDIX D – AERONET DEFINITIONS

The AERONET inverts the Aerosol Radiative Forcing (ARF_{aer}) and Aerosol Forcing Efficiency (AFE_{aer}) at BOA [237], confirming the equations below:

$$ARF_{aer} = F_{BOA}^{\downarrow} - F_{BOA}^{\downarrow 0} \quad (12.1)$$

$$AFE_{aer} = ARF_{aer}/AOD(550\,nm) \quad (12.2)$$

where $\downarrow$ stands for downward flux in Wm^{-2} and 0 stands for aerosol-free condition in the atmosphere. However, the radiative properties retrieved by the GRASP algorithm are estimated by Equations 3.21 and 3.22 according to Ref. [272].

APPENDIX E – PUBLICATIONS AND OTHERS

E.1 JOURNAL PAPERS

- Gil-Díaz, C.; Sicard, M.; Nabat, P.; Mallet, M.; Muñoz, C.; Comeron, A.; Rodriguez-Gomez, A.; **Oliveira, D.C.F.S. Dust Aerosol Radiative Effects During a Dust Event and Heatwave in Summer 2019 Simulated with a Regional Climate Atmospheric Model over the Iberian Peninsula.** *Remote sensing*. **2025**. Volume: 17. Number: 11. <https://doi.org/ 10.3390/rs17111817>
- **Oliveira, D.C.F.S.**; Sicard, M.; Rodriguez-Gomez, A.; Comeron, A.; Muñoz, C.; Gil-Díaz, C.; Dubovik, O.; Derimian, Y.; Lopatin, A. **Aerosol Forcing from Ground-Based Synergies over a Decade in Barcelona, Spain.** *Remote sensing*. **2025**. Volume: 17. Number: 8. <https://doi.org/10.3390/rs17081439>
- Gil-Díaz, C.; Sicard, M.; Sourdeval, O.; Saiprakash, A.; Muñoz, C.; Comeron, A.; Rodriguez-Gomez, A.; **Oliveira, D.C.F.S. Study of optical scattering properties and direct radiative effects of high-altitude cirrus clouds in Barcelona, Spain, with 4 years of lidar measurements.** *Atmospheric chemistry and physics*. **2025**. Volume: 25. Number: 6. pp.: 3445 ~ 3464. <https://doi.org/10.5194/acp-25-3445-2025>
- Münchow, G. B.; Oliveira, A. M.; Duarte, E. F. S.; **Oliveira, D.C.F.S.**; Araujo, B. M.; Rosário, N. M. E.; Hoelzemann, J. J. **Aerosol optical depth over Northeastern Brazil: A multi-platform intercomparison study.** *Atmospheric research*. **2024**. Volume: 315. Number: article 107864. <https://doi.org/10.1016/j.atmosres.2024.107864>
- Gil-Díaz, C.; Sicard, M.; Comeron, A.; **Oliveira, D.C.F.S.**; Muñoz, C.; Rodriguez-Gomez, A.; Lewis, J.; Welton, E.; Lolli, S. **Geometrical and optical properties of cirrus clouds in Barcelona, Spain: analysis with the two-way transmittance method of 4 years of lidar measurements.** *Atmospheric measurement techniques*. **2024**. Volume: 17. Number: 4. pp.: 1197 ~ 1216. <https://doi.org/10.5194/amt-17-1197-2024>
- **Oliveira, D.C.F.S.**; Sicard, M.; Rodriguez-Gomez, A.; Comeron, A.; Muñoz, C.; Gil-Díaz, C.; Lolli, S.; Dubovik, O.; Lopatin, A.; Herrera, M.; Herreras, M. **Evaluation of the accuracy of the aerosol optical and microphysical retrievals by the GRASP algorithm from combined measurements of a polarized sun-sky-lunar photometer and a three-wavelength elastic lidar.** *Remote sensing*. **2023**. Volume: 15. Number: 20, article 5010. <https://doi.org/10.3390/rs15205010>
- Lolli, S.; Sicard, M.; Amato, F.; Comeron, A.; Gil-Díaz, C.; Landi, T.; Muñoz, C.; **Oliveira, D.C.F.S.**; Dios, V.; Rocadenbosch, F.; Rodriguez-Gomez, A.; Alastuey, A.; Querol, X.; Reche, C. **Climatological assessment of the vertically resolved optical and microphysical aerosol properties by lidar measurements, sun photometer, and in situ observations over 17 years at Universitat Politècnica de Catalunya (UPC) Barcelona.** *Atmospheric chemistry and physics*. **2023**. Volume: 23. Number: 19. pp.: 12887 ~ 12906. <https://doi.org/10.5194/acp-23-12887-2023>

- Comeron, A.; Muñoz, C.; Rodriguez-Gomez, A.; Sicard, M.; Dios, V.; Gil-Díaz, C.; **Oliveira, D.C.F.S.**; Rocadenbosch, F. **An explicit formulation for the retrieval of the overlap function in an elastic and Raman aerosol lidar.** *Atmospheric measurement techniques*. **2023**. Volume: 16. Number: 11. pp.: 3015 ~ 3025. <https://doi.org/10.5194/amt-16-3015-2023>
- Sicard, M.; **Oliveira, D.C.F.S.**; Muñoz, C.; Gil-Díaz, C.; Comeron, A.; Rodriguez-Gomez, A.; Dios, V. **Measurement report: Spectral and statistical analysis of aerosol hygroscopic growth from multi-wavelength lidar measurements in Barcelona, Spain.** *Atmospheric chemistry and physics*. **2022**. Volume: 22. Number: 11. pp.: 7681 ~ 7697. <https://doi.org/10.5194/acp-22-7681-2022>
- **Oliveira, D.C.F.S.**; Montilla-Rosero, E.; Lopes, F.J.S.; Morais, F.G.; Landulfo, E.; Hoelzemann, J.J. **Aerosol properties in the atmosphere of Natal/Brazil measured by an AERONET Sun-photometer.** *Environmental Science and Pollution Research.* 2021. Volume: 28. pp.: 9806 ~ 9823. <https://doi.org/10.1007/s11356-020-11373-z>

E.2 CONFERENCE PROCEEDINGS

- **Oliveira, D.C.F.S.**; Rodriguez-Gomez, A.; Comeron, A.; Muñoz, C.; Dubovik, O.; Lopatin, A.; Herrera, M.; Sicard, M. **First results of inverted aerosol properties through GRASP algorithm, using polarized data from the multiwavelength sun-sky-lunar photometer in Barcelona, Spain**. *Proceedings of the 30th International Laser Radar Conference*. Springer. **2023**. ISBN/ISSN: 978-3-031-37817-1. <https://link.springer.com/book/10.1007/978-3-031-37818-8>
- Lolli, S.; Sicard, M.; Comeron, A.; Gil-Díaz, C.; **Oliveira, D.C.F.S.**; Landi, T.; Rodriguez-Gomez, A.; Muñoz, C.; Rocadenbosch, F.; Dios, V. **Analysis of atmospheric aerosol properties using lidar measurements and their impact on radiative budget in Barcelona over the past 20 years**. *Remote Sensing of Clouds and the Atmosphere XXVIII: 3-7 September 2023*. International Society for Photo-Optical Instrumentation Engineers (SPIE). **2023**. <https://www.spiedigitallibrary.org/conference-proceedings-of-SPIE/12730.toc>
- Rodriguez-Gomez, A.; Muñoz, C.; Zenteno-Hernández, J. A.; Comeron, A.; Dios, V.; Sicard, M.; Gil-Díaz, C.; **Oliveira, D.C.F.S.**; Mandal, C. **Use of pure rotational Raman channels for lidar measurement of aerosol extinction coefficient: the EARLINET/ACTRIS Barcelona station experience**. *Remote Sensing of Clouds and the Atmosphere XXVII: 5 September 2022, Berlin, Germany*. International Society for Photo-Optical Instrumentation Engineers (SPIE). **2022**. pp.: 1226507-1 ~ 1226507-11. ISBN/ISSN: 9781510655331. <https://www.spiedigitallibrary.org/conference-proceedings-of-spie/12265.toc>

E.3 PRESENTATION OF CONFERENCE PAPERS

- **Oliveira, D.C.F.S.**; Sicard, M.; Rodriguez-Gomez, A.; Comeron, A.; Muñoz, C.; Gil-Díaz, C.; Dubovik, O.; Herrera, M. **Noise-free sensitivity test for lidar volume depolarization ratio and sun-photometer DoLP in GRASP code for a case study**. *31st International Laser Radar Conference*. **27/06/2024**.

- **Oliveira, D.C.F.S.**; Sicard, M.; Rodriguez-Gomez, A.; Comeron, A.; Muñoz, C.; Gil-Díaz, C.; Dubovik, O.; Herrera, M. **Aerosol retrievals by combining lidar volume depolarization ratio and sun-photometer DoLP in the GRASP code**. *ACTRIS Science Conference 2024*. **15/05/2024**.
- **Oliveira, D.C.F.S.**; Sicard, M.; Rodriguez-Gomez, A.; Comeron, A.; Muñoz, C.; Gil-Díaz, C. **Analysis of radiative fluxes and aerosol optical depths over 14 years in Barcelona, Spain**. *ACTRIS Science Conference 2024*. **15/05/2024**.
- **Oliveira, D.C.F.S.**; Muñoz, C.; Comeron, A.; Rodriguez-Gomez, A.; Sicard, M. **Aerosol vertical hygroscopic growth from multi-wavelength lidar measurements in Barcelona, NE Spain: a spectral analysis**. *European Lidar Conference 2021*. **17/11/2021**.

E.4 STAYS IN R&D CENTERS

- **Guest. Laboratorie de l'Atmosphère et des Cyclones, Saint-Denis, La Réunion**. Purpose: Research. Comparable tasks: The secondment is associated with task 3.2 (Enhancement of UR student's scientific excellence and UR attracting capacity) from work package WP3 (Competence raising through capacity building) of the REALISTIC project. **01/09/2024 - 30/11/2024**.
- **Guest. Generalized Retrieval of Atmosphere and Surface Properties - GRASP SAS, Lezennes, France**. Purpose: Research. Comparable tasks: change in methodology for calculating the initial guesses; configuration of initial guesses, surface land BRDF Ross-Li and surface land polarized Maignan-Breon; and beginning of the scientific discussion of the first aerosol scenario. **01/03/2023 - 31/03/2023**.
- **Guest. Generalized Retrieval of Atmosphere and Surface Properties - GRASP SAS, Lezennes, France**. Purpose: Research. Comparable tasks: hands-on training of the parametrization and use of GRASP to invert both the UPC lidar system and MPL data + AERONET measurements during daytime and nighttime; optimization of the parametrization of the automatic GARRLiC inversions performed by ICARE/AERIS with the UPC lidar system + AERONET measurements during daytime and nighttime; and implementation in ICARE/AERIS and optimization of the parametrization of the automatic GARRLiC inversions with the UPC MPL + AERONET measurements during daytime and nighttime. **01/09/2021 - 30/11/2021**.

E.5 PARTICIPATION IN R&D CALLS

- **Teamwork**. **Synergetic passive and active remote sensing of the vertical profiling of atmospheric aerosols: Estimation of their contribution to the Earth energy budget**. Scientific coordinator: Muñoz, C.; Rodriguez-Gomez, A. 01/09/2024 - 31/12/2027. Duration: 03 years and 04 months. Funding: 203.750,00 €. Scope: National. Institution in which the research was undertaken: Department of Signal Theory and Communications. Funding body: AGENCIA ESTATAL DE INVESTIGACION.
- **Researcher**. **Solutions for Sustainable Access to Atmospheric Research Facilities**. Scientific coordinator: Rodriguez-Gomez, A.; Comeron, A. 01/04/2021

- 30/09/2025. Duration: 04 years and 06 months. Funding: 52.012,00 €. Scope: European. Institution in which the research was undertaken: Department of Signal Theory and Communications. Funding body: Commission of European Communities.

- **Researcher**. **Aerosol, Clouds and Trace Gases Research Infrastructure Implementation Project**. Scientific coordinator: Rodriguez-Gomez, A.; Comeron, A. 01/01/2020 - 31/12/2023. Duration: 04 years. Funding: 17.362,50 €. Scope: European. Institution in which the research was undertaken: Department of Signal Theory and Communications. Funding body: Commission of European Communities.
- **Research Assistant**. **Development of GRASP radiative transfer code for the retrieval of aerosol microphysics vertical-profiles from space measurements and its impact in ACE mission**. Scientific coordinator: Sicard, M.; Rodriguez-Gomez, A. 22/03/2019 - 28/08/2023. Duration: 04 years, 05 months, and 07 days. Funding: 36.000,00 €. Scope: European. Institution in which the research was undertaken: Department of Signal Theory and Communications. Funding body: Commission of European Communities.